The Copper(I)-catalyzed Azide–Alkyne Cycloaddition: A Modular Approach to Synthesis and Single-Molecule Spectroscopy Investigation into Heterogeneous Catalysis

Matthew Decan

Thesis submitted to the
Faculty of Graduate & Postdoctoral Studies
University of Ottawa
in partial fulfillment of the requirements for the degree of
Doctor of Philosophy in the

Ottawa-Carleton Chemistry Institute

uOttawa

Candidate	Supervisor
Matthew Decan	Professor J.C. Scaiano

© Matthew Decan, Ottawa, Canada, 2015

Abstract

Click chemistry is a molecular synthesis strategy based on reliable, highly selective reactions with thermodynamic driving forces typically in excess of 20 kcal mol^{-1}. The 1,3-dipolar cycloaddition of azides and alkynes developed by Rolf Huisgen saw dramatic rate acceleration using Cu(I) as a catalyst in 2002 reports by Barry Sharpless and Morten Meldal enabling its click chemistry eligibility. Since these seminal reports, the copper(I)-catalyzed azide-alkyne cycloaddition (CuAAC) has become the quintessential click reaction finding diverse utility.

The popularity of the CuAAC has naturally led to interest in new catalyst systems with improved efficiency, robustness, and reusability with particular focus on nanomaterial catalysts, a common trend across the field of catalysis. The high surface area of nanomaterials lends to their efficacy as colloidal and heterogeneous nanocatalysts, but the latter boasts the added benefit of easy separation and recyclability. With any heterogeneous catalyst, a common question arises as to whether the active catalyst species is truly heterogeneous or rather homogeneous through metal ion leaching. Differentiating these processes is critical, as the latter would result in reduced efficiency, higher cost, and inevitable environmental and heath side effects.

This thesis explores the CuAAC from an interdisciplinary approach. First as a synthetic tool, applying CuAAC-formed triazoles as functional, modular building blocks in the synthesis of optical cation sensors by combining azide and alkyne modified components to create a series of sensors selective for different metal cations. Next, single-molecule spectroscopy techniques are employed to observe the CuNP-catalyzed CuAAC in real time. Combining bench-top techniques with single-molecule microscopy to monitor single-catalytically generated products proves to be an effective method to establish catalysis occurs directly at the surface of copper nanoparticles, ruling out catalysis by ions leached into solution. This methodology is extended to mapping the catalytic activity of a commercial heterogeneous catalyst by applying super-localization analysis of single-catalytic events.

The approach detailed herein is a general one that can be applied to any catalytic system through the development of appropriate probes. This thesis demonstrates single-molecule microscopy as an accessible, effective, and unparalleled tool for exploring the catalytic activity of nanomaterials by monitoring single-catalytic events as they occur.

Acknowledgements

I am incredibly fortunate to have many wonderful people in my life to thank for their support and assistance during my studies, though this makes if difficult to decide where to begin.

First, I would never be where I am today without the amazing and endless support of my parents. For them it seems like there was never a choice, they allowed me to take my own path but were behind me every step of the way. Thank you so much for this and setting the bar to which I will always strive to meet.

Tito, you are an incredible scientist, supervisor, teacher, mentor, father, husband, ...the list is endless but every role fits you perfectly, or more accurately you fit every role perfectly. You make finding the balance look easy, I know it never is but you are proof that it is possible. I have had the experience of a lifetime working with you, learning from you. Thank you for your guidance, patience, your always-clever anecdotes and your famous BBQ weekends. I owe you a scotch!

Thanks to the Scaiano group. Such a dynamic bunch of individuals with a closeness than can only be described as family. There are too many names to list, but you know who you are. Thanks not only for all the great times, but also for the critical feedback that helps me improve. This open communication and cooperation are key reagents for quality, exciting science.

Finally, to my beautiful, talented, brilliant and caring wife Nathalie, words cannot express the thanks I feel everyday for having you in my life. Your smile makes the world a brighter place; your enthusiasm can make even the most daunting task seem trivial. You are truly my better half. Our synergy is invaluable, not only in our everyday lives, but in the inevitable scientific discussions at home. You are always ready with answers to my random queries in molecular biology, and I very much enjoy sharing my chemical knowledge with you. Together we made it through the gauntlet of grad studies, the future is an adventure lying ahead and I can’t wait to go on it with you.

Contents

3 Copper Nanoparticle Heterogeneous Catalytic ‘Click’ Cycloaddition Confirmed by Single-Molecule Spectroscopy 85

List of Abbreviations

AF488alkyne	Alexa Fluor 488 alkyne
AF594azide	Alexa Fluor 594 azide
APTES	3-aminopropyltriethoxysilane
AuNP	Gold nanoparticles
BaLM	Bleaching/blinking assisted localization microscopy
BOC	*tert*-butyloxycarbonyl
$(Boc)_2O$	di-*tert*-butyl dicarbonate
BODIPY	Boron-dipyrromethene (4,4-difluoro-4-bora-3a,4a-diaza-s-indacene) fluorophore
BP	Bandpass
COMPO	Backscattered electron composition
$C_{16}TAB$	Hexadecyltrimethylammonium bromide
Cu@MCM-41	Copper nanoparticles supported on MCM-41
Cu/C	Copper-in-charcoal
CuAAC	Copper-catalyzed azide-alkyne cycloaddition
$CuFe_2O_4$ NP	Copper ferrite nanoparticle(s)
CuNP	Copper nanoparticles
Cu_3N	Copper nitride
CuONP	Copper(II) oxide nanoparticle(s)
Cu_2ONP	Copper(I) oxide nanoparticle(s)
d	Evanescent field penetration depth
DCC	*N,N*-dicyclohexylcarbodiimide
DFT	Density functional theory
DMAP	4-(dimethylamino)pyridine
DMF	*N,N*-dimethylformamide
DMSO	Dimethylsulfoxide

Em	Emission
EM-CCD	Electron multiplying charged coupled device
ESI	Electrospray-ionization
EtOAc	Ethyl acetate
Ex	Excitation
FeNP	Iron (oxide) nanoparticles
FRET	Förster resonance energy transfer
FWHM	Full-width at half-maximum
GC-MS	Gas chromatography-mass spectrometry
HEPES	4-(2-hydroxyethyl)-1-piperazineethanesulfonic acid
HRMS	High-resolution mass spectrometry
hν	Light (photon)
HWHM	Half-width at half-maximum
I	Intensity
ICP-OES	Inductively coupled plasma optical emission spectrometry
ICT	Internal charge transfer
K_{sp}	Solubility product constant
KOAc	Potassium acetate
LP	Longpass
MAPT	Mapping using accumulated probe trajectories
***m*CPBA**	*m*-chloroperbenzoic acid
MeCN	Acetonitrile
MeOH	Methanol
n	Refractive index of a material
NA	Numerical aperture
NASCA	Nanometer accuracy by stochastic catalytic reactions (microscopy)
NP	Nanoparticle(s)
PAINT	Point accumulation for imaging nanoscale topography

PALM	Photoactivated localization microscopy
PEI	Polyethyleneimine
PET	Photo-induced electron transfer
PSF	Point spread function
PVP	Polyvinylpyrrolidone
QS	Quinine sulfate
RESOLFT	Reversible, saturable, optical fluorescence transition (microscopy)
RNA	Ribonucleic acid
ROMP	Ring-opening metathesis polymerization
ROS	Reactive oxygen species
RT	Room temperature
SEM	Scanning electron microscopy
SIM	Structured Illumination microscopy
SMLM	Single-molecule localization microscopy
SOFI	Stochastic optical fluctuation imaging
SPAD	Single-photo avalanche diode
SPM	Scanning probe microscopy
SR	Super-resolution
STED	Stimulated Emission Depletion (microscopy)
STORM	Stochastic optical reconstruction microscopy
STXM	Scanning transmission x-ray microscopy
SWNT	Single-walled nanotubes
TED	Total energy detector
TEM	Transmission electron microscopy
TEOS	Tetraethyl orthosilicate
TFA	Trifluoroacetic acid
THF	Tetrahydrofuran
TIR	Total internal reflection
TIRF(M)	Total internal reflection fluorescence (microscopy)

TLC	Thin layer chromatography
TOAB	Tetraoctylammonium bromide
TOF	Turn-over frequency
UV-VIS	Ultraviolet–visible
XPS	X-ray photoelectron spectroscopy
θ_C	Critical angle
λ	Wavelength
λ_{max}	Wavelength corresponding to maximum intensity
σ	Standard deviation
τ	Fluorescence lifetime
Φ	Quantum yield
2D	Two dimensional
3D	Three dimensional

List of Figures

List of Schemes

List of Tables

List of Equations

1. General Introduction

1.1 Click Chemistry

To say that the copper (I) catalyzed Huisgen 1,3-dipolar cycloaddition is likely the most important chemical reaction developed within the last 30 years is by no means an overstatement, yet comes with a caveat. That is, while Rolf Huisgen pioneered the dipolar cycloaddition of azides and alkynes nearly 50 years ago in 1967,[1] it wasn't truly accessible until Barry Sharpless[2] and Morten Meldal[3] independently reported that the dipolar cycloaddition was dramatically accelerated by factors up to 10^7 with enhanced regioselectivity using copper as a catalyst (**Scheme 1-1**).

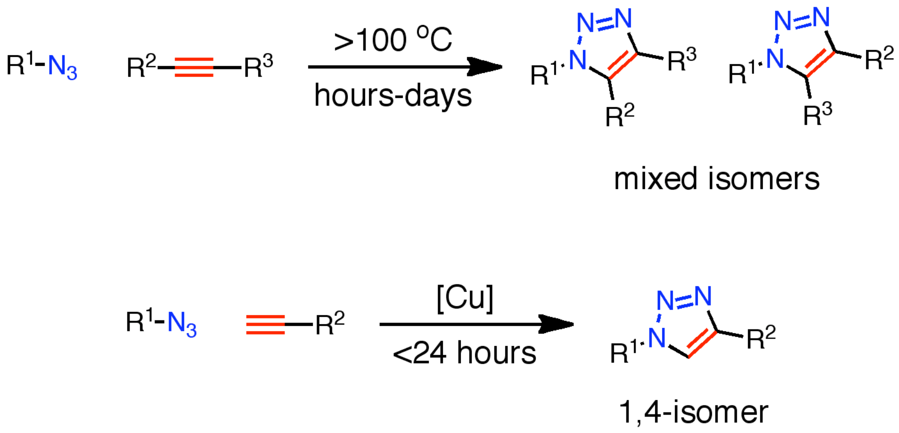

Scheme 1-1. Thermal (uncatalyzed) and Cu catalyzed 1,3-dipolar azide-alkyne cycloaddition reactions. Terminal alkynes ($R^3 = H$) under thermal reaction conditions afford mixed 1,4- and 1,5-isomers, while Cu catalysis affords the 1,4-isomer exclusively.

Inspiration for using copper as a catalyst for the 1,3-dipolar cycladdition of terminal alkynes with organoazides was drawn from previous work by Kenkichi Sonogoshira on the metal catalyzed substitution of acetylenic hydrogen with aryl or vinyl halides to give substituted acetylenes, now known as Sonogoshira cross-coupling.[4] Sonogoshira reported addition of CuI as co-catalyst with bis(triphenylphosphine)palladium dichloride afforded comparable yields to previous independent reports on the same Pd catalyzed coupling by Cassar[5] and Heck,[6] but with much milder conditions and lower catalyst loadings. The success of this reaction was attributed to the facile base-assisted insertion of Cu(I) into the C-H bond of terminal alkynes resulting in a polarization of the triple bond by covalently bound Cu.[3, 7]

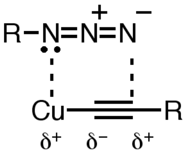

Scheme 1-2. Triple bond polarization induced by formation of Cu-acetylide complex.

Endeavoring to create a facile modular strategy for the synthesis of medicinally relevant molecules from simple organic building blocks, Kolb, Finn and Sharpless developed a new synthetic methodology based on highly selective, reliable reactions and coined the approach "click chemistry."[8] In defining click chemistry, Sharpless *et al.* compiled a set of criteria that must be met for a given reaction to fall under the umbrella term "click." For a process to be labeled "click chemistry":

- the reaction must be:
    - *modular and from readily available materials*
    - *wide in scope*
    - *high yielding*
    - *stereospecific*
    - *efficient under simple conditions (ideally insensitive to water and oxygen*
    - *selective, generating no or only inoffensive byproducts*

- and products must be:
    - *easily separated from the reaction mixture*
    - *easily isolated (i.e. nonchromotographic methods)*
    - *reasonably stable under physiological conditions*

Unsurprisingly, most of the characteristics outlined above that make click reactions unique arise due to large thermodynamic driving forces, usually in excess of 20 kcal mol^{-1}. Indeed, uncatalyzed cycloaddition of HN_3 with acetylene has been predicted to proceed exothermically by at least 52 kcal mol^{-1} using density functional theory (DFT) methods,[9] although high activation barriers and thus slow reaction rates preclude the uncatalyzed reaction from click chemistry eligibility.

While numerous reactions fit the criteria for click chemistry, the popularity of the Huisgen-type Cu(I) catalyzed azide-alkyne cycloaddition (CuAAC) has quickly made it the epitomic click reaction, and it is generally referred to simply as "the click reaction." The enormous popularity of the CuAAC reaction stems not only from its versatility in different reaction conditions and solvents, but increasingly as a result of its substantial azide and alkyne substrate scope while remaining impervious to most other functional groups.

1.2 Mechanistic aspects of Cu(I) catalysis

In their seminal report on the use of Cu(I) to facilitate 1,3-dipolarcycloadditions of azides with terminal alkynes,[2] Sharpless and Fokin proposed an early mechanism (**Scheme 1-3**) that has served as a surprisingly good springboard for many more recent mechanistic investigations. Citing unpublished results, they suggested the mechanism proceeds stepwise after the rapid formation of the copper(I)-acetylide as DFT calculations predict the concerted [2+3] cycloaddition to be strongly disfavored by 12-15 kcal. Their original stepwise proposal has the azide nitrogen proximal to carbon ligating to Cu of the copper(I)-acetylide, followed by concomitant formation of the first C-N bond and a double bond between copper and the C1 atom of the acetylide via attack of the distal azido nitrogen on C2 of the acetylide. This step results in an interesting six-membered organometallacycle containing a suspected Cu(III) atom, which then undergoes ring contraction to give a copper triazolide and release of the triazole product by protonation.

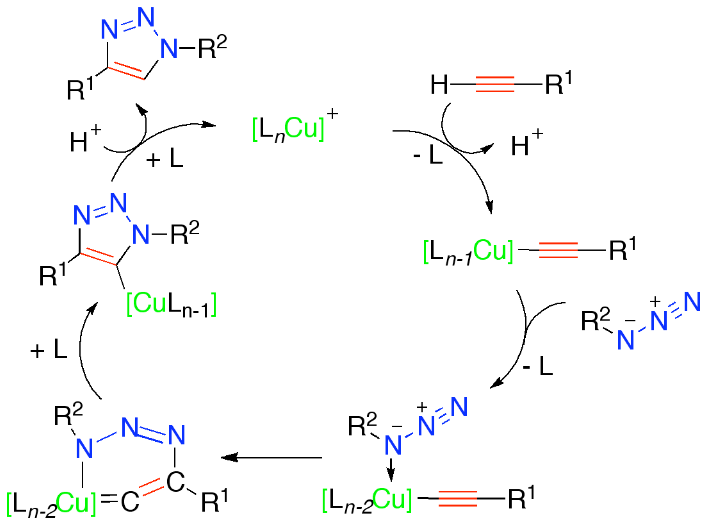

Scheme 1-3. Early CuAAC mechanism proposed by Sharpless and Fokin. Adapted with permission from Berg and Straub.[10]

Sharpless and Fokin later published the results of an extensive DFT study in 2005,[11] finding that an activation barrier of 23.7 kcal mol^{-1} rules out a concerted mechanism from the neutral copper-acetylide. Their calculations also predicted the activation barrier for the formation of this six-membered copper(III) metallacycle to be 14.9 kcal mol^{-1} compared to a barrier of 25.7 kcal mol^{-1} for the uncatalyzed cycloaddition providing an explanation for the enormous rate acceleration by copper. Interestingly, interaction of Cu with the π-system of propyne was calculated to lower the pK_a of the terminal proton by almost 10 units facilitating deprotonation, yet reaction from the non-deprotonated copper-alkyne π-complex was ruled even more unfavorable than the uncatalyzed reaction with a barrier of 27.8 kcal mol^{-1}.

Based on the precedent of Cu(I) inserting into acetylenic C-H bonds[12-14] and no evidence for internal triple bonds undergoing cycloaddition, it was assumed that formation of Cu(I)-acetylides was an important activation step in the mechanism.[12] While computational studies supported the involvement of Cu(I)-acetylides interacting with organoazides as suggested in Sharpless's original mechanistic proposal, these complexes were only assumptions until direct evidence was provided by Bernd Straub's group in 2007.[13] By reacting an N-heterocyclic carbene copper(I) acetylide complex with a sterically hindered organoazide, Straub and co-workers were able to crystallize and isolate a stable Cu(I)-triazolide complex (**Scheme 1-4**), which reacted quantitatively with acetic acid to give the expected triazole product within minutes. This isolated intermediate added complexity to already conflicting reports on the speciation and nuclearity of Cu in transition state and intermediary structures. Kinetic studies have determined the rate law to be first order in azide, between first and second order in alkyne and second order with respect to the copper ions.[17, 18] Other reports[10] are more conflicting, finding the order of reaction with respect to each reagent to vary greatly and even a negative order has been measured for the concentration of alkyne in certain systems.[14]

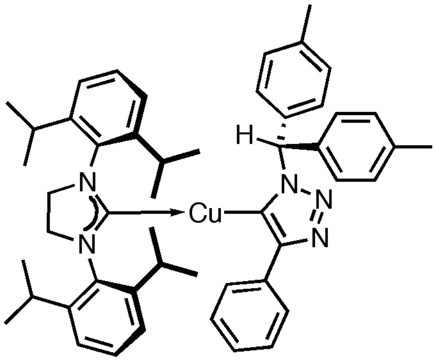

Scheme 1-4. Stable Cu(I)-triazolide complex isolated by Straub *et al.*[13]

It remains unclear whether mononuclear complexes such as Straub's Cu(I)-triazolide are catalytically active CuAAC species or precatalysts that form the active multinuclear catalyst through aggregation. In fact, in experiments by Fokin and co-workers, preformed and isolatable Cu-acetylides only reacted with benzyl azide with the addition of exogenous Cu. Without Cu added to the reaction mixture, no appreciable conversion to triazole products was observed, supporting a hypothesis that two copper atoms operate in discrete specialized roles; one as a purely σ-bound ligand, and the other acting solely through weak π-complexation.[15] Likewise, computational studies[16] have suggested that bridging dicopper(I,III) μ-alkenylidene intermediates are significantly more thermodynamically favourable compared to the doubly bonded carbon-copper(III) intermediate (**Scheme 1-3**) despite the entropically disfavoured inclusion of a second copper atom. The thermodynamic stability of the μ-alkenylidene complex was attributed to elimination of high ring strain in the mononuclear six-membered structure. In contrast, isotopic enrichment of triazole products from addition of an isotopically pure ^{63}Cu(I) coordination complex to preformed naturally abundant Cu-acetylides (^{63}Cu:^{65}Cu ratio of 69:31) in the presence of benzyl azide discount the hypothesis of Cu atoms acting in discrete roles, suggesting a mechanism in which two chemically equivalent copper atoms work in unison.[15] Based on these results and previous kinetic investigations, Fokin *et al.* proposed an updated mechanism whereby a σ-bound copper-acetylide bearing a π-complexed copper atom reacts with an organoazide forming a bridging dicopper μ-acetylide (**Scheme 1-5**).

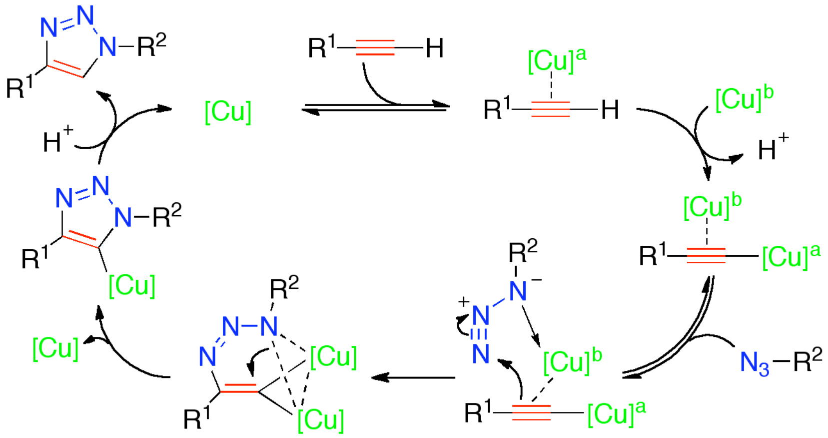

Scheme 1-5. Most recent (2013) CuAAC mechanism proposed by Fokin. Adapted from Worrell *et al.*[15] with permission from AAAS.

Although this mechanistic proposal represents the most up-to-date knowledge of the identity of important intermediates and transition states involved in the CuAAC reaction, it is clear that the very complex mechanism is still poorly understood and conflicting reports leave many questions unanswered. Moreover, while CuAAC pioneers are pessimistic that the exact structural details of key transition states responsible for the massive rate acceleration by Cu(I) catalysis will be determined in the near future,[7] Fokin has speculated that "superb catalysts are waiting to be found if we are adventurous enough to accept the uncertainty of not knowing the precise structure of the active catalytic species".[17]

1.3 Common CuAAC catalysts

The original two reports on the use of copper as a catalyst for the azide-alkyne cycloaddition featured two distinct sets of reagents and conditions for catalysis. Meldal's approach used copper(I) iodide as catalyst in tetrahydrofuran (THF) with a large excess of organic base such as NN-diisopropylethylamine; while nearly quantitative conversions were achieved the selectivity suffered as a consequence of side reactions.[3] In their seminal publication, Sharpless and Fokin found that although direct use of Cu(I) salts was effective, *in situ* generation of catalytic Cu(I) species via reduction of copper(II) sulfate with ascorbate was more reliable and afforded similar conversions with higher purity.[2] Indeed, the robustness of this approach led to widespread application and now the combination of inexpensive $CuSO_4{\bullet}5H_2O$ and ascorbic acid or sodium ascorbate in aqueous/alcohol solvent systems is referred to as the Sharpless-Fokin conditions.[10] The addition of reducing agents with Cu(II) salts not only provides a soluble source of Cu(I) but also renders the reaction significantly less sensitive to oxygen by reducing the formation of oxidative by-products such as unreactive polymeric Cu(I) acetylides, bis-triazoles, 5-hydroxytriazoles, acetylenic homocouplings, and 5-alkynyl substituted triazoles (**Scheme 1-6**).[18] Excess ascorbate has also been shown to facilitate Cu-acetylide formation by assisting in the deprotonation of acetylenic C-H.[19] Adding to the problems accompanying use of copper(I) as a direct catalyst source, the use of CuI under certain conditions has been shown to produce 1-iodoalkynes, which then undergo cyclization with azides to give 5-iodotriazole products.

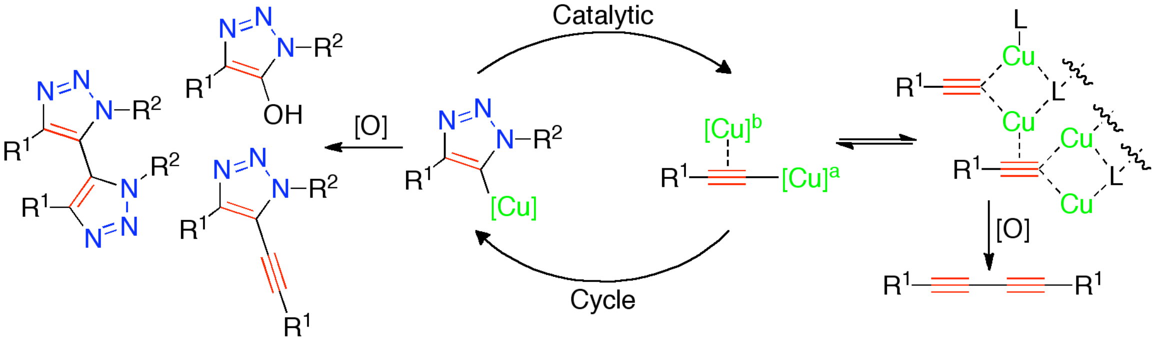

Scheme 1-6. Oxidative byproducts formed with Cu(I) catalysis. Adapted from Worrell *et al.*[15] with permission from AAAS.

These combinational effects have established the *in situ* reduction of Cu(II) salts as the preferred method of catalysis, although perhaps indicative of why the mechanism remains unclear, the CuAAC reaction functions extraordinarily well under nearly any conditions in which Cu(I) is present or generated in situ.[12] In fact, despite the robustness of the Sharpess-Fokin conditions, a great deal of research has gone into developing CuAAC catalysts from other copper sources. Although they suffer from considerable drawbacks mentioned previously, as well as generally requiring inert atmospheres and anhydrous solvents, copper(I) compounds remain a popular choice as direct CuAAC catalysts. Copper(I) salts with counterions such as iodide, bromide and acetate have been investigated along with many molecularly defined Cu(I) complexes. With the direct use of Cu(I) compounds, ligands are commonly added to facilitate coordination of N_3 to Cu[14] and prevent rapid disproportionation of active Cu(I) species to inactive Cu(II) and Cu(0).[25, 26] Ligands that bind strongly but are still rapidly labile are desirable as the disproportionation step depends on Cu(I) not being strongly coordinated to ligands,[20] yet ligand displacement is often necessary for coordination of organoazides. This approach is so successful it is often applied to Cu(II) reduction systems with organic bases and other such ligands commonly added to stabilize *in situ* generated Cu(I) species and accelerate azide complexation. Typical ligands are organic based compounds containing nitrogen centres available for coordination,[10] although phosphines have been shown to be successful by increasing the solubility of Cu(I) species in organic media[21] as have rare sulfur based ligands.

Metallic copper sources such as copper wire or shavings have also been used as readily available CuAAC catalysts in systems in which the use of a reducing agent is undesirable. With metallic copper precatalysts, the active Cu(I) catalyst species is generated via comproportionation of metallic Cu(0) and Cu(II) from the natural patina.[11, 25] Although claims of cycloadditions with Cu(II) catalysts have been reported,[22, 23] Cu(II) species are not competent catalysts and the observed reactivity in these reports is attributed to oxidation of organic species in solution by Cu(II) generating catalytically active Cu(I), specifically through Glaser-type cupric catalyzed oxidative acetylenic couplings.[24]

1.4 Copper nanomaterials as CuAAC catalysts

Although direct evidence has very recently been found,[15] surmise of the involvement of multiple copper centres in CuAAC intermediates and transition states launched interest in copper clusters with open coordination sites and novel copper nanomaterials as click catalysts. Given kinetic studies indicate the rate law obeys a second order dependence on copper concentration, it seems evident that pre-association of multiple copper atoms in a material would inevitably lead to improved CuAAC catalytic activity.

In a striking trend, the advent of nanomaterials is redefining the approach in which many areas of science are explored and has disposed of all preconceptions of transition metal catalysis.[25] While many quantum size effects arise from reducing the size of a bulk material down to the nanometric scale,[26] the paramount benefit to catalysis is the dramatic increase in surface area compared to corresponding bulk materials. The unique dispersion and distribution of active sites achieved with high surface area nanomaterials provides improved access for reagents to the reactive catalyst surface and thus improved efficiency over bulk catalyst counterparts.[27] Corma et al. explored this effect in detail for the aerobic oxidation of alcohols by gold nanoparticles and found the turn-over frequency (TOF) of the reaction directly correlates with the ratio of surface gold atoms to internal atoms in the catalyst (**Figure 1-1**).

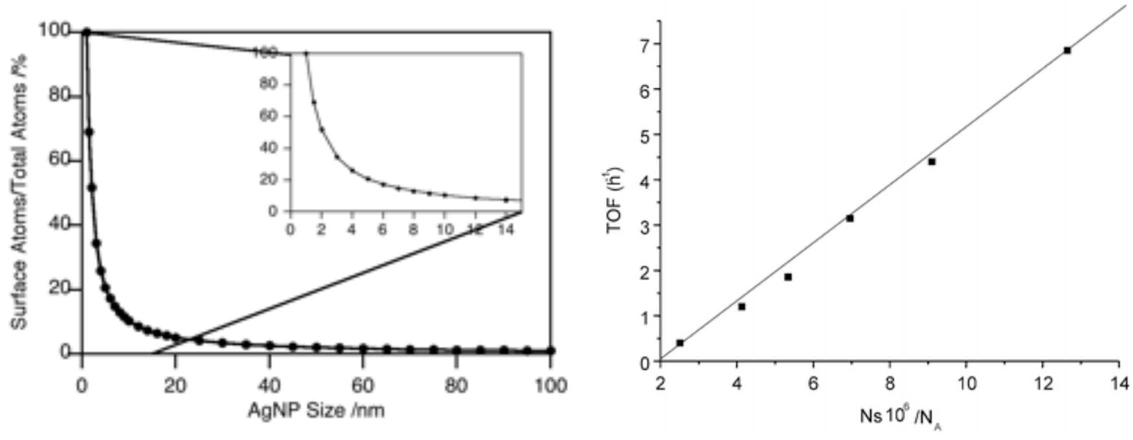

Figure 1-1. Ratio of surface atoms to total atoms with increasing Silver Nanoparticle size (left) and TOF values for the aerobic oxidation of cinnamyl alcohol *vs*. the number of external gold atoms (N_S) present in Au/TiO_2 catalysts with different particle size (right). Reproduced (in part) from Corma et al.[29] (right) with permission of The Royal Society of Chemistry and Stamplecoskie[28] (left).

Pioneering work on copper nanomaterials as CuAAC click catalysts came in the form of two independent reports published three weeks apart in early 2005. Orgueira and co-workers[30] first reported the use copper(0) nanopowder to generate the active copper(I) catalyst *in situ* elaborating on Sharpless and Fokin's copper shavings catalyst system.[2] Although technically published after Orgueira's report, Rothenberg's work on colloidal copper(0) nanoclusters has been more influential, boasting faster conversions at very low catalyst loadings (0.1 mol %) and a reusable catalyst rather than a 'reservoir' for Cu(I) ions.[31] Catalysis in this report, as well as others involving supposed 'copper(0)' nanomaterials is thought to be mediated by copper(I) on the particle surface. Although some authors claim the absence of detection of copper(I),[32] the lack of any evidence for copper(0) catalysis suggests that copper(I) species must be present.

Notable copper nanomaterials developed as click catalysts include CuNP, CuONP, Cu_2ONP, copper nitride (Cu_3N) NP, and magnetic copper ferrite NP among others with some even capable of completing reactions in 10 minutes that would require days or even weeks if left uncatalyzed. A summary of copper nanomaterials used as click catalysts is provided in **Table 1-1** detailing the variety of materials, supports and stabilizers explored as well as the broad range of conditions under which catalytic activity is optimized. Similar conversions for different nanomaterial catalysts with large variances in reaction rates, temperature and additive requirements leads one to question how the catalysts differ at the single-nanoparticle level. These discrepancies in activity may be due to factors such as copper ion leaching, coordination of ligands to NP surface, accessibility of Cu(I), the availability of Cu(I) generated *in situ* from Cu(0) and Cu(II), or perhaps may be attributed to a number of other factors. An intimate understanding of the complex dynamics of CuNP catalysts would allow for evaluation of the factors contributing to catalytic activity and open up avenues for intelligent catalyst design.

Table 1-1. Summary of copper nanomaterials used as CuAAC catalysts.

Nanocatalyst	Support/ stabilizer	Size (nm)	Shape	Reuse (times)	Optimized conditions	Ref
Cu powder	none	*	powder	dissolves	10 mol%, RT, 2 h, H_2O/tBuOH, Et_3N	30
CuNP	none	3±1.5	sphere	dissolves	10 mol%, 65°C, 30 min, THF Et_3N	33, 34
CuONP	none	100	hollow sphere	3	5 mol%, RT, 30 min, H_2O/tBuOH, Et_3N	35
CuNP	charcoal	6±2	sphere	5	0.5 mol%, 70°C, 3 h, H_2O	36, 37
CuONP	acetylene black/PVP	100	hollow sphere	10	3 mol%, 50°C, 5 h, H_2O/tBuOH	38
CuNP	TOAB	4	cluster	*	0.1 mol%, RT, 18 h, H_2O/tBuOH	31
Cu/Cu_2O	oleyamine	14	core-shell	*	20 mol%, RT, 2-4 h, toluene	39
CuNP	AlO(OH) nanofiber	5-8	sphere	5	3 mol%, RT, 1-24 h, hexane	40
CuNP	PVP	10-35	sphere	4	cat., RT, 15-45 min, formamide	41
CuNP	Al_2O_3	100	sphere	3	cat., RT, 3-8 h, H_2O	42
CuNP	SiO_2NP/PEI	5-6	sphere	3	0.05 mol%, RT, 10 min, DMSO	43
CuNP	PVP/ionic liquids	80-130	sphere	5	5 mol%, RT, 15 min, H_2O	44
Cu_3N/Fe_3N	SiO_2	100	core-shell	5	cat., RT, 12 h, CH_3CN, Et_3N	45
CuNP	graphitized carbon nanofibres	3	sphere	5	2.5 mol%, 40°C, 48 h, benzene, Et_3N	46
CuNP	montmorillonite	<10	sphere	3	cat., RT, 1.5 h, H_2O, Et_3N	32
CuNP**	TiO_2	1±0.4	sphere		0.5mol%, 70°C, 8 h, neat	47
Cu@FeNP	FeNP	*	*	4	5 mol%, RT, 12 h, H_2O	48
$CuFe_2O_4$ NP**	none	*	*	3	5 mol %, 70°C, 3 h, H_2O	49

TOAB – tetraoctylammonium bromide

[*] – Not reported

[**] – three component CuAAC

1.5 Applications of CuAAC click chemistry

A quick SciFinder search of the most cited articles involving copper click chemistry provides insight into the origin of the CuAAC reactions immense popularity; extreme diversity in application. Looking closely at the reaction, from reagents to products, helps identify the uniqueness of this reaction and contributing factors to its diverse utility. Not only do the stability and selective reactivity (toward each other) of the azide and alkyne reagents appeal to potential users, the triazole product also exhibits remarkable stability being largely inert to hydrolysis, oxidation and reduction processes, and also possesses aromatic character and a strong dipole moment (~ 5 Debye).[50] These features lend to the ability of the triazole moiety to interact with many biomolecules and can be found in many biologically relevant molecules such as antibiotics, antibacterials, and antivirals.[51, 52] Moreover, the triazole moiety's value as a pharmacophore combined with its ease of preparation has made copper click chemistry a hugely successful synthetic strategy for the creation of medicinally relevant molecules.[52-54] Triazoles also participate in a variety of intriguing and diverse supramolecular interactions including but not limited to anion complexation, hydrogen bonding, both C- and N-derived metal coordination, as well as the obvious relevance in molecular scaffolding.[55]

Click chemistry has been used for detection of copper ions in solution, through the colorimetric agglomeration of gold nanoparticles mediated by triazole cross-linking of labeled AuNPs,[56] and via CuAAC reaction of a fluorogenic azido-modified coumarin allowing for quantification of copper ions in solution by detection of generated emission.[57] Analogous fluorogenic click reactions have similarly been employed to fluorescently label proteins, viruses, DNA and other biopolymers, as well as metal-organic-frameworks.[58] The massive number of click chemistry applications makes it impossible to discuss the topic in any depth and is beyond the scope of this thesis; however, many excellent review articles have been written that focus specifically on the applications of click chemistry.[56, 58, 59, 64-68] Briefly, some notable research areas in which CuAAC chemistry has found utility include de novo peptide synthesis,[59] bioconjugation,[66, 69] live cell labeling,[60] post-synthetic RNA/DNA modification,[61] radiolabeling,[62] synthesis and cross-linking of polymers, dendrimers, hydrogels and micro gels[63] as well as preparation, labeling and modification of active surfaces, bio-sensors, microarrays, self-assembled monolayers and colloids.[59] Although this list is extensive, it is by no means comprehensive and is meant only to convey the expansive impact click chemistry has had and will continue to have as CuAAC research grows and evolves.

1.6 Examining nanosized catalysts

Aside from the obvious desire to improve catalytic efficiency, reaction yields, and product purity, all of which reduce the cost of making a product, many catalytically relevant transition metals have detrimental health effects which are a significant drawback to medically intended applications of catalysts or transition metal mediated processes used to synthesize biologically relevant molecules. As the use of nanosized catalysts in organic transformations rapidly expands, so does concern regarding catalyst impurities within the products and thus the safety of the product for the end-user. Indeed, using copper as an example, the low-redox potential between Cu(II) and Cu(I) (0.158 V in water) enables its participation in the generation of reactive oxygen species (ROS) in the presence of high copper concentrations ultimately leading to cellular oxidative stress with implications in a variety of disorders, the most noteworthy being neurodegenerative diseases.[64] With CuAAC formed triazoles becoming a more prominent pharmacophore in biologically relevant molecules, this highlights but one case in which an in depth understanding of transition metal catalysts (particularly heterogeneous ones) at the molecular level can aid in optimizing the performance of a catalyst while making it safer to use.

1.6.1 From classical to *in operando*

The term ‘classical’ in regard to the exploration of heterogeneous catalysts generally refers to nonmodern techniques that are older than one or two decades but most are much less than a century old, thus are hardly ‘classical’ in the truest sense of the word. These so called ‘classical’ methods are typecast to study catalytic materials in a macro sense although some of them are quite capable of achieving close to molecular resolution. The real limiting factor is the ability to probe reactions in real time under normal reaction conditions. Trying to study catalysis with a technique that is slower than the kinetics of the reaction necessitates ‘freezing’ the reaction in time through intermediates and transition states, but doing so opens the possibility that key stages in the reaction can be missed entirely. An additional pitfall of studying catalysts on a macroscopic level is behaviour that is unpredicted or differs from that of the majority can easily go unobserved, lost in the noise of the ensemble. Indeed, the nature (including identity), accessibility, and distribution of active sites can be heterogeneous within individual catalyst particles and even the activity of a single particle can vary with time.[65] Although some very valuable information can be obtained with the traditional methods typically used for studying catalysts, only when catalysis is observed on the same time scale as the reaction under the same operating conditions (*in operando*) of the catalyst at single molecule

– single particle level can the deep mechanistic details of heterogeneous catalysts be uncovered.

In the last decade considerable attention has been devoted to *in situ* and *operando* catalyst characterization, in fact an entire themed issue of Chemical Society Reviews was recently dedicated to '*in situ* characterization of heterogeneous catalysts' (*Chem. Soc. Rev.,* Vol. 39, Issue 12). Three notable research areas have received the majority of attention, these include combined time-resolved spectroscopy under more realistic reaction conditions, spectroscopy in the liquid phase and single molecule – single active site/catalyst particle spectroscopy.[66] An interesting trend is observed in the pages of the Chem. Soc. Rev. themed issue; all of the fastest advancing research tools for exploring heterogeneous catalysts *in operando* are based on spectroscopy, microscopy or a combination of the two. This trend is most likely a product of the advent of ultrafast pulsed light sources and very sensitive time-resolved detectors such as single-photon avalanche diodes (SPAD) and electron multiplying charged coupled devices (EM-CCD) enabling incredible spatiotemporal control of spectroscopic measurements and imaging at the single molecule – single catalytic particle level. The power of spectroscopy to probe vibrational and electronic transitions at the molecular and even atomic level is another major factor in the newfound success of *in operando* spectroscopies.

1.6.2 Single-molecule catalysis with Total Internal Reflection Fluorescence Microscopy

Optical microscopy techniques provide an interesting, low cost alternative to traditional techniques and methodologies used for studying catalyst materials (especially heterogeneous) as they often allow for direct visualization of active systems in real time – or so called *in operando* conditions. Of course, optical microscopy techniques (*operando* or otherwise) suffer some very real drawbacks that can detract from their application to the study of catalytic reactions. The most obvious impediment is also the most vital to its success; the necessary interaction with light limits accessible reactions and materials to those that absorb or scatter light. Fortunately using molecules that do absorb light (chromophores) as tags, a practice that has been employed for decades by biological researchers, this obstacle can be circumvented. Other technical difficulties with optical microscopies include impurities (competitive absorption or inner filter effect), chromophore stability, autofluorescence from biomolecules in biological systems and light pollution.

Adaptations of fluorescence microscopy are exceedingly popular tools for studying biological systems[67] and have successfully been applied to the examination of catalytic chemical systems.[68] In flood illumination techniques such as conventional epi-fluorescence microscopy, out-of-focus luminescence caused by blanket illumination of fluorophores both inside and outside the focal volume is a significant source of background fluorescence that contributes to the observed signal.

Elimination of signal from fluorophores outside the focal range significantly reduces background fluorescence and greatly increases the effective sensitivity and resolution of an imaging technique. For instance in confocal microscopy, light is passed through a small pinhole in order to filter out signal that originates from outside the confocal volume.[67] An alternative approach would be to selectively excite molecules only in a desired area of interest. While nominally this approach seems straightforward, in practice it is very difficult to selectively excite certain molecules in a sea of molecules all of which are smaller than the wavelength of incident light. That said, by exploiting optical 'tricks' light can be manipulated to restrict the volume of irradiation in a controlled manner.

Total internal refection (TIR) is a unique phenomenon that occurs as light travelling in a medium of high refractive index meets a medium of lower refractive index. When light meets the interface with a material of different refractive index it refracts due to a change in speed with the refractive angle (θ_2) dependant on the incident angle (θ_1) according to Snell's Law (**Equation 1-1**). Incident light at a certain critical angle (θ_C, **Equation 1-2**) will refract so that it travels exactly along the interface between the materials of differing refractive index, in this instance θ_2 is equal to 90° (**Figure 1-2**).

$$n_1 \sin\theta_1 = n_2 \sin\theta_2 \qquad \textbf{(1-1)}$$

$$\theta_2 = 90° \rightarrow \sin\theta_c = \frac{n_2}{n_1} \qquad \textbf{(1-2)}$$

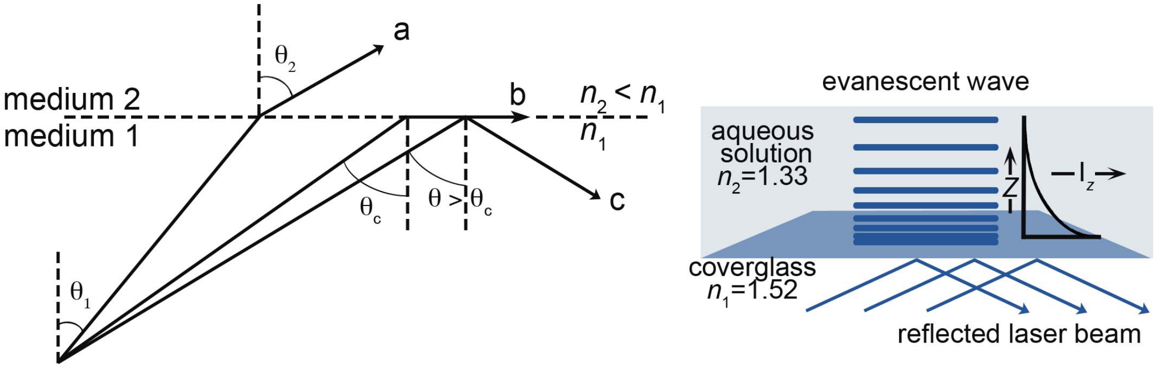

Figure 1-2. Path of light interacting with the interface between two materials of different refractive index ($n_2<n_1$). (**a**) Light travelling through the higher index material incident at an angle less than the critical angle encounters the interface and refracts into the lower index material. (**b**) Light incident at the critical angle refracts such that it travels along the interface (θ_2 = 90°). (**c**) Light incident at angles greater than the critical angle reflect back into the high index material (left). The intensity (I_z) of the evanescent field decays exponentially with increasing distance (z) from the interface (right). θ_1 – incident angle, θ_2 – refracted angle, θ_C – critical angle, n_1 and n_2 – refractive indices of the two media. Adapted with permission from Trache[69] and Fish.[70]

When light incident at an angle greater than θ_C encounters the interface with a medium of lower refractive index the beam is totally internally reflected back into the high-index material rather than refracted into the low-index material. When this occurs, some of the incident energy penetrates the low-refractive material generating an evanescent wave that propagates though the medium parallel to the interface. This 'evanescent field' decays exponentially with increasing distance, *z,* perpendicular from the interface; the field intensity $I(z)$ at a given distance can be determined using **Equation 1-3** with I_o depicting the intensity at the interface and the penetration depth (d) of the field is represented by **Equation 1-4**. Except for angles very near the critical angle, the intensity of the evanescent field at the interface, (I_o, z=0) is comparable to the intensity of incident light, thus a molecule located in the evanescent field at z=0 will be excited to the same extent as if it were located in the path of the incident beam. Since d varies with the wavelength of light (λ), so does the decaying intensity of the field, but typically the intensity of the field beyond 100 – 200 nm is negligible.

$$I(z) = I_o e^{-z/d} \qquad \textbf{(1-3)}$$

$$d = \frac{\lambda}{4\pi}(n_1^2 \sin\theta_1^2 - n_2^2)^{-1/2} \qquad \textbf{(1-4)}$$

The evanescent field induced by TIR irradiation creates a thin planar section of irradiation at the surface of a low-refractive medium such as water residing in contact with a high-refractive medium such as glass allowing for selective excitation of fluorophores located only within a short distance from the interface between the two materials. This is in contrast to the action of a pinhole in confocal microscopy, which eliminates out-of-focus emission signal, lending to improved z resolution of TIR over confocal microscopies.

Total internal reflection fluorescence (TIRF) microscopy (TIRFM) uses TIR irradiation to selectively excite fluorophores at or very near the surface of a glass coverslip placed in a microscope equipped for fluorescence detection. Using TIR irradiation eliminates fluorescence from outside the evanescent region allowing for very high contrast imaging. Further coupling to extremely sensitive detectors combined with dilute fluorophore concentrations enables single-molecule detection on TIRF microscopes. Even before the development of ultrasensitive EM-CCDs, since the maiden experiments by Axelrod in 1981[71]; prism-based TIRF, which passes the incident beam through a prism to obtain TIR has been applied to the cellular microscopy. While prism-based TIRF microscope configurations (**Figure 1-3**) are simple and inexpensive to implement, the necessity of the sample to be positioned between the prism and coverglass severely hinders access to the sample and limits manipulation of the sample during experimentation as well as the variety of cell reactors that can be used. Axelrod later introduced the first objective-based (prismless) TIRF microscope setup in 1989,[72] passing the incident beam through a high numerical aperture objective and focusing the beam off-axis on the back focal plane of the objective in order to obtain TIR (**Figure 1-3**). This method is more expensive due to the high cost of quality microscope objectives but makes TIR very easy to obtain by controlling the beam position with a micrometer and allows excellent access to the sample.[69] The schematic in **Figure 1-4** shows the light path within a typical inverted microscope equipped for objective-based TIRF.

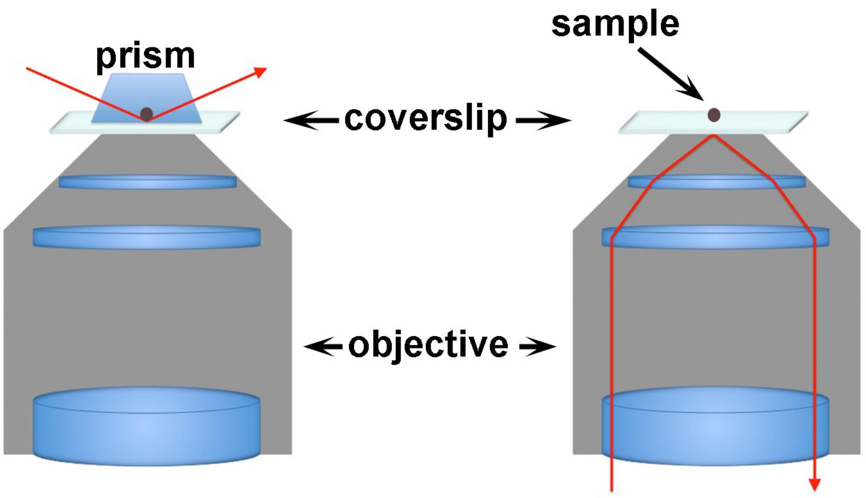

Figure 1-3. Prism (left) and objective (right) based TIRF configurations.

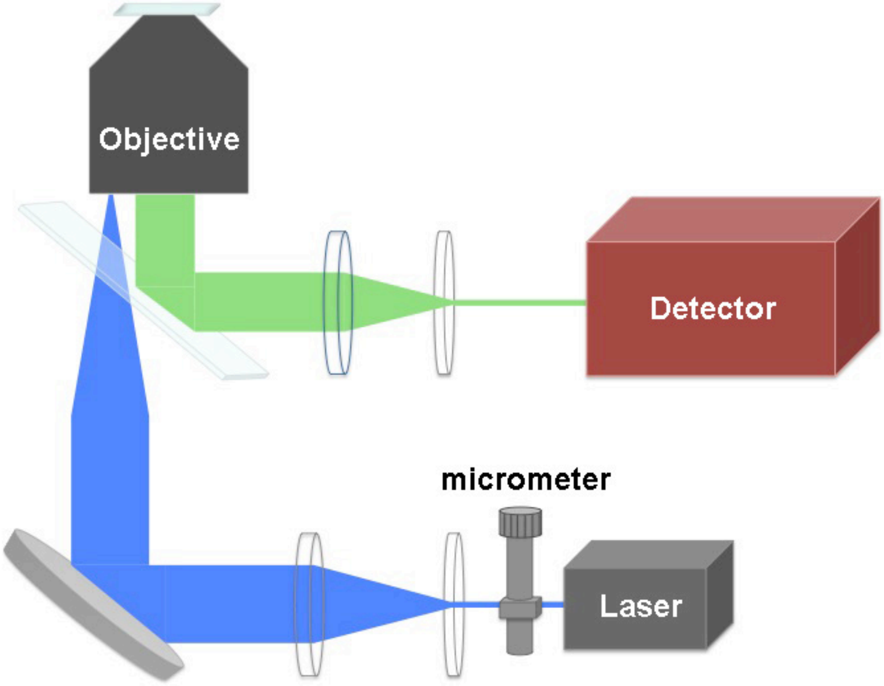

Figure 1-4. Typical inverted microscope objective-based TIRF configuration, the laser beam path is shown in blue and emitted signal in green.

Despite TIRF microscopy being developed as a means of investigating cellular membrane interactions, its simplicity and versatility lend to its particular suitability for examining surface chemistry and catalysts, specifically single-molecule studies although examples are limited. As previously mentioned, biological systems have been studied with single-molecule techniques such TIRFM for decades, yet application of these techniques to chemical systems is in its infancy. Suzanne Blum, a leader in the field of single-molecule catalysis, has suggested that perhaps that biggest factor contributing to the lag in chemical applications of single-molecule techniques is not the lack of commercial dye probes, low substrate specificity, or demanding chemical environments; but is instead a result of an "initial under-estimation within the synthetic chemistry community of the possibilities of single-molecule methods and their rapidly increasing ease of use."[73]

1.7 Within this thesis

This thesis explores the copper(I)-catalyzed azide-alkyne cycloadditoon click reaction from various points-of-view in an interdisciplinary manner. The second chapter of this thesis investigates CuAAC click chemistry from a synthetic chemistry angle, applying CuAAC catalysis as a synthetic tool for the modular synthesis of fluorescence turn-on sensors for metal cations in aqueous solutions. Recognizing analyte-binding and signal emitting regions of a sensor as separate modules we describe an approach which employs a fluorophore (signal emitter) combined with a variety of ionophores (analyte-binder) to create a series of fluorescent ion sensors each selective for a different metal cation. Combining fluorophore and ionophore with copper catalyzed click chemistry not only enables assembly of sensing and signaling 'modules' into a single molecule but also allows signal transduction between the two regions activating external transmission of analyte binding events. The method described in Chapter 2 uses traditional so called 'Sharpless-Fokin' CuAAC conditions with the *in situ* reduction $CuSO_4$ to form the triazole bridge between fluorophore and ionophore. We naturally had an interest in exploring different catalysts to link these modules and we began to investigate copper nanomaterial catalysts. Through examination of literature along with some of our own trial and error with CuNP catalysts we noticed the activity of seemingly similar materials varied dramatically. The ambiguity in NP catalysis led to the development of an interest in the mechanistic considerations of using CuNP as click catalysts. This interest was the genesis of the work in Chapters 3 and 4 which take an interdisciplinary approach applying organic synthesis, inorganic nanomaterial synthesis, spectroscopy and microscopy to explore CuAAC catalysis in real time at the single molecule – single nanoparticle level. Chapter 3 describes the development of a single-molecule microscopy method that allows for precise determination of the true active phase of catalysis. Combining ensemble bench-top chemistry with single-molecule microscopy monitoring individual catalytic turnovers we demonstrate that catalysis occurs directly on the surface of CuNP rather than in homogeneous solution via leaching of catalytically active Cu(I) ions. The methodology in Chapter 3 employs colloidal CuNP immobilized on glass microscope coverslips to monitor single-catalytic reactions. In Chapter 4 this approach is extended to supported nanomaterial heterogeneous systems that have the benefit of easy separation from reaction and reusability. Applying single-molecule localization microscopy techniques to the detection of single-catalytic turnovers we demonstrate mapping of catalytic activity on a commercial heterogeneous supported copper nanomaterial catalyst.

Although presentation of nanomaterial catalysis in this introduction has emphasized the rapid rise in popularity of copper nanomaterials as catalysts, the concepts extend to other noble metals and many transition metals. Indeed, a brief perspective published in Science in 2007 has labeled nanomaterials as “The New Face of Catalysis”,[74] and the field has continued to explode since this time. Such immense popularity has naturally led to an enormous number of unique nanomaterial catalysts, all with interesting and wonderful quirks that make their physical characteristics and catalytic activity distinct from the others. This thesis aims to demonstrate TIRF-based single-molecule microscopy as an accessible, effective, and unparalleled tool for exploring the catalytic activity of nanomaterials by monitoring single catalytic events as they occur. Moreover, this thesis will show that combining single-molecule microscopy with routine bench-top chemistry can decipher the true phase of catalysis providing a definitive answer to the question of whether a solid catalysis functions heterogeneously or homogeneously, and even map the reactivity heterogeneities within a single catalyst particle. In this case, the copper(I) catalyzed click reaction is used as an archetypical reaction, however, the approach taken within this thesis is a general one that can be applied to virtually any catalytic reaction though intelligent design of probe systems with appropriately functionalized fluorophores.

1.8 References

1. Huisgen, R., Szeimies, G. & Möbius, L. 1.3-Dipolare Cycloadditionen, XXXII. Kinetik der Additionen organischer Azide an CC-Mehrfachbindungen. *Chem. Ber.* 100, 2494-2507 (1967).
2. Rostovtsev, V.V., Green, L.G., Fokin, V.V. & Sharpless, K.B. A stepwise Huisgen cycloaddition process: Copper(I)-catalyzed regioselective "ligation" of azides and terminal alkynes. *Angew. Chem. Int. Ed.* 41, 2596-2599 (2002).
3. Tornøe, C.W., Christensen, C. & Meldal, M. Peptidotriazoles on solid phase: [1,2,3]-triazoles by regiospecific copper(I)-catalyzed 1,3-dipolar cycloadditions of terminal alkynes to azides. *J. Org. Chem.* 67, 3057-3064 (2002).
4. Sonogashira, K., Tohda, Y. & Hagihara, N. A convenient synthesis of acetylenes: catalytic substitutions of acetylenic hydrogen with bromoalkenes, iodoarenes and bromopyridines. *Tetrahedron Lett.* 16, 4467-4470 (1975).
5. Cassar, L. Synthesis of aryl- and vinyl-substituted acetylene derivatives by the use of nickel and palladium complexes. *J. Organomet. Chem.* 93, 253-257 (1975).
6. Dieck, H.A. & Heck, F.R. Palladium catalyzed synthesis of aryl, heterocyclic and vinylic acetylene derivatives. *J. Organomet. Chem.* 93, 259-263 (1975).
7. Meldal, M. & Tornoe, C.W. Cu-catalyzed azide-alkyne cycloaddition. *Chem. Rev.* 108, 2952-3015 (2008).
8. Kolb, H.C., Finn, M.G. & Sharpless, K.B. Click Chemistry: Diverse Chemical Function from a Few Good Reactions. *Angew. Chem. Int. Ed.* 40, 2004-2021 (2001).

9. Jones, G.O., Ess, D.H. & Houk, K.N. Activation Energies and Reaction Energetics for 1,3-Dipolar Cycloadditions of Hydrazoic Acid with C-C and C-N Multiple Bonds from High-Accuracy and Density Functional Quantum Mechanical Calculations. *Helv. Chim. Acta* 88, 1702-1710 (2005).
10. Berg, R. & Straub, B.F. Advancements in the mechanistic understanding of the copper-catalyzed azide-alkyne cycloaddition. *Beilstein J. Org. Chem.* 9, 2715-2750 (2013).
11. Himo, F. *et al.* Copper(I)-Catalyzed Synthesis of Azoles. DFT Study Predicts Unprecedented Reactivity and Intermediates. *J. Am. Chem. Soc.* 127, 210-216 (2005).
12. Bock, V.D., Hiemstra, H. & van Maarseveen, J.H. CuI-Catalyzed Alkyne–Azide "Click" Cycloadditions from a Mechanistic and Synthetic Perspective. *Eur. J. Org. Chem.* 2006, 51-68 (2006).
13. Nolte, C., Mayer, P. & Straub, B.F. Isolation of a Copper(I) Triazolide: A "Click" Intermediate. *Angew. Chem. Int. Ed.* 46, 2101-2103 (2007).
14. Rodionov, V.O., Presolski, S.I., Díaz Díaz, D., Fokin, V.V. & Finn, M.G. Ligand-Accelerated Cu-Catalyzed Azide-Alkyne Cycloaddition: A Mechanistic Report. *J. Am. Chem. Soc.* 129, 12705-12712 (2007).
15. Worrell, B.T., Malik, J.A. & Fokin, V.V. Direct Evidence of a Dinuclear Copper Intermediate in Cu(I)-Catalyzed Azide-Alkyne Cycloadditions. *Science* 340, 457-460 (2013).
16. Straub, B. μ-Acetylide and μ-alkenylidene ligands in "click" triazole syntheses. *Chem. Commun.*, 3868-3870 (2007).
17. Fokin, V.V. & Matyjaszewski, K. CuAAC: The Quintessential Click Reaction, in *Organic Chemistry – Breakthroughs and Perspectives*. (eds. K. Ding & L.-X. Dai) 247-277 (Wiley-VCH Verlag GmbH & Co. KGaA, Weinheim; 2012).
18. Hein, J. & Fokin, V. Copper-catalyzed azide–alkyne cycloaddition (CuAAC) and beyond: new reactivity of copper(I) acetylides. *Chem. Soc. Rev.* 39, 1302-1315 (2010).
19. Buckley, B.R., Dann, S.E. & Heaney, H. Experimental Evidence for the Involvement of Dinuclear Alkynylcopper(I) Complexes in Alkyne–Azide Chemistry. *Chem. Eur. J.* 16, 6278-6284 (2010).
20. Moen, A. & Nicholson, D.G. Reduction of copper(II) with subsequent disproportionation of copper(I) during the hydrothermal syntheses of microporous silicoaluminium phosphates sapo-5 and -11. *J. Chem. Soc., Faraday Trans.* 91, 3529-3535 (1995).
21. Gonda, Z. & Novák, Z. Highly active copper-catalysts for azide-alkyne cycloaddition. *Dalton Trans.* 39, 726-729 (2010).
22. Rajender Reddy, K., Rajgopal, K. & Lakshmi Kantam, M. Copper-alginates: a biopolymer supported Cu(II) catalyst for 1,3-dipolar cycloaddition of alkynes with

azides and oxidative coupling of 2-naphthols and phenols in water. *Catal. Lett.* 114, 36-40 (2007).

23. Fukuzawa, S.-i., Shimizu, E. & Kikuchi, S. Copper(II) Triflate as a Double Catalystfor the One-Pot Click Synthesis of 1,4-Disubstituted 1,2,3-Triazoles from Benzylic Acetates. *Synlett* 15, 2436-2438 (2007).
24. Glaser, C. Beiträge zur Kenntniss des Acetenylbenzols. *Ber. Dtsch. Chem. Ges.* 2, 422-424 (1869).
25. Serp, P. & Philippot, K. (eds.) *Nanomaterials in Catalysis*, Edn. First. (Wiley-VCH Verlag GmbH & Co. KGaA, Weinheim, Germany; 2013).
26. Scaiano, J.C. *et al.* Tuning plasmon transitions and thier applications in organic photochemistry. *Pure Appl. Chem.* 83, 913-930 (2011).
27. Ranu, B.C., Dey, R., Chatterjee, T. & Ahammed, S. Copper Nanoparticle-Catalyzed Carbon-Carbon and Carbon-Heteroatom Bond Formation with a Greener Perspective. *ChemSusChem* 5, 22-44 (2012).
28. Stamplecoskie, K.G. Doctoratal Thesis, Department of Chemistry, University of Ottawa. (Ottawa, 2013).
29. Corma, A. & Garcia, H. Supported gold nanoparticles as catalysts for organic reactions. *Chem. Soc. Rev.* 37, 2096-2126 (2008).
30. Orgueira, H., Fokas, D., Isome, Y., Chan, P.C.M. & Baldino, C.M. Regioselective synthesis of [1,2,3]-triazoles catalyzed by Cu(I) generated in situ from Cu(0) nanosize activated powder and amine hydrochloride salts. *Tetrahedron Lett.* 46, 2911-2914 (2005).
31. Pachón, L.D., van Maarseveen, J.H. & Rothenberg, G. Click Chemistry: Copper Clusters Catalyse the Cycloaddition of Azides with Terminal Alkynes. *Adv. Synth. Catal.* 347, 811-815 (2005).
32. Borah, B.J., Dutta, D., Saikia, P.P., Barua, N.C. & Dutta, D.K. Stabilization of Cu(0)-nanoparticles into the nanopores of modified montmorillonite: An implication on the catalytic approach for "Click" reaction between azides and terminal alkynes. *Green Chem.* 13, 3453-3460 (2011).
33. Alonso, F., Moglie, Y., Radivoy, G. & Yus, M. Copper nanoparticles in click chemistry: an alternative catalytic system for the cycloaddition of terminal alkynes and azides. *Tetrahedron Lett.* 50, 2358-2362 (2009).
34. Alonso, F., Moglie, Y., Radivoy, G. & Yus, M. Unsupported Copper Nanoparticles in the 1,3-Dipolar Cycloaddition of Terminal Alkynes and Azides. *Eur. J. Org. Chem.* 2010, 1875-1884 (2010).
35. Young Kim, J., Chan Park, J., Kang, H., Song, H. & Hyun Park, K. CuO hollow nanostructures catalyze [3 + 2] cycloaddition of azides with terminal alkynes. *Chem. Commun.* 46, 439-441 (2010).

36. Alonso, F., Moglie, Y., Radivoy, G. & Yus, M. Multicomponent Synthesis of 1,2,3-Triazoles in Water Catalyzed by Copper Nanoparticles on Activated Carbon. *Adv. Synth. Catal.* 352, 3208-3214 (2010).
37. Alonso, F., Moglie, Y., Radivoy, G. & Yus, M. Click chemistry from organic halides, diazonium salts and anilines in water catalysed by copper nanoparticles on activated carbon. *Org. Biomol. Chem.* 9, 6385-6395 (2011).
38. Kang, H. *et al.* Immobilized CuO Hollow Nanospheres Catalyzed Alkyne-Azide Cycloadditions. *J. Nanosci. Nanotechnol.* 10, 6504-6509 (2010).
39. Molteni, G., Bianchi, C.L., Marinoni, G., Santo, N. & Ponti, A. Cu/Cu-oxide nanoparticles as catalyst in the "click" azide-alkyne cycloaddition. *New J. Chem.* 30, 1137-1139 (2006).
40. Park, I.S., Kwon, M.S., Kim, Y., Lee, J.S. & Park, J. Heterogeneous copper catalyst for the cycloaddition of azides and alkynes without additives under ambient conditions. *Org. Lett.* 10, 497-500 (2008).
41. Sarkar, A., Mukherjee, T. & Kapoor, S. PVP-Stabilized Copper Nanoparticles: A Reusable Catalyst for “Click” Reaction between Terminal Alkynes and Azides in Nonaqueous Solvents *J. Phys. Chem. C* 112, 3334-3340 (2008).
42. Kantam, M.L., Jaya, V.S., Sreedhar, B., Rao, M.M. & Choudary, B.M. Preparation of alumina supported copper nanoparticles and their application in the synthesis of 1,2,3-triazoles. *J. Mol. Catal. A: Chem.* 256, 273-277 (2006).
43. Veerakumar, P., Velayudham, M., Lu, K.-L. & Rajagopal, S. Highly dispersed silica-supported nanocopper as an efficient heterogeneous catalyst: application in the synthesis of 1,2,3-triazoles and thioethers. *Catal. Sci. Tech.* 1, 1512-1525 (2011).
44. Raut, D. *et al.* Copper nanoparticles in ionic liquids: Recyclable and efficient catalytic system for 1,3-dipolar cycloaddition reaction. *Catal. Commun.* 10, 1240-1243 (2009).
45. Lee, B.S. *et al.* Copper nitride nanoparticles supported on a superparamagnetic mesoporous microsphere for toxic-free click chemistry. *Chem. Commun.* 46, 3935-3937 (2010).
46. Rance, G., Solomonsz, W. & Khlobystov, A. Click chemistry in carbon nanoreactors. *Chem. Commun.* 49, 1067-1069 (2013).
47. Albaladejo, M.J., Alonso, F., Moglie, Y. & Yus, M. Three-Component Coupling of Aldehydes, Amines, and Alkynes Catalyzed by Oxidized Copper Nanoparticles on Titania. *Eur. J. Org. Chem.* 2012, 3093-3104 (2012).
48. Hudson, R., Li, C. & Moores, A. Magnetic copper–iron nanoparticles as simple heterogeneous catalysts for the azide–alkyne click reaction in water. *Green Chem.* 14, 622-624 (2012).
49. Kumar, B.S.P.A., Reddy, K.H.V., Madhav, B., Ramesh, K. & Nageswar, Y.V.D. Magnetically separable CuFe2O4 nano particles catalyzed multicomponent

synthesis of 1,4-disubstituted 1,2,3-triazoles in tap water using 'click chemistry'. *Tetrahedron Lett.* 53, 4595-4599 (2012).

50. Wu, P. & Fokin, V.V. Catalytic Azide–Alkyne Cycloaddition: Reactivity and Applications. *Aldrich Chim. Acta* 40, 7-17 (2007).
51. Tron, G.C. *et al.* Click chemistry reactions in medicinal chemistry: Applications of the 1,3-dipolar cycloaddition between azides and alkynes. *Med. Res. Rev.* 28, 278-308 (2008).
52. Whiting, M. *et al.* Rapid Discovery and Structure-Activity Profiling of Novel Inhibitors of Human Immunodeficiency Virus Type 1 Protease Enabled by the Copper(I)-Catalyzed Synthesis of 1,2,3-Triazoles and Their Further Functionalization. *J. Med. Chem.* 49, 7697-7710 (2006).
53. Kolb, H.C. & Sharpless, K.B. The growing impact of click chemistry on drug discovery. *Drug Discov. Today* 8, 1128-1137 (2003).
54. Thirumurugan, P., Matosiuk, D. & Jozwiak, K. Click Chemistry for Drug Development and Diverse Chemical-Biology Applications. *Chem. Rev.* 113, 4905-4979 (2013).
55. Schulze, B. & Schubert, U.S. Beyond click chemistry - supramolecular interactions of 1,2,3-triazoles. *Chem. Soc. Rev.* 43, 2522-2571 (2014).
56. Hua, C. *et al.* A novel route to copper(II) detection using 'click' chemistry-induced aggregation of gold nanoparticles. *Analyst* 137, 82-86 (2012).
57. Varazo, K., Droumaguet, C.L., Fullard, K. & Wang, Q. Metal ion detection using a fluorogenic 'click' reaction. *Tetrahedron Lett.* 50, 7032-7034 (2009).
58. Le Droumaguet, C., Wang, C. & Wang, Q. Fluorogenic click reaction. *Chem. Soc. Rev.* 39, 1233-1239 (2010).
59. Lutz, J.-F. & Zarafshani, Z. Efficient construction of therapeutics, bioconjugates, biomaterials and bioactive surfaces using azide-alkyne "click" chemistry. *Adv. Drug Deliv. Rev.* 60, 958-970 (2008).
60. Hong, V., Steinmetz, N.F., Manchester, M. & Finn, M.G. Labeling Live Cells by Copper-Catalyzed Alkyne-Azide Click Chemistry. *Bioconjugate Chem.* 21, 1912-1916 (2010).
61. Gramlich, P.M.E., Wirges, C.T., Manetto, A. & Carell, T. Postsynthetic DNA Modification through the Copper-Catalyzed Azide–Alkyne Cycloaddition Reaction. *Angew. Chem. Int. Ed.* 47, 8350-8358 (2008).
62. Sirion, U. *et al.* An efficient F-18 labeling method for PET study: Huisgen 1,3-dipolar cycloaddition of bioactive substances and F-18-labeled compounds. *Tetrahedron Lett.* 48, 3953-3957 (2007).
63. Liang, L. & Astruc, D. The copper(I)-catalyzed alkyne-azide cycloaddition (CuAAC) "click" reaction and its applications. An overview. *Coord. Chem. Rev.* 255, 2933-2945 (2011).

64. Crisponi, G. *et al.* Copper-related diseases: From chemistry to molecular pathology. *Coord. Chem. Rev.* 254, 876-889 (2010).
65. Buurmans, I.L.C. & Weckhuysen, B.M. Heterogeneities of individual catalyst particles in space and time as monitored by spectroscopy. *Nat. Chem.* 4, 873-886 (2012).
66. Weckhuysen, B.M. Preface: recent advances in the in-situ characterization of heterogeneous catalysts. *Chem. Soc. Rev.* 39, 4557-4559 (2010).
67. Requejo-Isidro, J. Fluorescence nanoscopy. Methods and applications. *J. Chem. Biol.* 6, 97-120 (2013).
68. De Cremer, G., Sels, Bert F., De Vos, Dirk E., Hofkens, Johan, Roeffaers, Maarten B. J. Fluorescence micro(spectro)scopy as a tool to study catalytic materials in action. *Chem. Soc. Rev.* 39, 4702-4717 (2010).
69. Trache, A. & Meininger, G.A. Total Internal Reflection Fluorescence (TIRF) Microscopy, in *Curr. Protoc. Microbiol.* 2A.2.1-2A.2.22 (John Wiley & Sons, Inc., 2008).
70. Fish, K.N. Total Internal Reflection Fluorescence (TIRF) Microscopy, in *Curr. Protocol. Cytom.* (John Wiley & Sons, Inc., 2009).
71. Axelrod, D. Cell-substrate contacts illuminated by total internal reflection fluorescence. *J. Cell Biol.* 89, 141-145 (1981).
72. Stout, A.L. & Axelrod, D. Evanescent field excitation of fluorescence by epi-illumination microscopy. *Appl. Opt.* 28, 5237-5242 (1989).
73. Cordes, T. & Blum, S.A. Opportunities and challenges in single-molecule and single-particle fluorescence microscopy for mechanistic studies of chemical reactions. *Nat. Chem.* 5, 993-999 (2013).
74. Feldheim, D.L. The New Face of Catalysis. *Science* 316, 699-700 (2007).

2. A Click-Based Modular Synthesis of Fluorescent Metal Ion Sensors – A Functional CuAAC application

2.1 Introduction

2.1.1 Optical Metal Ion Sensing

Detection of metal cations has been of vast interest over the last few decades, and in more recent literature, optical sensing, predominantly using fluorescence, has become the most prominent method of sensing.[1] Photo-induced electron transfer (PET) has been particularly successful in the detection of cations with multiple examples of optical cation sensors utilizing PET quenching of a fluorophore as a sensing mechanism.[1, 2] PET based fluorescence sensors generally comprise of a fluorophore attached through a short linker to a nitrogen containing macrocycle or ionophore that selectively binds an analyte cation.[3] The cation-free ionophore engages the lone pair of electrons on nitrogen; when the attached chromophore is excited, electron transfer from the nitrogen is induced, quenching the chromophore's emissive excited state. Analyte binding within the ionophore utilizes the lone pair of electrons in binding, preventing electron donation to the chromophore, thus enabling fluorescence emission. The top panel of **Figure 2-1** depicts the fluorophore-spacer-ionophore design showing OFF and ON emissive states, while the corresponding frontier orbital energy diagrams are provided in bottom panel.

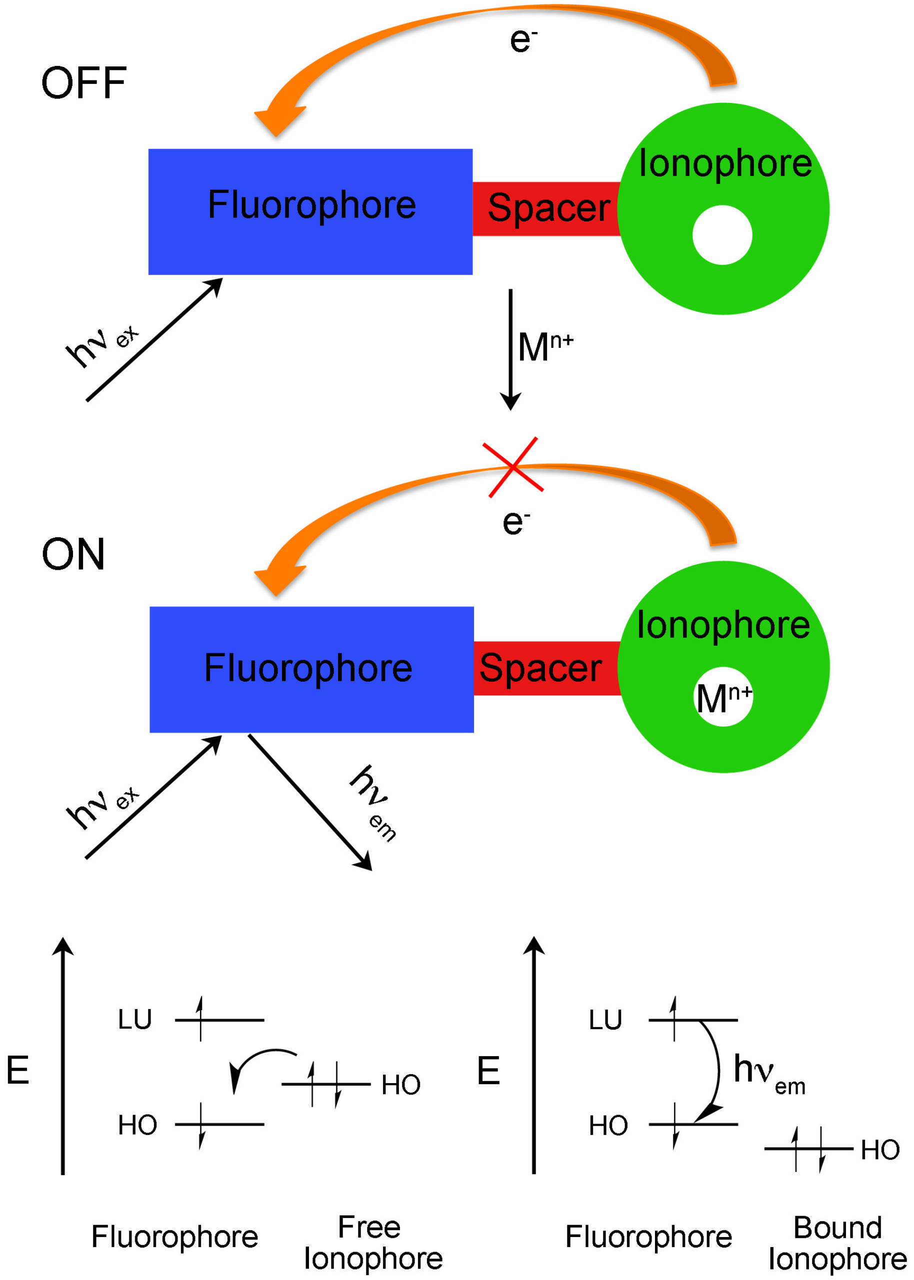

Figure 2-1. (Top) Spaced fluorophore – ionophore sensing system. In the "off" (ion-free) state, photo-induced electron transfer from the ionophore quenches the excited fluorophore. In the "on" (bound) state, metal binding makes PET to the fluorophore thermodynamically disfavored. (Bottom) Frontier orbital energy diagrams of PET sensors in the metal ion free and bound states.[22]

2.1.2 Ionophores

In typical analyte solutions, the analyte molecules in question are usually present in far lower concentrations than the solvent molecules with which they are solvated. To increase the effective analyte ion molarity in the vicinity of a fluorophore, chemosensor structures are designed to include a receptor region or ionophore that selectively traps the desired analyte and excludes non-analyte molecules. Decades of intuitive supramolecular design and tricks borrowed from nature have created a wealth of ionophore examples, many showing superb binding and selectivity for specific ions and molecules. In spite of their structural simplicity, azacrown ionophores are on par with, or exhibit better coordination for their respective analytes than far more structurally complicated receptor molecules, and are readily functionalized through a built in nitrogen heteroatom.[2, 5] Varying the ring size, carbon bridge length between heteroatoms, and substituting oxygen for other heteroatoms allows azacrown ethers to be tuned to selectively bind different ions based on the size and charge of the ion. Increasing the ring size of 1-aza-15-crown-5 by a methylene and one oxygen atom to 1-aza-18-crown-6 changes the binding selectivity from Na^+ to K^+ as potassium is too large to fit in the 15-crown-5 ionophore and sodium is too small to bind strongly in the 18-crown-6 ring. Some exemplar crown ether derived ionophores and the metal ions which they selectively coordinate are provided in **Scheme 2-1**.

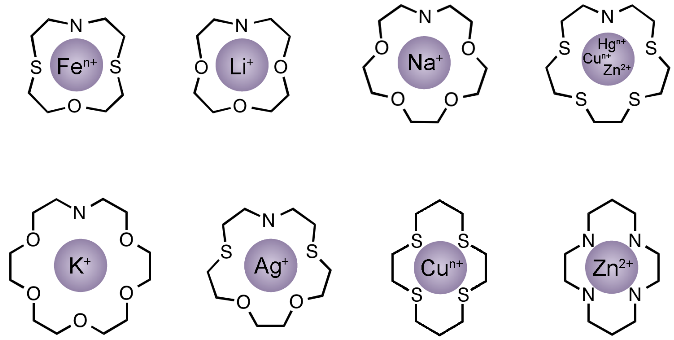

Scheme 2-1. Examples of crown ether derived ionophores selective for various metal cations[2, 5, 6].

2.1.3 Sensors based on CuAAC click chemistry

While there are many reported examples of ion-specific fluorescent turn-on optical sensors;[2, 7-9] the synthesis of individual sensors is typically very demanding and time consuming. A streamlined approach to sensor synthesis in which one common fragment or module can be used in many sensors would be much more efficient. Taking advantage of the efficiency of Cu(I)-catalyzed Huisgen 1,3-dipolar cycloaddition “click’ reaction of an azide and an alkyne to afford a 1,4-triazole linker between a chromophore and a number of ionophores allows for this modular type of synthesis.[10, 11] While the “click” cycloaddition of an azide with a terminal alkyne is well known to be Cu(I) catalyzed, it is much more convenient to reduce a Cu(II) salt such as copper sulphate in situ to Cu(I) with a mild reducing agent such as sodium ascorbate.[11]

Although numerous examples of chemosensors have been reported that feature CuAAC formed triazoles,[3, 12-14] the vast majority of examples simply use click chemistry as a structural building tool where the triazole is far separated from the receptor and fluorophore. In most of these examples the triazole plays no role in signal transduction, however, in rare cases the triazole group has been shown to assist the ionophore in metal binding. Despite previous literature proving PET sensing signal transduction across triazole groups,[12] there are no examples of CuAAC used in a modular approach to the preparation of a PET-based sensing library. Watkinson et al. have reported the first Zn^{2+} sensor based on the cyclam ionophore by linking N-ethylnaphthalimide chromophore with cyclam with the 1,4-triazole product of azide-alkyne click chemistry.[9] Addition of $Zn(ClO_4)_2$ to this sensor in HEPES buffer resulted in emission enhancement up to a factor of five. They later attached the same sensor to a glass surface through an alkyloxysilane tether as a proof-of-concept nanoarray.[15] Rutledge and coworkers expanded on Watkinson's success in creating a similar structure that uses a two carbon triazole ionophore spacer rather than a single carbon spacer, resulting in a fluorescence quenching sensor for Cu^{2+} and Hg^{2+} ions in acetonitrile/water mixtures.[16] Watkinson *et al.* also modified their original sensors by increasing the spacer length to two carbons and reversed the triazole attachment (alkynyl-fluorophore with azido-ionophore) to gain a small signal increase.[13] In another fluorescence quenching example, Wang *et al.* used CuAAC generated triazoles as spacer groups to attach iminodiacetate groups to an anthracene fluorophore creating a sensor that is quenched by Cu^{2+}.[17] A recent investigation by Holdt et al. included a π-conjugated phenyl-aza-18-crown-6 triazole sensor that showed fluorescence enhancement in acetonitrile, but poor selectivity for K^+ over Na^+.[18] The authors attribute the sensors significantly greater response to Na^+ over K^+ to the larger charge density of Na^+. For these sensors K^+/Na^+ selectivity is improved in water at physiological pH, although the sensitivity for both ions is drastically reduced. In another report, Holdt *et al.* synthesized a small series of 1-aza-18-crown-6 based sensors using Cu(I) click chemistry to attached 4-naphthalimide, mesophenyl-BODIPY and 9-anthracene fluorophores in order to tune emission properties.[14] In other interesting examples, a simple boronic acid based saccharide sensor synthesized via Cu(I) click chemistry has been reported by James et al.,[19] and CuAAC click chemistry has also been used to link receptors to pyrene in sensors that function through emission changes caused by analyte induced excimer formation.[20, 21]

2.1.4 A modular CuAAC approach

Fluorimetric ion sensing techniques are particularly suitable for agricultural applications as they typically are extremely sensitive, operate very well under aqueous and oxygen environments and can be optimized for average end-users who are not well versed in chemical systems or advanced sensing instrumentation.

Standard agricultural greenhouses operate drip-lines to transport nutrient feedstocks from a reservoir to individual plants,[4] allowing for control of the amount of feedstock introduced to the plant while excess feedstock solution is returned to reservoir. In-line analysis through ion-selective fluorimetric detection would allow for a feedback system in which accurate measurements of the concentrations of specific nutrients are used to continually optimize the feedstock composition, promoting healthy plant growth while limiting waste of valuable nutrients. This approach also enables remote control and monitoring of nutrient levels and plant health by incorporation of online systems.

With this in mind we were interested in designing a facile methodology for the synthesis of fluorescent ion sensors geared toward agricultural applications that function under aqueous systems. In this chapter we detail a modular approach to the synthesis of ion-specific optical sensors utilizing Cu (I) click chemistry allowing for the development of a small cation sensor library, from a single easy to synthesize chromophore, and a number of commercially available or prepared ionophores. The prepared sensors (**1-3**) are each selective for different analyte ions and fluorophore emission is turned-on rather than quenched with ion binding. The sensors have also been designed with a carboxylate handle for further modification such as possible polymer incorporation toward the end goal of an in-line ion sensing material.

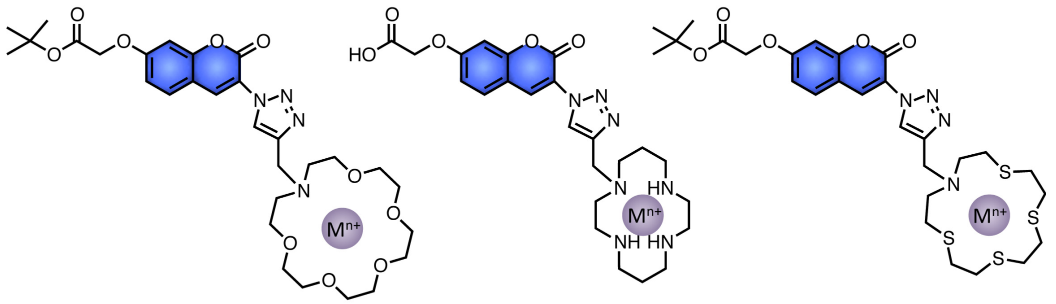

1 2 3

Scheme 2-2. Structures of modular click-based sensors **1-3** showing blue coumarin emission with metal cation binding.

2.2 Metal Cation Sensor Synthesis

2.2.1 Azido-tagged chromophore

The coumarin family of chromophores has been extensively studied, largely because of their strong luminescence,[22] biocompatibility, and the simplicity with which they are synthesized and modified.[23-25] In 2004, Wang and co-workers reported a series of azido-modified fluorogenic coumarins and demonstrated that the emission of these coumarins could be turned on via CuAAC reaction of pendant azide with a terminal alkyne.[24, 26] This motif was exploited as the backbone of sensors described in this chapter as it allows direct attachment of ionophores via CuAAC chemistry while ensuring that the chromophore's emission is not disturbed by the resultant triazole. The synthesis of the optical sensors (**1-3**) first begins with the synthesis of the azido-modified coumarin, 3-azido-7-hydroxycoumarin (**4**) via Pechmann reaction of 2,4-dihydroxybenzaldehyde and *N*-acetylglycine followed by azide incorporation through reaction of sodium azide with the corresponding coumarin diazonium salt.[26,27] The resulting hydroxy-coumarin was subsequently subjected to alkylation with *tert*-butyl bromoacetate in order to provide a functional handle for attachment to polymers or surfaces (**Scheme 2-3**).

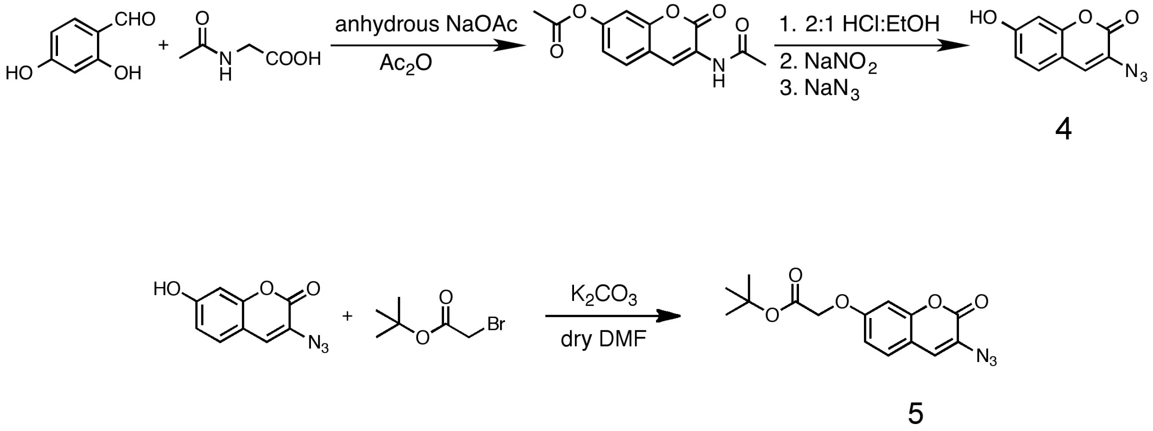

Scheme 2-3. Synthesis of azido-tagged coumarin chromophore **5**.

2.2.2 Terminal alkyne-tagged ionophores

The second module of the click-based sensors reported in this work is the alkyne-substituted ionophore. Certain ionophores such as 1-aza-18-crown-6 and cyclam are commercially available, however, 1-aza-15-thiacrown-5 is not sold commercially, and thus its preparation was required. The sulfur based macrocyclic precursor to ionophore **5** was synthesized by first preparing 3,6-dithia-1,8-octanedithiol according to a modified literature procedure[28] followed by nucleophilic attack on N-boc protected bis(2-chloroethyl)amine with the assistance of an inorganic base in N,N-dimethylformamide (DMF).[29] N-boc protected 1-aza-15-thiacrown-5 was then deprotected with trifluoroacetic acid (TFA) to give 13-aza-1,4,7,10-tetrathiacyclopentadecane (1-aza-15-thiacrown-5, **Scheme 2-4**).

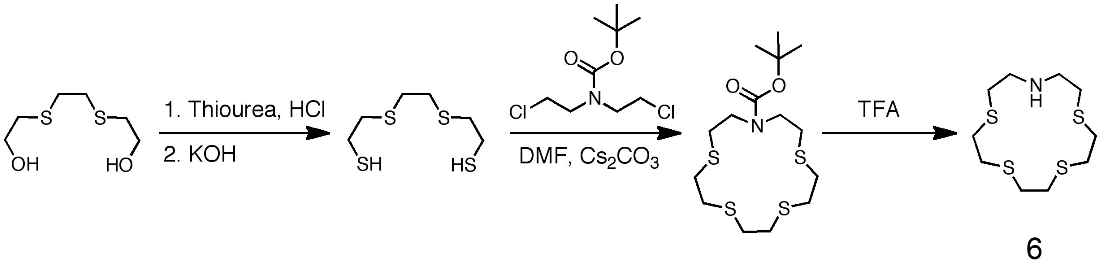

Scheme 2-4. Synthesis of 1-aza-15-thiacrown-5 ionophore.

As the cyclam ionophore contains four equivalent nitrogens, three of them were protected prior to further synthetic modification to prevent attachment of multiple chromophore molecules. Cyclam was tri-BOC protected by refluxing with 3 equivalents of di-tert-butyl dicarbonate and a carbonate base in acetonitrile (MeCN) giving 1,4,8-triboc-cyclam (**7**) in good yield (**Scheme 2-5**).[30]

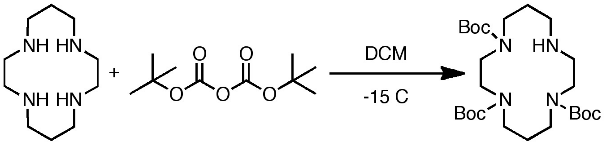

7

Scheme 2-5. Tri-BOC protection cyclam ionophore.

Synthetic modification of an alkyne tag onto the prepared and commercial ionophores was required for them to participate in click coupling chemistry. Alkyne modification of ionophores was achieved by nucleophilic substitution of bromide on propargyl bromide by the amino group of each ionophore under reflux conditions with the aide of a carbonate base. The corresponding terminal alkyne-tagged CuAAC click module ionophores were recovered in good yield after column chromatographic purification **Scheme 2-6**.

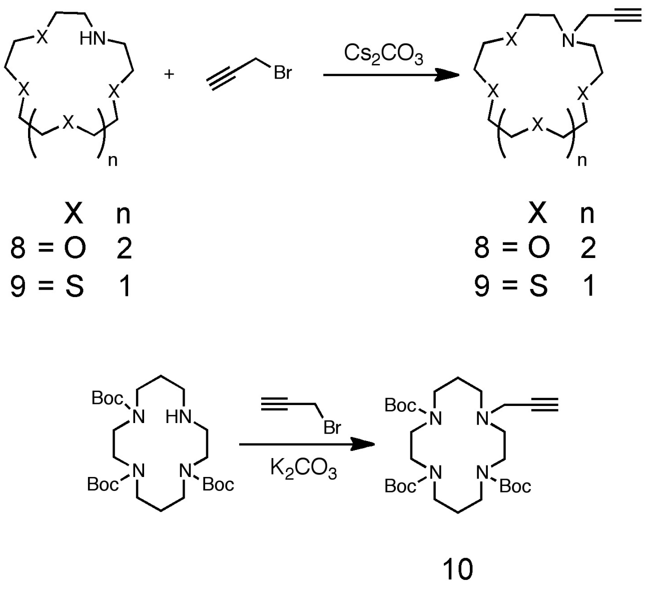

Scheme 2-6. Propargylation of commercial and prepared ionophores to give click modules **8-10**.

2.2.3 CuAAC chromophore and Ionophore conjugation

Once the sensor building blocks were prepared, the two modules were coupled together using the CuAAC click reaction of 3-azido-7-hydroxycoumarin with each individual propargylated ionophore (**Scheme 2-7**). Using this method, sensors **1-3** were synthesized in moderate yields. The preparation of Zn^{2+} sensor (**2**) differed from that of the other sensors by an additional deprotection step with TFA, which was required to remove *t*-boc groups from the cyclam nitrogens that were protected before propargylation. Consequently, the carboxylic acid group tethered to the coumarin chromophore was also deprotected during this step.

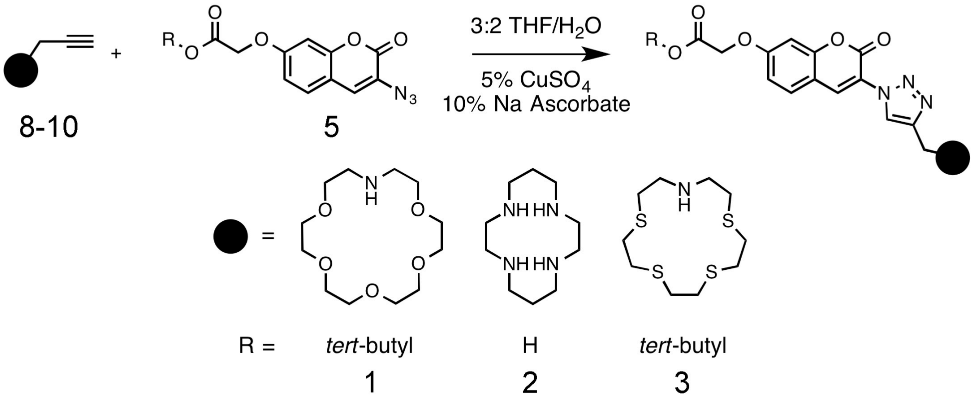

Scheme 2-7. CuAAC click reaction of modular azido-tagged Coumarin **5** and alkyne-tagged ionophores **8-10** to give metal cations sensors **1-3**.

2.3 Spectroscopy of 1

2.3.1 Metal sensing studies

Samples of sensors (**1-3**) were prepared for spectroscopic studies by making a concentrated stock solution (1-5 mM) of the sensor in methanol and diluting aliquots of this standard solution with either MilliQ water, basic/buffered MilliQ or basic/buffered salt solutions in MilliQ water. In the case of K^+ sensor (**1**), a 5 mM solution of the sensor in methanol was used as stock solution and aliquots of this were added to ion solutions that were buffered to pH 9.7 with Na_2HPO_4 and KOH. A final sensor concentration of 7 μM was maintained for each sample. When unbuffered solutions of **1** were excited with 340 nm light, the sensor exhibited stronger fluorescence than with analyte as can be seen in **Figure 2-2**. Buffering the sensor solutions reduced the baseline fluorescence significantly. Addition of potassium acetate to the buffered solutions resulted in a nearly 6.5 fold increase in emission intensity centered at 411 nm with concentration of K^+ increasing from 0 to 60 mM (**Figure 2-3**). The selectivity of this sensor for K^+ over other cations was also assessed by measuring the fluorescence emission of the sensor in buffered solutions of various cations at 100 mM concentration. The emission spectrum of the sensor with each cation is shown in **Figure 2-4B**, while **Figure 2-4A** compares the emission intensity at λ_{max} (411 nm) for the different cations.

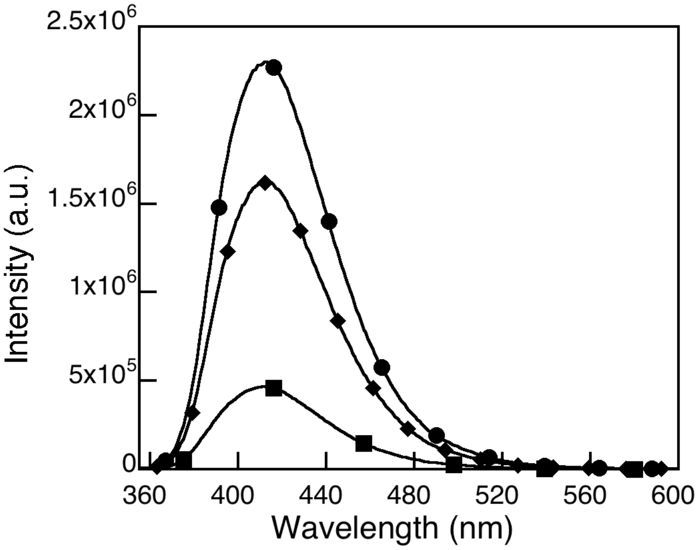

Figure 2-2. Fluorescence intensity of K^+ sensor (1) with (●) No Buffer, (■)Buffer at pH 9.7, (◆) Buffer @ pH 9.7 with 50 mM K^+. Step size is 1 nm.

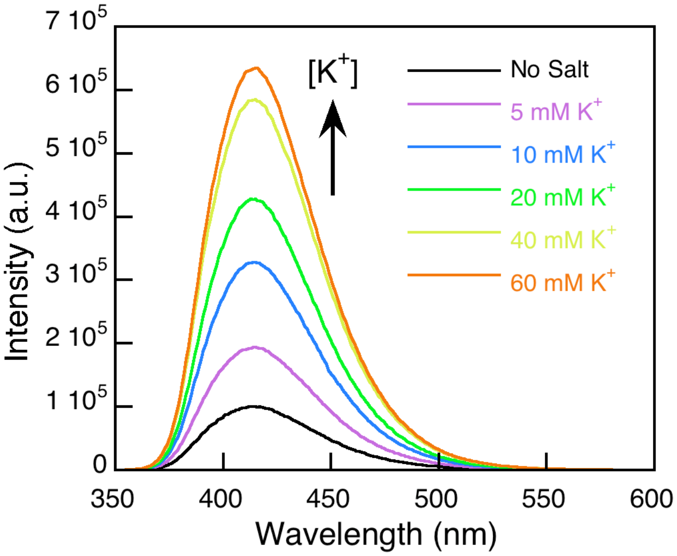

Figure 2-3. Fluorescence emission spectra of 7 μM solutions of K⁺ sensor (1) with K⁺ buffered at pH 9.7 with 340 nm excitation. [KOAc] = 0- 60 mM.

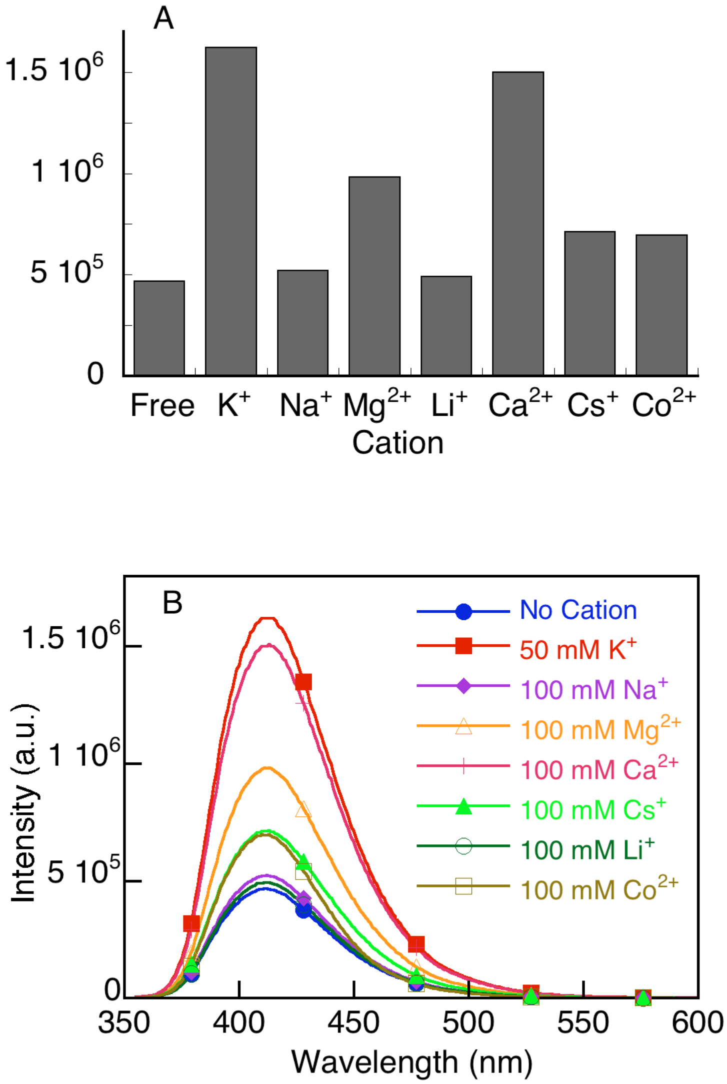

Figure 2-4. (**A**) Comparison of fluorescence emission intensity at 411 nm of 7 μM solutions of K^+ sensor (**1**) buffered at pH 9.7 with addition of 50 mM K^+ or 100 mM of various other cations with 340 nm excitation. The corresponding emission spectra are shown in (**B**).

2.3.2 Fluorescence Lifetime and Quantum Yield

The photophysical properties of **1** under different conditions were also investigated to explore the effect of buffered solutions and potassium ions on the sensor's emission. The fluorescence lifetime, τ_F, of **1** was determined in water, buffer and KOAc solutions by measuring the decay of fluorescence at 411 nm of each solution with 340 nm excitation while keeping the sensor concentration constant (**Figure 2-5**). Fluorescence decay traces were measured with a time-resolved fluorescence spectrometer and lifetimes were extracted from intensity data using the expression for single exponential decay (**Equation 2-1**).[31] Addition of pH 9.7 NaH_2PO_4 buffer to **1** resulted in a decrease in emission lifetime from 2.69 ns to 2.49 ns, while addition of K^+ to the buffered solution caused the emission lifetime to recover back to approximately 2.7 ns (**Table 2-1**).

$$I(t) = I_0 \exp(-t/\tau) \qquad \textbf{(2-1)}$$

The quantum yield of fluorescence of **1** was also determined in the presence and absence of buffer and potassium ions using Quinine sulfate (QS) in 0.1M H_2SO_4 as a quantum yield standard. For quantum yield measurements, five QS solutions in 0.1 M H_2SO_4 with increasing fluorophore concentrations were prepared and five solutions of **1** in water were then prepared to match the absorbance of QS solutions at 340 nm. The integrated emission intensity with 340 nm excitation was then measured for each solution and plotted against the absorbance to give a straight line (**Figures A2-3, A2-4, A2-5**). The quantum yield of fluorescence (Φ_1) of **1** is given by the ratio of the slope of this line over the slope of the line corresponding to the QS solution with matching absorbance at 340 nm multiplied by the known quantum yield of fluorescence of QS after correcting for refractive index differences (**Equation 2-2**). The same experiments were repeated with solutions of **1** containing NaH_2PO_4 buffer and KOAc for comparison of Φ_1 under these conditions. **Table 2-1** summarizes τ and Φ measured for **1** under neutral, basic and potassium salt conditions. The quantum yield changes with changing conditions follow a trend similar to the fluorescence lifetime with buffer causing a decrease in Φ_1 followed by an increase resultant with addition of K^+.

$$\Phi_1 = \Phi_{QS}\left(\frac{slope_1}{slope_{QS}}\right)\left(\frac{n_1^2}{n_{QS}^2}\right) \qquad \textbf{(2-2)}$$

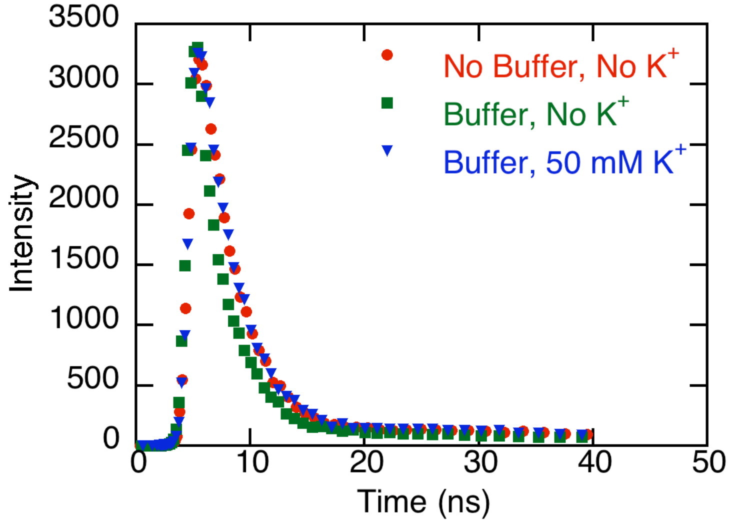

Figure 2-5. Decay of fluorescence signal at 411 nm with 340 nm excitation.

Table 2-1. Lifetime and quantum yield of fluorescence emission of **1** with and without Na_2HPO_4 buffer and K^+. Quantum yield was determined relative to Quinine sulfate in 0.1M H_2SO_4, $\Phi_{QS} = 0.577$.[31]

	Lifetime (τ_F, ns)	Quantum Yield (Φ)
No Buffer, No K^+	2.69	0.72
Buffer, No K^+	2.49	0.12
Buffer, 50 mM K^+	2.73	0.56

2.4 Spectroscopy of 2

In similar fashion to **1**, the spectroscopy of sensor **2** was investigated in aqueous solutions containing the intended analyte, Zn^{2+} in the case of the cyclam based sensor.[9] Aliquots of a 1 mM stock solution of sensor (**2**) in methanol were diluted with KOH solution in a 3 mL quartz cuvette, and appropriate amounts of water or concentrated aqueous $Zn(OAc)_2$ solution were added to each sample before measurement. While the amount of Zn^{2+} was varied between samples, the concentration of **2** was kept constant and the concentration of KOH was maintained at 1.2 mM for each sample. The emission spectra of these solutions with an excitation wavelength of 340 nm are shown in **Figure 2-6**. The observed emission, centered at 422 nm is slightly red-shifted compared to λ_{max} of **1**. When the concentration of Zn^{2+} was increased from 20 to 500 μM a 3-fold increase in emission intensity was observed. Increasing the concentration beyond 500 μM did not yield a corresponding change in emission intensity indicating that **2** is saturated at 500 μM Zn^{2+}.

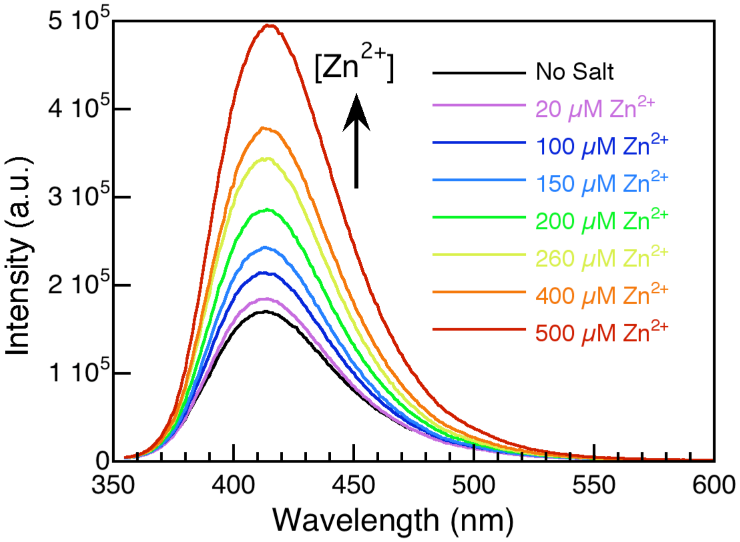

Figure 2-6. Fluorescence emission spectra of 24 μM Zn^{2+} sensor (2) in 1.2 mM KOH with $[Zn(OAc)_2]$ = 20- 500 μM.

The selectivity of **2** for Zn^{2+} over other metal cations was explored by measuring the emission of aqueous **2** solutions containing KOH and 50 mM metal salts. The response of this sensor to other cations with 340 nm excitation is shown in **Figure 2-7B**, and the emission intensities at 422 nm for samples containing the various cations are compared in **Figure 2-7A.** It is clear that Zn^{2+} binding elicits the largest spectral response from **2**, while very little signal change is observed for any other cation examined.

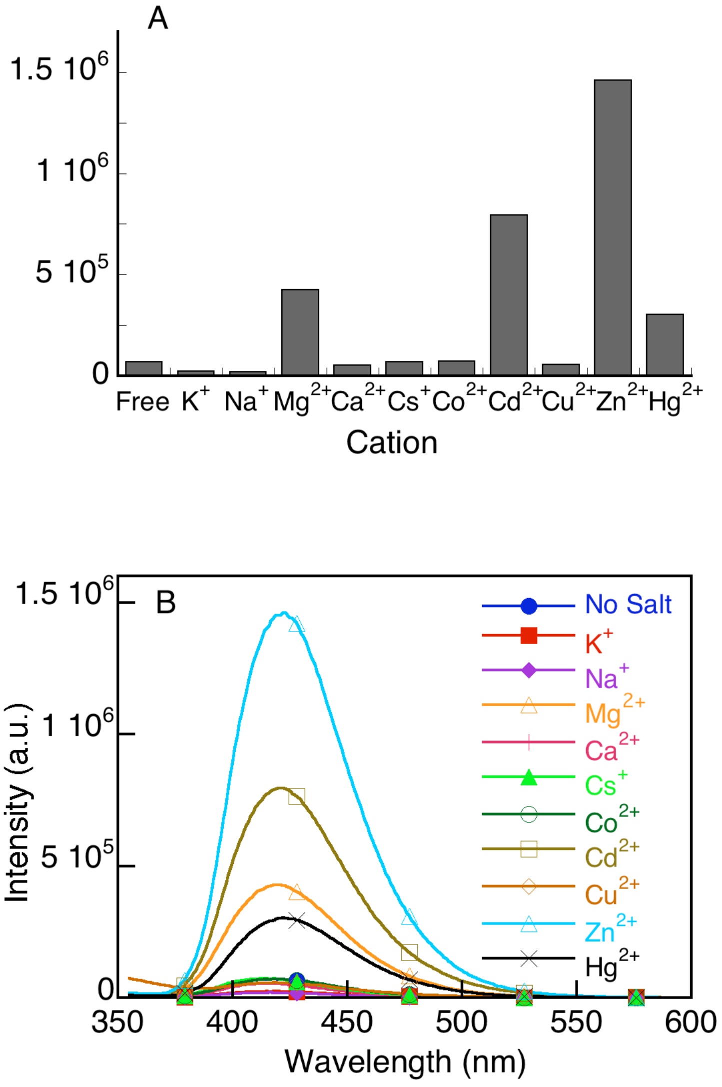

Figure 2-7. (**A**) Comparison of fluorescence emission intensity at 422 nm of 78 µM solutions of Zn^{2+} sensor (2) and 1.2mM KOH with addition of 500µM Zn^{2+} or 50 mM of various other cations with 340 nm excitation. The corresponding emission spectra are shown in (**B**).

2.5 Spectroscopy of 3

Experiments with sensor (**3**) were carried out at 29 μM of sensor with and without KOH. During preliminary studies with this sensor it was observed to have a more complex behaviour with analyte addition compared to sensors **1** and **2** in that **3** seemed to have different dynamic sensing ranges depending on whether or not KOH was added. Exploring this behaviour in greater detail, aliquots of a 2.5 mM stock solution of **3** were diluted with water and aqueous $HgCl_2$ solution giving samples with increasing amounts of Hg^{2+} while maintaining the concentration of **3**. The emission of these samples with 340 nm excitation was observed to increase with increasing salt concentration up to a 2.5-fold emission enhancement with 200 uM Hg^{2+} (**Figure 2-8**). When KOH was added and the sensor concentration maintained at 29 μM, the dynamic sensing range of **3** was extended to higher salt concentrations, with 200 μM Hg^{2+} producing a very small fluorescence increase and addition of 920 uM Hg^{2+} affording a noteworthy 72-fold increase in emission intensity over the sample without Hg^{2+} (**Figure 2-9**). The response of **3** for various metal cations was investigated by the addition of 50 mM salts to the basic sensor solution. The emission spectra of **3** with various cations are shown in **Figure 2-10B**, while **Figure 2-10A** compares emission intensities at λ_{max} (414 nm). The only cations other than Hg^{2+} to give a noteworthy response are Zn^{2+} and Cu^{2+} with 4.5 and 4-fold increases in emission intensity, respectively.

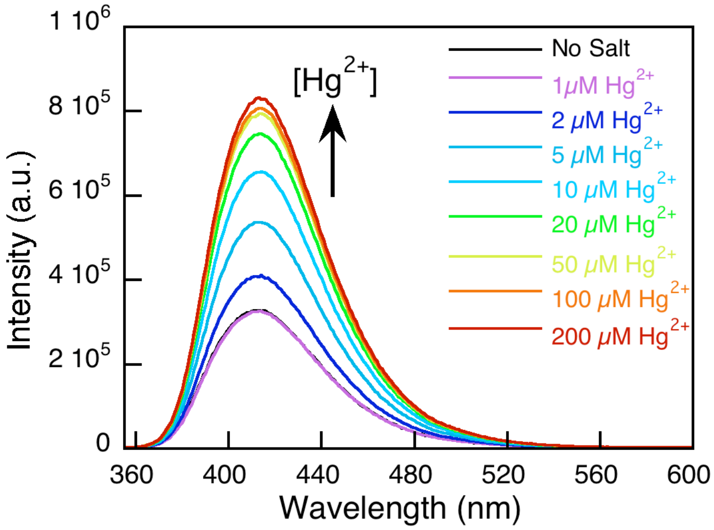

Figure 2-8. Fluorescence emission spectra of 29 μM Hg^{2+} sensor (**3**) in water with [$HgCl_2$] = 0- 200 μM.

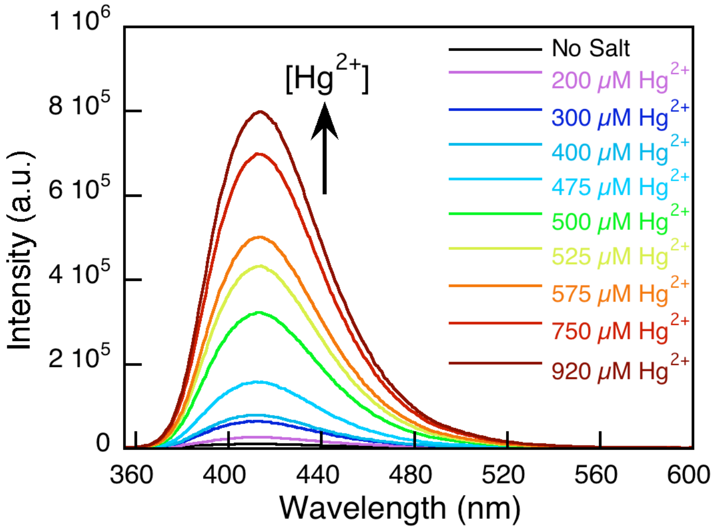

Figure 2-9. Fluorescence emission spectra of 29 μM Hg^{2+} sensor (**3**) in 1.2mM KOH with [$HgCl_2$] = 0- 920 μM.

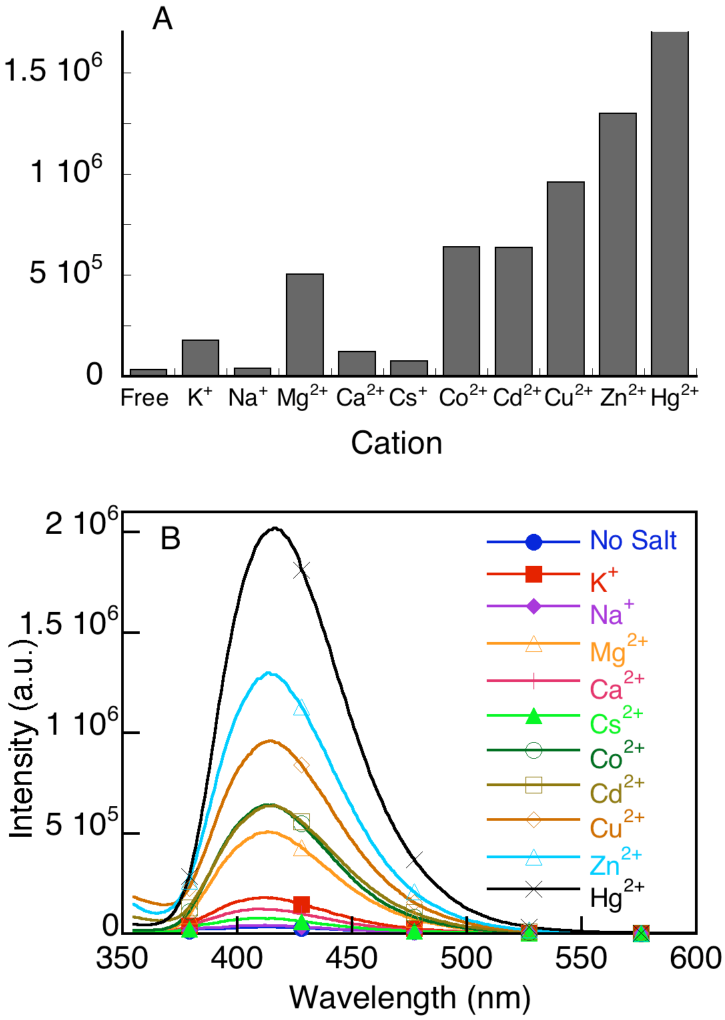

Figure 2-10. (**A**) Comparison of fluorescence emission intensity at 414 nm of 29 µM solutions of Hg^{2+} sensor (**3**) and 1.2 mM KOH with addition of 50 mM Hg^{2+} or 50 mM of various other cations with 340 nm excitation. The corresponding emission spectra are shown in (**B**).

2.6 Discussion

The choice to modify the ionophore with the alkyne moiety rather than the chromophore was for synthetic as well as practical reasons. The ionophore nitrogen atom is crucial to sensor signaling, as it is the lone pair of electrons on this nitrogen that quench the fluorescent excited state of the chromophore. For this reason the nitrogen must be the point in which the ionophore is attached to the chromophore. Modification of the azido group on an amine is not synthetically feasible. The use of an alkyl tether between the amine and azide is one synthetically viable option, however, this generates a problem with sensor signaling as the efficiency for electron transfer required for PET sensing mechanism decreases dramatically as the tether length increases.[32] Rather, the ionophore was modified with an alkyne, and the chromophore was chosen to bear the azido group. This allowed for the two modules of the sensors to be coupled via copper click chemistry, and the sensing mechanism still functions though the triazole ring of the product.

The ionophore nitrogen that is connected by a methylene bridge to the triazole ring carries a lone pair of electrons that may be donated through the triazole ring to the chromophore and quench its emissive excited state through photo-induced electron transfer. This makes the availability of this lone pair of electrons on this nitrogen crucial for the sensing mechanism to function. Quite often, however, this nitrogen is protonated from synthesis, preventing its lone pair of electrons from quenching the chromophore's excited state, resulting in a pre-activated sensor. As can be seen in **Figure 2-2**, deprotonation of the ionophore nitrogen by hydroxide or buffers decreases the fluorescence of the unactivated sensor to a reasonable baseline, opening up the ionophore coordination site for analyte ions. This is confirmed by the large decrease in fluorescence quantum yield of **1** with addition of buffer, and subsequent recovery with analyte ions (**Table 2-1**). Coordination of protons into sensor ionophores can give false positive responses, however, by controlling the sensing conditions, false signaling events can be eliminated. The intended agricultural and environmental applications of the sensors described in this work allow for carefully controlled sensing environments reducing or eliminating the probability of false positives due to pH changes.

After a reasonable fluorescence baseline was established by buffering the sensor solution (**Figure 2-2**), the sensitivity and sensing range of (**1**) was determined by titration with aqueous KOAc solution. K^+ concentrations as low as 1 mM result in a measurable increase in fluorescence intensity of **1**. Increases in emission intensity occur with increasing analyte concentration up to a 60 mM K^+ (**Figure 2-3**). The selectivity for the intended analyte cation over all other cations is nearly as important to the usefulness of a sensor as its sensitivity. To determine the selectivity for K^+ over other cations, the emission of **1** was measured in the presence of buffered 100 mM solutions of various cations (**Figure 2-4**). No shift in the emission spectra arose with the addition (**Figure A2-2**), however, significant fluorescent responses were seen with the addition of Ca^{2+} and Mg^{2+}, as well as minor responses to Co^{2+} and Cs^{+}. Fluorescence increases resulting from the addition of these cations to buffered sensor solutions can be misleading. The concentration of phosphate buffer is high enough to precipitate insoluble salts with small solubility product constants (K_{sp}) such as $Ca_3(PO_4)_2$ and $Mg_3(PO_4)_2$, which have K_{sp} values of 2.07×10^{-33} and 1.04×10^{-24}, respectively.[33] Samples containing these cations appeared cloudy upon visual inspection, confirming the formation of insoluble precipitates. Precipitation of these salts removes phosphate from the solution and decreases the pH. This change in pH causes the sensor's baseline fluorescence to increase as hydroxide and phosphate in the solution act to remove a coordinated proton from the ionophore. For this reason, it can be concluded that Ca^{2+} and Mg^{2+} do not actually coordinate to sensor (**1**), and any signal response measured is an artifact due to changes in pH.

Overall sensor (**1**) is quite selective for K^{+} and is rather insensitive to any other cation. Of particular interest with regard to K^{+} sensing is the selectivity of a sensor molecule for K^{+} over Na^{+}. This is a typical challenge with K^{+} ionophores that the 1-aza-18-crown-6 ionophore excels at; for azacrown ionophores, selectivity depends on the size and shape of the ionophore and the size and charge of metal cation. For 1-aza-18-crown-6, K^{+} exhibits the perfect balance of size and charge to coordinate to the ionophore. For this reason, the excellent K^{+}/Na^{+} selectivity (**Figure 2-4**) of sensor (**1**) was rewarding, but not unexpected.

In a similar manner, the sensing ability of molecule (**2**) was tested by titration of 24 μM solutions of **2** containing 1.2 mM KOH with aqueous $Zn(OAc)_2$. Sensor (**2**) exhibited a noticeable increase in fluorescence with the addition of as little as 20 μM Zn^{2+} and the emission intensity increased with increasing Zn^{2+} concentration up to 500 μM (**Figure 2-6**). The selectivity of this sensor for Zn^{2+} over other metal ions was studied by measuring the emission spectrum of the sensor with 340 nm excitation in basic aqueous solutions of various metal cations. It has been proposed that Zn^{2+} complexation within the cyclam ring is assisted by Zn^{2+} coordination with the nearby triazole nitrogens.[9] It has also been shown that increasing cyclam-triazole spacer to two carbons increases the coordinating ring size, making it more selective for Hg^{2+} and Cu^{2+}.[16] As our sensor (**2**) has only a single carbon cyclam-triazole spacer, it shows much higher selectivity for Zn^{2+}, over Hg^{2+} and Cu^{2+} (**Figure 2-7**). Other than Zn^{2+}, Cu^{2+} and Hg^{2+}, only Cd^{2+} elicits a noteworthy response from sensor (**2**). The concentrations of cadmium and hydroxide in solution exceed the solubility product constant of 7.2×10^{-15} for cadmium hydroxide[33] indicating that the cloudy precipitate seen in the sample is cadmium hydroxide. Again, the precipitation of hydroxide salts leads to removal of OH^- from solution and a subsequent observed change in baseline fluorescence. This also occurred when determining the selectivity of thiacrown sensor (**3**), as shown in **Figure 2-10**. Minor increases in the emission intensity can be seen for Mg^{2+} and Cd^{2+}, which are artifacts of changes in hydroxide concentration caused by precipitation. The sensor exhibits an excellent response to

Hg^{2+}, as it is the appropriate size and charge to fit in the 1-aza-15-thiacrown-5 ionophore, as well as small responses to Zn^{2+} and Cu^{2+}. Sensor **3** exhibits unique dual dynamic sensing ranges depending on the addition of KOH. Without KOH, the sensor displays a moderate increase in emission with increasing Hg^{2+} up to 200 μM addition of Hg^{2+} above this level does not give a corresponding emission increase. When KOH is added, however, Hg^{2+} concentrations up to ~ 1 mM give rise to a significant greater than 70-fold enhancement of emission intensity. It is conceivable that without KOH, the N in the 1-aza-15-thiacrown-5 ionopore of **3** is partially protonated creating a competitive binding scenario with Hg^{2+}. Addition of low concentrations of Hg^{2+} can then bind to the ionophore generating a response, but a large excess of Hg^{2+} contributes to fluorophore quenching, thus a continued increase in emission intensity is not observed. When KOH is added then, the N is deprotonated, leaving the ionophore to freely bind Hg^{2+} making the sensor sensitive to a larger concentration range. Alternatively, it is possible that hydroxide competes with sensor **3** in binding Hg^{2+} ions. In this scenario when KOH is added to the analyte solution some Hg^{2+} participates in binding hydroxide, thus more Hg^{2+} is required in solution to elicit a similar response from sensor **3** compared to that in the absence of hydroxide.

2.7 Summary

In this chapter a modular CuAAC based approach to the synthesis of aqueous fluorescent turn-on cation-specific sensors utilizing click chemistry to form the linker between chomophore and ionophore is described. Three sensors each selective for different ions have been prepared utilizing copper catalyzed click chemistry to couple the same coumarin chromophore with different ion-selective ionophores. We show that these sensors are each quite sensitive toward their respective analyte ions in aqueous solution, with good selectivity over other cations. To date, a number of optical click-based ion-selective sensors have been reported,[9, 16, 18] however, this is the first account employing a streamlined modular copper catalyzed click chemistry approach to the synthesis of multiple sensors.

The triazole groups that combine analyte-binding and signal transmitting modules of the sensors described in this chapter were formed by CuAAC reaction under classical 'Sharpless-Fokin' conditions of a Cu(II) salt reduced to catalytically active Cu(I) *in situ* with sodium ascorbate. The success of this synthetic approach led us to an interest copper nanomaterials as heterogeneous catalysts for the click reaction. Examination of recent literature reports on CuNPs used as catalysts for various reactions, particularly the scope of so called 'heterogeneous catalysts', provided motivation for the more mechanistic oriented investigation of click catalysis that lies ahead in Chapters 3 and 4.

2.8 Experimental Details

Sodium acetate was purchased from Fluka, sodium nitrite was purchased from Fisher Scientific, and bis(2-chloroethyl)amine hydrochloride was purchased from Alfa Aesar. All other reagents were purchased from Sigma-Aldrich. Unless specified, all reagents were used as received without further purification. ACS grade solvents were used for synthesis and spectroscopic grade solvents and Millipore deionized water from a MilliQ system (resistivity 18.2 MΩ at 25°C) was used for spectroscopic studies. Silica gel chromatography was performed using either 230-400 mesh silica gel, or Sigma-Aldrich octadecyl-functionalized silica gel. Salts used for sensor studies include cadmium perchlorate, calcium acetate, cesium acetate, cobalt chloride, copper sulphate, lithium chloride, magnesium chloride, mercury (II) chloride, nickel chloride, potassium acetate, sodium acetate, and zinc acetate.

^{1}H and ^{13}C NMR spectra were recorded with a Bruker Avance 400 or 500 MHz spectrometer in acetone-d_6, $CDCl_3$, DMSO-d_6, or methanol-d_4 and chemical shifts were referenced with the residual proton or carbon signal of the deuterated solvents. High-resolution mass spectra were recorded on a Kratos Concept II mass spectrometer. Electrospray-ionization (ESI) mass spectra were recorded on a Micromass Q-TOF mass spectrometer. Gas chromatography-mass spectra (GC-MS) were analyzed on an Agilent 6890N GC coupled with a 5973i mass selective detector.

2.8.1 Synthesis

3-Azido-7-hydroxy-chromen-2-one (3-azido-7-hydroxycoumarin) (4) – Prepared according to a modified literature procedure.[24] A round bottom flask was charged with 2,4-dihydroxybenzaldehyde (2.76 g, 20 mmol), N-acetylglycine (2.34 g, 20 mmol), and anhydrous sodium acetate (4.92 g, 60 mmol). Anhydrous acetic anhydride (70 mL) was added and the mixture was refluxed from 4 h, after which the reaction was poured over 40 mL of ice. The resulting yellow precipitate was filtered, washed with a small amount of cold water, and dissolved in a mixture of concentrated HCl and ethanol (2:1, 30 mL). This solution was refluxed for 1 h and then diluted with 40 mL ice water and cooled in an ice bath. $NaNO_2$ (2.76 g, 40 mmol) was slowly added to the cooled solution over 5 minutes and stirred for another 10 minutes, after which NaN_3 (3.9 g, 60 mmol) was added over a period of 10-15 minutes and the mixture was stirred for another 15 minutes. The resulting brown precipitate was filtered by suction, washed with ice-cold water, and dried overnight under reduced pressure in a desiccator with P_2O_5. The residue was purified by flash chromatography with ethyl acetate as eluent (1.52g, 37%). ^{1}H NMR (Acetone-d_6, 400 MHz): δ (ppm)= 9.45 (s, O*H*), 7.49 (d, *J*= 8.5 Hz,1H), 7.44 (s, 1H), 6.88 (dd, *J*= 8.5, 2.3 Hz, 1H), 6.80 (d, *J*= 2.3 Hz, 1H). ^{13}C NMR (Acetone-d_6, 400 MHz): δ (ppm)= 161.1, 154.4, 151.3, 130.0, 128.2, 126.0, 114.7, 113.0, 103.3. HRMS (EI): *m/z*: calcd. for $C_9H_5N_3O_3$, $[M]^+$: 203.0331, found: 203.0336.

3-Azido-7-(tert-butylcarboxy methoxy) coumarin (5) – Prepared according to a modified literature procedure.[34] In a small (50 mL) round bottom flask, 3-azido-7-hydroxycoumarin (**4**) (201 mg, 1 mmol) and K_2CO_3 (151 mg, 1.1 mmol) were suspended in anhydrous DMF (10 mL) and the flask was purged with argon with stirring for 10 minutes. The suspension was then heated to 40 °C, *tert*-butyl bromoacetate (160 µL, 1.1 mmol) was added and the reaction was stirred at this temperature for 4 h. The reaction was cooled to room temperature, diluted with ethyl acetate (150 mL) and washed with water (3x100 mL). The aqueous washes were extracted once with ethyl acetate (100 mL) and the organics combined, dried over $MgSO_4$, filtered and evaporated to leave a dark brown oil. The crude product was taken up in CH_2Cl_2 (10 mL) and added dropwise to hexanes (400 mL) with rapid stirring. The brown precipitate that forms was filtered from the yellow supernatant, and subjected to the precipitation procedure again. The yellow supernatants were combined and concentrated by rotary evaporation. The residue was further purified by flash column chromatography with ethyl acetate/hexanes (1:1, v/v) as eluent to give a bright yellow solid. (250 mg, 79%). ^{1}H NMR ($CDCl_3$, 400 MHz): δ (ppm)= 7.33 (d, *J*= 8.6 Hz, 1H), 7.17 (s, 1H), 6.90 (dd, *J*= 8.6, 2.4 Hz, 1H), 6.78 (d, *J*= 2.4 Hz, 1H), 4.57 (s, 2H), 1.50 (s, 9H). ^{13}C NMR ($CDCl_3$, 400 MHz): δ (ppm)= 167.0, 159.9, 157.6, 152.8, 128.3, 126.2, 123.9, 113.6, 113.3, 101.5, 83.1, 65.7, 28.1.

16-(prop-2-yn-1-yl)-1,4,7,10,13-pentaoxa-16-azacyclooctadecane (N-propargyl-1-aza-18-crown-6) (8) – To a round bottom flask containing 70 mL anhydrous acetonitrile were added K_2CO_3 (205 mg, 1.5 mmol) and 1,4,7,10,13-pentaoxa-16-azacyclooctadecane (1-aza-18-crown-6) (195 mg, 0.74 mmol). With stirring, propargyl bromide (77 µL, 0.89 mmol) was added and the mixture was refluxed overnight. Insoluble salts were removed by filtration after cooling the reaction to room temperature and the solvent was evaporated. The residue was dissolved in 100 mL CH_2Cl_2 and washed with water (3 x 75 mL). The organic phase was dried with $MgSO_4$, filtered and the solvent evaporated. The crude product was subjected to flash column chromatography with 90:10 CH_2Cl_2:MeOH as eluent to afford the product as an off-white solid (200 mg, 90%). ^1H NMR ($CDCl_3$, 400 MHz): δ (ppm)= 3.50-3.70 (m, 20H), 2.77 (t, *J*= 4.4, 4H), 2.16 (s, 1H), 1.86 (s, 2H). ^{13}C NMR ($CDCl_3$, 400 MHz): δ (ppm)= 74.2, 72.8, 70.4, 70.0, 69.9, 69.8, 67.2, 53.1, 22.7. HRMS (EI): *m/z*: calcd. for $C_{15}H_{26}NO_5$ ($[M]^+$-H): 300.1816, found: 300.1785.

N-boc-bis(2-chloroethyl)amine – Using a modified literature procedure,[29] a solution of sodium hydroxide (9 g, 224 mmol) in 250 mL water was prepared in a 500 mL round bottom flask. This solution was cooled to 0 °C and bis(2-chloroethyl)amine hydrochloride (10 g, 56 mmol) was added with stirring, followed by the addition of di-*tert*-butyl dicarbonate [$(Boc)_2O$] (13.4 g, 61.6 mmol) slowly over a period of 20 minutes. The reaction was allowed to warm to room temperature as it stirred overnight. The reaction mixture was extracted with EtOAc (3 x 200 mL), the organic layers were combined, dried over $MgSO_4$ and the solvent evaporated to give the N-boc protected product as a pale yellow oil (98%). ^1H NMR (DMSO-d_6, 400 MHz): δ (ppm)= 1.39 (s, 9H), 3.60 (m, 8H). MS (EI): *m/z*: calcd. for $C_9H_{17}Cl_2NO_2$, $[M]^+$: 241.06, found: 241.0.

3,6-Dithia-1,8-octanedithiol – Prepared according to a modified literature procedure.[28] A 100 mL round bottom flask was charged with 3,6-dithia-1,8-octanediol (5.78 g,, 31.7 mmol) and thiourea (4.83 g, 63.4 mmol). Concentrated HCl (15.5 mL) was added with stirring and the mixture was refluxed for 12 h, after which the solution was cooled and a solution of KOH (11.22 g, 0.2 mol) in water (70 mL) was added very slowly. This mixture was refluxed for 3 h, allowed to cool, and the organic phase was then separated from the aqueous phase, which was acidified with HCl and extracted with CH_2Cl_2 (2 x 100 mL) and ethyl acetate (2x100 mL), adding NaCl brine to break up any emulsion that forms. The combined organic layers were dried over $MgSO_4$ and concentrated by evaporation. The residue was purified by column chromatography resulting in white oily residue. The desired product was confirmed by GC-MS and 1H NMR. MS (EI): *m/z*: calcd. for $C_6H_{14}S_4$, $[M]^+$: 214.0, found: 214.0.

13-aza-1,4,7,10-tetrathiacyclopentadecane (6) – Prepared according to a modified literature procedure.[29] *N*-Boc-13-aza-1,4,7,10-tetrathiacyclopentadecane was prepared by making a suspension of Cs_2CO_3 (14 g, 43 mmol) in 150 mL anhydrous DMF in a 500 mL two-neck round-bottom flask and purging the mixture with argon. A solution of 3,6-dithia-1,8-octanedithiol (6.2 g, 29 mmol) and *N*-boc-bis(2-chloroethyl)amine (7.0 g, 29 mmol) in 75 mL anhydrous DMF was added slowly via an addition funnel to the stirring Cs_2CO_3 suspension at 65°C over a period of 96 h. The solvent was then evaporated by rotary-evaporation using a dry-ice/acetone solvent trap. The residue was dissolved in 300 mL CH_2Cl_2 and washed with water (3x150mL) to remove cesium salts. The organic phase was dried with $MgSO_4$ and the solvent evaporated leaving a white oily residue which was subjected to column chromatography using a gradient eluent from 1:1 CH_2Cl_2: Hexanes to pure CH_2Cl_2. The white residue was deprotected immediately by stirring for 20 minutes in a solution of 15 mL CH_2Cl_2 and 10 mL trifluoroacetic acid (TFA). After deprotection was verified to be completed by TLC, the solvent and excess TFA were removed by rotary evaporation, 75 mL of water was added and the pH was adjusted to 14 via addition of saturated $NaHCO_3$ and NaOH and the solution was extracted with CH_2Cl_2 (3 x 100 mL). The combined organics were dried with $MgSO_4$ and the solvent evaporated, leaving 13-aza-1,4,7,10-tetrathiacyclopentadecane as a white solid (75%). ^1H NMR ($CDCl_3$, 400 MHz): δ (ppm)= 1.97 (broad s, 1H), 2.62-2.90 (m, 20H). HRMS (EI): *m/z*: calcd for $C_{10}H_{22}NS_4$, ($[M]^+$+H): 284.0635, found: 284.0642.

13-(prop-2-yn-1-yl)-1,4,7,10-tetrathia-13-azacyclopentadecane (N-propargyl-1-aza-15-thiacrown-5) (9) – To 250 mL round bottom flask containing 100 mL anhydrous acetonitrile were added Cs_2CO_3 (4.14 g, 12.7mmol) and 13-aza-1,4,7,10-tetrathiacyclopentadecane (6) (1.80 g, 6.34 mmol). With stirring, propargyl bromide (0.66 mL, 7.61mmol) was added and the mixture was refluxed overnight. The reaction was filtered after cooling to room temperature to remove insoluble salts and the solvent was evaporated. The residue was dissolved in 150 mL CH_2Cl_2 and washed with water (3 x 100 mL). The organic phase was dried with $MgSO_4$ and the solvent evaporated to give the product as a viscous orange residue (1.9 g, 93%). ^1H NMR ($CDCl_3$, 400 MHz): δ (ppm)= 2.03 (s, 1H), 2.63-2.88 (m, 20H), 3.45 (m, 2H). ^{13}C NMR ($CDCl_3$, 400 MHz): δ (ppm)= 78.3, 73.4, 53.9, 43.1, 33.0, 32.6, 32.3, 29.1. HRMS (EI): *m/z*: calcd for $C_{13}H_{23}NS_4$, $[M]^{+}$: 321.0713, found: 321.0721.

1,4,8-Tris(tert-butoxycarbonyl)-1,4,8,11-tetraazacyclotetradecane (1,4,8-triboc-cyclam) (7) – This compound was prepared according to a literature procedure.[30]

11-(prop-2-yn-1-yl)-1,4,8,11-tetraaza-cyclotetradecane-1,4,8-tri-carboxylic acid tri-tert-butyl ester

(N-propargyl-1,4,8-triboc-cyclam) (**10**) **–** To a 100 mL round bottom flask containing 70 mL anhydrous acetonitrile were added K_2CO_3 (138 mg, 1 mmol) and 1,4,8-triboc-cyclam (**7**) (256 mg, 0.5 mmol). With stirring, propargyl bromide (67 µL, 0.6 mmol) was added and the mixture was refluxed overnight. The reaction was filtered after cooling to room temperature to remove insoluble salts and the solvent was evaporated. The residue was dissolved in 100 mL CH_2Cl_2 and washed with water (3 x 75 mL). The organic phase was dried with $MgSO_4$ and the solvent evaporated to give an off-white residue that was subjected to column chromatography with a gradient eluent of ethyl acetate/hexanes (1:1, v/v) and increasing the eluent polarity to pure ethyl acetate. The purified product was recovered as a white solid (257 mg, 93%).^{1}H NMR ($CDCl_3$, 400 MHz): δ (ppm)= 3.39-3.29 (br m, 14H), 2.67 (m, 2H), 2.50 (d, *J*= 5.7, 2H), 2.16 (br s, 1H), 1.88 (br m, 2H), 1.69 (br m, 2H), 1.46 (s, 27H). MS (ESI): *m/z*: calcd. for $C_{28}H_{51}N_4O_6$ ($[M]^+$+H): 539.38, found: 539.53.

N-boc protected Zn^{2+} sensor (N-boc-2) – In a 25 mL round bottom flask, 3-azido-7-(*tert*-butylcarboxy methoxy) coumarin (**5**) (228 mg, 0.72 mmol) and N-propargyl-1,4,8-triboc-cyclam (**10**) (390 mg, 0.72 mmol) were dissolved in THF/H_2O (3:2, 10mL). While stirring, $CuSO_4 \bullet 5H_2O$ (5 mol %, 9 mg, 0.036 mmol) and sodium ascorbate (10 mol %, 14 mg, 0.072 mmol) were added and the solution was stirred overnight. After the reaction was verified to be complete by TLC with EtOAc as eluent; the solution was diluted with 150 mL EtOAc and washed with water (2 x 100 mL) and NaCl brine (75 mL). The aqueous phase was extracted twice with EtOAc, and the combined organics were dried over $MgSO_4$, filtered and condensed by rotary evaporation. The crude residue was purified by flash column chromatography with a gradient eluent of ethyl acetate/hexanes (1:1 to 1:0, v/v) to give the pure product as a light yellow solid (294 mg, 48%). ^1H NMR ($CDCl_3$, 400 MHz): 8.53 (s, 1H), 8.50 (s, 1H), 7.62 (d, J=8.7 Hz, 1H), 7.01 (dd, J=2.4, 8.7 Hz, 1H), 6.88 (d, J=2.3 Hz, 1H), 4.66 (s, 2H), 3.88 (s, 2H), 3.35 (m, 12H), 2.69 (m, 2H), 2.50 (m, 2H), 1.95 (m, 2H), 1.75 (m, 2H), 1.52 (s, 9H), 1.44-1.47 (m, 27H). ^{13}C NMR (DMSO-d_6, 400 MHz): δ (ppm)= 166.24, 161.37, 155.25, 154.45, 154.30, 154.22, 153.68, 142.93, 134.53, 129.89, 123.60, 120.10, 113.13, 111.57, 101.36, 81.34, 65.92, 52.42, 50.74, 47.68, 46.58, 46.15, 45.99, 45.60, 44.72, 27.76, 27.57, 27.54, 27.20, 26.05. MS (ESI): *m/z*: calcd. for $C_{43}H_{66}N_7O_{11}$ ($[M]^+$+H): 856.48, found: 856.60.

K$^+$ sensor (1) – In a 25 mL round bottom flask, 3-azido-7-(*tert*-butylcarboxy methoxy) coumarin (**5**) (118 mg, 0.37 mmol) and *N*-propargyl-1-aza-18-crown-6 (**8**) (123 mg, 0.41 mmol) were dissolved in THF/H_2O (3:2, 10mL). While stirring, $CuSO_4$•$5H_2O$ (5 mol %, 5 mg, 0.019 mmol) and sodium ascorbate (10 mol %, 7 mg, 0.037 mmol) were added and the solution was stirred overnight. After the reaction was complete (verified by TLC with 9/1 CH_2Cl_2/MeOH eluent) the solution was diluted with 150 mL CH_2Cl_2 and washed with water (2 x 100 mL) and NaCl brine (1 x 75 mL). The aqueous phase was extracted twice with EtOAc, and the combined organics were dried over $MgSO_4$, filtered and condensed by rotary evaporation. The crude residue was purified by flash chromatography with an eluent of CH_2Cl_2/MeOH (9:1, v/v) to give the pure product as a yellow solid (110 mg, 48%). ^1H NMR ($CDCl_3$, 400 MHz): δ (ppm)= 8.54 (s, 1H), 8.50 (s, 1H), 7.70 (d, *J*= 8.6, 1H), 6.98 (dd, *J*= 8.6, 2.2, 1H), 6.84 (d, *J*=2.1, 1H), 4.61 (s, 2H), 4.10-3.50 (br m, 22H), 2.84 (br m, 4H) 1.50 (s, 9H). ^{13}C NMR (Acetone-d_6, 400 MHz): δ (ppm)= 166.8, 162.2, 155.7, 154.5, 154.3, 130.6, 130.6, 128.6, 120.3, 113.6, 111.8, 101.3, 81.8, 69.7, 69.5, 69.2, 68.9, 65.4, 52.3, 48.7, 27.1. MS (ESI): *m/z*: calcd. for $C_{30}H_{43}N_4O_{10}$ ($[M]^+$+H): 619.30, found: 619.35.

Zn^{2+} sensor (2) – In a 100 mL round bottom flask, **N-boc-2** (294 mg, 0.34 mmol) was dissolved in 25 mL CH_2Cl_2 and trifluoroacetic acid (5 mL, 65 mmol) was added. The reaction was stirred overnight at room temperature. After the reaction was complete (verified by TLC with EtOAc as eluent) it was diluted with 75 mL CH_2Cl_2 then washed with saturated $NaHCO_3$ (2 x 75 mL). The aqueous phase was then acidified with HCl until strongly acidic and extracted with CH_2Cl_2 (2 x 50 mL) and EtOAc (50 mL). All organics phases were combined, dried over $MgSO_4$, filtered and condensed by rotary evaporating leaving a yellow residue (154 mg, 90%). ^1H NMR (DMSO-d_6, 400 MHz): δ (ppm)= 8.61 (s, 1H), 8.55 (s, 1H), 7.79 (d, *J*= 8.8, 1H), 7.04 (dd, *J*= 8.6, 2.4, 1H), 6.98 (d, *J*= 2.4, 1H), 4.42 (s, 2H), 3.86 (br s, 2H), 3.6-3.1 (br m, 15H), 2.8-2.6 (br m, 4H), 2.0-1.75 (br m 4H). ^{13}C NMR (DMSO-d_6, 500 MHz): δ (ppm)=168.87, 162.13, 155.92, 154.35, 142.27, 135.98, 130.48, 124.78, 120.39, 113.64, 111.91, 101.82, 65.68, 51.74, 50.64, 47.10, 46.95, 45.46, 45.22, 44.43, 43.59, 30.31, 23.90, 22.28. MS (ESI): *m/z*: calcd. for $C_{24}H_{34}N_7O_5$ ([M]$^+$+H): 500.26, found: 500.44.

Hg^{2+} sensor (3) – In a 25 mL round bottom flask, 3-azido-7-(*tert*-butylcarboxy methoxy) coumarin (**5**) (504 mg, 1.6 mmol) and N-propargyl-1-aza-15-thiacrown-5 (**9**) (510 mg, 1.6 mmol) were dissolved in THF/H_2O (3:2, 15mL). While stirring, $CuSO_4$•$5H_2O$ (5 mol %, 20 mg, 0.08 mmol) and sodium ascorbate (10 mol %, 31 mg, 0.16 mmol) were added and the solution was stirred overnight. After the reaction was complete (verified by TLC with EtOAc eluent) the solution was diluted with 150 mL EtOAc and washed with water (2 x 100 mL) and NaCl brine (1 x 75 mL). The aqueous phase was extracted twice with EtOAc, and the combined organics were dried over $MgSO_4$, filtered and condensed by rotary evaporation. The crude residue was purified by flash column chromatography with a gradient eluent of acetone/methanol (1:0 to 9:1, v/v) to give the pure product as a yellow oily solid (190 mg, 19%). ^{1}H NMR (CDCl$_3$, 400 MHz): δ (ppm)=8.60 (s, 1H), 8.51 (s, 1H), 7.59 (*J*= 8.6, 1H), 6.98 (dd, *J*= 8.6, 2.4, 1H), 6.84 (d, *J*= 2.3, 1H), 4.61 (s, 2H), 4.02 (s, 1H), 3.1-2.6 (m, 20H), 1.48 (s, 9H). ^{13}C NMR (DMSO-d_6, 500 MHz): δ (ppm)=166.25, 161.52, 155.27, 153.82, 153.79, 135.00, 130.03, 124.69, 119.92, 113.14, 111.50, 101.40, 81.37, 65.62, 55.35, 52.43, 47.50, 32.74, 32.25, 32.12, 32.05, 31.77, 29.65, 28.98, 27.22. MS (ESI): *m/z*: calcd. for $C_{28}H_{38}CuN_4O_5S_4$ ($[M]^+$+Cu): 701.10, found: 701.34.

2.8.2 Spectroscopy

Fluorescence emission spectra were recorded using a Photon Technology International spectrofluorometer equipped with a LPS-220 lamp power supply and either an 810 or 814 photomultiplier tube detector in a 10 mm x 10 mm quartz cell. UV-VIS Absorption spectra were recorded on an Agilent Cary-50 Spectrophotometer which was zeroed before sample measurement and spectra were baseline subtracted by measuring the pure solvent. Fluorescence lifetime measurements were recorded on an EasyLife LS Fluorescence Lifetime System from Photon Technology International (PTI). Solutions of sensor **1** in MilliQ water were prepared with and without the addition of NaH_2PO_4 buffer and KOAc while maintaining sensor concentration. The absorption of each solution was kept below 0.1 at 340 nm. The decay of emission signal with excitation from a 340 nm diode was measured for each sample. Recorded fluorescence decay traces were analyzed with Felix analysis software (PTI). Traces were corrected for the instrument response before fitting with the equation for a single-exponential decay to extract lifetime information. Quantum yield measurements for **1** under various sensing conditions (MilliQ water, buffer and 50 mM KOAc) were performed using Quinine sulfate (QS) in 0.1M H_2SO_4 as a standard (Φ_{QS} = 0.577). For each sensing condition, five solutions of sensor **1** were prepared with increasing sensor concentration, keeping the absorption at 340 nm under 0.1 for each sample. Five Quinine sulfate solutions of increasing concentration were prepared in 0.1M H_2SO_4 such that the absorption of these solutions at 340 nm matched the absorption of the five sample solutions at this wavelength (**Figures A2-3 – A2-5**). The emission spectrum of each sensor and QS standard solution was recorded with 340 nm excitation and the integrated emission intensity for each sample was determined by calculating the area under the emission curve. The integrated emission intensity for each sample was plotted against the sample absorption at 340 nm for both the sensor and QS standard. The resultant plot exhibits two straight lines (**Figures A2-3 – A2-5**), one for the sample and one for the standard. The slopes of these lines were determined by linear regression and used to calculate the quantum yield using **Equation 2-2**. This process was repeated for all other sensing conditions.

2.9 References

1. McDonagh, C., Burke, C.S. & MacCraith, B.D. Optical chemical sensors. *Chem. Rev.* **108**, 400-422 (2008).
2. de Silva, A.P. *et al.* Signaling Recognition Events with Fluorescent Sensors and Switches. *Chem. Rev.* **97**, 1515-1566 (1997).
3. de Silva, A.P., Fox, D.B., Moody, T.S. & Weir, S.M. The development of molecular fluorescent switches. *Trends Biotechnol.* **19**, 29-34 (2001).

4. Giroux, R. *et al.* Greenhouses in extreme environments: The Arthur Clarke Mars Greenhouse design and operation overview. *Adv. Space Res.* **38**, 1248-1259 (2006).
5. Tanaka, M. *et al.* Synthesis and metal-ion binding properties of monoazathiacrown ethers. *J. Org. Chem.* **66**, 7008-7012 (2001).
6. Loudet, A. & Burgess, K. BODIPY Dyes and Their Derivatives: Syntheses and Spectroscopic Properties. *Chem. Rev.* **107**, 4891-4932 (2007).
7. Buhlmann, P., Pretsch, E. & Bakker, E. Carrier-based ion-selective electrodes and bulk optodes. 2. Ionophores for potentiometric and optical sensors. *Chem. Rev.* **98**, 1593-1687 (1998).
8. Baruah, M. *et al.* A highly potassium-selective ratiometric fluorescent indicator based on BODIPY azacrown ether excitable with visible light. *Org. Lett.* **7**, 4377-4380 (2005).
9. Tamanini, E., Katewa, A., Sedger, L.M., Todd, M.H. & Watkinson, M. A Synthetically Simple, Click-Generated Cyclam-Based Zinc(II) Sensor. *Inorg. Chem.* **48**, 319-324 (2009).
10. Kolb, H.C., Finn, M.G. & Sharpless, K.B. Click chemistry: Diverse chemical function from a few good reactions. *Angew. Chem. Int. Ed.* **40**, 2004-+ (2001).
11. Rostovtsev, V.V., Green, L.G., Fokin, V.V. & Sharpless, K.B. A stepwise Huisgen cycloaddition process: Copper(I)-catalyzed regioselective "ligation" of azides and terminal alkynes. *Angew. Chem. Int. Ed.* **41**, 2596-2599 (2002).
12. Lau, Y.H., Rutledge, P.J., Watkinson, M. & Todd, M.H. Chemical sensors that incorporate click-derived triazoles. *Chem. Soc. Rev.* **40**, 2848-2866 (2011).
13. Ast, S., Rutledge, P.J. & Todd, M.H. Reversing the Triazole Topology in a Cyclam-Triazole-Dye Ligand Gives a 10-Fold Brighter Signal Response to Zn2+ in Aqueous Solution. *Eur. J. Inorg. Chem.* **2012**, 5611-5615 (2012).
14. Ast, S. *et al.* Integration of the 1,2,3-Triazole “Click” Motif as a Potent Signalling Element in Metal Ion Responsive Fluorescent Probes. *Chem.-Eur. J.* **19**, 2990-3005 (2013).
15. Tamanini, E. *et al.* Cyclam-Based "Clickates": Homogeneous and Heterogeneous Fluorescent Sensors for Zn(II). *Inorg. Chem.* **49**, 3789-3800 (2010).
16. Lau, Y., Price, J., Todd, M.H. & Rutledge, P. A Click Fluorophore Sensor that Can Distinguish Cu-II and Hg-II via Selective Anion-Induced Demetallation. *Chem.-Eur. J.* **17**, 2850-2858 (2011).
17. Varazo, K., Xie, F., Gulledge, D. & Wang, Q. Synthesis of triazolyl anthracene as a selective fluorescent chemosensor for the Cu(II) ion. *Tetrahedron Lett.* **49**, 5293-5296 (2008).
18. Ast, S. *et al.* High Na+ and K+-induced fluorescence enhancement of a pi-conjugated phenylaza-18-crown-6-triazol-substituted coumarin fluoroionophore. *Chem. Commun.* **47**, 4685-4687 (2011).

19. Scrafton, D.K., Taylor, J.E., Mahon, M.F., Fossey, J.S. & James, T.D. "Click-fluors": Modular fluorescent saccharide sensors based on a 1,2,3-triazole ring. *J. Org. Chem.* **73**, 2871-2874 (2008).
20. Fujimoto, K., Yamada, S. & Inouye, M. Synthesis of versatile fluorescent sensors based on Click chemistry: detection of unsaturated fatty acids by their pyrene-emission switching. *Chem. Commun.*, 7164-7166 (2009).
21. Hung, H.-C., Cheng, C.-W., Wang, Y.-Y., Chen, Y.-J. & Chung, W.-S. Highly Selective Fluorescent Sensors for Hg2+ and Ag+ Based on Bis-triazole-Coupled Polyoxyethylenes in MeOH Solution. *Eur. J. Org. Chem.* **2009**, 6360-6366 (2009).
22. Kuznetsova, N.A. & Kaliya, O.L. Photochemistry of Coumarins. *Usp. Khim.* **61**, 1243-1267 (1992).
23. Sethna, S.M. & Shah, N.M. The Chemistry of Coumarins. *Chem. Rev.* **36**, 1-62 (1945).
24. Le Droumaguet, C., Wang, C. & Wang, Q. Fluorogenic click reaction. *Chem. Soc. Rev.* **39**, 1233-1239 (2010).
25. O'Kennedy, R. & Thornes, R.D. (eds.) *Coumarins, Biology, Applications and Mode of Action*. (John Wiley and Sons, Chichester; 1997).
26. Sivakumar, K. *et al.* A fluorogenic 1,3-dipolar cycloaddition reaction of 3-azidocoumarins and acetylenes. *Org. Lett.* **6**, 4603-4606 (2004).
27. Bräse, S., Gil, C., Knepper, K. & Zimmermann, V. Organic Azides: An Exploding Diversity of a Unique Class of Compounds. *Angew. Chem. Int. Ed.* **44**, 5188-5240 (2005).
28. Rosen, W. & Busch, D.H. Nickel(II) Complexes of Cyclic Tetradentate Thioethers. *J. Am. Chem. Soc.* **91**, 4694- (1969).
29. Glenny, M.W. *et al.* Improved synthetic methods to mixed-donor thiacrown ethers. *Polyhedron* **25**, 599-612 (2006).
30. Fabbrizzi, L. *et al.* Light-emitting molecular machines: pH-induced intramolecular motions in a fluorescent nickel(II) scorpionate complex. *Chem.-Eur. J.* **8**, 4965-4972 (2002).
31. Lakowicz, J.R. *Principles of Fluorescence Spectroscopy*, Edn. Second Edition. (Kluwer Academic, New York, N.Y.; 1999).
32. Sankaran, N., Nishizawa, S., Watanabe, M., Uchida, T. & Teramae, N. Designing ratiometric fluorescent sensors for alkali metal ions from simple PET sensors by controlling spacer length. *J. Mater. Chem.* **15**, 2755 (2005).
33. *CRC Handbook of Chemistry and Physics*, Edn. 92nd. (Internet Version, 2011-2012).
34. Dirks, A.J., Cornelissen, J.J.L.M. & Nolte, R.J.M. Monitoring Protein-Polymer Conjugation by a Fluorogenic Cu(I)-Catalyzed Azide-Alkyne 1,3-Dipolar Cycloaddition. *Bioconjugate Chem.* **20**, 1129-1138 (2009).

3. Copper Nanoparticle Heterogeneous Catalytic ‘Click’ Cycloaddition Confirmed by Single-Molecule Spectroscopy

3.1 Introduction

3.1.1 Copper nanoparticles as CuAAC catalysts

The Cu(I)-catalyzed 1,3-dipolar Azide-Alkyne Cycloaddition (CuAAC) click reaction introduced independently by Sharpless[1] and Meldal[2] in 2002, finds utility in many disciplines beyond synthetic organic chemistry.[3-7] There is an interest in improving efficiency, reducing cost as well as byproducts, and discovering new catalysts[5, 7-12] for this powerful conjugation tool. Copper nanoparticles (CuNP) are being explored as click catalysts in the hope of improving reusability and efficiency compared to their solution counterparts.[13-21] Despite recent proof-of-concept examples of CuNP-catalyzed click reactions, few investigate the catalytic activity of CuNP, and generally it is difficult, if not impossible, to establish if the true catalyst is the CuNP, copper ions leaching from it,[22] or if the CuNP acts as a reductant converting Cu(II) to Cu(I).

3.1.2 Where the action is – deciphering the phase of catalysis

The question as to whether heterogeneous catalysts promote homogeneous catalysis is as common as it is difficult to answer.[23] In a recent click study using Cu/Fe nanocatalysts this question was examined in some detail allowing the identification of systems involving true heterogeneous catalysis, and those where catalysis was due to leaching, including extreme examples where the 'catalyst' dissolved in the reaction media.[20] Demonstrating that their bimetallic copper-iron nanoparticles were catalytically active in the heterogeneous phase required Hudson and co-workers to remove the catalyst from reaction mixtures and analyze the supernatant with expensive ICP-OES. Cases where heterogeneous catalysis prevails in spite of ion leaching, whether or not these ions are also catalysts, are difficult to characterize.[24-26] More so, systems involving simultaneous dynamic catalyst dissolution and aggregation have been shown to increasingly complicate the characterization of the active phase of catalysis.[27] Single-molecule TIRF microscopy has been employed by Blum to unequivocally determine the heterogeneous vs. homogeneous nature of a ruthenium polymerization catalyst, where the latter was found to dominate.[28, 29] Blum and Co-workers directly imaged ring-opening metathesis polymerization (ROMP) by incorporating a BODIPY labeled olefin tag as co-monomer, using the BODIPY emission to observe Ru leached from the solid Grubbs II material actively catalyzing ROMP in solution and followed the polymer product as it precipitated from solution (**Figure 3-1**). Interestingly, the BODIPY labeled olefin probe showed no affinity for the solid phase Grubbs II catalyst ruling out heterogeneous catalysis. Blum's methodology has proved to be quite successful in demonstrating homogeneous catalysis through ions leached into solution, however, demonstrating discreet heterogeneous catalysis is a more formidable challenge. A logical and investigative approach must look for clues that can only arise out of heterogeneous reactivity.

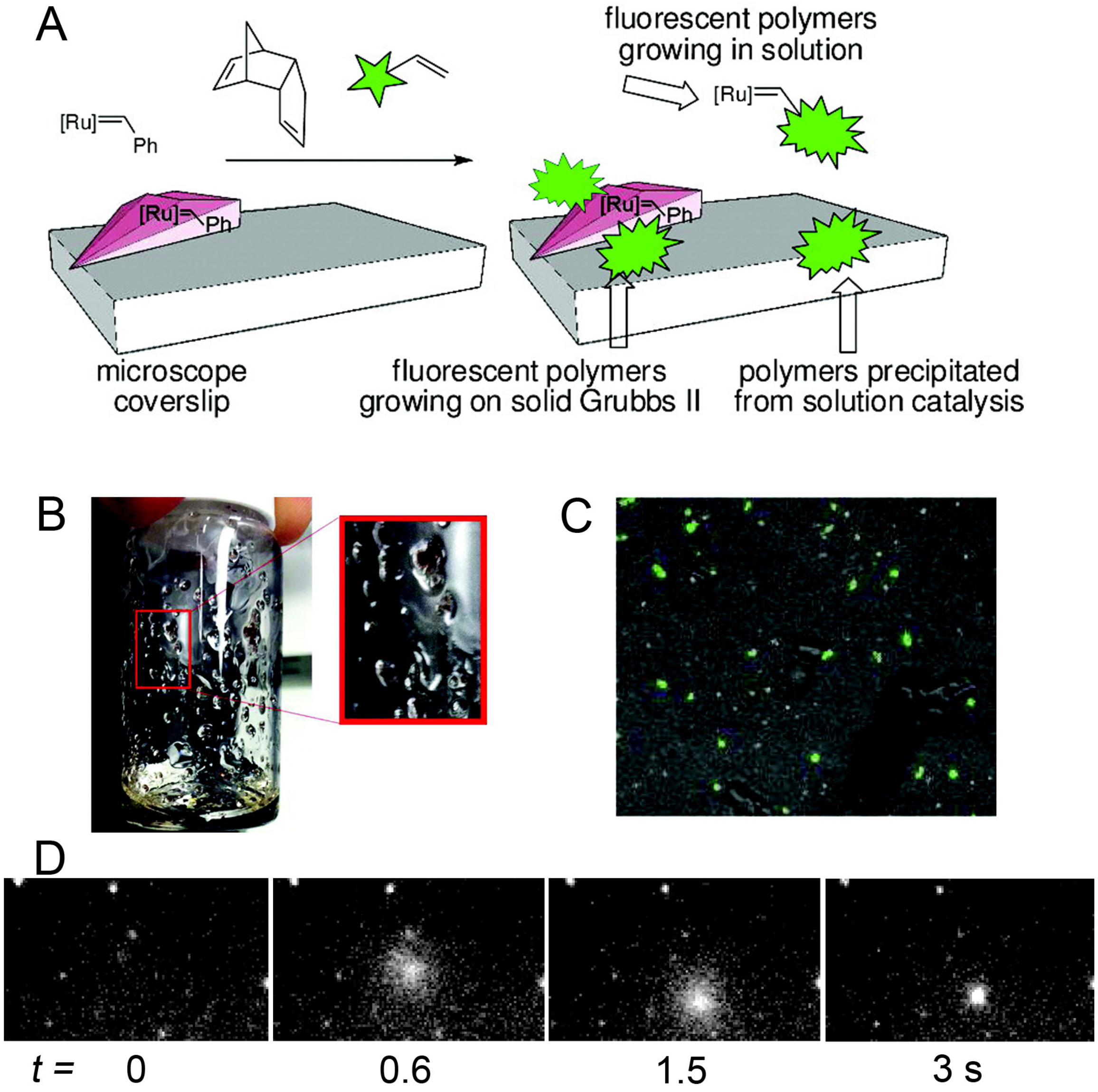

Figure 3-1. (**A**) ROMP of dicyclopentadiene with BODIPY-tagged olefin as co-monomer catalyzed by Grubbs II Ru catalyst leached into solution. (**B**) Bench-top reaction depicts polymers encapsulating the solid Grubbs II catalyst. (**C**) White light image of catalyst overlayed with colour added TIRFM image. (**D**) Time-correlated TIRFM images of polymer precipitating from solution and becoming visible as embedded BODIPY tag enters evanescent region.[28] Figure adapted with permission from Blum *et al.*, J. Am. Chem. Soc. 133, 18145. Copyright (2011) American Chemical Society.

3.1.3 Single-molecule microscopy of catalytic reactions

While examples to determine the phase of the catalyst remain rare, discerning the active regions of catalysts has been the focus of a number of recent single-molecule catalysis reports. Hofkens used single-molecule spectroscopy of fluorogenic furfuryl alcohol polymerization to probe acidity[30] and map catalytic activity of zeolites.[31] The same group employed the catalytic epoxidation of a BODIPY-conjugated olefin to probe the activity of TiO_2 based mesoporous materials,[32] while a similar BODIPY structure was used by Herten to investigate competing pathways in stoichiometric m-chloroperbenzoic acid (*m*CPBA) epoxidations.[33] Blum used a BODIPY-tagged platinum complex to probe Pt ligand exchange reactivity with thiourea on functionalized surfaces.[34, 35] Single-molecule techniques have also been used to observe crystal-face-dependent catalysis of layered double hydroxides,[36] and face-dependent catalysis of gold nanoparticles[37-39] and has also been the subject of recent reviews.[40-43] Chen *et al.* have also taken a single-molecule approach to high-throughput catalyst screening which uses single-molecule catalysis to identify high activity catalyst particles in mixtures of catalysts and activity correlations to assess reactions that do not involve fluorescence.[44] While many of these reports indicate probable heterogeneous activity, this is not analogous to proving true heterogeneous catalysis and the absence of homogeneous catalysis. The reactions and dyes described in these reports are summarized in **Figure 3-2**.

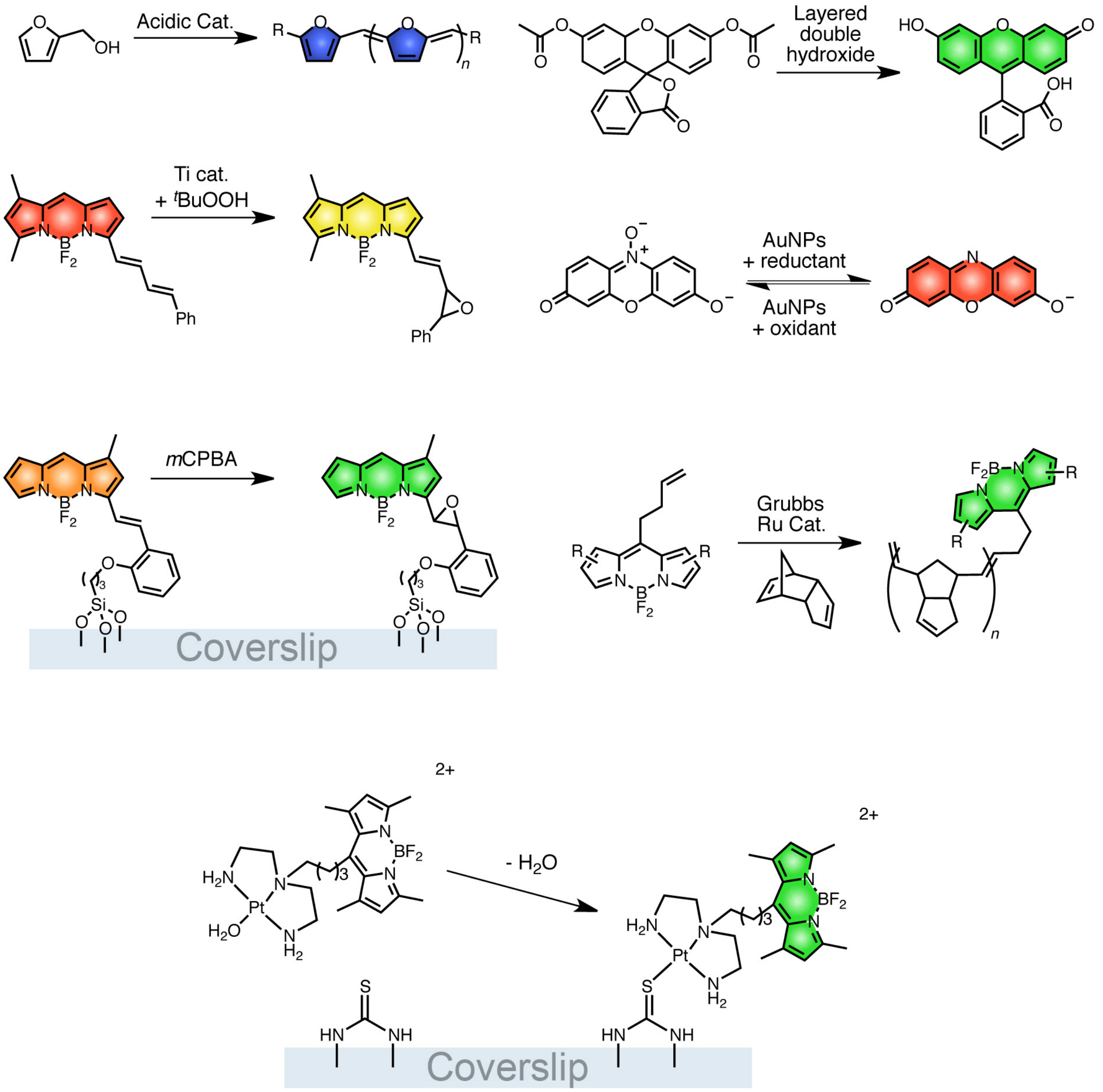

Figure 3-2. Summary of fluorophores used in single-molecule spectroscopy to probe chemical reactions. In order, from left to right, top to bottom: acidic zeolite catalyzed polymerization of furfuryl alcohol,[30] Li^+ and Al^{3+} double hydroxide catalyzed ester hydrolysis of 5-carboxyfluorescein diacetate,[36] Ti-MCM-41 catalyzed epoxidation of phenylbutadienyl-BODIPY,[32] AuNP catalyzed redox reactions of resorufin and resazurin,[37] epoxidation of styryl-BODIPY,[33] Grubbs II catalyzed ROMP of dicyclopentadiene with BODIPY-tagged olefin as co-monomer[28] and ligand exchange on a Pt-BODIPY complex.[35, 43]

The success of TIRFM as a single-molecule technique hinges on the generation of an evanescent wave at the glass-sample interface that only allows irradiation of the sample within approximately 100 nm from the glass support surface.[45] Single-molecule microscopy requires a change in optical signal in order to measure a molecular response. The preferred signaling processes are those that activate emission from a dye or shift its emission wavelength. Chemical reactions studied with single-molecule microscopy can be separated into two categories: those that change the structure of a molecule altering its emission properties[36] and those that require a tag such as an attached dye to probe the reaction;[34] the dyes in these two categories have been termed participants and spectators, respectively.[43] The CuAAC click reaction falls into the second category since azide and alkyne reactive groups do not emit and an attached dye is required to visualize the reaction. Förster resonance energy transfer (FRET) between pairs of dyes has been extensively used as a molecular ruler in TIRF microscopy (e.g., to study protein-protein interactions).[46-51] This strategy can be applied in the investigation of the CuAAC click reaction using heterogeneous catalysts by using appropriately functionalized azides and alkynes.

3.1.4 Our approach

In our strategy, we apply the nascent area of single-molecule techniques to determine unequivocally if catalysis is truly heterogeneous. Further, for those cases where improving the heterogeneous nature of the reaction is desirable, single-molecule – single nanoparticle studies can be a powerful tool for catalyst optimization.[28, 29, 32, 41-44] We combine bench scale reactions with single-molecule studies using Total Internal Reflectance Microscopy (TIRFM), an effective tool in studying heterogeneous nanoscale catalyst surface dynamics and reactivity.[28, 31, 32, 35-44, 52]

We demonstrate here that CuNP can catalyze the click reaction between an alkyne conjugated to a donor dye and an azide modified with an acceptor dye; further, we show that the process involves true heterogeneous catalysis, rather than homogeneous catalysis induced by ions released from the CuNP. The product of the reaction is a 1,2,3-triazole that brings the two dyes in close proximity, thus enabling FRET energy transfer; this results in acceptor emission that can be monitored by single-molecule spectroscopy.

3.2 CuNP Synthesis and CuAAC activity on the bench

The CuNP used for catalysis were prepared by a slightly modified method based on that reported by Khlobystov for the synthesis of CuNP encapsulated in hollow graphitized carbon nanofibers.[15] This two-phase sodium borohydride reduction method produces monodisperse thiolate-capped spherical CuNPs approximately 3 nm in diameter (**Figure 3-3**, **Figure 3-4**). The catalytic activity of these colloidal CuNP was verified at the bench-top scale in the reaction of azide **11** with phenylacetylene (**Scheme 3-1**). It produced exclusively the 1,4-regioisomer 1,2,3-triazole product **12** in good yield (See 3.7 Experimental Details and Appendix). BODIPY azide **11** was synthesized by trifluoroacetic acid catalysed condensation of 4-formylbenzoic acid and 2,4-dimethylpyrrole. The resulting dipyrromethane was converted to dipyrromethene with a benzoquinone followed by subsequent reaction with BF_3-OEt_2 with triethylamine as additive to afford the desired carboxy BODIPY backbone. BODIPY-COOH was subjected to N,N-dicyclohexylcarbodiimide (DCC) / 4-(dimethylamino)pyridine (DMAP) esterification with 10-bromo-decanol to introduce a carbon chain tether followed by substitution of the bromide with an azido group by reaction with sodium azide.

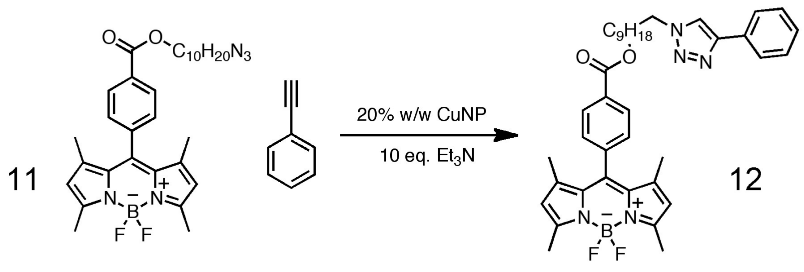

Scheme 3-1. Bench-top scale CuNP catalyzed CuAAC of **11** and phenylacetylene to give triazole product **12**.

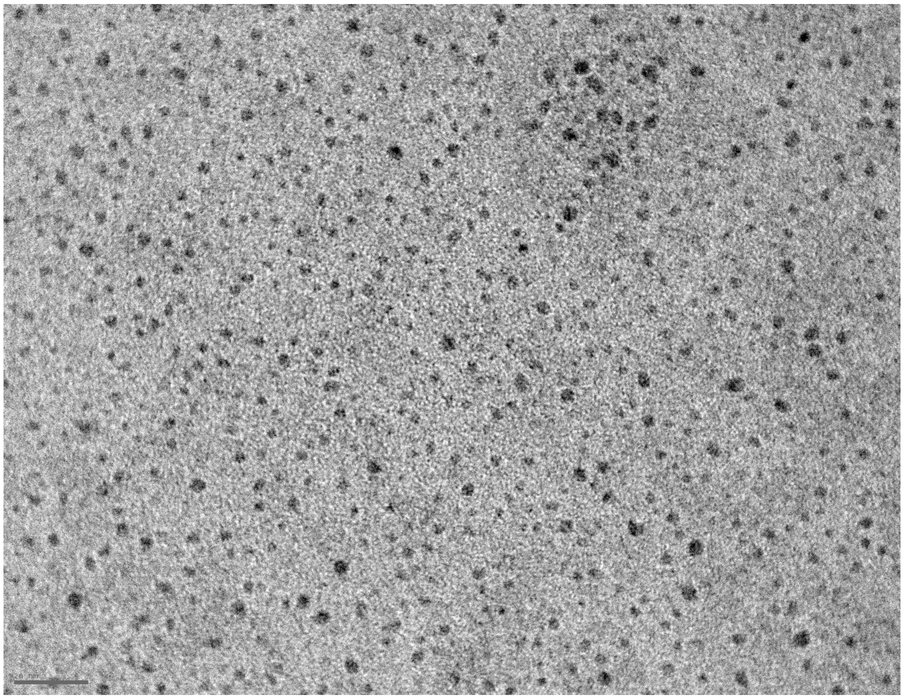

Figure 3-3. TEM image of copper nanoparticles. Scale bar is 20 nm.

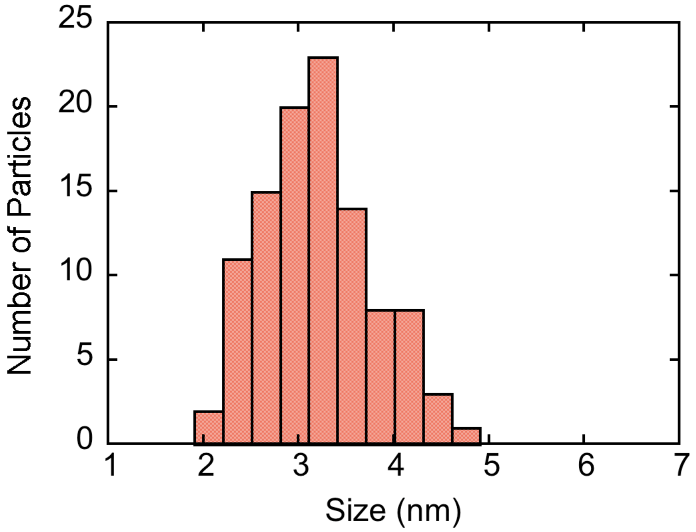

Figure 3-4. Histogram of CuNP sizes from TEM image. Median size is 3.2±0.6 nm.

3.3 Single-molecule TIRF imaging of CuNP catalyzed CuAAC

3.3.1 Single-molecule imaging

Single-molecule imaging experiments were performed by flowing an aqueous solution of 100 pM AlexaFluor 488 alkyne (AF488alkyne, **13**), 100 pM AlexaFluor 594 azide (AF594azide, **14**), and 1 nM triethylamine at 1 mL h^{-1} through the flow cell reactor (Chamlide model CF-S25-B) over a round glass microscope coverslip previously spin coated with CuNP which was placed over the objective of an Olympus TIRF microscope system (**Figure 3-5**, see 3.7 Experimental Details for instrument setup). To image the CuAAC reaction between **13** and **14**, a solution of the two dyes was irradiated with 488 nm laser light at the critical TIRF angle and the resulting emission was recorded by an EM-CCD at 10 frames s^{-1} after being passed through a 550 nm long-pass (LP) filter to eliminate most of the residual donor emission. The collected emission is observed as bright bursting events on a dark background (**Figure 3-5**).

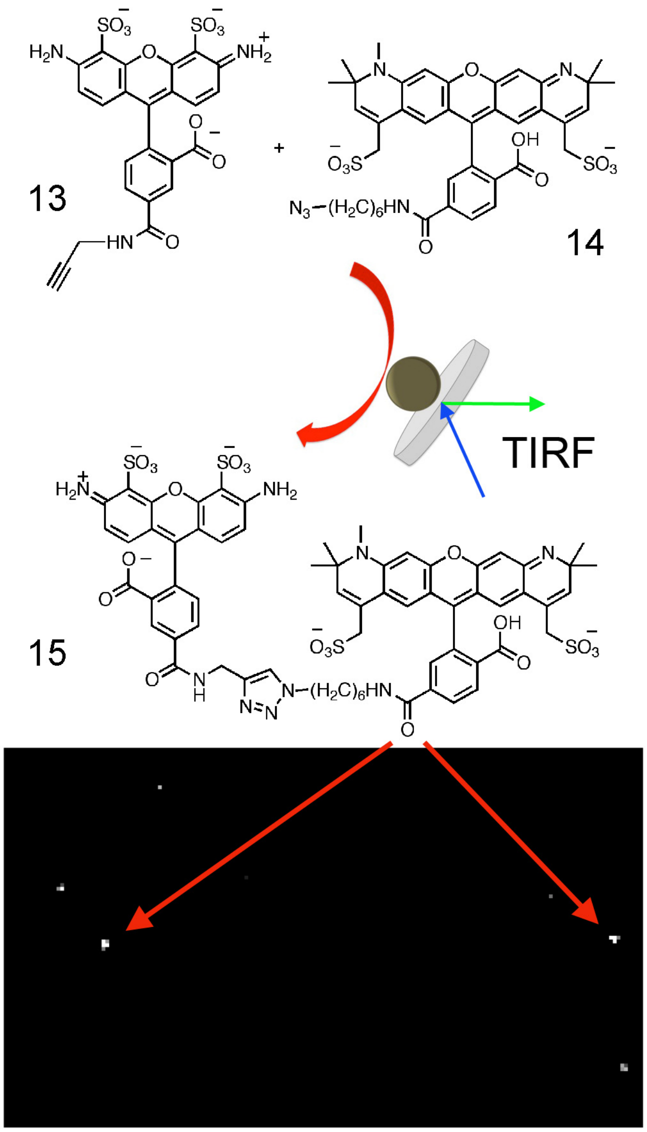

Figure 3-5. CuNP catalyzed CuAAC of AF488alkyne (**13**) and AF594azide (**14**) to give click product **15**, and the expanded TIRFM image showing spots of AF594azide-derived emission resulting from energy transfer between 1,2,3-triazole conjugated donor and acceptor.

3.3.2 Spectroscopic properties

The AlexaFluor dyes AF488 and AF594 were chosen as probe molecules to investigate CuNP catalyzed CuAAC with single-molecule spectroscopy as they exhibit optimal spectral overlap for Förster energy transfer and the donor (AF488, **13**) has a strong absorption centered at the 488 nm laser line equipped on our microscope system. The spectroscopic properties are shown in **Figure 3-6**. The spectral overlap between the donor emission and acceptor absorption extends from approximately 500-600 nm. These commercially available probes are conveniently pre-modified with CuAAC functional groups as their intended use is tagging and imaging of biomolecules, also lending to their superb photostability.

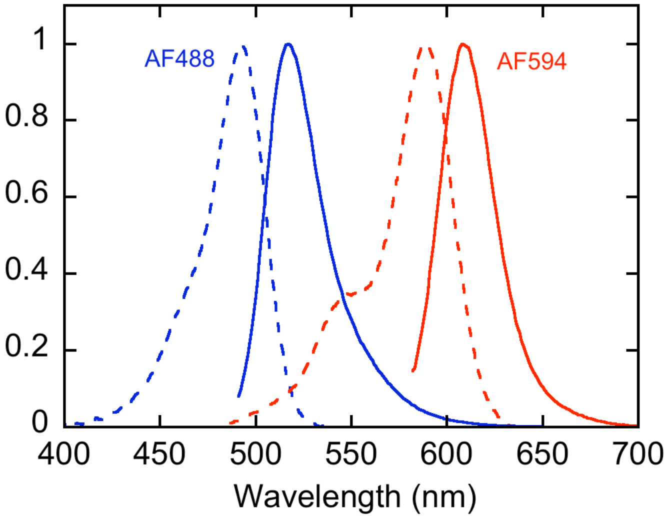

Figure 3-6. Normalized absorption (dashed) and emission (solid) spectra of AlexaFluor 488 alkyne (**13**) and AlexaFluor 594 azide (**14**).

Employing the Andor spectrograph equipped on our single-molecule microscope system, we measured the emission spectra of bright events observed when a solution of 100 pM donor **13**, 100 pM acceptor **14** and 1 nM Et_3N was flowed over CuNPs. With 488 nm excitation, the emission spectra of bursts exhibit two distinct peaks, one centered around 520 nm and the other around 615 nm, corresponding to **13** and **14** respectively (**Figure 3-6**). The two traces in **Figure 3-7** display very different relative intensities of the 520 nm and 615 nm emissions. The blue trace is dominated by an emission corresponding to **13** with emission from **14** appearing as a small shoulder; while the band from **14** is much more intense in red trace. The grey box in **Figure 3-7** shows the spectral region excluded in TIRFM experiments by a 550 nm LP emission filter that is used to exclude most residual donor emission.

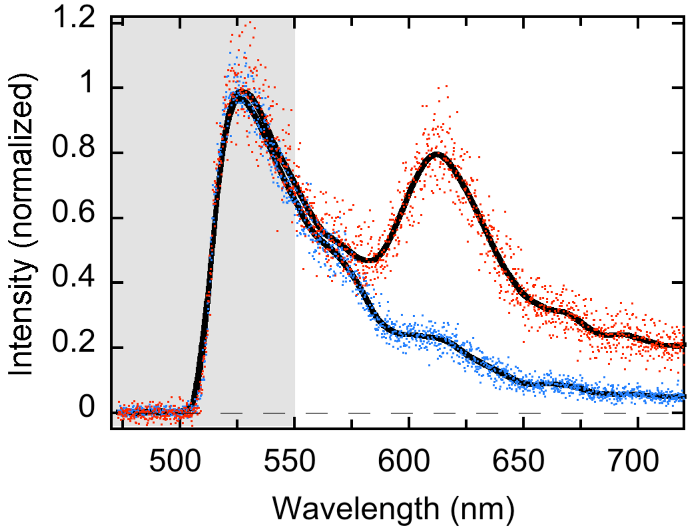

Figure 3-7. Single-molecule emission spectra (blue and red points) of two different bright spots and the spectral region excluded in TIRFM experiments by a 550 nm LP filter (grey area). The spectra show emission from both **13** and **14**, indicating that CuNP catalyzed CuAAC has occurred enabling energy transfer from chromophore **13** to **14**.

To be sure that any remaining donor emission does not contribute to the observed signal causing false positive triazole formation, a solution of 100 pM alkyne donor (**13**) with 1 nM Et_3N was flowed over CuNPs and the resulting signal was imaged first with a 525/45 nm bandpass (BP) filter to allow donor emission to pass, and subsequently imaged with the 550 LP filter used in other experiments. The frame-to-frame standard deviation of the signal collected with these two filters was compared using 3-D representations in **Figure 3-8**, highlighting subtle differences in the intensity of each pixel from one frame to the next. The 550 LP filter removes nearly all donor emission, with the remaining signal contributing to background fluorescence rather than discrete bursting events that can be observed when the 525 nm BP filter is used.

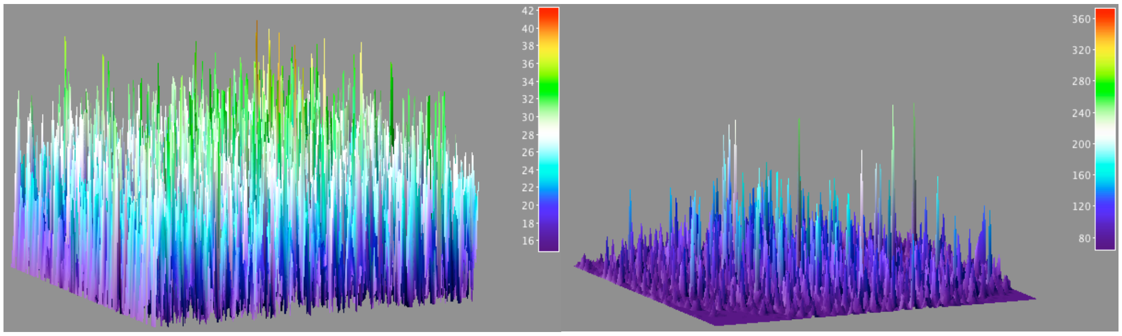

Figure 3-8. 3D projection of the standard deviation of each pixel measured between each frame (500 frames) of TIRFM video of 100 pM **13** imaged with (left) 550 nm longpass and (right) 525/45 nm bandpass emission filters. The area shown corresponds to an 80 μm square.

3.3.3 Burst analysis

The analysis of bursts at localized spots yields fluorescence intensity vs. time trajectories showing stochastic intensity bursts over a dark background as shown in **Figure 3-9**. Sharp jumps in intensity indicate CuNP catalyzed CuAAC triazole formation creating acceptor emission from energy transferred by the excited donor. Sudden drops in intensity can be caused by a number of circumstances including fluorophore photobleaching, photoblinking, or product desorption from the catalyst. These avenues will be explored in detail in the coming sections.

The intensity vs. time trajectories for three representative individual burst events are given in **Figure 3-9**, clearly depicting the stochastic nature of bursting events in the focal area. Expanded time-correlated images of the bursting event corresponding to the uppermost trajectory show bright pixels becoming dark as the signal turns off and then bright again with the return of signal. In order to quantitatively evaluate the observed bursting, we measured the “on-time” of each emissive event with intensity above a set threshold of 200 counts. The grey areas in **Figure 3-9** highlight on-times of the representative trajectories based on the threshold level above the background signal. The median length of bursting events was determined to 2.9 ± 0.9 s (**Figure 3-10**).

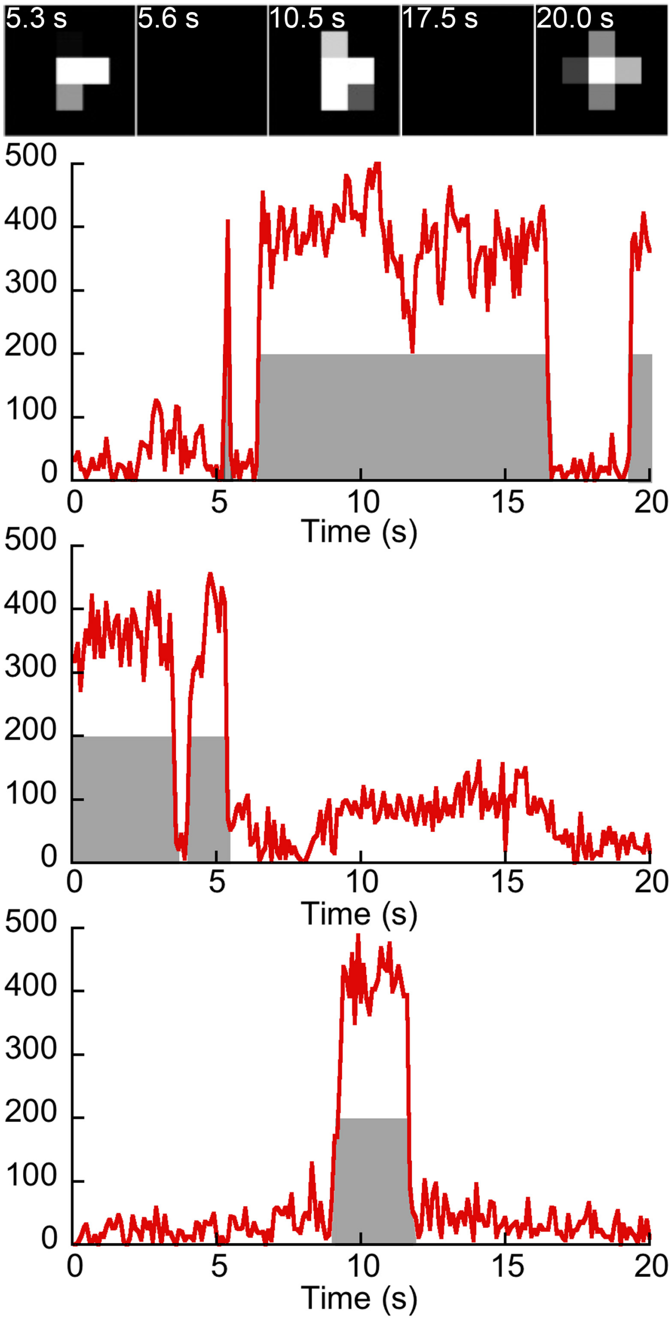

Figure 3-9. (Top) Expanded still frames images from TIRFM video of CuAAC of **13** and **14** and representative fluorescence intensity trajectories of single catalytic spots showing multiple stochastic on/off events (bottom). The grey areas show the times 'on' based on a 200 count threshold. Note that the 'on' times always have an intensity of about 400 counts. Still frame images correspond to bursting event depicted in uppermost trajectory.

3.3.4 Power dependence

The intensity vs. time trajectories in **Figure 3-9** depict the recorded signal of bursting events over time, enabling the CuAAC reaction between **13** and **14** to be monitored through the emission of resultant triazole product. The intensity of bursting events depicted in these trajectories eventually falls sharply down to the baseline as a result of product decomposition or desorption from the catalyst surface. To differentiate between these two pathways we imaged a solution of 100 pM **13**, 100 pM **14** and 1 nM Et_3N over CuNPs at different laser irradiance. If these off-events were to be attributed to decomposition of the emissive triazole product the average on-time would be expected to be shorter with higher incident laser irradiance. In fact, for full laser irradiance the median “on” time was 2.9 ± 0.9 s (average of 26 spots) and 1.7 ± 1.0 s for 20% irradiance based on 47 spots (**Figure 3-10**, **Figure 3-11**); clearly the “on” times are not longer with reduced irradiance.

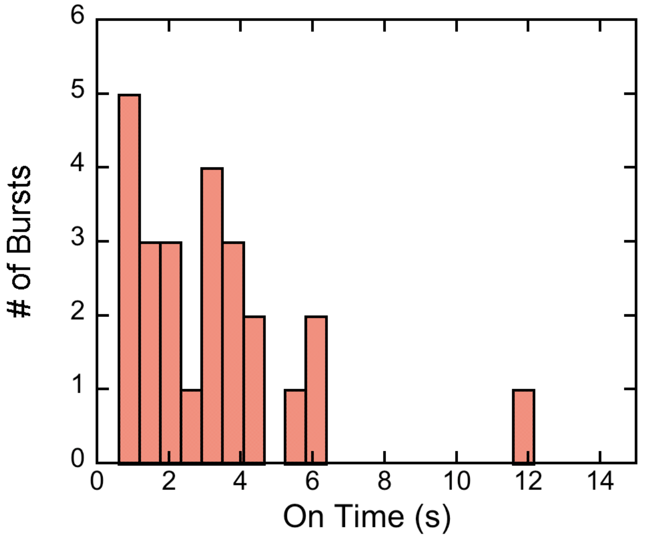

Figure 3-10. Histogram showing "on" times of bursts with 100 pM **13**, 100 pM **14** and 1 nM Et_3N at full laser irradiance.

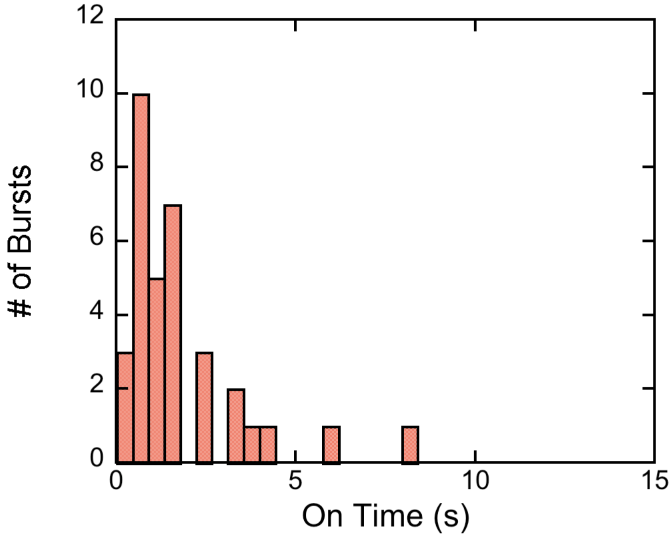

Figure 3-11. Histogram showing "on" times of bursts with 100 pM **13**, 100 pM **14** and 1 nM Et_3N at 20% laser irradiance.

3.3.5 Alkyne concentration dependence

Videos showing bursting events as they occur at full laser irradiance with concentrations of **13** of 300 and 100 pM were recorded and analyzed to explore the effect the concentration of alkyne **13** has on the observed emission signal and corresponding bursting events. The plot on the right in **Figure 3-12** depicts an attempt to show the intensity profile of accumulated bursting events throughout the focal area in a printable graph. A 3-D surface projection of this experiment repeated at 3× the concentration of alkyne (300 and 100 pM **13**, 100 pM **14**, and 1 nM Et_3N) highlights the availability of open active sites on the catalyst manifested through a marked increase in product-forming events in the same time frame (**Figure 3-12**). While the number of catalytic events was observed to increase with higher alkyne concentrations, analysis of bursting events did not yield a significant difference in on-times with increasing alkyne concentration: 2.9 +/- 0.9 s at 100 pM and 1.8 +/- 1.5 s at 300 pM both based on 26 randomly selected spots (**Figure 3-10** and **Figure 3-13**, respectively).

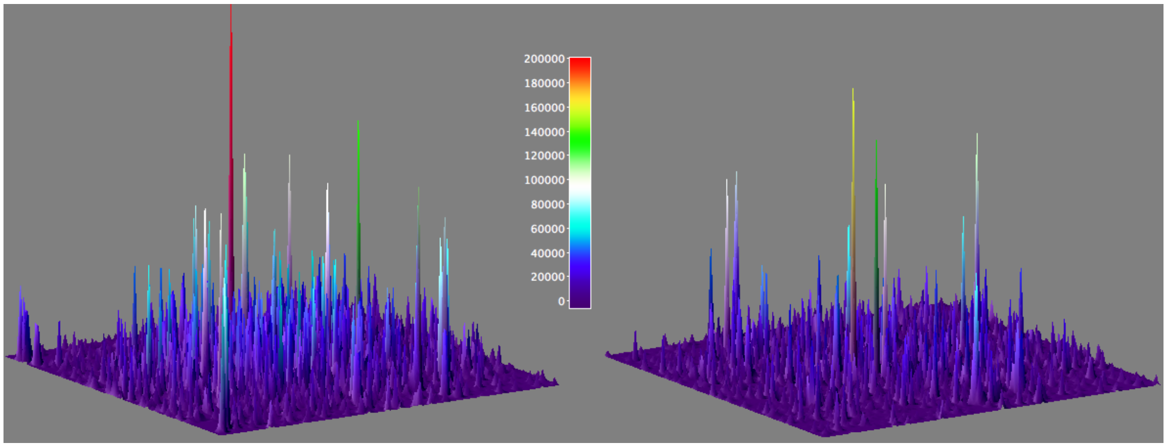

Figure 3-12. 3D accumulated bright events (500 frames) at **13** concentrations of 300 pM (left) or 100 pM (right), both with 100 pM **14**, and 1 nM Et$_3$N. The area shown corresponds to an 80 μm square.

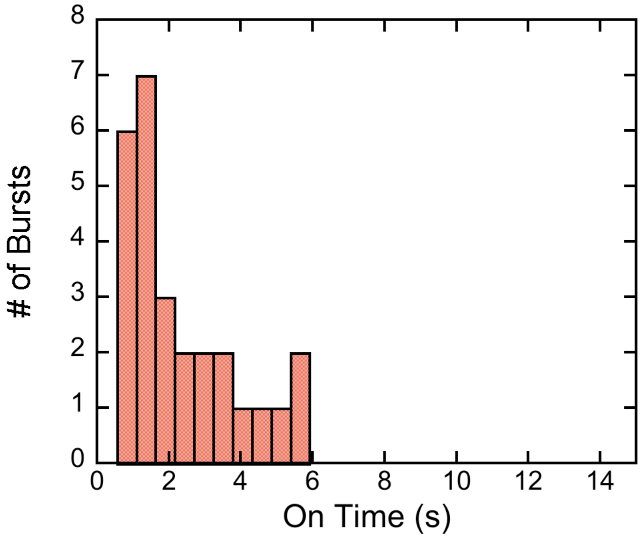

Figure 3-13. Histogram showing "on" times of bursts with 300 pM **13**, 100 pM **14** and 1 nM Et$_3$N at full laser irradiance.

3.3.6 Control experiments

To confirm that the observed bursting is in fact due to emission as a result of copper-catalyzed click reaction enabling energy transfer between the alkyne and azide modified FRET pairs, a number of control experiments were performed using the same experimental conditions. No bright bursting spots were observed in the absence of CuNP (**Figure 3-14**), or when solutions containing only one or neither of the FRET pair dyes were used (**Figure 3-15**, **Figure 3-16**, **Figure 3-17**).

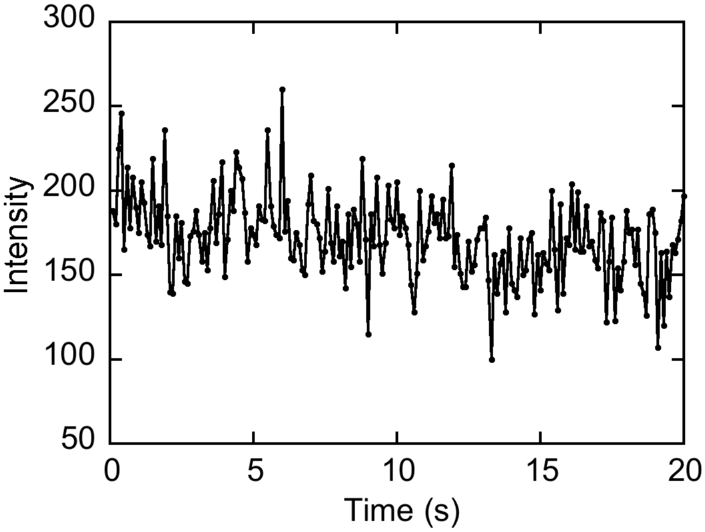

Figure 3-14. Intensity trajectory of luminous spot in TIRFM experiment with aqueous solution of 100 pM **13**, 100 pM **14**, and 1 nM Et_3N flowed over a glass coverslip without CuNPs.

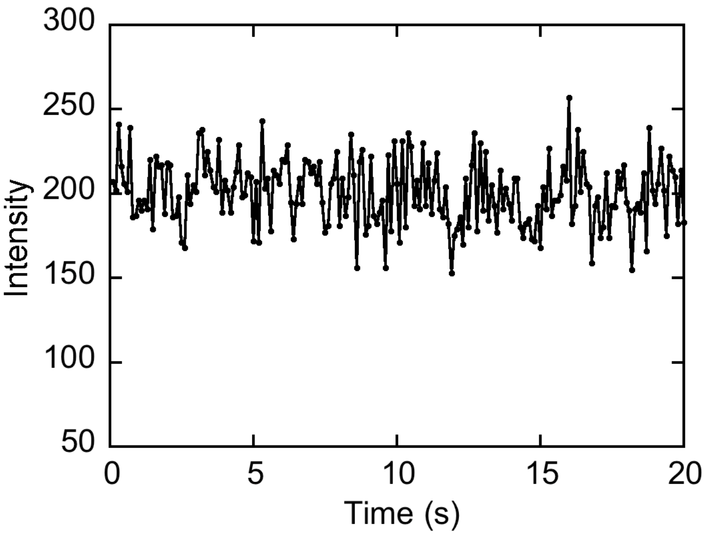

Figure 3-15. Intensity trajectory of luminous spot in TIRFM experiment with aqueous solution of 1 nM Et_3N flowed over a glass coverslip modified with CuNPs.

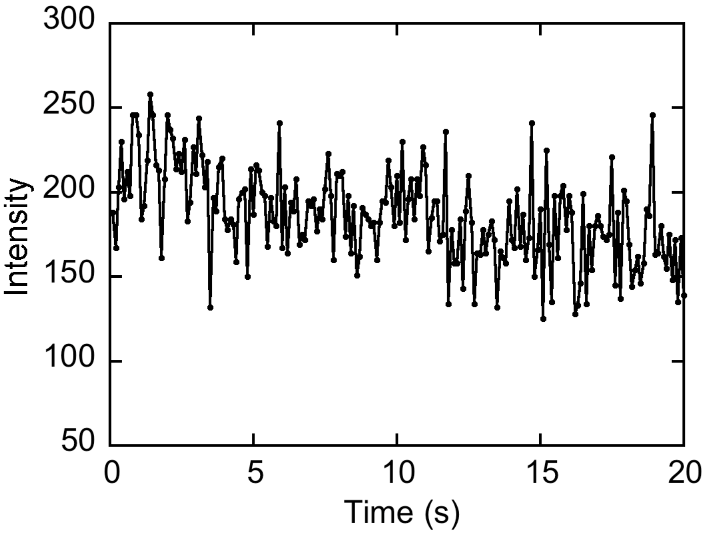

Figure 3-16. Intensity trajectory of luminous spot in TIRFM experiment with aqueous solution of 100 pM (**13**) and 1 nM Et_3N flowed over a glass coverslip modified with CuNPs.

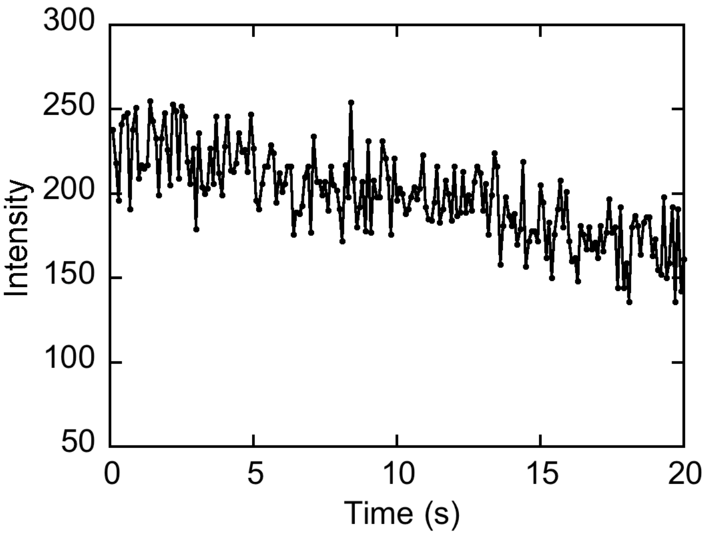

Figure 3-17. Intensity trajectory of luminous spot in TIRFM experiment with aqueous solution of 100 pM (**14**) and 1 nM Et_3N flowed over a glass coverslip modified with CuNPs.

3.3.7 Correlating alkyne adsorption and triazole formation

To clearly demonstrate catalysis occurring in the heterogeneous state on the surface of a nanoparticle requires identifying the adsorption of reagents in the same location as product generation is detected. To this end, a solution of the alkyne **13** was first imaged with a 525/45 nm BP emission filter to observe donor emission exclusively. The emission filter was then changed to a 550 LP filter without moving the catalyst and a solution containing both **13** and **14** was imaged with the same 488 nm incident irradiation. Panels **A1** and **B1** of **Figure 3-21** are still frame images from these experiments with yellow boxes highlighting two regions that are in identical locations in each image. These regions are examples of the alkyne coordinating to a

CuNP imaged using the 525 BP filter, and subsequent CuAAC of **13** and **14** is imaged with the 550 LP filter in the same location. Discrete bursting events in these locations are visualized with the intensity vs. time trajectories of these regions (**Figure 3-21 A2-3, B2-3**).

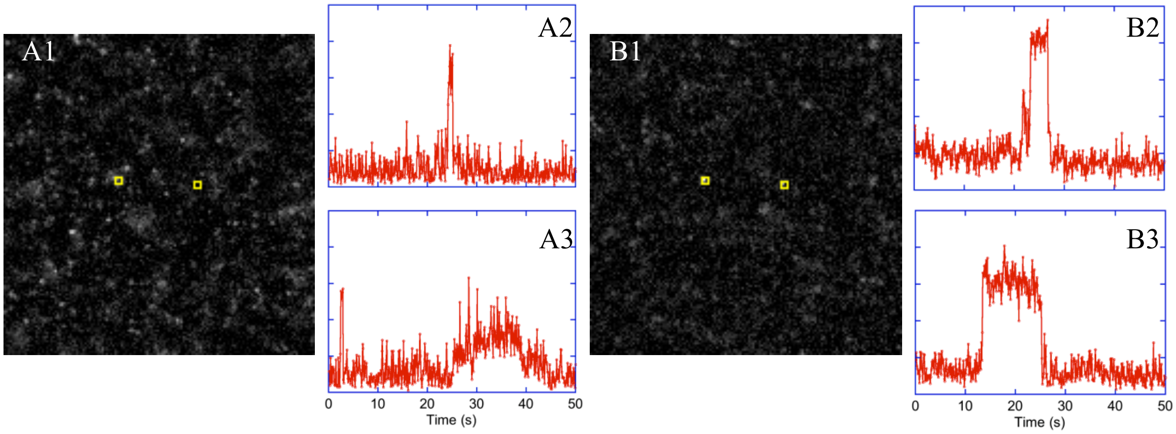

Figure 3-18. TIRFM images of (**A1**) emission from donor (**13**) imaged with 525/45 nm BP filter and (**B1**) acceptor-derived emission resulting from energy transfer between 1,2,3-triazole conjugated donor and acceptor imaged with 550 nm LP filter. Yellow boxes highlight identical locations in the two images from which the corresponding fluorescence intensity trajectories (**A2-3**, **B2-3**) of single catalytic spots showing stochastic on/off events were derived. The trajectories show bursting resulting from donor emission (**A2** and **A3**) occurs in the same location as bursting originating from triazole-forming CuAAC reaction enabled FRET activation of acceptor (**B2** and **B3**).

3.4 SM TIRF imaging of triazole product

3.4.1 TIRF microscope detection limit

With very low working concentrations of single-molecule spectroscopy some technical issues arise that are not prevalent in standard microscopy techniques. Short exposure times and fast frame rate imaging becomes difficult simply because the number of fluorescent molecules is low as is the number of emitted photons. Increasing the exposure time alleviates this problem, however, at the expense of frame rate. The slow frame rate we used for imaging the CuNP catalyzed CuAAC of **13** and **14** leaves open the possibility that rapid diffusion of product molecules prevents us from detecting catalysis occurring in solution by Cu potentially leached from the heterogeneous CuNP. In addressing the likelihood of this scenario we ask ourselves, can we observe triazole product **15** in solution and if so what is the detection limit of **15** on our instrument? To rule out homogeneous catalysis, triazole product **15** was prepared on the bench using classical *in situ* Cu(II) reduction CuAAC and imaged in solution without CuNPs at 100 pM, 10 pM and 1 pM to get an estimate of the detection limit of **15** with our microscope. The resulting videos are represented graphically in **Figure 3-19**. On our instrument we have excellent signal from **15** in solution at 10 frames s^{-1} enabling easy detection of the triazole product at 10 pM concentration. At 1 pM, however, emission from **15** is barely detectable to the trained eye; therefore we believe that our realistic detection limit for **15** is approximately 5 pM.

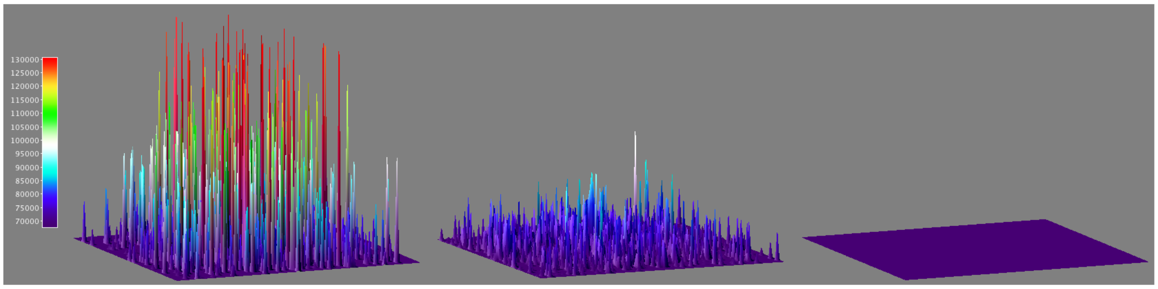

Figure 3-19. 3D accumulated bright events (500 frames) of **15** at concentrations of 100 pM (left), 10 pM (middle), and 1 pM (right) showing the detection limit of **15** on the TIRF microscope system used for imaging. The area shown corresponds to an 80 μm square.

3.4.2 Triazole affinity for catalyst

As further evidence against products formed in solution adsorbing to CuNP and to verify product desorption from the catalyst causes bursting off-events we took advantage of the bench-top synthesized **15** to investigate its affinity for the CuNP catalyst. Conceivably, if **15** has little or no affinity for CuNP the emission signal detected from **15** with 488 nm irradiation would be eliminated with the removal of **15**. Indeed, stochastic bursting was observed throughout the focal area when imaging a solution of **15** flowing over CuNP, and consequently disappeared when flowing water over the same catalyst. The bursting signal was subsequently recovered after flowing **15** over the catalyst again (**Figure 3-20**).

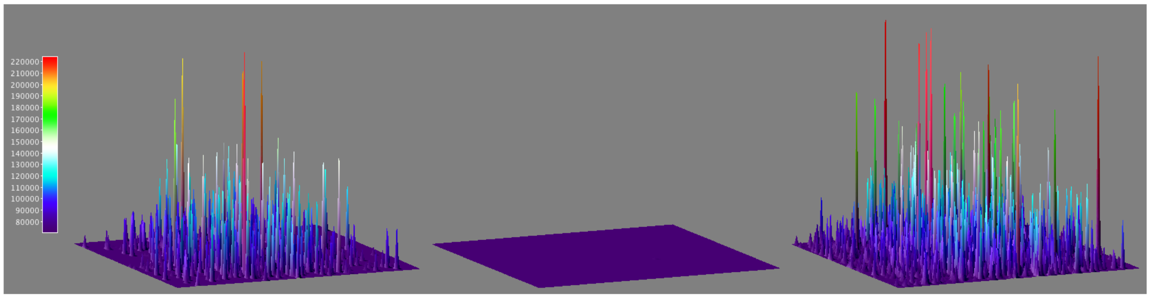

Figure 3-20. 3D accumulated bright events (500 frames) of **15** at 100 pM concentration (left), disappearance of signal after flowing water (middle), and recovery of signal after flowing 100 pM **15** again (right). The area shown corresponds to an 80 μm square.

3.5 Discussion

For our work AlexaFluor 488 alkyne (AF488alkyne, **13**), and AlexaFluor 594 azide (AF594azide, **14**) dyes (**Figure 3-5**) were chosen as FRET donor/acceptor pair, since they exhibit good photostability, excellent FRET overlap and optimal spectral properties for 488 nm laser irradiation.[49] AF488alkyne has a large absorption at 488 nm, while AF594azide absorbs very little at 488 nm (**Figure 3-6**) maximizing FRET efficiency between the donor and acceptor and diminishing the effect of direct acceptor excitation. In single-molecule studies, concentrations in the picomolar range help make the effect of non-specific energy transfer statistically negligible.[51]

Copper-catalyzed cycloaddition between **13** and **14** brings the donor and acceptor close to each other allowing the AF594 acceptor to emit light following energy transfer from a proximal excited AF488 (see structure **15**). Although CuNP catalyzed CuAAC have been shown to proceed with good efficiency,[13] it is often the case that the rate of reaction suffers dramatically at low reactant concentrations. To overcome this issue, amines such as triethylamine are commonly added in CuAAC chemistry as ligands to accelerate the reaction and protect the catalyst by facilitating coordination of the azide to copper and preventing the formation of unreactive polynuclear copper(I) acetylides.[3]

Numerous bright emitting spots are observed in the microscope video of a solution of 100 pM **13**, 100 pM **14** and 1 nM Et_3N flowing over CuNP with 488 nm TIRF excitation. Fluorescence intensity vs. time trajectories for **15** show the bursting emission of single catalytic spots. The bursting reveals that the catalytic spots repeat themselves, ruling out random solution events. On average these spots are 'on' about 30% of the time with 'on' events lasting an average of ~3 s. Time-correlated still frame images of a single bursting spot are shown in **Figure 3-9**. Although unlikely at picomolar concentration, considering a resolution of a few hundred nanometers, each bright spot could potentially contain multiple donor and acceptor pairs of molecules. Analyzing the intensity of bursting bright spots provides information on the number of emitters within a bright spot. The rise and fall of intensity level in the trajectories in **Figure 3-9** is consistent with bursts where the bright spot is due only to a single donor and acceptor pair. Multiple dyes within a bright spot often result in a step-wise change in "on" intensity within a trajectory.[37]

Each on-off event in the trajectory represents one catalytic turnover, where a sharp jump in intensity from the baseline denotes a catalytic product-forming event, and a sudden drop in intensity marks product degradation or desorption from the catalyst; power dependence studies support the latter. Thus, to establish if 'off' events resulted from product migration away from the catalytic site or were due to photobleaching, we compared the "on-time" of bursts at different laser irradiance; increased irradiance should reduce the duration of "on" events if off events were due to photobleaching (i.e., photodegradation of **15**). The determined median "on" time indicates that "off" events are not the result of photobleaching, and thus can be attributed to photophysical blinking or, more plausibly, migration away from the evanescent field region. The disappearance of signal when flowing water following a solution of **15** suggests the triazole product does not have such a strong affinity for CuNPs and "off" events can thus be attributed to product migration out of the evanescent field. Although **15** contains many functional groups that may chelate to Cu, this result is not unexpected as the surface of CuNPs is modified with alkylthiolates preventing high affinity binding. Since emission bright spots are repeated at a single location and the reagents are being flowed over the catalyst, a nanoparticle must be at this location catalyzing the reaction; thus localized bursting behavior is clearly indicative of nanoparticle catalysis, as catalysis due to leaching would be expected to occur at random locations.

Despite evidence that triazole **15** has no strong affinity for CuNPs (**Figure 3-20**), one can argue that Cu (I) ions leached into solution are homogeneously catalyzing CuAAC, and that the slow imaging frame rate prevents us from observing FRET enabled emission from **15** until it binds to heterogeneous CuNPs. Nevertheless, given the measured detection limit of our instrument, 5 pM of CuAAC product **15** or 5 % of the theoretical yield would have originate from homogeneous catalysis in order to meaningfully contribute to the detected signal. At realistically less than quantitative conversions, the contribution of homogenous catalysis would need to substantially increase in order to be observable. While this does not exclude the possibility of homogeneous catalysis, it strongly supports our conclusion of heterogeneous catalysis as the dominant process leading to product formation.

A unique benefit of the flow reactor microscopy cell in which we perform TIRF imaging is the ability to seamlessly change the reagent solution without disturbing the microscope optics or displacing the sample, allowing us to image the same catalyst particles under various experimental conditions. Taking advantage of this and in order to confirm our ability to clearly distinguish between different signals alkyne **13** was first imaged with a 525/45 nm BP emission filter, followed by a solution of **13** and **14** imaged with a 550 nm LP filter without disturbing the catalyst or focus. **Figure 3-18** shows still frames from these experiments with two highlighted regions that are in the exact location in each experiment. The trajectories provided show the mean intensity of these 3x3 pixel areas monitored over time for each of these two locations in both experiments; they clearly demonstrate stochastic bursting from the donor is observed in the same location as bursting from the acceptor via FRET, thus supporting our conclusion of heterogeneous over homogeneous catalysis.

We were also able to measure the emission spectra of multiple bright emitting spots within a single focal area using an Andor spectrograph coupled to our inverted microscope FLIM/TIRF system. AF594azide absorbs very little 488 nm light; therefore emission from direct excitation is not anticipated. Rather, the observed emission at 615 nm is due to AF594 emission from an excited state generated by energy accepted from an excited donor molecule. The difference in these two spectra in **Figure 3-7** is likely attributed to partial quenching of acceptor emission in the blue trace leaving donor emission.[49, 53] These spectra were measured without any emission filter allowing the entire spectrum to be collected, but in TIRF experiments, any residual donor emission that is not removed by the 550 nm LP filter is not resolved into discreet bursting events, but rather results in non-specific emission that contributes to the background signal (**Figure 3-8**). This verifies that the bursting observed in TIRFM experiments is due to CuNP catalyzed CuAAC linking FRET pairs, enabling energy transfer from donor to acceptor.

We also looked at the effect of the concentration of **13** on the catalytic events in order to address three questions: (a) Are the catalyst active sites saturated at 100 pM **13**?; (b) Is the frequency of "on" events affected by the concentration of **13**?, and

(c) Can **13** displace product **15** from the catalytic sites? We note that positive answers to questions (b) and (c) would result in faster catalysis in ensemble experiments; single-molecule experiments can address both questions independently. As the amount of catalyst was maintained, an increasing number of bursts and their intensity with higher concentration of alkyne signifies that the catalyst active sites are not saturated at 100 pM **13** and multiple alkyne molecules can coordinate to CuNP resulting in faster catalytic turnover (**Figure 3-12**).

As already noted, higher concentrations of **13** lead to increased frequency of catalytic events, indicating that at the lower concentration (100 pM **13**), the catalytic sites are not saturated with **13**, and thus more sites are activated as the concentration of **13** increases. We expected that **13** would contribute to the displacement of the reaction to produce **15** because this phenomenon has been previously observed in the catalytic reduction of rezasurin on gold nanoparticles.[37, 38, 41] When the concentration of **13** was increased from 100 pM to 300 pM, however, an increase was not observed within the error of the measurement: 2.9 +/- 0.9 s at 100 pM and 1.8 +/- 1.5 s at 300 pM both based on 26 randomly selected spots (**Figure 3-10** and **Figure 3-13**, respectively). The absence of detection of a change in displacement rate may be due to the current limitations of single-molecule approaches to detect small changes or due to the limited working concentrations associated with these experiments, or may reflect that the concentration of **13** has no effect on the displacement rate under the conditions of our experiment. The concentration effect observed in **Figure 3-12** would be expected to be more important at typical organic synthesis concentrations (as much as 10^6 times higher than those for single-molecule work) when catalytic sites may saturate.

3.6 Summary

This chapter demonstrated the ability of CuNP to catalyze the CuAAC click reaction on scales from bench-top to single-molecule TIRFM studies involving FRET activation through formation of 1,2,3-triazoles that bring donor-acceptor dyes in close proximity. Single-molecule studies reveal that the reaction proceeds through initial formation of Cu-acetylides on the nanoparticle surface followed by azide attack. At the concentrations used only one catalytic event per nanoparticle takes place at a given time and the product has a residence time around 3 s following surface reaction. The systematic repetition of bursting locations is unequivocal proof that the reaction involves the CuNP surface and not ions leaching from the nanoparticle. The generic versatility of our strategy, together with studies that combine molar and molecular scales, can provide unequivocal answers as to whether a given heterogeneous catalyst operates by true heterogeneous catalysis or by promoting homogeneous catalytic events.

3.7 Experimental Details

Unless otherwise specified, all chemicals were purchased from Sigma-Aldrich or Fisher Scientific and used without further purification. AlexaFluor probes were purchased from Invitrogen (Life Technologies). All reactions were monitored by thin-layer chromatography, using aluminum sheets coated with silica (60, F_{254}). NMR spectra were recorded at room temperature with a Bruker Avance 300 and chemical shifts were referenced with the residual proton or carbon signal of the deuterated solvent. High-resolution mass spectra were acquired on a HRES, EI, Concept S1, Magnetic Sector mass spectrometer and Electrospray Ionization mass spectra were acquired on a Micromass Q-TOF mass spectrometer. All mass spectrometry was conducted in the John L. Holmes Mass Spectrometry Facility at the Department of Chemistry, University of Ottawa.

3.7.1 Synthesis

The synthesis of BODIPY-COOH, BODIPY-decylbromide and BODIPY-Azide was graciously performed by S. Impellizzeri.

(CuNP) – Copper nanoparticles were prepared using a method analogous to that reported by Khlobystov *et al.*[15] based on a modified Brust-Shiffrin reduction.[54] Briefly, a solution of tetraoctylammonium bromide (2.19 g, 4 mmol) in toluene (160 mL) was added to a stirring solution of copper nitrate hemipentahydrate (140 mg, 0.6 mmol) in MilliQ water (60 mL) at ambient temperature and rapid stirring was continued for 10 minutes. A solution of dodecanethiol (216 μL, 0.9 mmol) in toluene (2 mL) was added to the biphasic mixture and stirring was continued for an additional 10 minutes. A freshly prepared sodium borohydride (378 mg, 10 mmol) solution in MilliQ water (50 mL) was added dropwise and the mixture was stirred for 16 hours. The phases were then separated, the organic phase was washed with MilliQ water (3 x 100 mL), dried over $MgSO_4$ and concentrated to 5 mL with rotary evaporation. The CuNP product was precipitated by addition of 400 mL acetone and standing at -25°C for 24 hours. The resulting residue was vacuum filtered, washed with acetone (300 mL) and ethanol (300 mL) and dried under vacuum affording a brown solid (78 mg).

(BODIPY-COOH) – A solution of 2,4-dimethylpyrrole (1.1 mL, 10.5 mmol), 4-formylbenzoic acid (800 mg, 5.3 mmol), and CF_3CO_2H (20 μL, 0.2 mmol) in CH_2Cl_2 (300 mL) was stirred for 12 h at r.t. under Ar. After the addition of 2,3-dichloro-5,6-dicyano-p-benzoquinone (DDQ; 1.2 g, 5.3 mmol) in CH_2Cl_2 (30 mL), the mixture was stirred for an additional 30 min. Et_3N (9.4 mL, 74 mmol) and $BF_3 \cdot Et_2O$ (11.7 mL, 84 mmol) were added, and the mixture was stirred for an additional 30 min, washed with H_2O (3 × 100 mL), and dried over $MgSO_4$. The solvent was distilled off under reduced pressure, and the residue was purified by column chromatography

[SiO_2/Hexanes-$MeCO_2Et$ 1:1 (v/v)] to yield the product (800 mg, 55%) as a red powder. EI-MS: calc'd *m/z* $[M]^+$: 368.2 found 368.2. ^1H NMR (300 MHz, $CDCl_3$): 8.23 (2H, d, 8 Hz), 7.43 (2H, d, 8 Hz), 5.98 (2H, s), 2.54 (6H, s), 1.35 (6H, s). ^{13}C NMR (300 MHz, $CDCl_3$): 168.3, 155.7, 142.5, 140.3, 139.6, 131.2, 130.9, 130.1, 129.2, 128.4, 128, 125.4, 121.6, 17.4, 14.5, 12.9, 12.1.

(BODIPY-decylbromide) – A solution of N,N-dicyclohexylcarbodiimide (DCC; 290 mg, 1.4 mmol) in CH_2Cl_2 (8 mL) was added dropwise over the course of 20 min to a solution of BODIPY-COOH (395 mg, 1.1 mmol), 10-bromo-decanol (256 μL, 1.28 mmol), and 4-(dimethylamino)pyridine (DMAP; 30 mg, 0.2 mmol) in CH_2Cl_2 (25 mL) maintained at 0°C under Ar. The reaction mixture was allowed to warm to ambient temperature and was stirred for 12 h under these conditions. The precipitate was filtered off, and the solvent was distilled off under reduced pressure. The residue was purified by column chromatography [SiO_2: Hexanes-$MeCO_2Et$ 9:1 (v/v)] to afford the product (453 mg, 73%) as a red solid. ESI-MS: calc'd *m/z* $[M + K^+]$: 626.4, found 626.3. ^1H NMR (300 MHz, $CDCl_3$): 8.12 (2H, d, 8.7 Hz), 7.32 (2H, d, 8.4 Hz), 5.90 (2H, s), 4.27-4.32 (2H, t, 13.5 Hz), 3.31-3.36 (4H, m), 2.50 (6H, s), 1.73-1.84 (8H, m), 1.49-1.52 (4H, m), 1.34-1.36 (8H, m). ^{13}C NMR (300 MHz, $CDCl_3$): 165.9, 155.8, 142.8, 140.3, 139.6, 131, 130.8, 130.3, 129, 128.3, 128.1, 125.2, 121.4, 65.5, 34.9, 32.8, 29.4, 28.7, 28.1, 26, 25.7, 14.5, 14.4.

(BODIPY-Azide, 11) – A solution of BODIPY-decylbromide (135 mg, 0.23 mmol) and NaN_3 (75 mg, 1.15 mmol) in *N*,*N*-Dimethylformamide (5 mL) was degassed under Ar for 15 min, and then stirred under Ar at ambient temperature until completion. After the addition of H_2O (10 mL), the reaction was extracted in $MeCO_2Et$ (4 × 15 mL). The organic fractions were combined, dried over $MgSO_4$, and the solvent was evaporated under reduced pressure. The residue was purified by column chromatography [SiO_2: Hexanes-$MeCO_2Et$ 8:1 (v/v)] to afford the product as a red solid. ESI-MS: calc'd *m/z* [M + K^+]: 588.3, found 588.2. ^1H NMR (300 MHz, $CDCl_3$): 8.13 (2H, d, 8 Hz), 7.36 (2H, d, 8 Hz), 5.95 (2H, s), 4.32 (2H, t, 13.5 Hz), 3.22 (2H, t, 13.7 Hz), 2.50 (6H, s), 1.72-1.74 (6H, m), 1.52-1.57 (6H, m), 1.32-1.35 (8H, m). ^{13}C NMR (300 MHz, $CDCl_3$): 166.0, 155.9, 142.8, 140.3, 139.7, 131.1, 130.9, 130.3, 128.3, 121.4, 60.4, 51.4, 29.6, 29.4, 29.2, 28.8, 26.7, 26, 20.1, 14.6, 14.5.

(12 via CuNP catalyzed CuAAC of azide 11 with phenylacetylene) – In a 5 mL round bottom flask, phenylacetylene (10 µL, 87.4 µmol), and Et_3N (24 µL, 174 mmol) were added to a solution of **5** (9.6 mg, 17.4 µmol) in 2 mL t-BuOH. A colloidal solution of CuNPs (2 mg, 20 % w/w) in CH_2Cl_2 (0.5 mL) was then added and the combined mixture was stirred in the dark for 24 hours. The product was isolated by evaporation of the solvent under reduced pressure followed by preparative TLC purification of the resultant residue [SiO_2: $CHCl_3$-CH_3OH 98:2 (v/v)] giving **12** as an orange-red solid (10.6 mg, 93%). ESI-MS: Calc'd *m/z* [M+Na]: 674.4, found: 674.4. ^1H

NMR (300 MHz, $CDCl_3$): 8.17 (2H, d, 8.4 Hz), 7.83 (2H, dd, 8.4 Hz, 1.6 Hz), 7.74 (1H, s), 7.38 (5H, m), 5.99 (2 H, s), 4.40 (2H, t, 7 Hz), 4.35 (2H, t, 6.8 Hz), 2.56 (6H, s), 1.95 (2H, m), 1.79 (2H, m), 1.3-1.4 (12H, m), 1.26 (6H, s).

3.7.2 Copper Nanoparticle Characterization

Transmission Electron Microscope (TEM) images were acquired at the University of Ottawa's Centre for Catalysis Research and Innovation (CCRI) with a Jeol JEM-2100F field emission transmission electron microscope. TEM samples were prepared by drop casting a CH_2Cl_2 solution of CuNPs (0.25 mg/mL (w/v)) onto 400 square mesh carbon coated copper grids (Electron Microscopy Sciences). Particle sizes were determined with ImageJ analysis of TEM images.

3.7.3 Spectroscopy

All spectroscopic measurements were performed in spectroanalyzed grade ethanol (BODIPYs) or MilliQ sub-micronfiltered water (AlexaFluors). UV-VIS Absorption spectra were recorded on a Agilent Cary-50 Spectrophotometer which was zeroed before sample measurement and spectra were baseline subtracted by measuring the pure solvent. Fluorescence emission spectra were collected with a luminescence spectrometer from Photon Technology International (PTI).

3.7.4 TIRFM sample preparation

Glass coverslips (25 mm, Fisher) were cleaned by soaking in piranha solution for 30 minutes followed by thorough washing with MilliQ H_2O, then dried with argon and baked at 120°C for 5 minutes. The clean, dry coverslips were then placed in a solution (4% in toluene) of 3-aminopropyltriethoxysilane (APTES) and agitated on an orbit shaker (Lab-line Instruments) for 90 min, followed by successive washing with toluene, acetone, ethanol and MilliQ water. APTES treated coverslips were stored in MilliQ water until use. Copper nanoparticles (CuNP) were deposited onto argon dried, APTES treated coverslips by spin-coating 100 µL of a 0.25 mg/mL CuNP solution in dichloromethane at 1200 rpm. Catalyst coated coverslips were placed in Chamlide flowcell above the objective of a TIRF enabled inverted-microscope for imaging (**Figure 3-21**).

Figure 3-21. Chamlide flowcell reactor design and orientation in TIRF microscope. Images adapted from Chamlide (www.chamlide.com) and Olympus Microscopy (http://www.olympuscanada.com).

3.7.5 TIRF image acquisition

Fluorescence imaging was performed with an Olympus FV1000 TIRF. The instrument is equipped with a CW laser (488 nm Ar laser) and an EM-CCD (Rolera EM-C^2, Q-Capture). The laser beam was collimated and focused through a fiber-coupling unit. A beam splitter cube with a 550 nm long pass emission filter or 50 nm bandpass filter centred at 525 (Semrock) was used to reflect the excitation light into the oil immersion TIR (total internal reflection) objective (100**X**, NA1.45, Olympus, PLAPO). Fluorescence spectra were recorded with a Fluorescent Lifetime Imaging System (FLIM, PicoQuant). The instrument is equipped with a picosecond pulsed diode laser (485 nm, 100 ps, 40 MHz, LDH-D-C-485, PicoQuant). The laser beam was collimated and focused through a fiber-coupling unit. A beam splitter (500dcxr, Chroma) was used to reflect the excitation light into the oil immersion TIR objective (100X, NA1.45, Olympus, PLAPO).

3.7.6 TIRF Image analysis

All fluorescence microscope images were analyzed using ImageJ (NIH). Background subtraction of microscopy videos was performed with a rolling ball algorithm using a 10-pixel ball radius. Bursts were identified by visual analysis and burst locations were selected by adding the 3 x 3 pixel area around bright events into the Region-of-Interest (ROI) manager within ImageJ. Intensity-time trajectories of bursts were constructed by extracting the mean intensity of 3 x 3 pixel areas around burst spots for each frame using the multi-measure function in ImageJ and plotting the intensity as a function of time. 3D surface projections of TIRF videos were done by first creating intensity sum projections and standard deviation projections of the entire image stack, followed by merging of the resultant images and plotting the composite image as a 3D surface. The intensity sum projection is a simple sum of the intensity of each pixel over time, while calculating the standard deviation of each pixel's intensity value through time creates the standard deviation projection. Plotting the simple intensity sum projection on a 3D surface exaggerates long "on" events, while merging the sum and standard deviation projections allows for adequate representation of both long and short lived bursts.

3.8 References

1. Rostovtsev, V.V., Green, L.G., Fokin, V.V. & Sharpless, K.B. A stepwise Huisgen cycloaddition process: Copper(I)-catalyzed regioselective "ligation" of azides and terminal alkynes. *Angew. Chem. Int. Ed.* **41**, 2596-2599 (2002).
2. Tornøe, C.W., Christensen, C. & Meldal, M. Peptidotriazoles on solid phase: [1,2,3]-triazoles by regiospecific copper(i)-catalyzed 1,3-dipolar cycloadditions of terminal alkynes to azides. *J. Org. Chem.* **67**, 3057-3064 (2002).
3. Hein, J. & Fokin, V. Copper-catalyzed azide–alkyne cycloaddition (CuAAC) and beyond: new reactivity of copper(I) acetylides. *Chem. Soc. Rev.* **39**, 1302-1315 (2010).
4. Kolb, H.C., Finn, M.G. & Sharpless, K.B. Click chemistry: Diverse chemical function from a few good reactions. *Angew. Chem. Int. Ed.* **40**, 2004 (2001).
5. Meldal, M. & Tornoe, C.W. Cu-catalyzed azide-alkyne cycloaddition. *Chem. Rev.* **108**, 2952-3015 (2008).

6. Moses, J.E. & Moorhouse, A.D. The growing applications of click chemistry. *Chem. Soc. Rev.* **36**, 1249-1262 (2007).
7. Thirumurugan, P., Matosiuk, D. & Jozwiak, K. Click Chemistry for Drug Development and Diverse Chemical−Biology Applications *Chem. Rev.* **113**, 4905-4979 (2013).
8. Cintas, P., Barge, A., Tagliapietra, S., Boffa, L. & Cravotto, G. Alkyne–azide click reaction catalyzed by metallic copper under ultrasound. *Nat. Protoc.* **5**, 607-616 (2010).
9. Hong, V., Presolski, S., Ma, C. & Finn, M. Analysis and Optimization of Copper-Catalyzed Azide-Alkyne Cycloaddition for Bioconjugation. *Angew. Chem. Int. Ed.* **48**, 9879-9883 (2009).
10. Kappe, C. & Van Der Eycken, E. Click chemistry under non-classical reaction conditions. *Chem. Soc. Rev.* **39**, 1280-1290 (2010).
11. Pachón, L., Van Maarseveen, J. & Rothenberg, G. Click Chemistry: Copper Clusters Catalyse the Cycloaddition of Azides with Terminal Alkynes. *Adv. Synth. Catal.* **347**, 811-815 (2005).
12. Adzima, B. *et al.* Spatial and temporal control of the alkyne–azide cycloaddition by photoinitiated Cu(II) reduction. *Nat. Chem.* **3**, 258-261 (2011).
13. Jin, T., Yan, M. & Yamamoto, Y. Click Chemistry of Alkyne-Azide Cycloaddition using Nanostructured Copper Catalysts. *ChemCatChem* **4**, 1217-1229 (2012).
14. Woo, H. *et al.* Azide-Alkyne Huisgen [3+2] Cycloaddition Using CuO Nanoparticles. *Molecules* **17**, 13235-13252 (2012).
15. Rance, G., Solomonsz, W. & Khlobystov, A. Click chemistry in carbon nanoreactors. *Chem. Commun.* **49**, 1067-1069 (2013).
16. Alonso, F., Moglie, Y., Radivoy, G. & Yus, M. Unsupported Copper Nanoparticles in the 1,3-Dipolar Cycloaddition of Terminal Alkynes and Azides. *Eur. J. Org. Chem.*, 1875-1884 (2010).
17. Alonso, F., Moglie, Y., Radivoy, G. & Yus, M. Multicomponent Synthesis of 1,2,3-Triazoles in Water Catalyzed by Copper Nanoparticles on Activated Carbon. *Adv. Synth. Catal.* **352**, 3208-3214 (2010).
18. Raut, D. *et al.* Copper nanoparticles in ionic liquids: Recyclable and efficient catalytic system for 1,3-dipolar cycloaddition reaction. *Catal. Commun.* **10**, 1240-1243 (2009).
19. Kumar, B.S.P.A., Reddy, K.H.V., Madhav, B., Ramesh, K. & Nageswar, Y.V.D. Magnetically separable CuFe2O4 nano particles catalyzed multicomponent synthesis of 1,4-disubstituted 1,2,3-triazoles in tap water using ‘click chemistry’. *Tetrahedron Lett.* **53**, 4595-4599 (2012).
20. Hudson, R., Li, C. & Moores, A. Magnetic copper–iron nanoparticles as simple heterogeneous catalysts for the azide–alkyne click reaction in water. *Green Chem.* **14**, 622 (2012).

21. Sarkar, A., Mukherjee, T. & Kapoor, S. PVP-Stabilized Copper Nanoparticles: A Reusable Catalyst for "Click" Reaction between Terminal Alkynes and Azides in Nonaqueous Solvents *J. Phys. Chem. C* **112**, 3334-3340 (2008).
22. Pacioni, N.L., Filippenko, V., Presseau, N. & Scaiano, J.C. Oxidation of copper nanoparticles in water: mechanistic insights revealed by oxygen uptake and spectroscopic methods. *Dalton Trans.* **42**, 5832-5838 (2013).
23. Davies, I.W., Matty, L., Hughes, D.L. & Reider, P.J. Are Heterogeneous Catalysts Precursors to Homogeneous Catalysts? *J. Am. Chem. Soc.* **123**, 10139-10140 (2001).
24. Witham, C.A. *et al.* Converting homogeneous to heterogeneous in electrophilic catalysis using monodisperse metal nanoparticles. *Nat. Chem.* **2**, 36-41 (2010).
25. Kurokhtina, A.F.S.a.A.A. Distinguishing between the Homogeneous and Heterogeneous Mechanisms of Catalysis in the Mizoroki-Heck and Suzuki-Miyaura Reactions: Problems and Prospects. *Kinet. Catal.* **53**, 714-730 (2012).
26. Nishina, Y., Miyata, J., Kawai, R. & Gotoh, K. Recyclable Pd-graphene catalyst: mechanistic insights into heterogeneous and homogeneous catalysis. *RSC Adv.* **2**, 9380-9382 (2012).
27. Reetz, M.T. & Westermann, E. Phosphane-Free Palladium-Catalyzed Coupling Reactions: The Decisive Role of Pd Nanoparticles. *Angew. Chem. Int. Ed.* **39**, 165-168 (2000).
28. Esfandiari, N.M. & Blum, S.A. Homogeneous vs Heterogeneous Polymerization Catalysis Revealed by Single-Particle Fluorescence Microscopy *J. Am. Chem. Soc.* **133**, 18145-18147 (2011).
29. Hensle, E.M. & Blum, S.A. Phase Separation Polymerization of Dicyclopentadiene Characterized by In Operando Fluorescence Microscopy. *J. Am. Chem. Soc.* **135**, 12324-12328 (2013).
30. Roeffaers, M.B.J. *et al.* Relating Pore Structure to Activity at the Subcrystal Level for ZSM-5: An Electron Backscattering Diffraction and Fluorescence Microscopy Study. *J. Am. Chem. Soc.* **130**, 13516-13517 (2008).
31. Roeffaers, M.B.J. *et al.* Super-Resolution Reactivity Mapping of Nanostructured Catalyst Particles. *Angew. Chem. Int. Ed.* **48**, 9285-9289 (2009).
32. De Cremer, G. *et al.* High-Resolution Single-Turnover Mapping Reveals Intraparticle Diffusion Limitation in Ti-MCM-41-Catalyzed Epoxidation. *Angew. Chem. Int. Ed.* **49**, 908-911 (2010).
33. Rybina, A. *et al.* Distinguishing Alternative Reaction Pathways by Single-Molecule Fluorescence Spectroscopy. *Angew. Chem. Int. Ed.* **52**, 6322-6325 (2013).
34. Canham, S.M. *et al.* Toward the Single-Molecule Investigation of Organometallic Reaction Mechanisms: Single-Molecule Imaging of Fluorophore-Tagged Palladium(II) Complexes *Organometallics* **27**, 2172-2175 (2008).

35. Esfandiari, N.M. *et al.* Single-Molecule Imaging of Platinum Ligand Exchange Reaction Reveals Reactivity Distribution *J. Am. Chem. Soc.* **132**, 15167-15169 (2010).
36. Roeffaers, M.B.J. *et al.* Spatially resolved observation of crystal-face-dependent catalysis by single turnover counting. *Nature* **439**, 572-575 (2006).
37. Xu, W., Kong, J.S., Yeh, Y.-T.E. & Chen, P. Single-molecule nanocatalysis reveals heterogeneous reaction pathways and catalytic dynamics. *Nat. Mater.* **7**, 992-996 (2008).
38. Zhou, X., Xu, W., Liu, G., Panda, D. & Chen, P. Size-Dependent Catalytic Activity and Dynamics of Gold Nanoparticles at the Single-Molecule Level *J. Am. Chem. Soc.* **132**, 138-146 (2010).
39. Zhou, X. *et al.* Quantitative super-resolution imaging uncovers reactivity patterns on single nanocatalysts. *Nat. Nanotechnol.* **7**, 237-241 (2012).
40. Chen, P. *et al.* Single-molecule fluorescence imaging of nanocatalytic processes. *Chem. Soc. Rev.* **39**, 4560-4570 (2010).
41. Chen, P. *et al.* Spatiotemporal catalytic dynamics within single nanocatalysts revealed by single-molecule microscopy. *Chem. Soc. Rev.* **43**, 1107-1117 (2014).
42. Buurmans, I.L.C. & Weckhuysen, B.M. Heterogeneities of individual catalyst particles in space and time as monitored by spectroscopy. *Nat. Chem.* **4**, 873-886 (2012).
43. Cordes, T. & Blum, S.A. Opportunities and challenges in single-molecule and single-particle fluorescence microscopy for mechanistic studies of chemical reactions. *Nat. Chem.* **5**, 993-999 (2013).
44. Zhou, X., Choudhary, E., Andoy, N.M., Zou, N. & Chen, P. Scalable Parallel Screening of Catalyst Activity at the Single-Particle Level and Subdiffraction Resolution. *ACS Catal.* **3**, 1448-1453 (2013).
45. Fiolka, R., Belyaev, Y., Ewers, H. & Stemmer, A. Even illumination in total internal reflection fluorescence microscopy using laser light. *Microsc. Res. Tech.* **71**, 45-50 (2007).
46. Jares-Erijman, E. & Jovin, T. FRET imaging. *Nat Biotechnol* **21**, 1387-1395 (2003).
47. Roy, R., Hohng, S. & Ha, T. A practical guide to single-molecule FRET. *Nat. Methods* **5**, 507-516 (2008).
48. Kasper, L. *et al.* Probing the free-energy surface for protein folding with single-molecule spectroscopy. *Nature* **419**, 743-747 (2002).
49. Chung, H., Louis, J. & Eaton, W. Distinguishing between Protein Dynamics and Dye Photophysics in Single-Molecule FRET Experiments. *Biophys. J.* **98**, 696-706 (2010).
50. Hohlbein, J., Craggs, T. & Cordes, T. Alternating-laser excitation: single-molecule FRET and beyond. *Chem. Soc. Rev.* **ASAP** (2013).

51. Greenleaf, W.J., Woodside, M.T. & Block, S.M. High-Resolution, Single-Molecule Measurements of Biomolecular Motion. *Annu. Rev. Biophys. Biomol. Struct.* **36**, 171-190 (2007).
52. Wee, T., Schmidt, L.C. & Scaiano, J.C. Photooxidation of 9-Anthraldehyde Catalyzed by Gold Nanoparticles: Solution and Single Nanoparticle Studies Using Fluorescence Lifetime Imaging *J. Phys. Chem. C* **116**, 24373-24379 (2012).
53. Di Fiori, N. & Meller, A. The Effect of Dye-Dye Interactions on the Spatial Resolution of Single-Molecule FRET Measurements in Nucleic Acids. *Biophys. J.* **98**, 2265-2272 (2010).
54. Brust, M., Walker, M., Bethell, D., Schiffrin, D.J. & Whyman, R. Synthesis of thiol-derivatised gold nanoparticles in a two-phase Liquid-Liquid system. *J. Chem. Soc., Chem. Commun.*, 801-802 (1994).

4. Single-molecule microscopy mapping of CuAAC Reactivity on Supported Copper Nanomaterials

4.1 Heterogeneous catalysis beyond the diffraction limit

4.1.1 Supported nanomaterials as heterogeneous catalysts

The previous chapter explored in detail the single-molecule catalytic cycloaddition of an azide and alkyne by colloidal CuNPs immobilized on a glass coverslip. While making soluble nanomaterials heterogeneous by attaching them onto a glass surface makes sample preparation and examination of catalytic activity by TIRFM rapid and straightforward, the ultimate benefit of heterogeneous catalysts is the ease of separation of catalyst from reagents. The ability to efficiently remove a catalyst from a reaction mixture improves not only the purity of the product, but also reusability of the catalyst. Both of these factors are critical in the usefulness of a particular catalyst material in industrial applications as they affect the bottom line, the cost of producing a product.[1] Often, homogeneous catalytic nanomaterials are supported on relatively inert solids such as silica, alumina, metal oxides or insoluble carbonaceous materials in order to improve catalyst recovery.[2] Moreover, nanomaterials functionalized on support materials are generally more stable than their non-functionalized nanomaterials as they do not suffer from aggregation and agglomeration to the same extent.[1, 2]

Aside from the benefits of improved recovery, stability and recyclability achieved by functionalizing nanomaterials on a support material, these heterogeneous catalysts suffer the same if not increased difficulty in characterization at the molecular level. It is often the case that heterogeneous catalysts are much more heterogeneous and dynamic than expected.[3] If the performance of a catalyst were to be solely evaluated at the macroscopic level, nanoscale heterogeneities within individual catalyst particles or fluctuations in catalytic activity would be overlooked. For this reason, it is critical to observe catalyst activity at the molecular level to gain the necessary insight into the physiochemical properties of a catalyst that allows for its rational optimization.

As mentioned in the introductory chapter of this thesis, a number of modern techniques have been pioneered that approach or achieve the resolution required to investigate catalysts at the molecular level. Many of these techniques, such as scanning probe microscopies (SPM), or scanning transmission X-ray microscopy (STXM) make it possible to examine the chemical nature and structure of a single catalyst particle. There are however, significant drawbacks to these techniques, they either lack the appropriate combination of spatial and temporal resolution, or their implementation becomes overbearingly complicated or impossible under normal operating conditions.[4] Catalysts are dynamic by nature and can be greatly affected by their environment; hence it is of upmost importance to examine them at the molecular level under *in situ* or *in operando* catalytic conditions. State-of-the-art fluorescence microscopy techniques have rapidly become the most powerful methods for investing heterogeneous catalysts at the molecular level largely because they are relatively inexpensive, widely applicable, and capable of achieving single-molecule resolution at *in operando* conditions.[4]

4.1.2 The diffraction limit and how to surpass it

It was realized in the 19th century by Abbe that spatial resolution of microscopy is fundamentally limited to the diffraction of light by a point object.[5] This effect was later described quantitatively by Abbe when he defined the resolution limit as the minimum separation at which two point objects can be differentiated, and introduced formulae for determining the resolution limit in both the lateral (perpendicular to optical path) and axial (along the optical path) dimensions.[6] Abbe determined that the lateral resolution (*x,y*) was proportional to the wavelength of light (λ), but inversely dependent on the Numerical Aperature (NA) of the microscope objective (**Equation 4-1**); while the axial resolution is not only dependent on the wavelength of light, but also the refractive index of the medium and inversely proportional to the square of the numerical aperture (**Equation 4-2**).

$$r_{x,y} \approx \frac{0.5\lambda}{NA} \qquad \textbf{(4-1)} \qquad\qquad r_{x,z} \approx \frac{2n\lambda}{NA^2} \qquad \textbf{(4-2)}$$

This diffraction of light by point source objects in microscopy is manifested in the lateral (*x,y*) dimension though the observation of a intense spot centered at the point source with a series of low intensity concentric rings; this interference pattern is known as the Airy diffraction pattern and generally referred to as the Point Spread Function (PSF), with the central spot termed Airy disk (**Figure 4–1**).[7] The PSF is the smallest observable feature in optical microscopy, thus any object in the focal region of a microscope smaller than the lateral resolution appears as a diffraction-limited spot.[8]

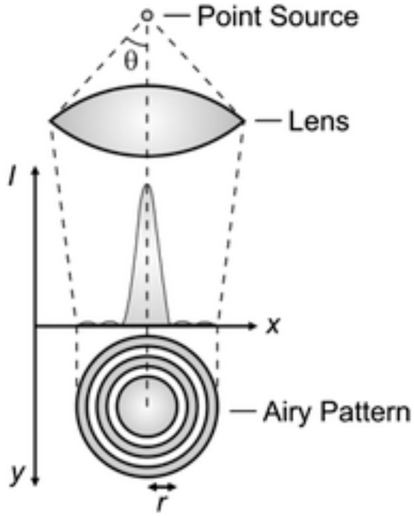

Figure 4–1. Diffracted light from a point source object forming an Airy disk and corresponding concentric rings on the focal plane. Adapted from Raymo *et al*.[7] with permission of The Royal Society of Chemistry.

In fluorescence microscopy, if we consider each individual fluorescent molecule as a potential point source object from which light originates, diffraction limits the resolution to which we can localize these nanosized point sources to ~200 - 300 nm for emission in the visible region.[9] Consequentially, two fluorescent molecules cannot be distinguished with classical microscopy if they are within ~200 nm of each other, nor can the emission from a single emitter be confined to a nanoscale location (**Figure 4–2**). Fortunately, although the specific details of a single nanosized emitter are irresolvable, the centre position of the PSF, and hence its location can be determined to much higher resolution than its diffraction limited resolution.[8] The desire to resolve features at the molecular or near-molecular level has driven significant advancement in sub-diffraction technologies, with recent developments capable of achieving spatial resolution with an order of magnitude improvement over conventional light microcopies.[10] The blanket term Super-Resolution (SR) microscopy is given to optical microscopic techniques with sub-diffraction resolution.

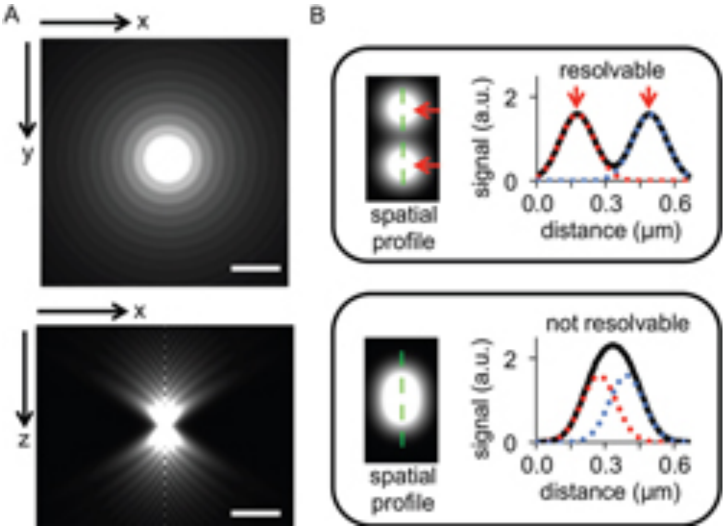

Figure 4–2. Resolution limit of point spread functions (**A**) Example PSF profile in the xy-plane (scale bar = 200 nm) and xz-plane (scale bar = 600 nm); (**B**) microscopy images of two particles at resolvable and irresolvable distances and corresponding intensity profiles of regions denoted by green lines. The centers of resolvable particles are indicated with red arrows, while dotted red and blue lines correspond to the profile of the upper and lower particles, and the black line to the summed profile of both particles. Reproduced from Henriques *et al.*[11] with permission of Cambridge University Press.

As previously stated, super-resolution microscopy improves resolution beyond the diffraction limit by accurately determining the central position of individual emitters PSFs. This position can be determined to within tens of nanometers by fitting the PSF with a function;[12, 13] it so happens that a theoretical 2D Gaussian is an excellent approximation to the shape of the true PSF.[14-16] In theory, this is conceptually simple, but is significantly more complicated in practice as single emitter PSFs are required in order to apply fitting parameters with confidence. The key then to any super-resolution technique is confinement of the number of simultaneously active fluorophores either spatially or temporally. In other words, the number of concurrent emissive fluorophores in a super-resolution experiment must be limited within any given space or time dimension so as to allow for observation of individually separable PSFs from single emitters.

4.1.3 Super-resolution (SR) microscopy

Great ingenuity in pursuit of improved resolution has yielded a number of innovative methods of modulating the proportion of active fluorophores; the likes of which can be separated into three primary categories[10] that are summarized in a non-exhaustive manner in **Table 4-1**. The first category is patterned illumination-based SR microscopies, these methodologies improve resolution through the use of patterned illumination to limit the number of simultaneously active fluorophores in a defined area[10]. In STED for example, all fluorophores within a focal region are excited by an excitation laser and those on the periphery of the focal spot are immediately depleted back down to the ground state by a second laser with a doughnut-shaped beam profile removing them from the resultant image.[17] The second category is a single-molecule location based SR imaging; techniques in this group rely on stochastic activation or modulation (photo-induced or otherwise) of individual fluorescent molecules to ensure only a small subset of emitters are active at any given time.[18] This category is probably the most diverse as stochastic modulation of dyes can be photo-induced as is the case for PALM[19] and STORM,[20, 21] or can be affinity or reactivity dependent with PAINT,[22, 23] MAPT[24] and NASCA[25, 26] as quintessential examples. More recent super-resolution techniques such as SOFI[27] and BaLM[28] comprise the last category termed bleaching/blinking-based super-resolution imaging. These methods take advantage of the inherent fluctuation in emission intensity to achieve super-resolution by recording a series of images with high fluorophore density and continuous excitation followed by post-imaging processing to locate single emitters based on bleaching or blinking behaviour.[29] While methods in all of these categories are capable of providing resolution on the scale of tens of nanometers, their instrumental and experimental complexity varies significantly as does their applicability to the investigation of chemical reactions. For this reason, this chapter will focus specifically on the second category, that is single-molecule localization microscopies (SMLM).

Table 4-1. Summary of selected super-resolution methodologies

Technique	Basic Principle	Citation
Patterned Illumination		
STED	*Stimulated Emission Depletion* – stimulated emission after excitation drives fluorophores in periphery of focal spot to dark state.	17
RESOLFT	*Reversible, saturable, optical fluorescence transition* – switching metastable dark and light states of fluorescent proteins on the periphery of a spot	30
SIM	*Structured Illumination microscopy* – modulation and demodulation of fine structure through patterned illumination.	31, 32
SM Localization		
PALM	*Photoactivated localization microscopy* – individual photoactivation of fluorescent molecules to generate and localize only a few emitters per frame	19
STORM/*d*STORM	*Stochastic optical reconstruction microscopy* – photoswitches fluorescent probes (or pairs) in the presence of thiols between bright on- and dark off-states with long lifetime (>1 s)	20, 21
PAINT	*Point accumulation for imaging nanoscale topography* – transient labeling of cell surfaces such that emitter is activated upon binding	22, 23
MAPT	*Mapping using accumulated probe trajectories* – use the trajectories of probe molecules to image structures based on the heterogeneity of probe–surface interactions	24
NASCA	*Nanometer accuracy by stochastic catalytic reactions microscopy* – high-resolution reconstruction based on catalytic conversion of fluorogenic substrates.	25, 26
Bleaching/Blinking		
SOFI	*Stochastic optical fluctuation imaging* – localization based on statistical analysis of spontaneous fluctuations (blinking) of fluorophores as a function of time	27
BaLM	*Bleaching/blinking assisted localization microscopy* – bleaching/blinking fluorophores are identified by subtracting from each image in a series the subsequent image.	28

4.1.4 Single-molecule localization microscopy methods and applications in catalysis

Since its inception in 2006 with the development of PALM[19] and STORM,[20] single-molecule localization microscopy has exploded as a field of research[10, 11, 18, 29] and has been the class of super-resolution microscopies to be particularly successful in transitioning from biological to chemical applications.[3, 4, 26, 33-35] This is largely due to the seemingly unlimited avenues to achieve the basic concept that all SMLM techniques have in common, stochastic activation of individual fluorophores. Methods such PALM and STORM for example, use known photoactivation pathways dyes to generate a sparse subset of active fluorophores at any given time.[18] The precise locations of these fluorophores are then determined by fitting of their PSFs, and super-resolution images can be generated from the accumulation of locations from a large series of photoactivation and deactivation cycles.[36, 37] Selective photoactivation has been shown to be very effective for imaging static systems,[36, 37] but alternative techniques have been developed for investigating systems that are more dynamic in nature. One such method was reported by Cang *et al.* in which they used the selective adsorption of freely diffusing dyes onto silver clusters to image 15 nm fluorescent enhancement hotspots, they termed this method Point Accumulation for Imaging Nanoscale Topography (PAINT).[23] With MAPT (mapping using accumulated probe trajectories), Walder *et al.*[24] extend this idea of using dye adsorption to map topography by creating surface maps of other absolute physical quantities (adsorption/desorption rates, local diffusion coefficient, and surface coverage) determined from many single-molecule probe trajectories. Due to the nature of the data used to generate a map in this method, extremely large numbers of single-molecule trajectories are needed, thus experiments are very computationally demanding and require high probe densities that are difficult to achieve in single-molecule catalysis.

The most interesting SMLM method in regard to chemical catalysis comes from the Hofkens and Roeffaers research groups at the University of Leuven, Belgium. While their original 2006 Nature letter[38] didn't focus on nanometer resolution, it pioneered the concept of measuring single-turnover catalytically generated fluorescent products to observe chemical catalysis on a single catalyst particle. In a subsequent 2009 report[25], they coin the term NASCA (Nanometer Accuracy by Stochastic Catalytic reActions microscopy) to describe super-resolution image reconstruction based on single-molecule catalytic conversion of fluorogenic substrates. In this report, the acid-catalyzed reaction of furfuryl alcohol to generate a fluorescent polymer was used to map catalytic activity of ZSM-22 and ZSM-5 zeolite crystals. Single-turnover catalytic generation of fluorescent products were observed over a series of frames as single-emitter PSFs, which were then fit to 2D Gaussian functions to yield a list of PSF centre locations, and a reactivity map was reconstructed by accumulating the localized positions (**Figure 4–3.**). Although Hofkens and Roeffaers were the first to use catalytic generation of fluorogenic substrates to obtain detailed information on chemical catalysts at sub-diffraction resolution and the first to apply a name (NASCA) to this approach, other authors have not adopted this term when publishing works based on the same concept. Nevertheless, some excellent super-resolution heterogeneous catalysis investigations have appeared in literature as a result of this pioneering work, and the rapidly growing field has been the subject of a number of reviews.[3, 4, 26, 33, 34, 39]

The large number of articles reviewing works that examine heterogeneous catalysis through super-resolution fluorescence microscopy can mislead a reader unfamiliar with the literature into believing that a wide variety of catalysts and reactions have been explored. In fact, the breadth of research is actually quite limited. Aside from their work on ZSM zeolites which successfully demonstrated activity heterogeneities within a single catalyst crystal,[25] Hofkens and Roeffaers were able to map the catalytic epoxidation of a butadienyl-substituted BODIPY on Ti-MCM-41, revealing intraparticle diffusion.[40] Tachikawa and Majima have probed photocatalytic active sites on single zeolite photocatalyst particles with redox-responsive aminophenyl fluorescein,[41] and examined the crystal-face dependence of TiO_2 photocatalysts through the reduction of non-fluorescent 3,4-dinitrophenyl-BODIPY to fluorescent 4-hydroxyamino-3-nitrophenyl-BODIPY, identifying large surface defects as highly active sites.[42] They extended this reaction to noble metal nanoparticle (Au, Pt) doped TiO_2 meso and nanocomposites investigating photocatalytic charge carrier generation, electron transport[43, 44] and plasmonic catalysis.[45] Chen *et al.* have made extensive use of only two reactions in examining catalysis by gold nanoparticles, both convert non-fluorescent reagents to fluorescent resorufin. The first is the reductive N-deoxygenation of resazurin with ammonium hydroxide, and the second is the oxidative N-deacetylation of amplex red with hydrogen peroxide[34]. Using these two reactions in conjunction, they were able to map catalysis on gold nanomaterials of various dimensions, showing site-specific activity.[46, 47] They then extrapolated their imaging strategy to a scalable method for screening high-activity nanoparticles in a polydisperse inhomogeneous mixture.[48] In an earlier account, Chen *et al.* used the catalytic redox generation of resorufin to examine electrocatalysis by single-walled nanotubes (SWNT) with sub-diffraction resolution.[49]

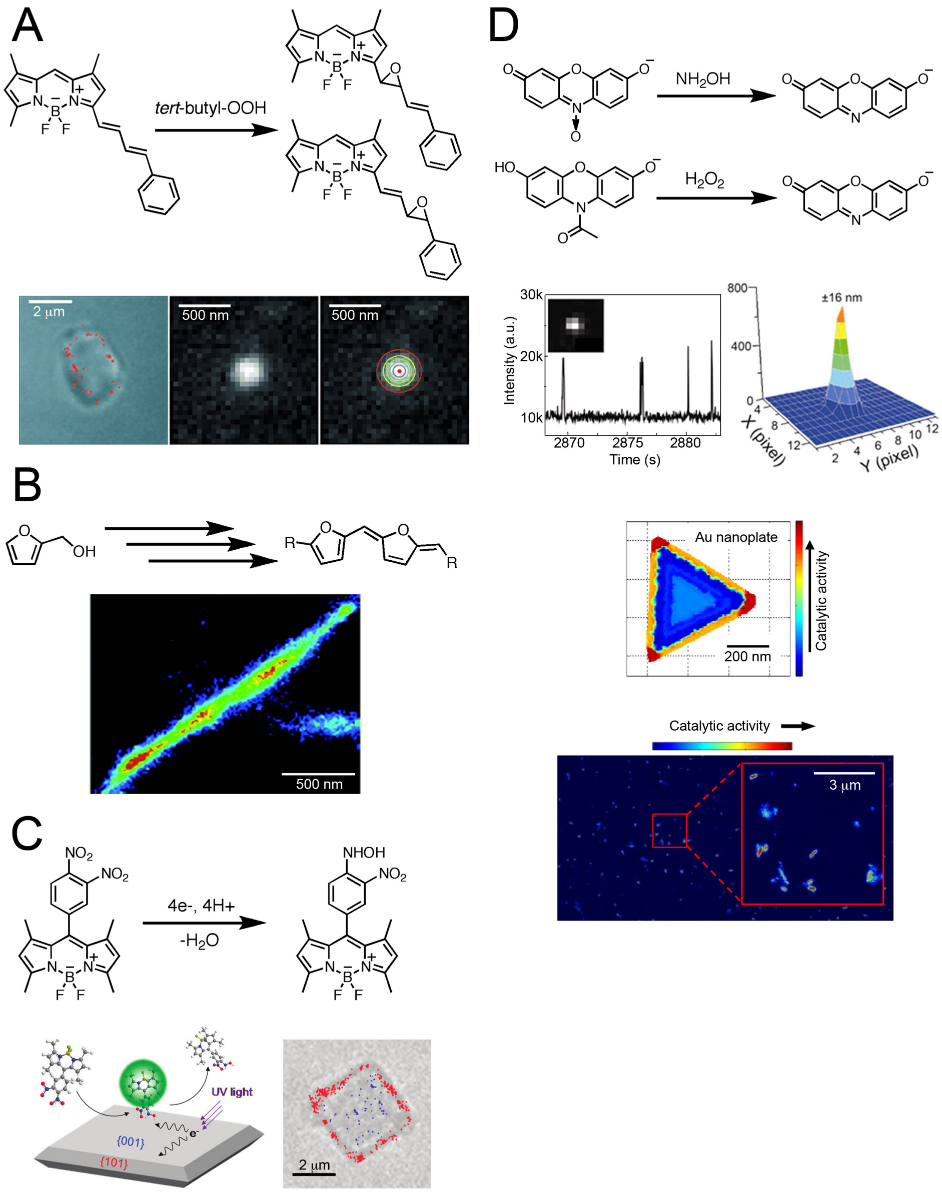

Figure 4–3. Summary of reactions examined with super-resolution fluorescence microscopy. (**A**) Fluorescence switching of a BODIPY probe by epoxidation with *tert*-butylhydroperoxide on Ti-MCM-41, adapted with permission from De Cremer *et al.*[40] (**B**) Reactivity of a single ZSM crystal mapped by generation fluorescent products in the polymerization of furfuryl alcohol, adapted with permission from Roeffaers *et al.*[25] (**C**) Photocatalytic redox reaction of a BODIPY probe on TiO_2, adapted with permission from Tachikawa *et al.*[42] Copyright (2011) American Chemical Society. (**D**) Catalytic reduction of resazurin and oxidation of amplex red to generate fluorescent resorufin on gold nanoparticles, adapted with permission from Chen *et al.*[47, 48] Copyright (2013) American Chemical Society.

4.1.5 Our approach

From examination of the literature it is plainly obvious that while some excellent research has helped define a paradigm in this novel field, creativity is needed to advance the state-of-the-art past the sparse few reactions and catalysts that have been investigated. As this is a fluorescence microscopy technique, the path to broadening the scope of accessible catalysts and reactions begins with finding innovative new ways to use fluorescent or fluorogenic probes to explore them. The previous chapter of this thesis demonstrated a novel method for investigating the azide-alkyne cycloaddition click reaction catalyzed by immobilized colloidal CuNPs. Triazole formation between an alkyne modified donor molecule and azide modified acceptor molecule brings donor and acceptor within close enough proximity to allow energy transfer. We confirmed catalysis occurs in a heterogeneous fashion on the nanoparticle surface rather than in solution from leached copper ions. In this chapter, our investigation into heterogeneous CuAAC reaction is expanded to copper nanomaterials immobilized on support materials, true heterogeneous catalysts. First, we use novel azide and alkyne functionalized BODIPY fluorophores to map copper nanoparticles supported on MCM-41 by monitoring the adsorption of single alkyne molecules at diffraction-limited resolution. Next, we will show that the CuAAC activity of commercially available nanoparticulate copper on activated carbon can be mapped with sub-diffraction resolution using the novel FRET activation of AlexaFluor488 alkyne and A594 azide discussed previously.

4.2 Mapping CuAAC reactivity of nanoparticulate Cu supported on mesoporous silicate MCM-41

Our success exploring the single-molecule reactivity of colloidal CuNPs toward the azide-alkyne cycloaddition of functionalized AlexaFluor dyes led us to an interest in developing a similar method to establish CuNP catalytic properties in supported nanoparticle systems. Initial attempts to adapt our AlexaFluor CuAAC-activated FRET method to colloidal CuNPs supported on metal oxides or silicates afforded little success due to low signal and high levels of light scattering by the supports. To overcome these challenges we sought to design a new single-molecule method that would allow us to investigate CuAAC reactions on supported CuNPs.

4.2.1 Designing a new single-molecule approach

To achieve the desired increase in signal above the scattered light background we modified our approach to one in which the emission of an azide modified fluorophore would be activated by participation of the azide group in the CuAAC reaction with an arbitrary alkyne. Fluorophore quenching by a proximal azide functionality is a known to occur via internal charge transfer (ICT).[50-53] The difficulty lies in developing a robust probe with a chromophore that exhibits spectral properties accessible by the irradiation sources we have available within our microscope system, all of which are in the visible spectrum at wavelengths greater than 450 nm. This limitation rules out the utility of the azido-coumarin that was used as the cornerstone of a small library of cation sensors in chapter 2. Wang and co-workers reported a promising BODIPY dye with an azido modification at the 3-position that exhibits a marked increase in fluorescence intensity after CuAAC reaction of the azide with various terminal alkynes.[52] To investigate the applicability of this probe to our single-molecule catalysis system we repeated the synthesis that Wang reported, however, during preliminary studies a rapid colour change in the solution was observed when it was left on the bench top in ambient lighting. The influence of this distinct colour change from bright red to pale yellow-orange on its application as fluorogenic probe was examined by irradiating with a pulsed 488 nm laser, the same wavelength used in single-molecule studies. A striking decrease in absorption was observed very rapidly upon laser irradiation (**Figure 4–4**) hinting that decomposition of the dye chromophore was evident. UV photolysis of aryl azides yields photoelimination of N_2, generating reactive nitrenes that tend to react with anything in close proximity, including solvent molecules and can also induce intermolecular ring expansions.[51, 54] Thus, it is likely that irradiation of **16** results in the photolysis of the azide group and generation of a reactive nitrene that contributes to the destruction of the BODIPY chromophore. There is an alternative to directly attaching the azido functionality to a chromophore; that is, separating the chromophore from the azido by way of a spacer group such as a carbon chain. Removing the azido from the chromophore's proximity increases the dye photostabilty and concomitantly alters the approach to single-molecule experiments, which will be the topic of further discussion.

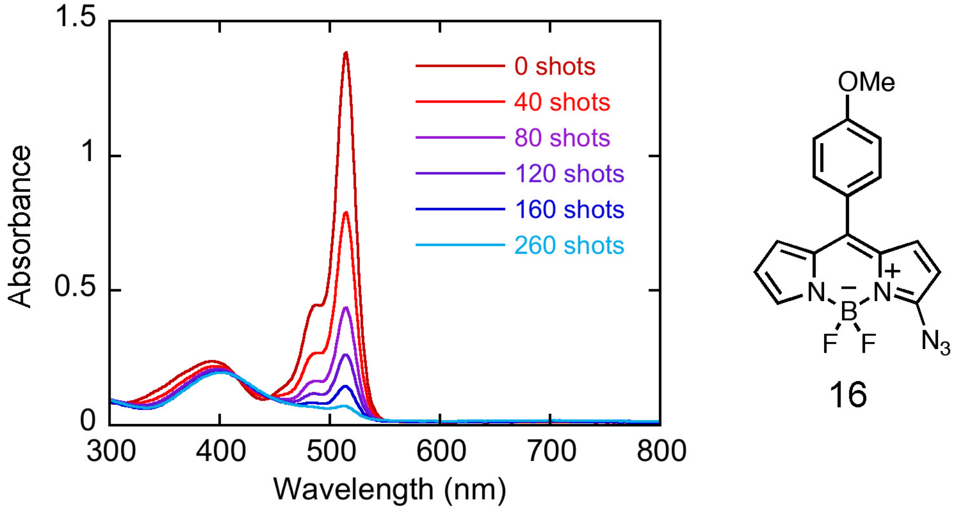

Figure 4–4. Decrease of the absorption of 3-azido substituted BODIPY (**16**) with 488 nm pulsed laser irradiation. Laser dose was 12 mJ/shot.

Discounting the concept of monitoring single-molecule CuAAC reactions through fluorogenic azides, a more direct approach was taken and two new BODIPY probe molecules were synthesized, one modified with an alkyne and one with an azide. There are a number of notable differences between these BODIPY probes and the AlexaFluor FRET pair described earlier that affect how they can be used in single-molecule microscopy experiments. First, both chromophores of **17** and **18** are the same, with identical spectroscopic properties, eliminating selective excitation in a mixture of the two probes impossible. Furthermore, as a carbon tether is used to separate chromophores from their respective functional groups, neither has an effective quencher directly bound to the chromophore, thus are always “on” resulting in greater signal compared to FRET-based single-molecule experiments and reducing the effects of scattering. These two factors present a stark contrast to the AlexaFluor system that allowed FRET transfer to occur between the dye pair with Cu-catalyzed cycloaddition. Without selective excitation or emission switching there is no means of spectrally separating the alkyne and azide molecules in a mixture, nor a way of differentiating products from reactants. Rather than collecting emission from individual CuAAC product molecules, the strong affinity of alkynes for Cu (I) and the resultant Cu-acetylide complex can be exploited to examine the CuAAC reactivity of supported CuNPs. In this method (**Figure 4–5**), when dilute aqueous solutions of alkyne (**17**) are flowed over CuNPs supported on 3-aminopropyltriethoxysilane (APTES) modified silicate MCM-41 (Cu@MCM-41), discreet bursting events can be accumulated to map the formation of Cu-acetylide complexes on the surface of the support. Analysis of the bursting events and well-designed control experiments will confirm that this observed bursting definitively occurs at CuNPs located on the MCM surface.

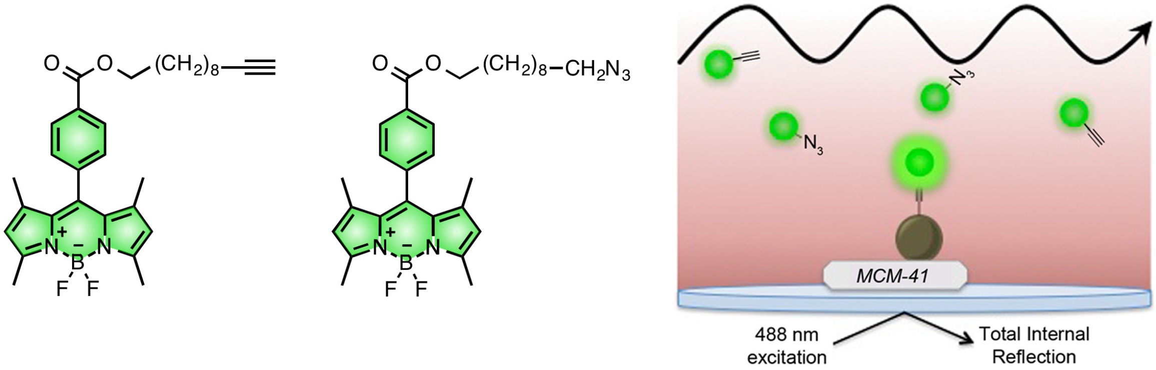

Figure 4–5. Structures of BODIPY alkyne (**17**) and azide (**18**) and pictorial depiction of TIFM experimental design showing propagating evanescent wave with 488 nm TIRF excitation. Alkyne modified BODIPY molecules form Cu-acetylide complexes with CuNPs (brown) supported on MCM-41 producing an observable bursting signal while azide modified BODIPY molecules do not coordinate to Cu, thus their emission contributes to the background signal.

4.2.2 Synthesis of supported nanomaterials and dyes

Our first attempt at immobilizing colloidal CuNPs on a support material was with nanoparticles synthesized using a strategy that our research group developed and optimized for various noble metal particles[55-59] including copper.[60] This strategy is facile and efficient; employing photochemically generated radicals to reduce metal salts *in situ* affording unprotected metallic nanoparticles. In the case of copper, the unprotected nature of the particles produced leaves them susceptible to rapid oxidation.[61] Attempts to support photochemically generated CuNPs on materials such as hydrotalcite, ZnO, MgO, MCM-41, SBA-15, SiO_2, carbon nanofibres and activated carbon were unsuccessful under oxygen or inert atmosphere. Typically, support material was added to an aqueous solution of photochemical CuNPs and the mixture was stirred or sonicated for up to 24 hours. Quite often the supernatant remained pink coloured indicating colloidal CuNPs remained in solution, or the solution changed to a grey colour indicating oxidation of Cu(0) to Cu(II).[61] These difficulties led to change a in tactics, and we next made use of the thiolate-protected CuNPs previously investigated with single-molecule TIRFM (see Chapter 3). Repeating the same experiments with these nanoparticles as with the photochemical variety, the most success was found with silicate materials such as SBA-15, SiO_2 and MCM-41, yet it was obvious that my procedure could still be improved as the supernatant from mixtures of these materials with thiolated CuNPs remained slightly coloured after precipitation of the support. Our research group has had previous success immobilizing gold nanoparticles on MCM-41 that was pretreated with APTES grafting to introduce amines on the material surface.[62] The APTES-grafted MCM-41 happens to be an excellent support for CuNPs as the particles quickly adsorb to the material, leaving the supernatant completely colourless.

In general, BODIPY probes **16**, **17**, and **18** were synthesized by trifluoroacetic acid catalyzed condensation of corresponding phenylaldehyde and substituted pyrrole. The resulting dipyrromethane was mono-chlorinated with N-chlorosuccinimide if required, before reduction to dipyrromethene with a benzoquinone. Subsequent reaction with BF_3-OEt_2 with triethylamine as additive afforded the desired BODIPY backbone, which was modified accordingly to obtain substituted BODIPYs. For **16**, mono-chlorinated BODIPY was reacted with sodium azide, while BODIPY-COOH was subjected to N,N-dicyclohexylcarbodiimide (DCC) / 4-(dimethylamino)pyridine (DMAP) esterification with terminal alcohols 10-undecyn-1-ol or 10-bromo-decanol to introduce carbon chain tethers present in **17** and **18**. Bromide on the resulting BODIPY-bromide was then substituted for an azido group by reaction with sodium azide.

4.2.3 Spectroscopic properties

Alkyne and azide probes **17** and **18**, are derivatives of the same BODIPY chromophore. Their respective functional groups are tethered far enough from the chromophore such that their spectroscopic properties are not altered, thus their absorption and emission are identical (**Figure 4–6**). Separating the chromophore and the azido group has the added benefit of increased photostability as excitation of the chromophore does not result in photolysis of the azide. This consequence is highlighted in **Figure 4–7**.

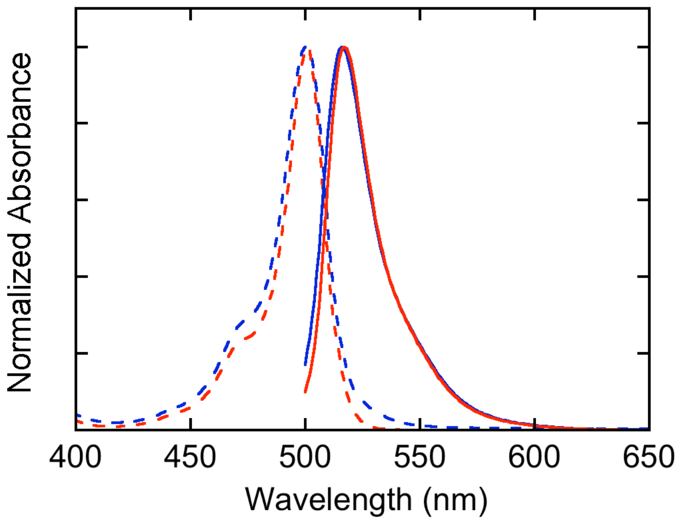

Figure 4–6. Normalized absorption (dashed) and emission (solid) spectra of BODIPY alkyne (**17**) and BODIPY azide (**18**).

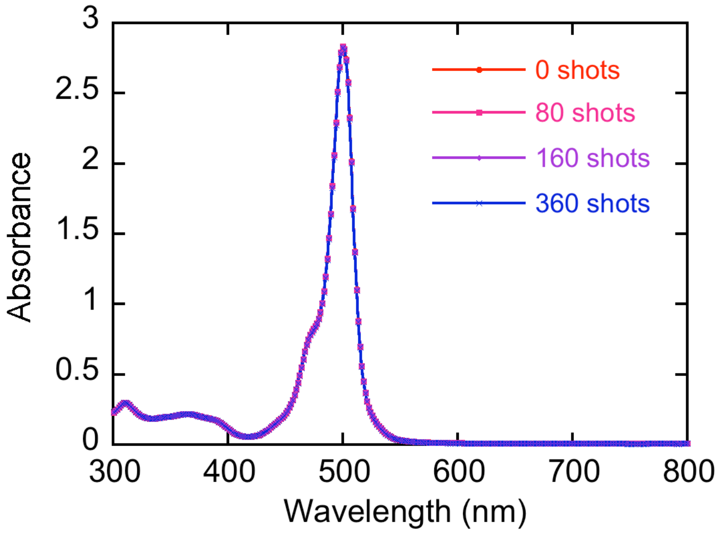

Figure 4–7. Absorption of azido-tethered BODIPY (**18**) remains unchanged with 488 nm pulsed laser irradiation. Laser dose was 12 mJ/shot.

4.2.4 Single-molecule fluorescence microscopy

Single-molecule fluorescence microscopy experiments were performed in the Chamlide microcope flow cell reactor that has been described previously in this thesis. A dilute ethanol solution of alkyne **17** was flowed at a rate of 1 mL/h over a round glass microscope coverslip previously spin coated with CuNP@MCM-41 which was placed over the objective of an Olympus TIRF microscope system. When 488 nm laser irradiation was introduced at the critical angle for total internal reflection (TIR), emissive bursts were observed (**Figure 4–8**).

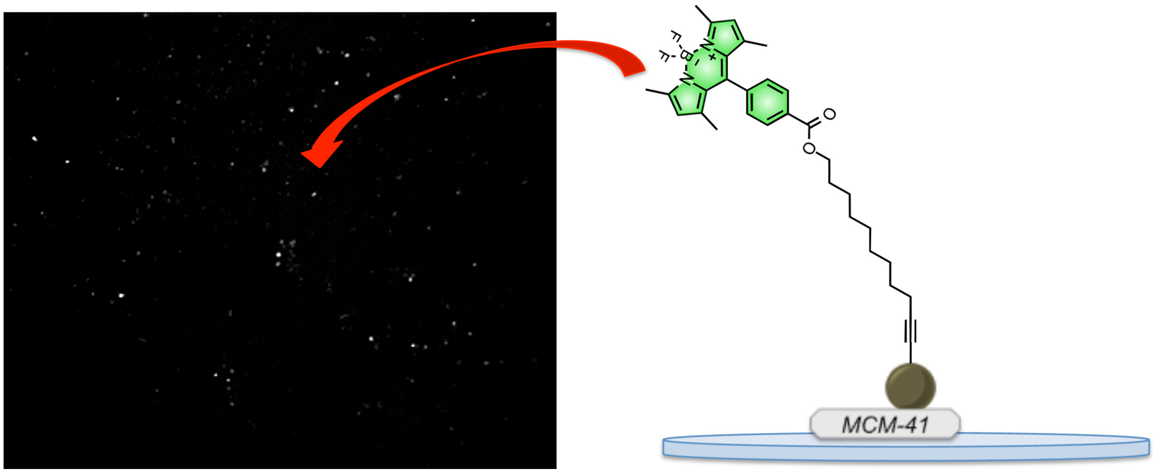

Figure 4–8. Image of bursting events accumulated from 200 frame TIRFM video of a solution of alkyne (**17**) flowing over CuNP@MCM-41. Left image represents a 54 x 47 µm area. Bursting events are observed with the formation of Cu-acetylide complex between **17** and CuNP.

Analysis of individual spots in the resulting video yields the corresponding trajectory showing fluorescence intensity of the bursting spot over time. A representative region of the TIRFM video is shown in the left panel of **Figure 4–9** as 2x expanded accumulation of bright events in the 200 frame video. The red box in the in the left panel highlights the region from which the intensity vs. time trajectory in the bottom right panel was created. Still frame images of this bursting event are presented in the top right panel showing the fluorescence intensity of pixels changing over time as the alkyne coordinates to a CuNP initiating the observed bursting event, and subsequently turns off following desorption from the catalyst.

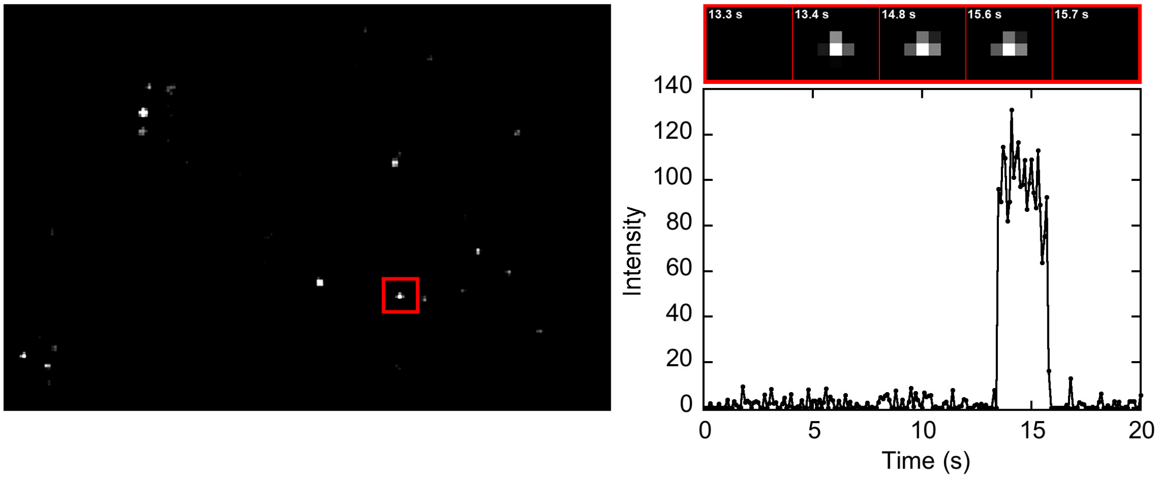

Figure 4–9. Magnified (2x) 31 x 21 μm area of accumulated TIRFM image with selected region surrounding a bursting event of interest highlighted in red (left). Further magnified time-correlated still frame images of the same region highlighted in red (top right), and the fluorescence intensity vs. time trajectory of the highlighted region (bottom right). Region highlighted in red represents a 1.12 x 0.96 μm area.

Accumulating bursting events from an entire TIRFM video into a single image allows for localizing a series of bursting events clustered in one small area. Since MCM-41 particles are larger than the diffraction limit, the support material can be imaged with a white light source in the standard bright light mode of an inverted microscope. Overlaying this white light image with the composite accumulated image allows for determining the position of bursting events on the MCM-41 particle. Bursting events over support material are thus indicative of the location of CuNPs on the support. Using this method, the location and reactivity of CuNPs were effectively mapped on the MCM-41 particle, as demonstrated in the top panels in **Figure 4–10**. Panel A shows the low resolution white light image of a 5 x 4 μm area of a glass coverslip spin coated with CuNP@MCM-41 catalyst, a small MCM-41 particle approximately 3 x 2 μm in size is visible as darker pixels on a grey background. An ethanolic solution of alkyne **17** (1 nM) and Et_3N (10 nM) was flowed over this catalyst and irradiated with 488 nm TIRF excitation; a TIRFM video of the resulting emission was recorded. Panel B shows accumulated bright events in the same 5 x 4 μm area from the recorded 200 frame TIRFM video. When the white light image is overlayed with the accumulated TIRFM image at 50% transparency the bursting events can be seen to occur over the visible MCM-41 particle. This effect is more clearly depicted in the 3D projection of the accumulated fluorescence intensity (**Figure 4–10B**).

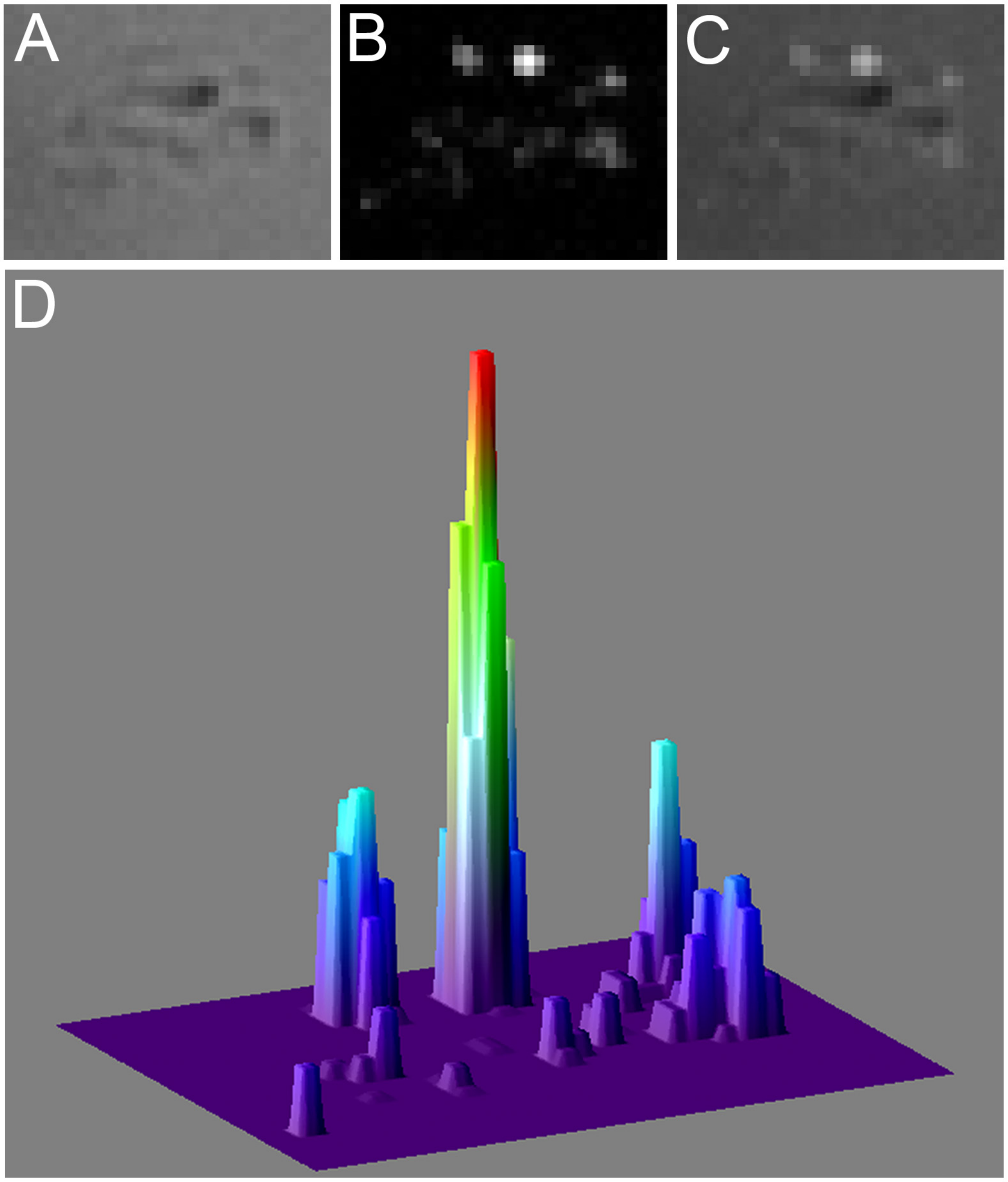

Figure 4–10. (**A**) Magnified (4x) white light image of CuNP@MCM-41, (**B**) image of the emission intensity at the same location accumulated over 200 frames in TIRFM mode with 488 nm laser irradiation of a solution of 1 nM **17** and 10 nM Et_3N, (**C**) white light image (A) of CuNP@MCM-41 overlayed by TIRFM image (B). (**D**) 3D projection of the accumulated intensity image in (B). Each image represents an area of 5 x 4 µm.

4.2.5 Single-molecule fluorescence microscopy control reactions

In conjunction with the insight gained through the course of the previous chapter, a number of control reactions were performed to be certain that the observed bursting with TIRF excitation of alkyne (**17**) over the supported catalyst CuNP@MCM-41 is a result of Cu-acetylide formation between **17** and Cu on the support surface. Foremost, it must be confirmed that bursting is not observed when the experiment is repeated with support material that is not laden with CuNPs. This control experiment was performed by spin coating CuNP free MCM-41-APTES onto a microscope cover slip and imaging a flowing solution of 1 nM **17** and 10 nM Et_3N with 488 nm TIRF excitation. No distinct bursting was detected in the resulting video; rather only fluctuations in light scattering are visible. To accurately represent the fluctuation in scattering intensity observed in the TIRF video, the standard deviation of fluorescence intensity from frame to frame was measured for each pixel over the length of the video and compiled into a single image (left panel, **Figure 4-11**). Standard deviation projections of TIRFM videos are useful for highlighting small intensity variations over a fluctuating background. Any real bursting event would appear as a cluster of bright pixels, whose fluorescence intensity over time would give rise to sharp rises and falls in intensity (**Figure 4-9**) rather than inconsistent small intensity fluctuations. MCM-41 particles are very slightly visible in the standard deviation image in **Figure 4–11** as the support material inhomogeneously scatters laser light causing the intensity to fluctuate from one frame to the next. Analysis of bright spots in the TIRFM video affords trajectory vs. time traces that show only small intensity variations and no sharp rises and drops in intensity indicative of bursting events confirming that any bright spots in the absence of Cu are due to light scattering, not interaction of alkyne **17** with the support.

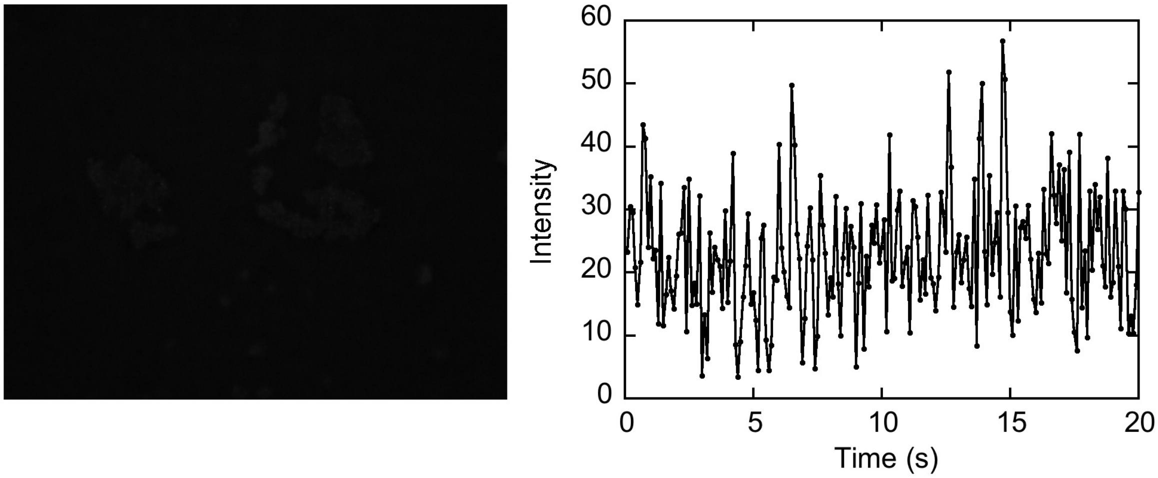

Figure 4–11. Accumulated fluorescence intensity image of a 63 x 48 μm area from the TIRFM video recording of 1 nM alkyne **17** and 10 nM Et_3N flowed over glass coverslip spin coated with MCM-41 without CuNP (left) and representative fluorescence intensity vs. time trajectory of a luminous spot in the video (right).

Similarly, when a solution of azide **18** flowing over CuNP@MCM-41 was imaged with 488 nm TIRF excitation, no bursting events were observed. Again, only scattering from the support is observed with no bright spots exhibiting trajectories characteristic of bursting events. The left panel of **Figure 4–12** is an accumulated

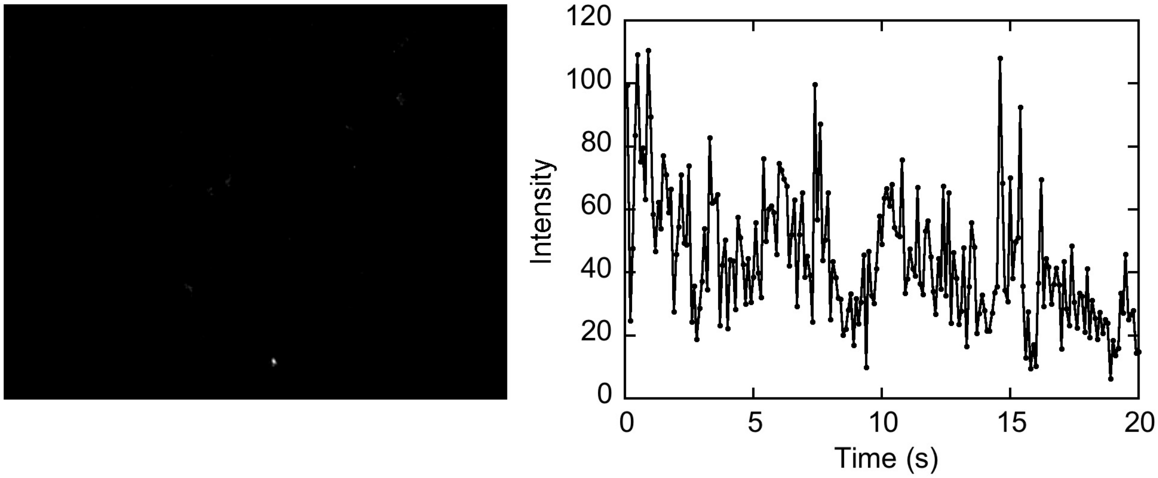

Figure 4–12. Accumulated fluorescence intensity image of a 63 x 48 µm area from the TIRFM video recording of 1 nM azide **18** and 10 nM Et_3N flowed over glass coverslip spin coated with CuNP@MCM-41 (left) and representative fluorescence intensity vs. time trajectory of a luminous spot in the video (right).

fluorescence intensity image of this experiment, while the right panel is a typical intensity vs. time trajectory of a 3 x 3 pixel area around a luminous spot in the TIRFM video clearly depicting light scattering rather than distinct bursting. As the azide does not and is not expected to coordinate to CuNP in the absence of an alkyne,[63, 64] this confirms Cu-acetylide formation between **17** and CuNPs on the MCM-41 surface is the source of bursting events rather than non-selective interaction of the BODIPY fluorophore with the catalyst. These results will be explored in greater detail in the ensuing discussion section.

4.3 Mapping CuAAC reactivity of Copper on Activated Carbon with nanometer resolution

The CuNP@MCM-41 catalyst proved to be an excellent material for mapping Cu-acetylide formation with a novel BODIPY alkyne dye, however, this system is only capable of probing the first step of the azide-alkyne cycloaddition, not complete turnover of the catalytic cycle. While the Cu-acetylide step in this cycloaddition is the most interesting mechanistically, there remains an information void when part of the catalytic cycle is invisible to the elucidation method. Additionally, the mapping resolution achieved is still relatively low when compared to state-of-the-art single-molecule fluorescence microscopy.[4, 10, 29, 39] With this in mind, this section details the development of a novel method for super-resolution mapping of CuAAC reactivity on supported nanomaterials via complete conversion of the catalytic cycle.

4.3.1 Designing an approach to super-resolution CuAAC mapping

In the pursuit of a novel methodology for investigating CuAAC at sub-diffraction resolution inspiration can be drawn from pioneering super-resolution microscopies such as NASCA. Using this approach, a system can be designed in which the emission of alkyne or azide reagents is activated or modulated with and only with stochastic catalytic conversion to triazole products. The AlexaFluor CuAAC activated FRET system examined in Chapter 3 achieves the requisite modulation of emission with stochastic Cu-catalyzed reaction of the FRET pair. Triazole formation between alkyne labeled donor and azide labeled acceptor enables energy transfer between donor and acceptor, activating emission from the AlexaFluor 594 acceptor. Detection of catalytically generated acceptor emission allows one to determine the temporal and spatial position of the catalyst with sub-diffraction resolution by fitting the emitter PSF with a Gaussian function. As previously mentioned in this chapter, the AlexaFluor FRET system has some drawbacks, the most significant of which is inherently lower intensity acceptor emission signal compare to the BODIPY probes **17** and **18** which can make it difficult to detect bursting signal in the presence of high levels of light scattering from support materials. To circumvent this shortcoming, nanoparticulate copper can be supported on a material that does not cause such high levels of light scattering. Bruce Lipshutz and his research group at UC Santa Barbara have developed a heterogeneous copper-in-charcoal (Cu/C) catalyst and demonstrated its activity towards catalytic hydrosilylations,[65] cross-couplings reactions[66, 67] and CuAAC.[68, 69] Recently, Sigma-aldrich has commercialized Lipshutz's 3% copper-in-charcoal (Cu/C) catalyst making it an inexpensive ($19/g), efficient and readily accessible CuAAC catalyst. The carbonaceous support of this Cu/C catalyst is black in colour rather than the white siliceous MCM-41 lending to lower levels of light scattering, thus it is suitable for mapping CuAAC reactivity with single-molecule FRET activation. A schematic representation of the experimental design we have developed for mapping activity of Cu/C catalyst towards CuAAC is given in **Figure 4–13**.

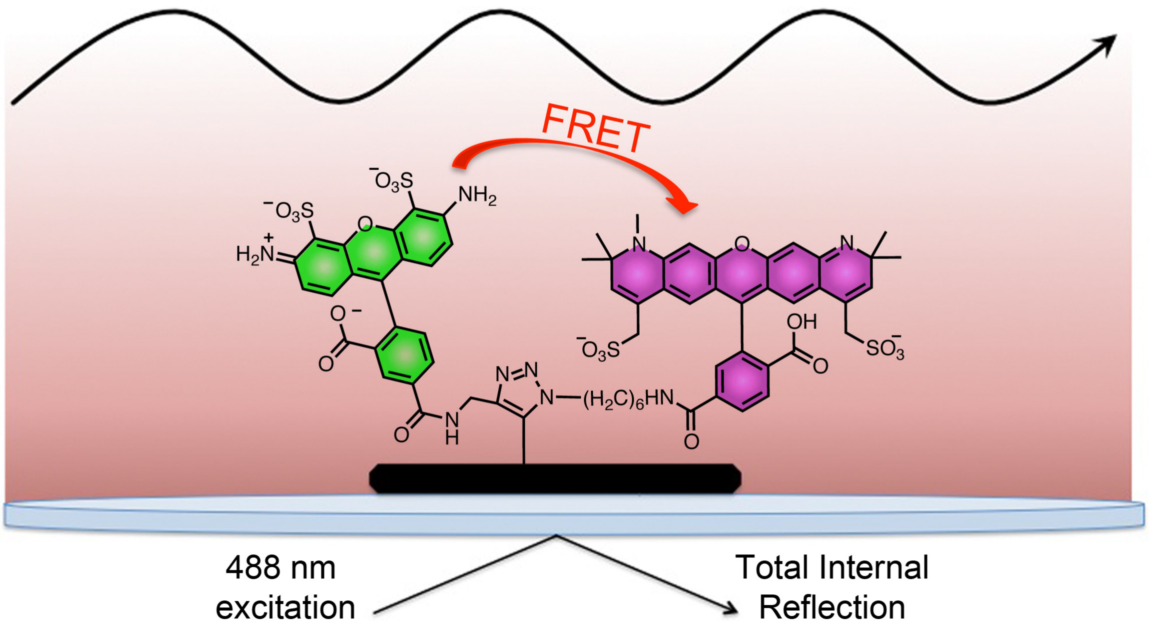

Figure 4–13. Pictorial depiction of TIFM experimental design showing propagating evanescent wave with 488 nm TIRF excitation. Cu/C catalyzed triazole formation between AlexaFluor 488 alkyne (donor, green, **13**) and AlexaFluor 594 azide (acceptor, purple, **14**) allows energy transfer between the two dyes facilitating acceptor emission.

4.3.2 Characterization of commercial Cu/C

In reported works on their heterogeneous Cu/C catalyst, Lipshutz and co-workers characterized the material with TEM, X-ray photoelectron spectroscopy (XPS), and inductively coupled plasma – optical emission spectroscopy (ICP-OES).[65, 68, 69] While information gained from the reported electron microscopy images is quite limited, they do indicate that the distribution of Cu on the activated carbon is heterogeneous, and Cu particles are in fact nanosized (**Figure 4–14**). The authors also concluded from XPS studies that the supported copper exists in the form of oxides, both CuO and Cu_2O with the Cu(II) state being more prevalent. The catalyst was also shown to be rather stable, with no copper detectable by ICP-OES in reaction solutions suggesting no appreciable leaching of Cu from the catalyst. As can be seen in the **Figure 4–14A** TEM image, deciphering Cu particles from the support material is quite difficult and inconclusive.

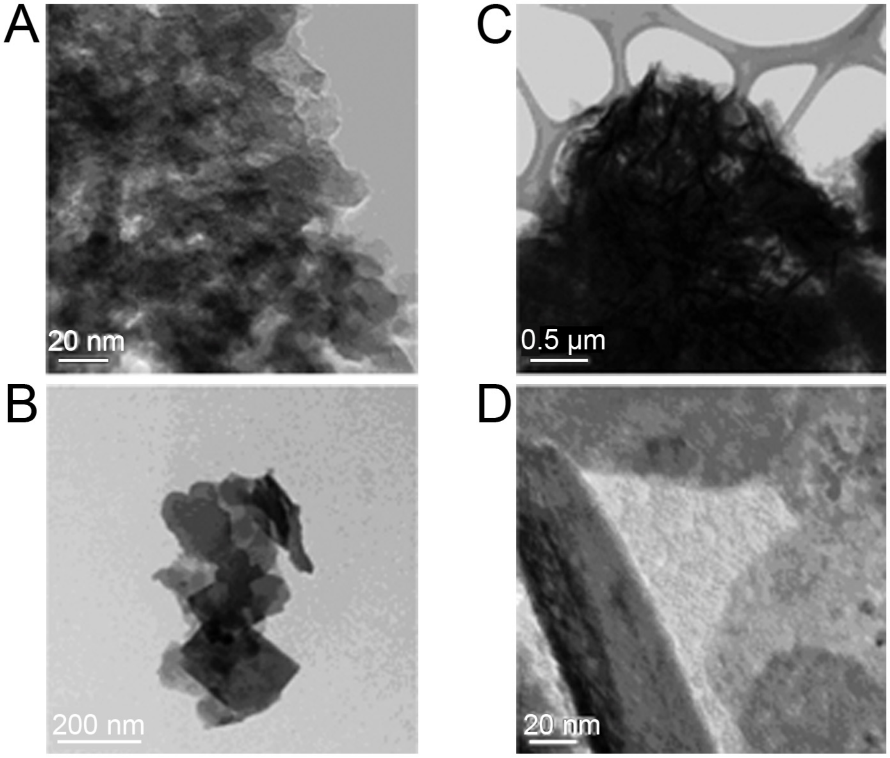

Figure 4–14. TEM images of Cu/C: (**A**) bright field image showing dispersion of copper atoms; (**B**) clusters of copper atoms; (**C**) needles of copper atoms in a cluster; (**D**) higher magnification of a copper cluster. Images adapted with permission from Lipshutz *et al.*[65]

Attempting to obtain more conclusive information on the location and distribution of Cu on the carbon support, we imaged the commercial material with a scanning electron microscope (SEM) in total energy detector (TED) mode and backscattered electron composition (COMPO) mode. In TED mode, both the carbon support and Cu_xO clusters appear dark on a bright background, while in COMPO mode denser objects such as metal oxides appear brighter than less dense materials enabling Cu to be imaged on the carbon support. The TED image in the top panel shows that the material is very polydisperse in size and shape with some particles being smaller than 50 nm and others larger than a few microns. In the COMPO image in the bottom panel, copper oxides should appear brighter than the carbon support and some brighter areas are observed, however, low contrast between bright and dark regions inhibits drawing reliable conclusions as it is also possible that brighter areas are due to a thicker layer of carbon. The images in **Figure 4–15**, confirm that SEM imaging of the commercial Cu/C provides inconclusive information about the material as it is very difficult to discern between carbon and copper in the images. This limitation makes single-molecule fluorescence microscopy studies all the more valuable for examining heterogeneous reactivity of supported catalysts.

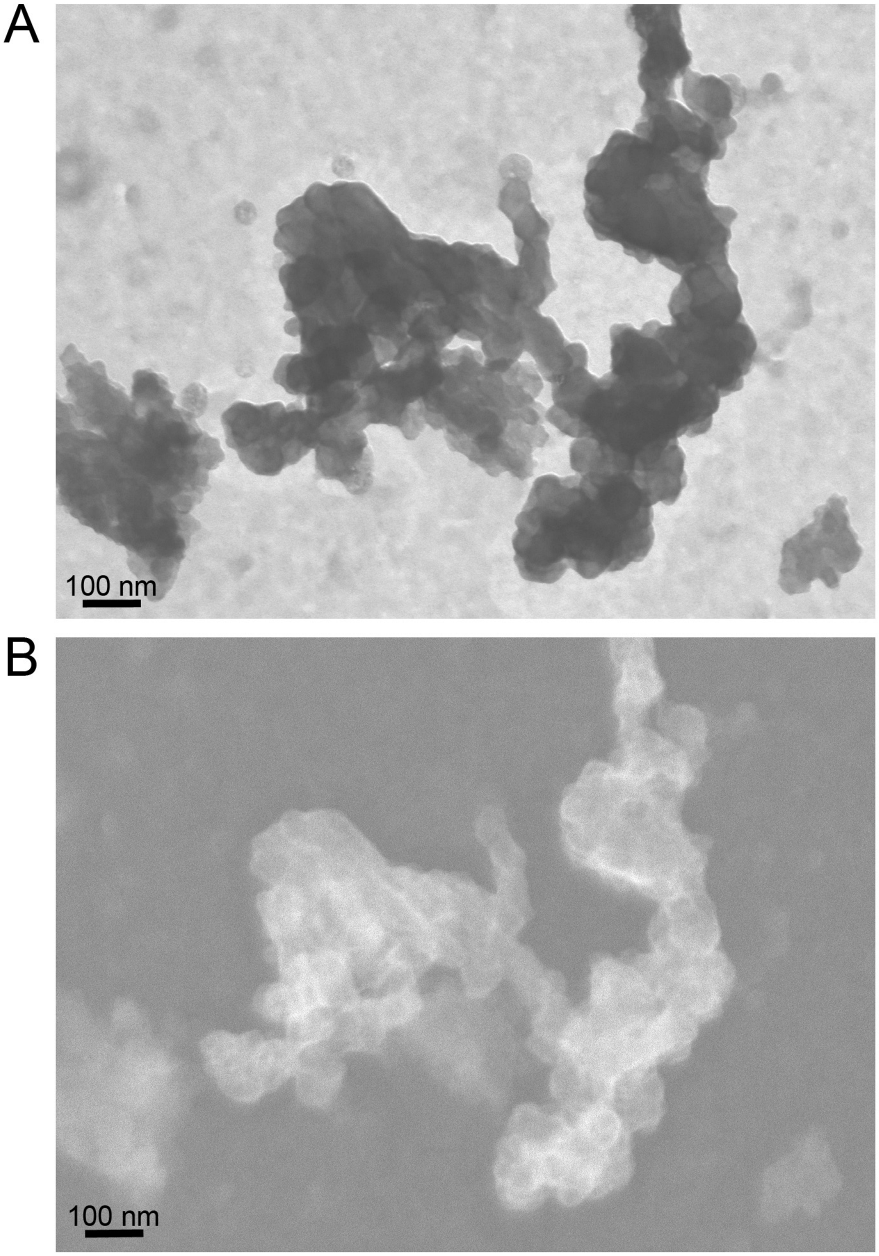

Figure 4–15. SEM images of commercial Cu/C catalyst. (**A**) Image recorded in TED mode. (**B**) Image recorded in backscattering composition (COMPO) mode.

4.3.3 Spectroscopic properties

The spectroscopic properties of AlexaFluor488 alkyne (**13**) and AlexaFluor 594 azide (**14**) were reported in Chapter 3.

4.3.4 Single-molecule fluorescence microscopy

To image the CuAAC reaction catalyzed by the commercial heterogeneous copper-in-charcoal, a solution of 100 pM **13**, 100 pM **14** and 1 nM triethylamine was flowed though a Chamlide flowcell reactor at 1 mL /hour over a microscope coverslip previously spin coated with Cu/C catalyst and placed over the TIRF objective. Irradiation of the solution with 488 nm TIRF excitation caused bright bursting events to appear throughout the focal area. Analysis of bright events confirmed the nature of the bursting is consistent with that observed for colloidal thiolate CuNPs immobilized on a glass surface. The image in **Figure 4–16A** shows the accumulated bright events from a 500 frame video recording of this experiment. In conjunction with previous control experiments, these bright events are attributed Cu/C catalyzed triazole formation between AF488 alkyne and AF594 alkyne allowing FRET to occur resulting in emission from AF 594 chromophore to be observed. The plot in **Figure 4–16** depicts the fluorescence intensity changes over time with a marked jump in fluorescence denoting catalytic generation of a triazole product, and a sharp decrease in signal indicating product desorption from the catalyst.

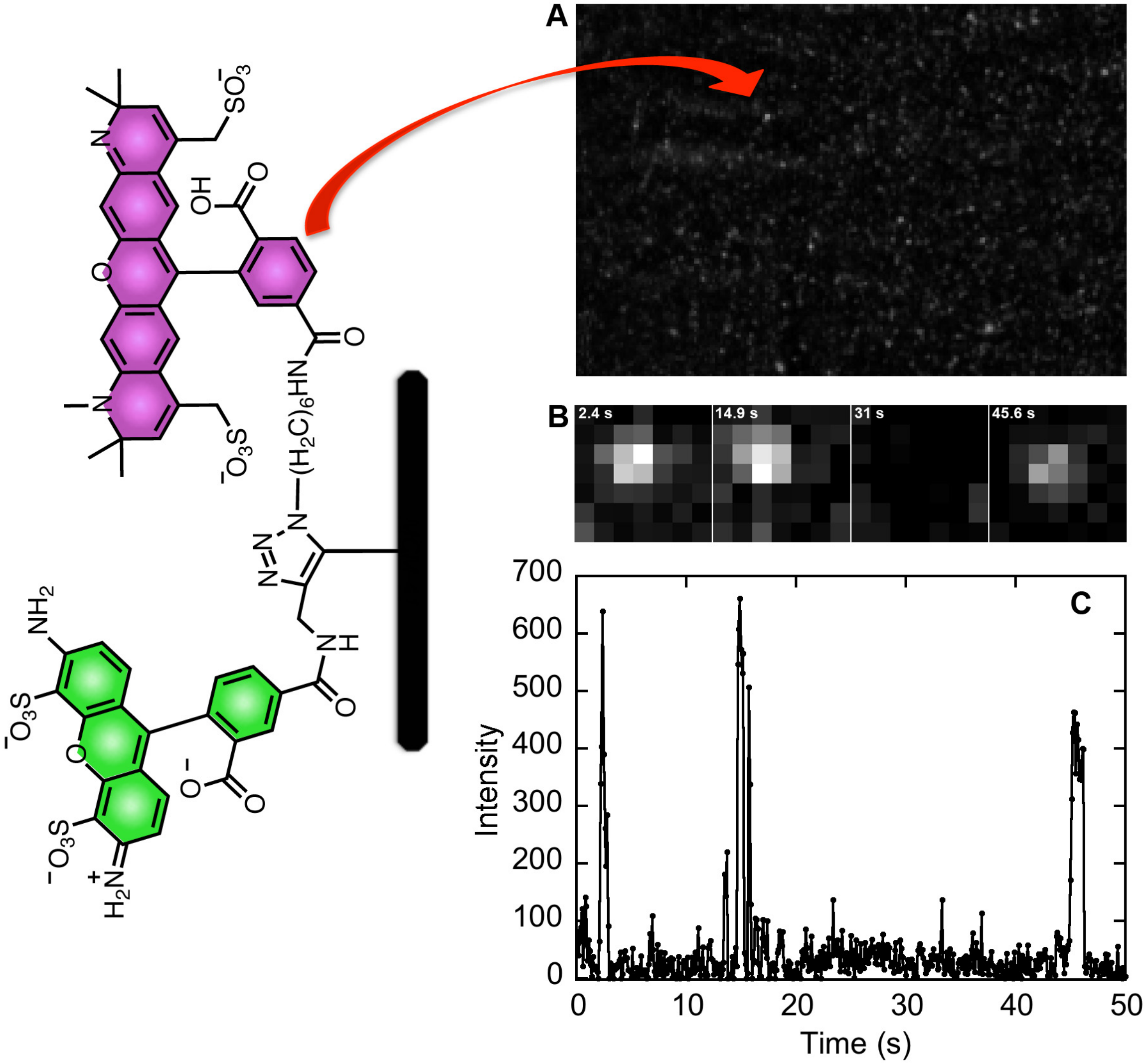

Figure 4–16. Cu/C catalyzed CuAAC of AF488alkyne (**13**) and AF594azide (**14**) to give click product **15** (left panel), and the expanded TIRFM image showing spots of AF594azide-derived emission resulting from energy transfer between 1,2,3-triazole conjugated donor and acceptor (**A**). Time-correlated still frame images of a 1.12 um^2 area around a bursting event (**B**), and the corresponding fluorescence intensity vs. time trajectory of this area (**C**).

The images in **Figure 4–16B** are time-correlating still-frame images from the TIRF video showing pixilated areas corresponding to bursting events depicted in the trajectory plot. Superposition of the white-light image of the catalyst on the coverslip with the accumulated TIRF image allows for mapping CuAAC reactivity of the Cu/C catalyst within the focal area. This will be discussed in more detail in the next sub-section.

4.3.5 Single-molecule localization microscopy reactivity mapping

The previous section showed single-molecule CuAAC of alkyne **13** and azide **14** catalyzed by commercial Cu/C at diffraction-limited resolution. By post-imaging processing of the raw microscopy data, the PSFs of bursting events in the TIRFM video can be fit with Gaussian distributions to localize the central position of the PSF. Details of the fitting routine are outlined in the upcoming experimental section. An example of PSF fit with a 2D Gaussian function and a 3D representation showing the intensity profile of the fitted PSF can be seen in **Figure 4–17**. The fitting routine identifies bursts as a region of bright pixels over a dark background, and fits the surrounding area with a 2D Gaussian function based on an estimate of the point spread function determined from imaging parameters.[70] The centre of each fitted Gaussian fitted PSF is determined and list of localized positions is generated. With the precise central position of all identified PSF known, a super-resolution image of the TIRFM image was reconstructed by accumulating all of the localizations into a single image with enhanced pixel resolution. The diffraction unlimited super-resolution reconstruction of a 4.2 x 5.4 μm area around a Cu/C catalyst particle is shown in **Figure 4–18C3**, and compared to the diffraction limited TIRFM image in **Figure 4–18C1**. Superposition of the diffraction limited white-light image of this region with super-resolution reconstruction allows for mapping the CuAAC reactivity on the catalyst particle (**C4**) with greatly enhanced resolution compared to the standard TIRFM image (**C2**). This effect is truly epitomized with 3D representations of the intensity of each of these images (**D1-4**). Bursting was confirmed by measuring the intensity vs. time of the bright event (**Figure 4–18B**).

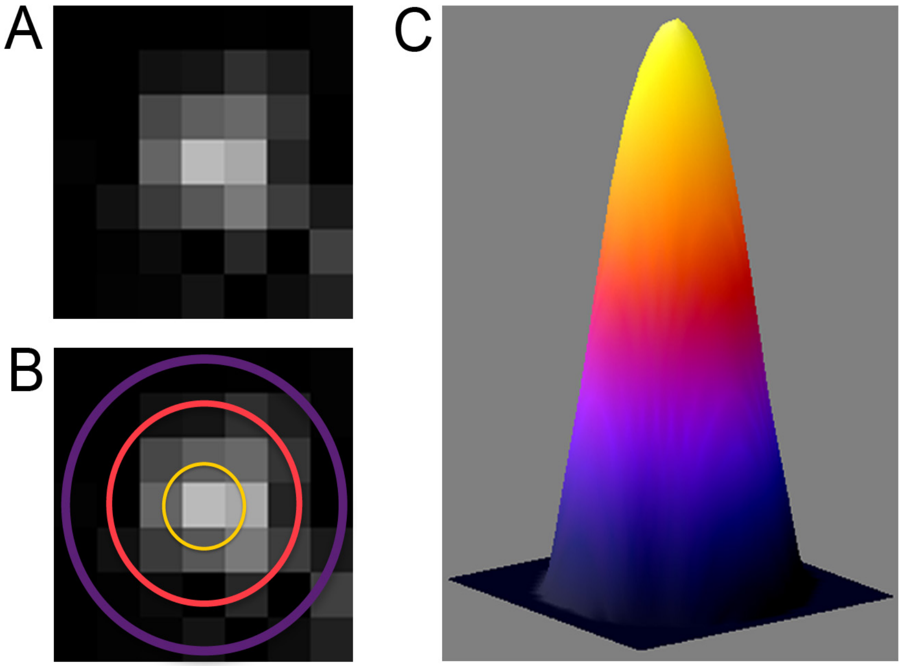

Figure 4–17. Fitting the point spread function of a bursting event with a PSF. Expanded still-frame image of a bursting event from the TIRFM video of a solution of 100 pM **13**, 100 pM **14**, and 1 nM Et_3N (**A**). The same still-frame image showing a 2D Gaussian function fit to the PSF (**B**), and a 3D representation of the Gaussian fit PSF showing the central position (**C**). Each image represents a 1.12 μm^2 area.

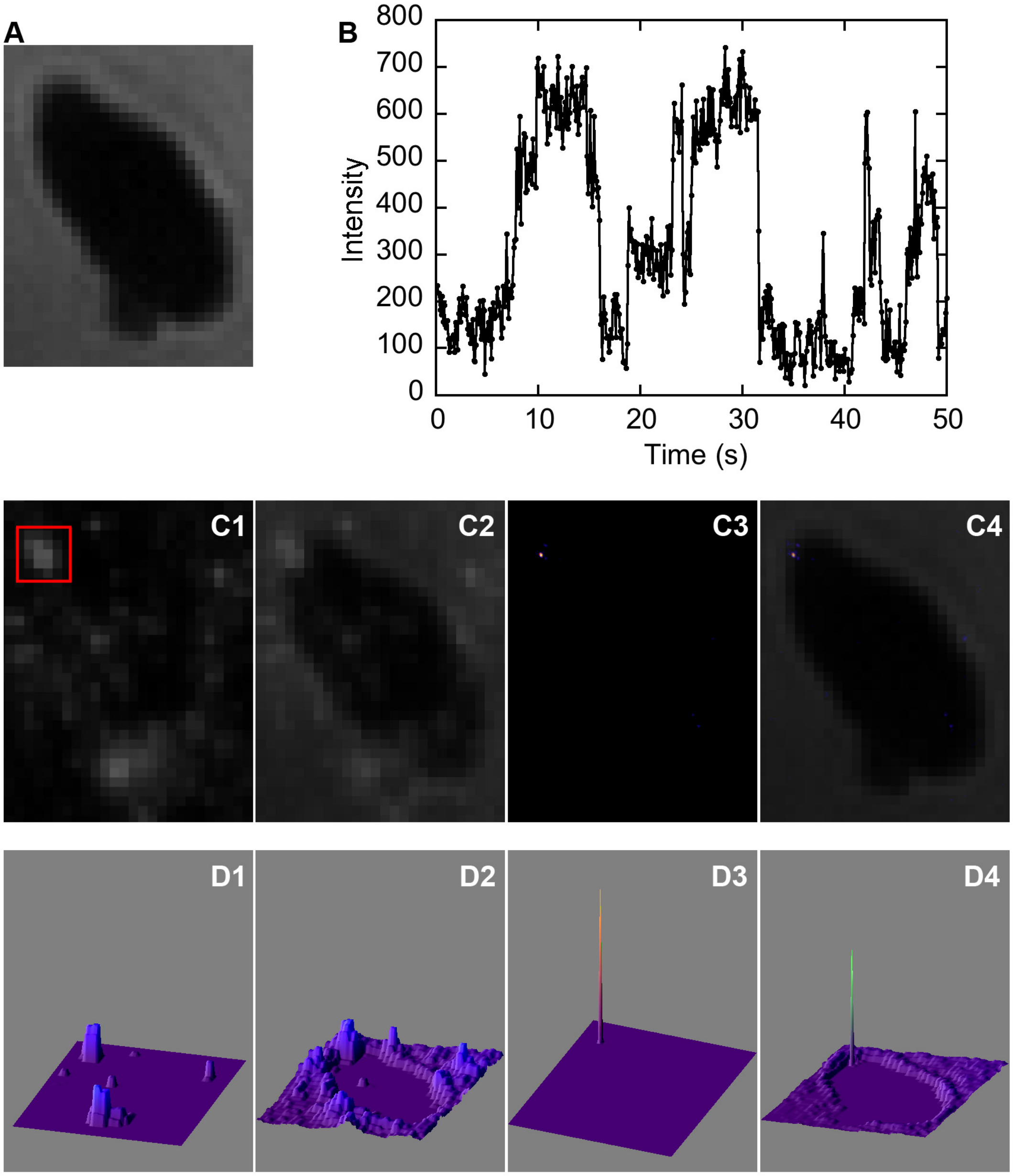

Figure 4–18. A. White-light image of a piece of Cu/C catalyst. **B.** Fluorescence intensity vs. time trajectory of the region on the catalyst highlighted with a red box. Expanded accumulated TIRF image (**C1**), the TIRF image overlaying the white light image of the catalyst (**C2**), and the respective 3D representations of these images (**D1-2**). The reconstructed super-resolution image of the same region of the TIRFM video (**C3**), the SR image overlaying the white light image (**C4**), and the respective 3D representations of these images (**D3-4**). Each image represents a 4.2 x 5.4 µm area. The pixel size is 160 nm C/D 1-2, and 20 nm for C/D 3-4.

The approximation to a Gaussian function allows for measuring the FWHM (full-width at half-maximum) to determine the standard deviation, σ, which is commonly used as a measure of the localization precision of a fitted PSF with the following equation where n is the number of estimates of $x_{p,i}$ and $\overline{x_p}$ is the mean of the measured position coordinates.[71]

$$\sigma_x = \sqrt{\frac{1}{n-1}\sum_{i=1}^{n}(x_{p,i} - \overline{x_p})^2} \qquad \textbf{(4-3)}$$

Using this method the precision of each fitted location was determined and plotted in **Figure 4–19**. It was determined that the average precision of the Gaussian fits was 19 nm.

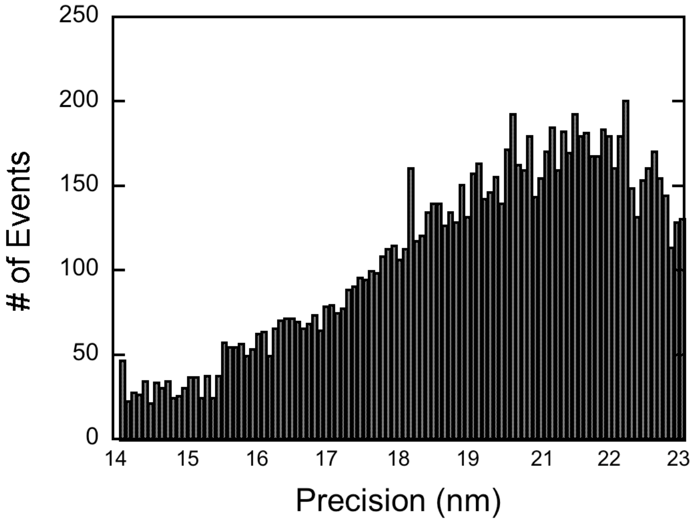

Figure 4–19. Plot of the precision of Gaussian fits and the number of events fitted with each precision.

4.3.6 Single-molecule fluorescence microscopy control reactions

To confirm observed bursting is in fact due to energy transfer from AlexaFluor 488 to AlexaFluor 594 acceptor as a result of copper catalyzed triazole formation on the surface of Cu/C catalyst a number of control reactions were performed (**Figure 4–20**). No bursting events were observed when a solution of AlexaFluor dyes was imaged with no catalyst was present, or when activated carbon without copper was used as catalyst. Likewise, imaging solutions containing only the donor and only the acceptor proved that both reagents are necessary for bursting to occur.

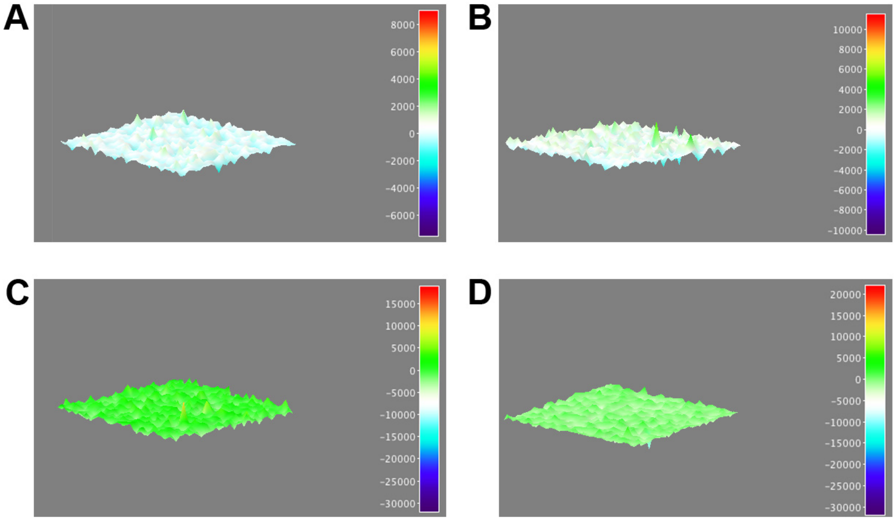

Figure 4–20. 3D projections of control TIRFM control reactions calculated by subtracting the accumulated intensity of the last half of the video from the first half. A solution of 100 pM AF dyes and 1 nM Et_3N imaged without catalyst (**A**), and the same solution imaged over G60 activated carbon without Cu (**D**). A solution of alkyne and 1 nM Et_3N without AF594 azide imaged over Cu/C (**B**), and a solution of azide with 1 nM Et_3N without AF488 alkyne imaged over Cu/C (**C**).

4.4 Discussion

The results in section 4.2 demonstrate a novel method for mapping reactivity between an alkyne modified BODIPY probe and small thiolate stabilized CuNPs supported on MCM-41. The improved signal from the BODIPY chromophore allowed for detection of Cu-acetylide formation over relatively high levels of light scattering from the support material. Reaction between the alkyne probe and CuNPs on the support surface was confirmed by analysis of the bursting events resulting from TIRF excitation of a solution of BODIPY alkyne **17** flowed over CuNP@MCM-41 catalyst particles. Conversely, when the same experiment was repeated with a solution of azide **18**, no emissive bursts were observed, thus bursting is not a result of non-selective interaction of the BODIPY fluorophore with the catalyst. As the irradiation intensity decays exponentially from the point of total internal reflectance, effectively, only the area within approximately 100 nm of the glass coverslip surface receives laser irradiation, thus any emission detected originates only from dyes on particles near the glass surface. Since emissive bursting was observed in the case of the alkyne and not the azide and only in the presence of CuNPs, this is confirmatory evidence that the alkyne coordinates to Cu on the surface of the nanoparticle in the first step of the reaction, in a similar fashion to colloidal CuAAC catalysts. This observation also indicates that organoazide interaction with Cu-acetylide is strongly favored over the free Cu center, in agreement with computational and experimental reports on the involvement of Cu-acetylides in click chemistry.[63, 64, 72, 73] When an organoazide coordinates to a Cu-acetylide complex, the formation of the first C-N bond is driven by synergistic electrophilic activation of the azide and nucleophilic activation of the alkyne. Therefore, by using MCM-41 as a support, the reaction can be readily mapped to the CuNP on it, suggesting that the mechanistic details observed with colloidal nanoparticles in chapter 3 also apply to supported systems that have the practical advantage of catalyst separation after reaction.

To enable observation and reactivity mapping of complete catalytic CuAAC turnovers and catalytic generation of triazole products on the surface of a heterogeneous copper catalyst a new catalyst and probe system was adopted. The same AlexaFluor triazole FRET activation system developed in Chapter 3 with immobilized colloidal CuNPs was successfully applied to the supported heterogeneous catalyst copper-in-charcoal. Irradiating a solution of alkyne modified donor **13**, azide modified acceptor **14** and triethylamine with 488 nm TIRF excitation focused on a coverslip coated with Cu/C resulted in emissive bursting events that mapped the cycloaddition reactivity of the catalyst. The resolution of this mapping is dramatically increased beyond the diffraction limit by fitting the point-spread functions of observed bursts with 2D Gaussians, the centre of which was determined to sub-diffraction precision. Lack of bursting in a series of control reactions (**Figure 4–20**) signifies that the emission observed in the presence of both AF488 and 594 with Cu/C can definitively be attributed to triazole formation between the azide and alkyne allowing energy transfer to occur enabling emission from the 594 acceptor.

While use of the dark Cu/C catalyst resulted in a significant decrease in observed light scattering compared to Cu@MCM-41, a few persistent bright spots could still be observed in the diffraction limited TIRF image. The bright spot near the bottom centre of the TIRF image in **Figure 4–18C1** is an example of persistent bright spots due to scattering. The intensity vs. time trajectory (appendix **Figure A4-1**) measured for this spot confirms that the spot is due to scattering rather than catalytically generated product formation. This bright spots and others like it appear in accumulated TIRF images because the CCD pixels are constantly recording fluctuating signal, but are eliminated from the super-localization image reconstructed from the fitted spot localizations. The PSFs of these spots often exhibit too low signal-to-noise or are too broad to fit to the Gaussian function determined from the estimated PSF of a point source emitter. With spots arising from scattering filtered out, super-positioning the fitted localizations over white-light images of the catalyst precisely maps the reactivity, and thus the location of Cu(I) on the carbon surface of the catalyst material. Since the centre location of the Gaussian function can be determined with greater precision than the 160 nm pixel size of our instrument this mapping image can be reconstructed at much higher pixel resolution. The super-resolution images in **Figure 4–18** have been reconstructed with 20 nm pixels.

It is also noteworthy to compare super-resolution mapping information of this material with that obtained from electron microscopy. The SEM images we recorded as well as those reported by Lipshutz *et al.* are too convoluted to draw any solid conclusion about the location of Cu on the material surface. Moreover, if any copper is actually detectable in electron micrographs, its is impossible to differentiate between CuAAC active Cu(I) and inactive Cu(II). Super-localization analysis of fluorescence microscopy images allows for the precise localization of the catalytically active Cu(I) species. While the approach described herein draws on previous examples by authors such as Hofkens, Roeffaers, and Chen an important distinction must be drawn that separates our approach from the excellent work of these scientists. Although only Roeffaers and Hofkens utilize the term NASCA, all super-resolution heterogeneous catalysis investigations in literature apply the same concept of using stochastic catalytic generation of emissive products to identify location of catalysis. Close inspection of each example reveals that every system is designed with a specific reaction in mind with dyes designed to modulate emission upon catalytic conversion to products. The pitfall of this design is that observed signal is a direct result of chemical reaction investigated thus super-localization reconstruction also depends directly on the chemistry. In contrast, with our approach super-localization is not a direct result of the chemistry we are studying, but rather a result of energy transfer caused by catalytic reactions bringing together FRET donor and acceptor dyes. This generates a significant distinction between the two methodologies as the approach taken by researchers such as Hofkens and Chen requires development of an entirely new probe system for each reaction of interest, while our approach is much more easily adaptable to studying different chemical systems simply by changing the functional groups labeled on FRET dyes.

4.5 Summary

Herein, a method to map Cu-acetylide formation of a alkyne modified BODIPY probe with CuNPs supported on the surface of MCM-41 particles using total internal reflection fluorescence single-molecule microscopy was described. This methodology was adapted to mapping complete catalytic conversion of the copper catalyzed click reaction of an alkyne labeled donor dye and an azide labeled acceptor dye by copper species on the surface of a commercial heterogeneous catalyst. Catalytic triazole formation brings donor and acceptor dyes within proximity to allow energy transfer manifesting acceptor emission at the location of catalysis, generating a reactivity map.

Although the specific example using catalytic CuAAC reactions to map the location of Cu(I) on an activated carbon support was described here, this super-resolution methodology can be applied as a general approach to mapping any heterogeneous catalytic system. Conceptually, this method can be applied to the investigation of any catalytic bimolecular reaction through the design of functionalized dyes that are able to participate in energy transfer processes as a result of catalytic reaction. It is also noteworthy that super-localization images created using this method enable visualization of the catalyst material under *in-operando* conditions, *i.e.* the normal working conditions of the catalyst. This fact should not be understated since it has a direct impact on research towards the rational and intelligent optimization of a catalyst material.

4.6 Experimental Details

All chemicals were purchased from Sigma-Aldrich or Fisher Scientific with the exception of AlexaFluor 488 alkyne and AlexaFluor 594 azide, which were purchased from Molecular Probes (Life Technologies). Nanoparticulate copper in charcoal (3 wt. %) was purchased from Sigma-Aldrich (product # 709107). All chemicals were used as received without further purification. Water was purified by passing it through a sub-micron filter with a Millipore MilliQ system (resistivity of 18.2 MΩ). All reactions were monitored by thin-layer chromatography, using aluminum sheets coated with silica (60, F_{254}). NMR spectra were recorded at room temperature with a Bruker Avance 300 and chemical shifts were referenced with the residual proton or carbon signal of the deuterated solvent. High-resolution mass spectra were acquired on a HRES, EI, Concept S1, Magnetic Sector mass spectrometer and Electrospray Ionization mass spectra were acquired on a Micromass Q-TOF mass spectrometer.

All mass spectrometry was conducted in the John L. Holmes Mass Spectrometry Facility at the Department of Chemistry, University of Ottawa.

4.6.1 Synthesis

The synthesis of BODIPY-COOH, BODIPY-decylbromide and BODIPY-Azide was graciously performed by S. Impellizzeri. Experimental information for the synthesis of these compounds is provided in Chapter 3.

(MCM-41) – MCM-41 synthesis was adapted from a literature procedure.[62] Briefly, hexadecyltrimethylammonium bromide (C_{16}TAB, 4.4 g, 12 mmol) was dissolved in 400 mL distilled water with stirring. Ammonium hydroxide (NH_4OH; 19.2 mL, 141 mmol) was added after 30 minutes of stirring, followed by addition of tetraethyl orthosilicate (TEOS; 23.3 mL, 100 mmol) and stirring was continued for 1 hour. The gel was transferred to a Teflon-lined autoclave bottle and placed in an 80°C oven for 24 hours. After cooling to room temperature the mixture was vacuum filtered and the resulting solid was washed with distilled water and ethanol consecutively followed dried at 60°C overnight. Finally, the dried material was calcined at 550°C for 8 hours with a ramp of 2°C/min. The product was collected as a powdery white solid.

(MCM-41-APTES) – Following activation in a 200 °C for 2 hours, MCM-41 (1 g) was suspended in 50 mL anhydrous toluene and APTES (466 μL, 2 mmol) was added with stirring. The mixture was refluxed for 12 hours, at which time the hot mixture was filtered and washed with toluene (3 x 50 mL). The resulting residue was dried in a 60°C oven overnight and the pure MCM-41-APTES was collected as a powdery white solid.

(CuNP) – The synthesis of thiolate-stabilized colloidal nanoparticles based on a modified literature[74] was reported in the experimental section of Chapter 3.

(CuNP@MCM-41) – The supported copper catalyst CuNP@MCM-41 was prepared by stirring a solution of CuNP (1 mg, 30% w/w) in CH_2Cl_2 with MCM-41 for 2 hours before precipitation by centrifugation at 3500 rpm, and washed successively with CH_2Cl_2 and EtOH. The product was collected by centrifugation and dried under vacuum in a desiccator.

(azido-BODIPY) – Synthesized according to a literature procedure.[52]

(BODIPY-Alkyne) – A solution of DCC (103 mg, 0.5 mmol) in CH_2Cl_2 (5 mL) was added dropwise over the course of 20 min to a solution of BODIPY-COOH (141 mg, 0.38 mmol), 10-undecyn-1-ol (88.3 μL, 0.46 mmol), and DMAP (9.4 mg, 77 μmol) in

CH_2Cl_2 (25 mL) maintained at 0 °C under Ar. After stirring for 1 hour at 0 °C, the reaction mixture was allowed to warm to ambient temperature and was stirred for 18 h under these conditions. The precipitate was filtered off, and the solvent was distilled off under reduced pressure. The residue was purified by column chromatography [SiO_2: Hexanes-$MeCO_2Et$ 9:1 (v/v) to $MeCO_2Et$-CH_3OH 9:1 (v/v) gradient eluent] to afford the product (34 mg, 17%) as an iridescent orange solid. EI-HRMS: calc'd *m/z* $[M]^+$: 518.2916, found: 518.2928. ^1H NMR (300 MHz, $CDCl_3$): 8.18 (2H, d, 8.7 Hz), 7.40 (2H, d, 8.7 Hz), 5.99 (2H, s), 4.36 (2H, t, 6.5 Hz), 2.56 (6H, s), 2.19 (2H, dt, 2.6Hz, 6.9 Hz), 1.93 (1H, s, 2.6 Hz), 1.81 (2H, m), 1.30-1.50 (18H, m). ^{13}C NMR (300 MHz, $CDCl_3$): 165.9, 156.0, 143.0, 140.4, 139.6, 131.0, 130.9, 130.3, 128.3, 121.5, 84.8, 68.1, 65.4, 29.3, 29.2, 29.0, 28.7, 28.4, 26.0, 18.4, 14.6, 14.5.

4.6.2 Spectroscopy

All spectroscopic measurements were performed in spectroanalyzed grade ethanol (BODIPYs) or MilliQ sub-micronfiltered water (AlexaFluors). UV-VIS Absorption spectra were recorded on a Agilent Cary-50 Spectrophotometer which was zeroed before sample measurement and spectra were baseline subtracted by measuring the pure solvent. Fluorescence emission spectra were collected with a luminescence spectrometer from Photon Technology International (PTI).

4.6.3 Microscopy sample preparation

Glass coverslips (25 mm, Fisher) were cleaned and APTES treated before use as outlined in Chapter 3 section 3.6. Supported CuNP microscopy samples (Cu@MCM-41 or Cu@C) were prepared by spin coating at 1200 rpm 50 µL of a suspension of the supported catalyst in EtOH (1 mg/mL) onto piranha cleaned glass coverslips.

4.6.4 TIRFM image acquisition

TIRFM instrument and image acquisition details have been reported in Chapter 3 section 3.7.

4.6.5 TIRFM Image analysis

Details on the TIRFM image analysis routine have been reported in Chapter 3 section 3.7.

4.6.6 Super-resolution image analysis

Super-resolution imaging was performed using freely available PeakFit software operating as an ImageJ plugin. PeakFit uses an implentation of the data processing routine created for *d*STORM analysis by Wolter *et al.*[70] summarized in **Figure 4–21**. Briefly, An estimation of the PSF width was determined from imaging parameters, and further tuned by reiterative fitting the image until convergence. Noise reduction of raw microscope videos was performed by smoothing with a mean filter with using a patch size of 3 times the PSF half-width at half-maximum (HWHM). Fluorescent bursting events were first identified as maxima in the smoothed image using a built in peak finding algorithm, and subsequently fit to a 2-dimensional Gaussian using the non-linear least squares Levenberg-Marquardt method. Fitted spots were filtered using signal-to-noise, width and coordinate shift criteria to eliminate peaks that were too wide or of low intensity. From the list of peak localizations generated, a super-localization reconstruction image of the bursting events was created using 20 nm as the pixel size.

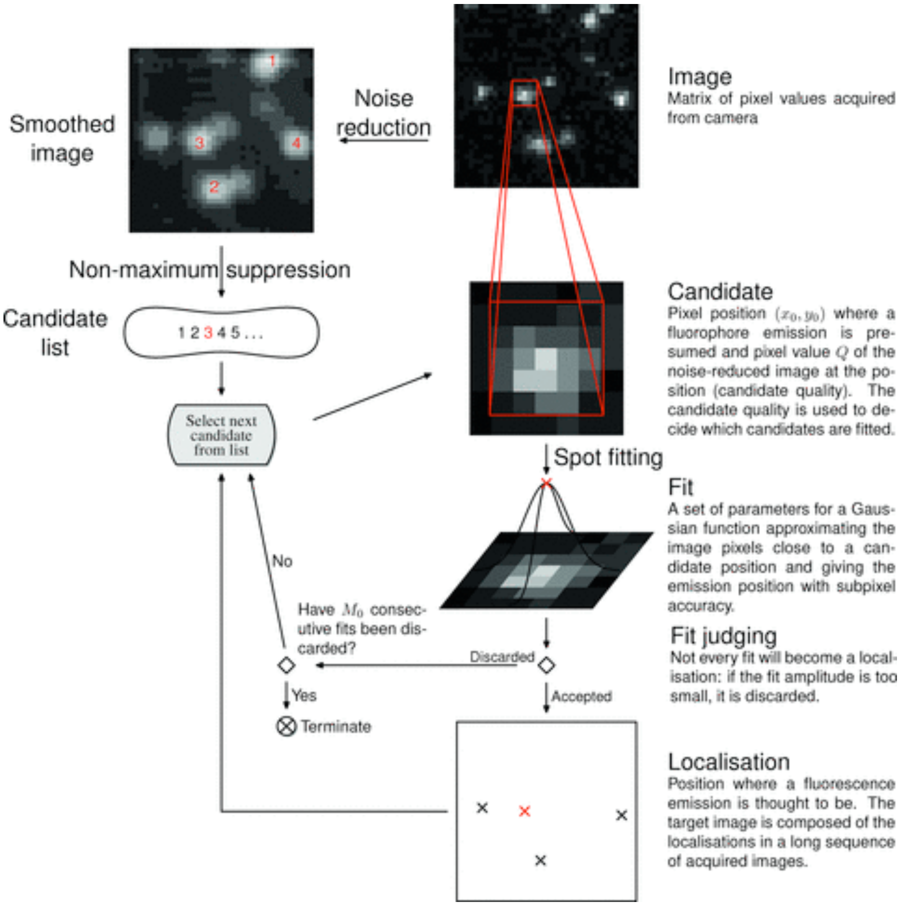

Figure 4–21. Visualization of the rapid data processing scheme for photoswitching microscopy. From top to bottom, the data are processed from raw image form to a set of likely candidates for emission positions (spots), fitted by a Gaussian point spread function model and, given that this fit yields acceptable values, considered localizations. These localizations can be visualized in a result image or analyzed quantitatively. Reproduced with permission from Wolter *et al.*[70]

4.7 References

1. Serp, P. & Philippot, K. (eds.) *Nanomaterials in Catalysis*, Edn. First. (Wiley-VCH Verlag GmbH & Co. KGaA, Weinheim, Germany; 2013).
2. Roucoux, A., Schulz, J. & Patin, H. Reduced Transition Metal Colloids: A Novel Family of Reusable Catalysts? *Chem. Rev.* **102**, 3757-3778 (2002).
3. Buurmans, I.L.C. & Weckhuysen, B.M. Heterogeneities of individual catalyst particles in space and time as monitored by spectroscopy. *Nat. Chem.* **4**, 873-886 (2012).
4. Janssen, K.P.F. *et al.* Single molecule methods for the study of catalysis: from enzymes to heterogeneous catalysis *Chem. Soc. Rev.* **43**, 990-1006 (2014).
5. Abbe, E. Contributions to the theory of the microscope and microscopic detection (Translated from German). *Arch. Mikroskop. Anat.* **9**, 413-468 (1873).
6. Abbe, E. The relations of aperture and power in the microscope. *J. Roy. Micro. Soc.* **2**, 300-309 (1882).
7. Cusido, J., Impellizzeri, Stefania, Raymo, Francisco, M. Molecular Strategies to read and write at the nanoscale with far-field optics. *Nanoscale* **3**, 59-70 (2011).
8. Thompson, R.E., Larson, Daniel R., and Webb, Watt W. Precise Nanometer Localizartion Analysis for Individual Fluorophore Probes. *Biophys. J.* **82**, 2775-2783 (2002).
9. Sahl, S.J. & Moerner, W.E. Super-resolution fluorescence imaging with single molecules. *Curr. Opin. Struct. Biol.* **23**, 778-787 (2013).
10. Han, R.C., Li, Z.H., Fan, Y.Y. & Jiang, Y.Q. Recent Advances in Super-Resolution Fluorescence Imaging and Its Applications in Biology. *J. Genet. Genomics* **40**, 583-595 (2013).
11. Herbert, S., Soares, Helena, Zimmer, Christophe. and Henriques, Ricardo Single-Molecule Localization Super-REsolution MIcroscopy: Deeper and Faster. *Microsc. Microanal.* **18**, 1419-1429 (2012).
12. Toraldo di Francia, G. Resolving Power and Information. *J. Opt. Soc. Am.* **45**, 497-501 (1955).
13. Cox, I.J. & Sheppard, C.J.R. Information Capacity and Resolution in an Optical-System. *J. Opt. Soc. Am. A* **3**, 1152-1158 (1986).
14. Bobroff, N. Position Measurement with a Resolution and Noise-Limited Instrument. *Rev. Sci. Instrum.* **57**, 1152-1157 (1986).
15. Cheezum, M.K., Walker, W.F. & Guilford, W.H. Quantitative comparison of algorithms for tracking single fluorescent particles. *Biophys. J.* **81**, 2378-2388 (2001).

16. Zhang, B., Zerubia, J. & Olivo-Marin, J.-C. Gaussian approximations of fluorescence microscope point-spread function models. *Appl. Opt.* **46**, 1819-1829 (2007).
17. Hell, S.W. & Wichmann, J. Breaking the Diffraction Resolution Limit by Stimulated-Emission - Stimulated-Emission-Depletion Fluorescence Microscopy. *Opt. Lett.* **19**, 780-782 (1994).
18. Klein, T., Proppert, S. & Sauer, M. Eight years of single-molecule localization microscopy. *Histochem. Cell Biol.* (2014).
19. Betzig, E. *et al.* Imaging intracellular fluorescent proteins at nanometer resolution. *Science* **313**, 1642-1645 (2006).
20. Rust, M.J., Bates, M. & Zhuang, X. Sub-diffraction-limit imaging by stochastic optical reconstruction microscopy (STORM). *Nat. Methods* **3**, 793-795 (2006).
21. Heilemann, M. *et al.* Subdiffraction-resolution fluorescence imaging with conventional fluorescent probes. *Angew. Chem. Int. Ed.* **47**, 6172-6176 (2008).
22. Sharonov, A. & Hochstrasser, R.M. Wide-field subdiffraction imaging by accumulated binding of diffusing probes. *P. Natl. Acad. Sci. USA* **103**, 18911-18916 (2006).
23. Cang, H. *et al.* Probing the electromagnetic field of a 15-nanometre hotspot by single molecule imaging. *Nature* **469**, 385-388 (2011).
24. Walder, R., Nelson, Nathaniel, and Schwartz, Daniel K. Super-resolution surface mapping using the trtajectories of molecular probes. *Nat. Commun.* **2**, 515 (2011).
25. Roeffaers, M.B.J. *et al.* Super-Resolution Reactivity Mapping of Nanostructured Catalyst Particles. *Angew. Chem. Int. Ed.* **48**, 9285-9289 (2009).
26. De Cremer, G., Sels, Bert F., De Vos, Dirk E., Hofkens, Johan, Roeffaers, Maarten B. J. Fluorescence micro(spectro)scopy as a tool to study catalytic materials in action. *Chem. Soc. Rev.* **39**, 4702-4717 (2010).
27. Dertinger, T., Colyer, R., Iyer, G., Weiss, S. & Enderlein, J. Fast, background-free, 3D super-resolution optical fluctuation imaging (SOFI). *P. Natl. Acad. Sci. USA* **106**, 22287-22292 (2009).
28. Burnette, D.T., Sengupta, P., Dai, Y., Lippincott-Schwartz, J. & Kachar, B. Bleaching/blinking assisted localization microscopy for superresolution imaging using standard fluorescent molecules. *P. Natl. Acad. Sci. USA* **108**, 21081-21086 (2011).
29. Requejo-Isidro, J. Fluorescence nanoscopy. Methods and applications. *J. Chem. Biol.* **6**, 97-120 (2013).
30. Hell, S.W. Toward fluorescence nanoscopy. *Nat. Biotechnol.* **21**, 1347-1355 (2003).
31. Gustafsson, M.G.L. Surpassing the lateral resolution limit by a factor of two using structured illumination microscopy. *J. Microsc.* **198**, 82-87 (2000).

32. Gustafsson, M.G.L. Nonlinear structured-illumination microscopy: Wide-field fluorescence imaging with theoretically unlimited resolution. *P. Natl. Acad. Sci. USA* **102**, 13081-13086 (2005).
33. Chen, P. *et al.* Single-molecule fluorescence imaging of nanocatalytic processes. *Chem. Soc. Rev.* **39**, 4560-4570 (2010).
34. Chen, P. *et al.* Spatiotemporal catalytic dynamics within single nanocatalysts revealed by single-molecule microscopy. *Chem. Soc. Rev.* **43**, 1107-1117 (2014).
35. Cordes, T. & Blum, S.A. Opportunities and challenges in single-molecule and single-particle fluorescence microscopy for mechanistic studies of chemical reactions. *Nat. Chem.* **5**, 993-999 (2013).
36. Hell, S.W. Far-Field Optical Nanoscopy. *Science* **316**, 1153-1158 (2007).
37. Hell, S.W. Microscopy and its focal switch. *Nat. Methods* **6**, 24-32 (2009).
38. Roeffaers, M.B.J. *et al.* Spatially resolved observation of crystal-face-dependent catalysis by single turnover counting. *Nature* **439**, 572-575 (2006).
39. Sambur, J.B. & Chen, P. Approaches to Single-Nanoparticle Catalysis. *Annu. Rev. Phys. Chem.* **65**, 395-422 (2014).
40. De Cremer, G. *et al.* High-Resolution Single-Turnover Mapping Reveals Intraparticle Diffusion Limitation in Ti-MCM-41-Catalyzed Epoxidation. *Angew. Chem. Int. Ed.* **49**, 908-911 (2010).
41. Tachikawa, T., Yamashita, S. & Majima, T. Probing Photocatalytic Active Sites on a Single Titanosilicate Zeolite with a Redox-Responsive Fluorescent Dye. *Angew. Chem. Int. Ed.* **49**, 432-435 (2010).
42. Tachikawa, T., Yamashita, S. & Majima, T. Evidence for Crystal-Face-Dependent TiO2 Photocatalysis from Single-Molecule Imaging and Kinetic Analysis. *J. Am. Chem. Soc.* **133**, 7197-7204 (2011).
43. Wang, N., Tachikawa, T. & Majima, T. Single-Molecule, single-particle observationof size -dependent photocatalytic activity in Au/TiO2 nanocomposites. *Chem. Sci.* **2**, 891-900 (2011).
44. Bian, Z., Tachikawa, T., Kim, W., Choi, W. & Majima, T. Superior Electron Transport and Photocatalytic Abilities of Metal-Nanoparticle-Loaded TiO2 Superstructures. *J. Phys. Chem. C* **116**, 25444-25453 (2012).
45. Tachikawa, T., Yonezawa, T. & Majima, T. Super-Resolution Mapping of Reactive Sites on Titania-Based Nanoparticles with Water-Soluble Fluorogenic Probes. *ACS Nano* **7**, 263-275 (2013).
46. Zhou, X. *et al.* Quantitative super-resolution imaging uncovers reactivity patterns on single nanocatalysts. *Nat. Nanotechnol.* **7**, 237-241 (2012).
47. Andoy, N.M. *et al.* Single-Molecule Catalysis Mapping Quantifies Site-Specific Activity and Uncovers Radial Activity Gradient on Single 2D Nanocrystals. *J. Am. Chem. Soc.* **135**, 1845-1852 (2013).

48. Zhou, X., Choudhary, E., Andoy, N.M., Zou, N. & Chen, P. Scalable Parallel Screening of Catalyst Activity at the Single-Particle Level and Subdiffraction Resolution. *ACS Catal.* **3**, 1448-1453 (2013).
49. Xu, W. *et al.* Single-Molecule Electrocatalysis by Single-Walled Carbon Nanotubes. *Nano Lett.* **9**, 3968-3973 (2009).
50. Sivakumar, K. *et al.* A fluorogenic 1,3-dipolar cycloaddition reaction of 3-azidocoumarins and acetylenes. *Org. Lett.* **6**, 4603-4606 (2004).
51. Lord, S.J. *et al.* A photoactivatable push-pull fluorophore for single-molecule imaging in live cells. *J. Am. Chem. Soc.* **130**, 9204-+ (2008).
52. Wang, C., Xie, F., Suthiwangcharoen, N., Sun, J. & Wang, Q. Tuning the optical properties of BODIPY dye through Cu(I) catalyzed azide-alkyne cycloaddition (CuAAC) reaction. *Sci. China Chem.* **55**, 125-130 (2012).
53. Montoya, L.A. & Pluth, M.D. Selective turn-on fluorescent probes for imaging hydrogen sulfide in living cells. *Chem. Commun.* **48**, 4767-4769 (2012).
54. Schriven, E.F.V. (ed.) *Azides and Nitrenes: Reactivity and Utility*. (Academic Press, Orlando, Fl.; 1984).
55. McGilvray, K.L., Decan, M.R., Wang, D. & Scaiano, J.C. Facile Photochemical Synthesis of Unprotected Aqueous Gold Nanoparticles. *J. Am. Chem. Soc.* **128**, 15980-15981 (2006).
56. Marin, M.L., McGilvray, K.L. & Scaiano, J.C. Photochemical Strategies for the Synthesis of Gold Nanoparticles from Au(III) and Au(I) Using Photoinduced Free Radical Generation. *J. Am. Chem. Soc.* **130**, 16572-16584 (2008).
57. Scaiano, J.C. *et al.* Photochemical routes to silver and gold nanoparticles. *Pure Appl. Chem.* **81**, 635-647 (2009).
58. Gonzalez, C.M., Liu, Y. & Scaiano, J.C. Photochemical Strategies for the Facile Synthesis of Gold-Silver Alloy and Core-Shell Bimetallic Nanoparticles. *J. Phys. Chem. C* **113**, 11861-11867 (2009).
59. Scaiano, J.C. *et al.* Tuning plasmon transitions and thier applications in organic photochemistry. *Pure Appl. Chem.* **83**, 913-930 (2011).
60. Pacioni, N.L., Pardoe, A., McGilvray, K.L., Chretien, M.N. & Scaiano, J.C. Synthesis of copper nanoparticles mediated by photogenerated free radicals: catalytic role of chloride anions. *Photochem. Photobiol. Sci.* **9**, 766-774 (2010).
61. Pacioni, N.L., Filippenko, V., Presseau, N. & Scaiano, J.C. Oxidation of copper nanoparticles in water: mechanistic insights revealed by oxygen uptake and spectroscopic methods. *Dalton Trans.* **42**, 5832-5838 (2013).
62. Marquez, D.T., Carrillo, A.I. & Scaiano, J.C. Plasmon Excitation of Supported Gold Nanoparticles Can Control Molecular Release from Supramolecular Systems. *Langmuir* **29**, 10521-10528 (2013).
63. Hein, J. & Fokin, V. Copper-catalyzed azide–alkyne cycloaddition (CuAAC) and beyond: new reactivity of copper(I) acetylides. *Chem. Soc. Rev.* **39**, 1302-1315 (2010).

64. Worrell, B.T., Malik, J.A. & Fokin, V.V. Direct Evidence of a Dinuclear Copper Intermediate in Cu(I)-Catalyzed Azide-Alkyne Cycloadditions. *Science* **340**, 457-460 (2013).
65. Lipshutz, B.H., Frieman, B.A. & Tomaso, A.E. Copper-in-Charcoal (Cu/C): Heterogeneous, Copper-Catalyzed Asymmetric Hydrosilylations. *Angew. Chem. Int. Ed.* **45**, 1259-1264 (2006).
66. Lipshutz, B.H., Unger, J.B. & Taft, B.R. Copper-in-Charcoal (Cu/C) Promoted Diaryl Ether Formation. *Org. Lett.* **9**, 1089-1092 (2007).
67. Lipshutz, B.H., Nihan, D.M., Vinogradova, E., Taft, B.R. & Bošković, Ž.V. Copper + Nickel-in-Charcoal (Cu-Ni/C): A Bimetallic, Heterogeneous Catalyst for Cross-Couplings. *Org. Lett.* **10**, 4279-4282 (2008).
68. Lipshutz, B.H. & Taft, B.R. Heterogeneous Copper-in-Charcoal-Catalyzed Click Chemistry. *Angew. Chem. Int. Ed.* **45**, 8235-8238 (2006).
69. Lee, C.-T., Huang, S. & Lipshutz, B.H. Copper-in-Charcoal-Catalyzed, Tandem One-Pot Diazo Transfer-Click Reactions. *Adv. Synth. Catal.* **351**, 3139-3142 (2009).
70. Wolter, S. *et al.* Real-time computation of subdiffraction-resolution fluorescence images. *J. Microsc.-Oxford* **237**, 12-22 (2010).
71. Deschout, H., Zanacchi, Francesca C., Mlodzianoski, Michael, Diaspro, Alberto, Bewersdorf, Joerg, Hess, Samuael T., Braeckmans, Kevin. Precisely and accurately localizing single emitters in fluorescence microscopy. *Nat. Methods* **11**, 253-266 (2014).
72. Ahlquist, M.r. & Fokin, V. Enhanced Reactivity of Dinuclear Copper(I) Acetylides in Dipolar Cycloadditions *Organometallics* **26**, 4389-4391 (2007).
73. Straub, B. μ-Acetylide and μ-alkenylidene ligands in “click” triazole syntheses. *Chem. Commun.*, 3868 (2007).
74. Rance, G., Solomonsz, W. & Khlobystov, A. Click chemistry in carbon nanoreactors. *Chem. Commun.* **49**, 1067-1069 (2013).

5. Conclusions and Outlook

5.1 Conclusions

The work described in this thesis was derived from two main inspirations; first the elegant reactivity and extreme diversity of the CuAAC reaction and secondly (but of questionable greater significance) the power that single-molecule microscopy holds if one has the interdisciplinary skill set to direct that power to the study of single-catalytic turnovers.

The second chapter of this thesis explores the viability of the CuAAC reaction as a synthetic tool. Ample precedent has laid the groundwork for use of the CuAAC formed triazole as a structural building block in synthetic chemistry. We extend upon this in creating a small library of aqueous metal cation sensors in which the triazole moiety not only plays a crucial structural role linking fluorophore and ionophore, but also participates in transduction of signal from its generation upon analyte binding in the ionophore to the emission of signal from the fluorophore.

'Clicking' the same 7-azidocoumarin fluorophore with different ionophores varying in size and heteroatom identity we created three unique fluorescent sensors each sensitive for a different metal cation (**Scheme 2-2**). Sensor **1** with 1-aza-18-crown-6 ionophore selectively binds K^+ over other cations, even in a large excess of Na^+, which typically can be a problem cation for potassium sensors. Sensor **2** exhibits a cyclam ionophore lending to its excellent selectivity for Zn^{2+} over other metals, while sensor **3** is largely selective for Hg^{2+}, but also responds minimally to Zn^{2+} and

Cu^{2+}. Sensor **3** features an interesting two-stage sensing range, switchable with the addition of KOH. In the absence of KOH the emission of **3** increases with the addition of increasing amounts of Hg^{2+} in the range of 0-200 μM; this concentration range is extended to ~ 1 mM Hg^{2+} when KOH is added to the solution, resulting in an astounding 70-fold emission enhancement.

We also measured the photophysical properties of the coumarin chromophore using K^+ selective sensor **1** and reported the values in **Table 2-1**; notably the quantum yield of fluorescence was determined to vary with different solution environments. With **1** alone in water, Φ was measured to be 0.72, in Na_2HPO_4 buffered solution it was found to be 0.12, and increased to 0.56 with addition of KOAc. While these values were recorded only for sensor **1**, by extension they are likely very similar for the other two sensors (**2** and **3)** as all three sensors feature the same linkage of coumarin chromophore conjugated to a tertiary amine through a 1,4-substituted triazole.

With the use of nanomaterials in catalysis rapidly exploding from proof-of-concept examples to becoming 'the new face of catalysis', we saw the incredible power of single-molecule microscopy as an opportunity to investigate catalysts beyond conversions, turn-over numbers, and isolation of intermediates by examining catalytic reactions in real time at the single-molecule – single-catalytic nanoparticle level. We sought to provide a methodology to answer the recurrent question of whether a heterogeneous nanomaterial catalyst acts truly heterogeneously or as a catalyst reservoir via leaching of the true active homogenous species. Chapter 3 describes the TIRFM based methodology we developed in order to answer this question using CuNP catalyzed CuAAC cycloaddition click reaction as a model. This system uses the 1,2,3-triazole ring formed during click reaction to bring in close proximity an alkyne labeled FRET donor dye (AlexaFluor 488, **13**) and an azide labeled FRET acceptor dye (AlexaFluor 488, **14**) enabling detection of CuAAC catalysis at the CuNP surface by recording acceptor emission though FRET transfer from the excited donor.

We demonstrated in chapter 3 that stochastic bursting repeats itself in the same location, thus a nanoparticle is at this location catalyzing the conjugation of alkyne **13** and azide **14**. We were also able to show that alkyne **13** forms a Cu-acetylide complex with a CuNP in the same location as generation of triazole product **15** was observed solidifying that catalytic activity is in the heterogeneous phase rather than homogeneous via Cu(I) ions leached from the nanomaterial. Although immobilization on a glass substrate heterogenizes the nanoparticles in this work, this experimental design detracts from the real benefits of heterogeneous catalysis, that is, easy separation from the reaction medium and reusability. The work described in Chapter 4 bridges the gap between nanomaterial colloids and immobilization on a glass coverslip by investigating the single-molecule CuAAC reaction between **13** and **14** catalyzed by a commercial heterogeneous copper on activated carbon catalyst. The copper in this catalyst, which was developed by

Lipshutz and commercialized by Sigma-Aldrich, exists in both Cu(I) and Cu(II) oxides although only Cu(I) sites are catalytically active. Differentiation of these two oxidation states is very difficult using traditional characterization techniques (**Figures 4-14** and **4-15**), however, by observing the CuAAC reaction of **13** and **14** in real time with single-molecule TIRF super-resolution microscopy we are able to map the activity of the catalyst (**Figure 4-18**) beyond the diffraction limit, deciphering the location of active Cu(I) species.

A separate set of experiments described in Chapter 4 compare the affinity of CuNP for alkyne and azide substrates through single-molecule investigation of BODIPY dyes **17** and **18**, which only differ by functionality at terminal end of a long carbon tether, one alkyne and the other azide modified, respectively. Single-molecule mapping of BODIPY-alkyne (**17**) and BODIPY-azide (**18**) interaction (or lack thereof) with heterogeneous catalyst CuNP@MCM-41 is direct confirmatory evidence that Cu-acetylide formation occurs before azido nitrogen attack on the alkynyl C-C bond.

As highlighted in **Figure 3-2**, to date only a handful of unique chemical reactions have been explored with single-molecule spectroscopy, and examples of novel dye systems capable of probing reactions at the single-molecule level are even more rare. The FRET based probe system presented in Chapters 3 and 4 of this work represents a significant advancement to the field in many aspects. First, using FRET to identify individual catalytically generated products is an entirely new approach to the study of catalytic reactions at the single-molecule level never before reported in literature. This work also represents the first single-molecule investigation of the copper(I) azide-alkyne cycloaddition click reaction, or any click reaction, and is also the first example of AlexaFluor dyes employed to study catalysis at the single molecule level.

For the synthetically challenged catalysis researcher, the single-molecule microscopy approach described in Chapter 4 is a ‘holy grail’ technique, applying commercial dyes to probe catalytic activity of a commercial catalyst. Although this will not always be the case (CuNP in Chapter 3 are not commercially available for example), the FRET system is entirely adaptable to other catalytic systems and appropriate probes may already be available since Molecular Probes (Life Technologies) has commercialized enough probes to fill a 1000 page handbook.[1] The increasing ease of use of TIRF microscopy and other single-molecule spectroscopies further contributes to the accessibility of this approach for those unfamiliar with the field. The microscope system used for this work is entirely commercial from Olympus, and most major microscope manufactures sell similar systems also as complete packages. For the more budget conscious researcher (or more adventurous), TIRF systems can be home-built with relative ease from rather inexpensive components and a standard inverted fluorescence microscope. With this in mind, this thesis and the work contained within it should serve as a springboard for further development of advanced probe systems and methodologies capable of examining catalytic and non-catalytic reactions and materials at the single-molecule – single-catalytic turnover level.

5.2 Future Directions

5.2.1 Modular click-based approach to optical sensors

A significant drawback of the click-formed triazole-based sensors detailed in Chapter 2 is the pH sensitivity and required addition of buffers or hydroxide base. Sensors **1**, **2**, and **3** exhibit some emission signal in the absence of their respective analyte ions if base or buffer is not added to the sample solutions, although the case of sensor **3** is more complicated (the reader is directed to Chapter 2). While this thesis focuses on the use of CuAAC chemistry as a modular approach to the synthesis of optical sensors, the pH sensitivity of these sensors should be investigated further if they are to find utility.

It has been observed that N atoms of aza-crown ionophore based sensors exhibit reduced basicity when they can participate in a delocalized π-system, for example anilino-modified ionophores.[2] This makes modular sensor synthesis difficult however. One possible solution to introduce aromaticity around the azacrown nitrogen could be to position an anilino spacer between the azacrown nitrogen and the terminal alkyne by means of *para* alkyne substituted aniline. The anilino spacer will serve the same purpose as the alkyl spacer sensors **1-3** currently exhibit as well as provide the much needed electron delocalization to reduce the basicity of the PET signal producing azacrown nitrogen.

All of the work in this thesis on sensors **1-3** was in aqueous media and shows that the sensors function excellently in solution phase. The desirable end product of sensors such as these, however, would be sensors incorporated into a heterogeneous material such as a hydropolymer in which analyte solutions can be flowed over to allow for in-line analysis. Sensors **1-3** were designed around the same chromophore exhibiting a *tert*-butyl ester at the coumarin 7-position, which is transformed into a functional handle by hydrolysis to the carboxylate. In preliminary work not presented in the thesis, EDC-NHS amide coupling of the carboxylate analogue of **1** with a low molecular weight amino-terminated polyethylene glycol (PEG) did not alter the sensing properties of **1**. Although PEG-modified **1** is still soluble in aqueous solution, this is proof-of-concept that these sensors can be functionalized to polymers leaving the door open for more thorough efforts towards conjugation to hydrogels.

5.2.2 Single-molecule microscopy of catalytic reactions

In the original report by Khlobystov *et al.* on the CuNP catalysts that we used for study in Chapter 3, the nanoparticle catalysts afforded complete conversion of alkyne and azide reagents after up to 72 hours of reaction at 40°C. These CuNP are far from the most active copper nanomaterials reported to date, especially considering the required temperature (**Table 1-1**). Single-molecule microscopy imaging of the same FRET system described in Chapter 3 with a variety of nanomaterials of differing reported activity would provide valuable insight into how the materials are unique at the single-particle level. For simplicity, we chose only a single nanomaterial catalyst to demonstrate the power of this technique in deciphering the phase of catalysis. To proceed, the next logical step would be applying our knowledge to investigate other reported nanomaterials as well as materials we have developed ourselves with the objective of designing an optimized, highly active and reusable heterogeneous CuAAC catalyst.

Many copper nanomaterials, including the commercially available copper-on-carbon catalyst with which we demonstrated super-localization CuAAC activity mapping in Chapter 4 are known to exhibit catalytic activity for reactions outside of the CuAAC cycloaddition. For example, some CuNPs have shown high activity for catalyzing C-C, C-S and C-N bond forming reactions among others. Investigating the activity of copper-on-charcoal catalyst toward other catalytic bond-forming reactions by developing appropriate dye probe systems is a direction we may take in the future leading to the possible development an inexpensive commercial 'catalyst-of-all-trades'.

5.3 Claims to Original Research

1. Development of a novel small library of ion sensors based on CuAAC formed triazoles participating in signal transduction, including a unique sensor that displays a variable two-stage sensing range, modulated with the addition of KOH.

2. First single-molecule observation of CuAAC catalysis in real time.

3. Development of a single-molecule approach to deciphering the phase of catalysis; determining whether a catalyst is truly heterogeneous or acts homogeneously through leaching of catalytically active Cu(I) ions. This approach is easily applied to other catalytic systems through intelligent design of fluorescent (fluorogenic) probes to study the reaction.

4. Development of a BODIPY based probe system for studying Cu-acetylide formation between dye labeled alkyne and heterogeneous CuNP on a solid support (joint work with S. Impellezzeri).

5. First example of super-localization reactivity mapping of CuAAC activity on a heterogeneous supported Cu catalyst.

5.4 Publications

5.4.1 Contributing to this thesis

1. Decan, M. R., Impellizzeri, S., Marin, M. L., Scaiano, J. C. Copper nanoparticle heterogeneous catalytic 'click' cycloaddition confirmed by single-molecule spectroscopy. *Nature Communications* **5**:4612 (2014).
doi: 10.1038/ncomms5612.

5.4.2 Not contributing to this thesis

2. Scaiano, J. C.*, Netto-Ferreira, J.C., Alarcon, E., Billone, P., Bueno Alejo, C., Crites, C.O., Decan, M. R., Fasciani, C., González-Béjar, M., Hallett-Tapley, G., Grenier, M., McGilvray, K.L., Pacioni, N.L., Pardoe, A., René-Boisneuf, L., Schwartz-Narbonne, R., Silvero, M.J., Stamplecoskie, K. G., and Wee, T. S. Tuning plasmon transitions and their applications in organic photochemistry. *Pure and Applied Chemistry* **83**(4); 913-930 (2011).

3. McGilvary, K., Decan, M. R., Wang, D., Scaiano, J. C. Facile photochemical synthesis of unprotected aqueous gold nanoparticles. *The Journal of the American Chemical Society* **128**(50); 15980-15981 (2006).

5.4.3 Manuscripts in preparation

4. Decan, M. R., Scaiano, J. C. A Click-Based Modular Synthesis of Fluorescent Metal Ion Sensors. (*Manuscript in preparation*).

5. Decan, M. R., Scaiano, J. C. Super-localization Click Activity Mapping of a Heterogeneous Copper-in-Charcoal Supported Catalyst. (*Manuscript in preparation*).

6. Scaiano, J.C., Decan, M. R., Hodgson, G., Impellizzeri, S., Lanterna, A., McTiernan, C., Pitre, S., Determining the phase of catalysis through single-molecule spectroscopy. *Catal. Sci. Technol. (Invited review in preparation*).

5.5 References

1. Johnson, I. & Spence, M. (eds.) *The Molecular Probes Handbook, A Guide to Fluorescent Probes and Labelling Technoogies*, Ed. 11. (Invitrogen by Life Technologies, USA; 2010).
2. de Silva, A.P. *et al.* Signaling Recognition Events with Fluorescent Sensors and Switches. *Chem. Rev.* **97**, 1515-1566 (1997).

Appendix

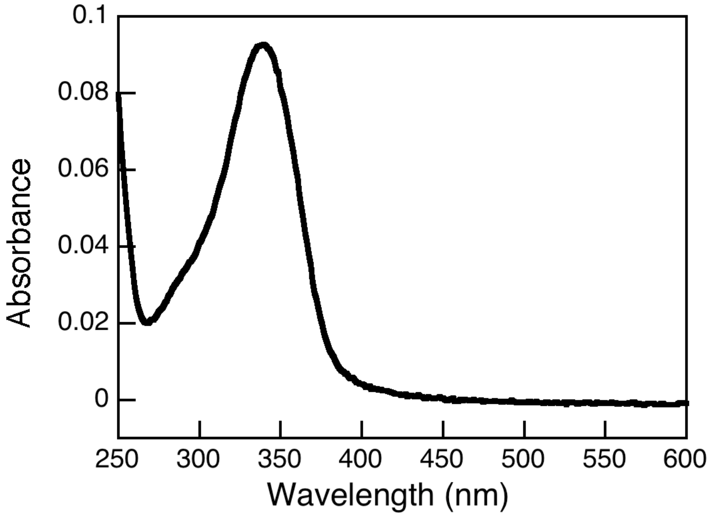

Figure A2-1. Absorbance spectrum of 8.5 μM **1** in aqueous Na_2HPO_4 buffer.

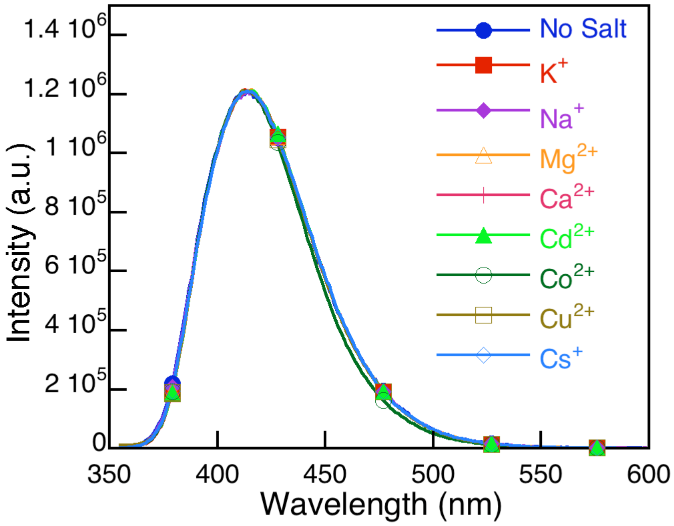

Figure A2-2. Normalized fluorescence emission spectra of K^+ sensor (**1**) buffered at pH 9.7 with 50 mM K^+ and 100 mM of various other cations with 340 nm excitation showing no shift in λ_{max}.

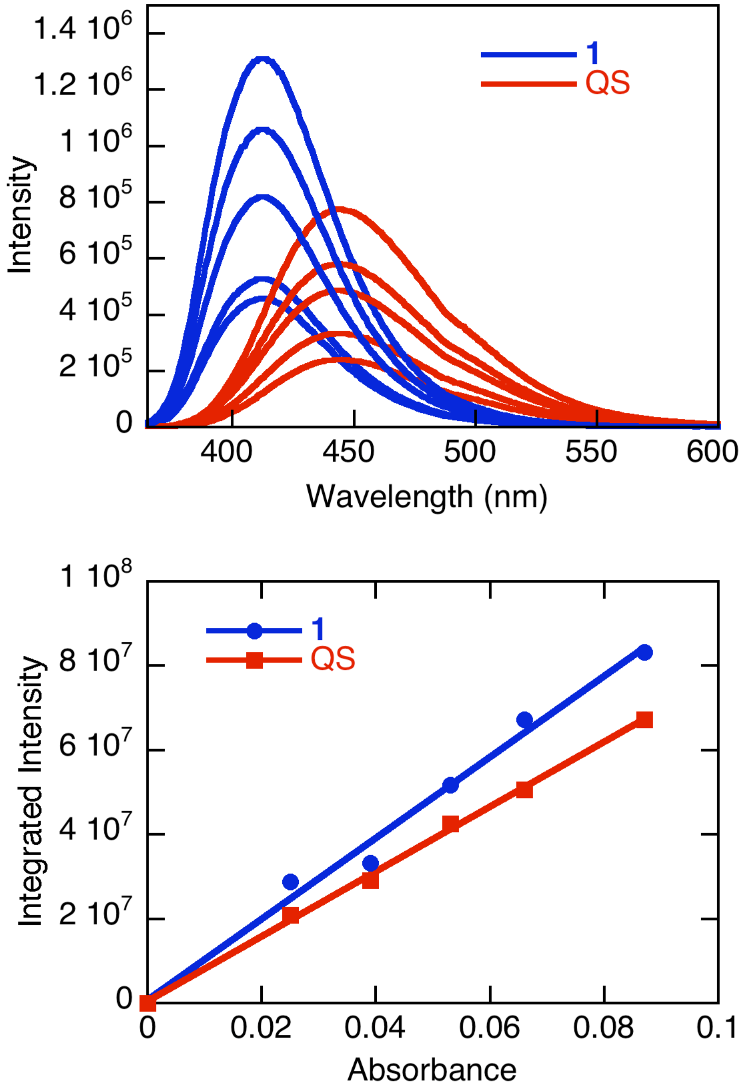

Figure A2-3. Emission spectrum of solutions of 1 in water and Quinine Sulfate in 0.1M H_2SO_4 with matching absorptions at 340 nm (top), and the corresponding integrated emission intensity of each solution plotted against the absorbance (bottom).

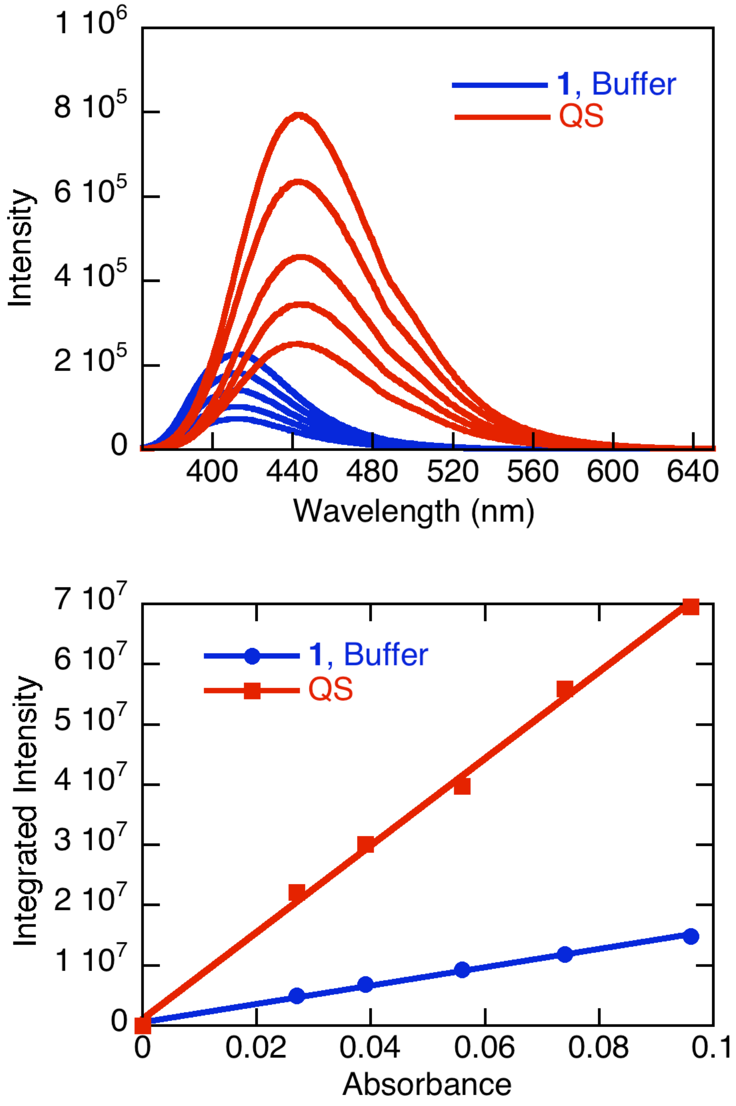

Figure A2-4. Emission spectrum of solutions of 1 in Na$_2$HPO$_4$ buffer and Quinine Sulfate in 0.1M H$_2$SO$_4$ with matching absorptions at 340nm (top), and the corresponding integrated emission intensity of each solution plotted against the absorbance (bottom). The slope of the line in the bottom plot is equal to the quantum yield of fluorescence.

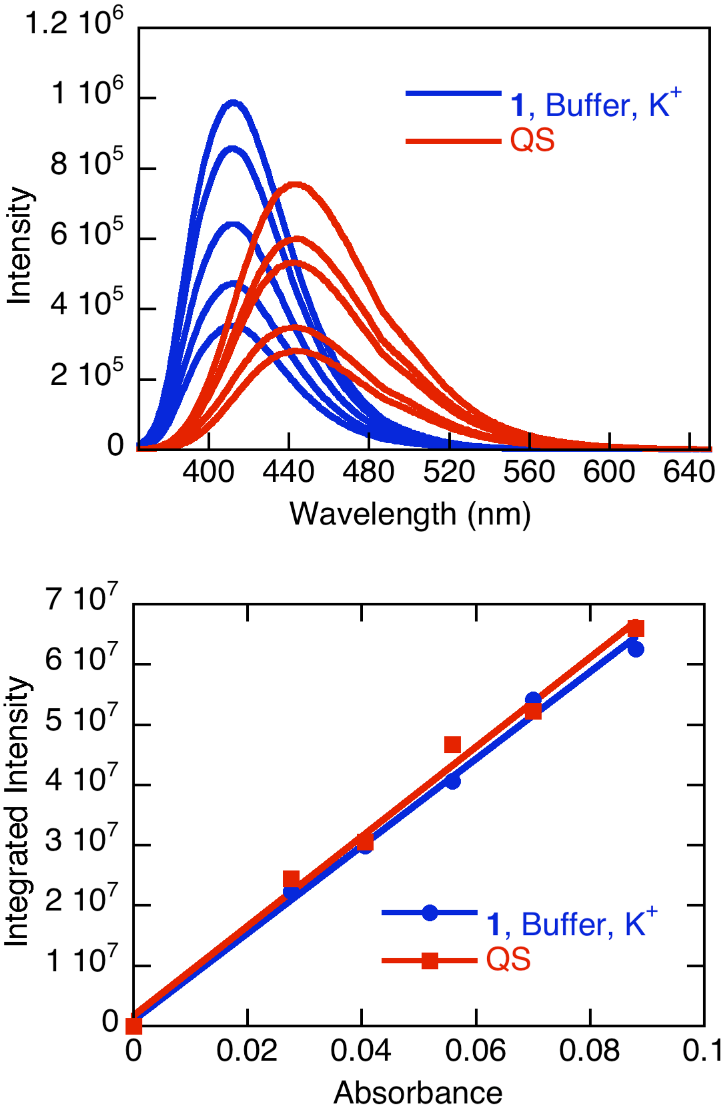

Figure A2-5. Emission spectrum of solutions of 1 in Na_2HPO_4 buffer with 50 mM K^+ and Quinine Sulfate in 0.1M H_2SO_4 with matching absorptions at 340nm (top), and the corresponding integrated emission intensity of each solution plotted against the absorbance (bottom). The slope of the line in the bottom plot is equal to the quantum yield of fluorescence.

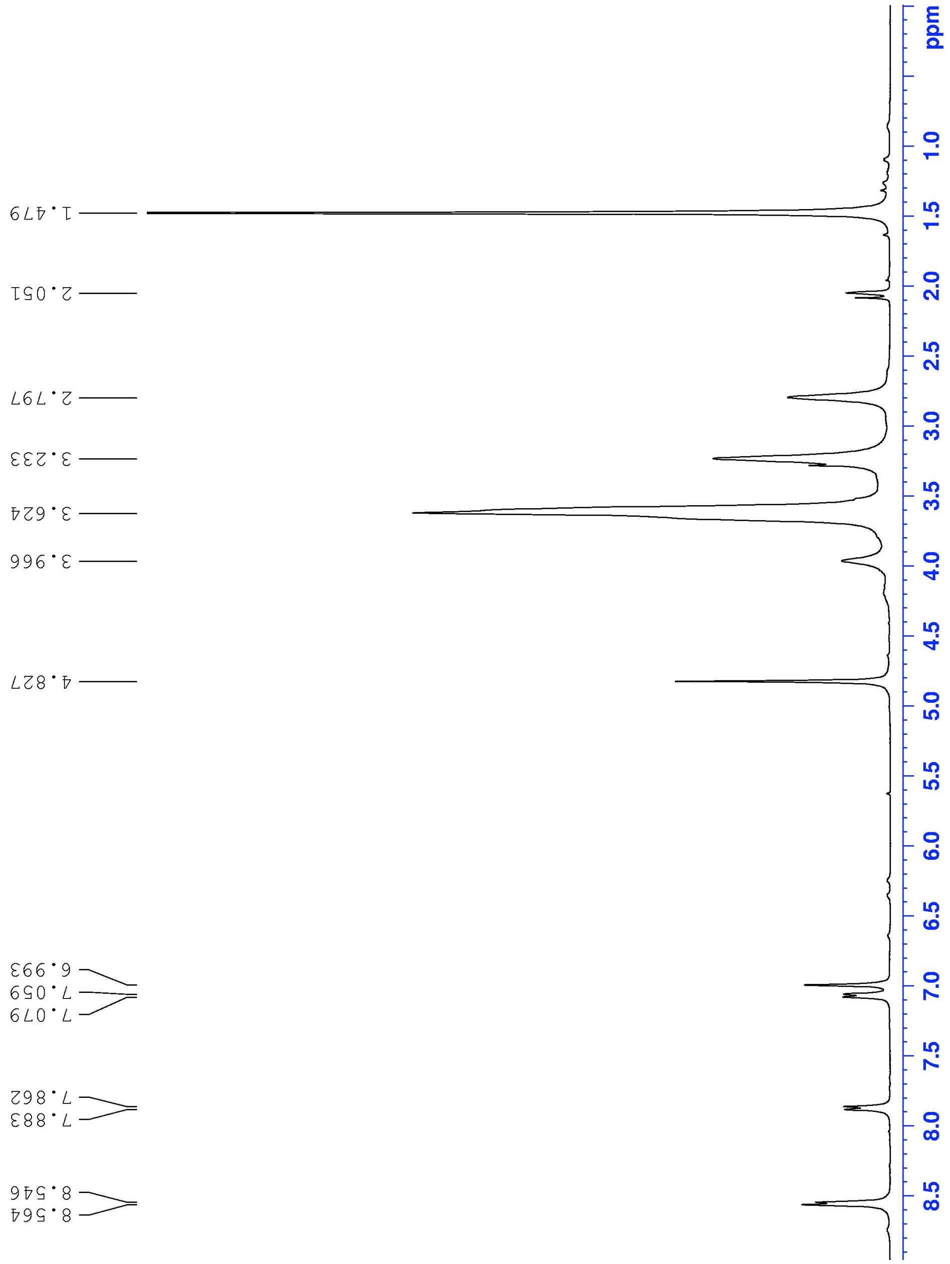

Figure A2-6. ^{1}H NMR spectrum of sensor **1**.

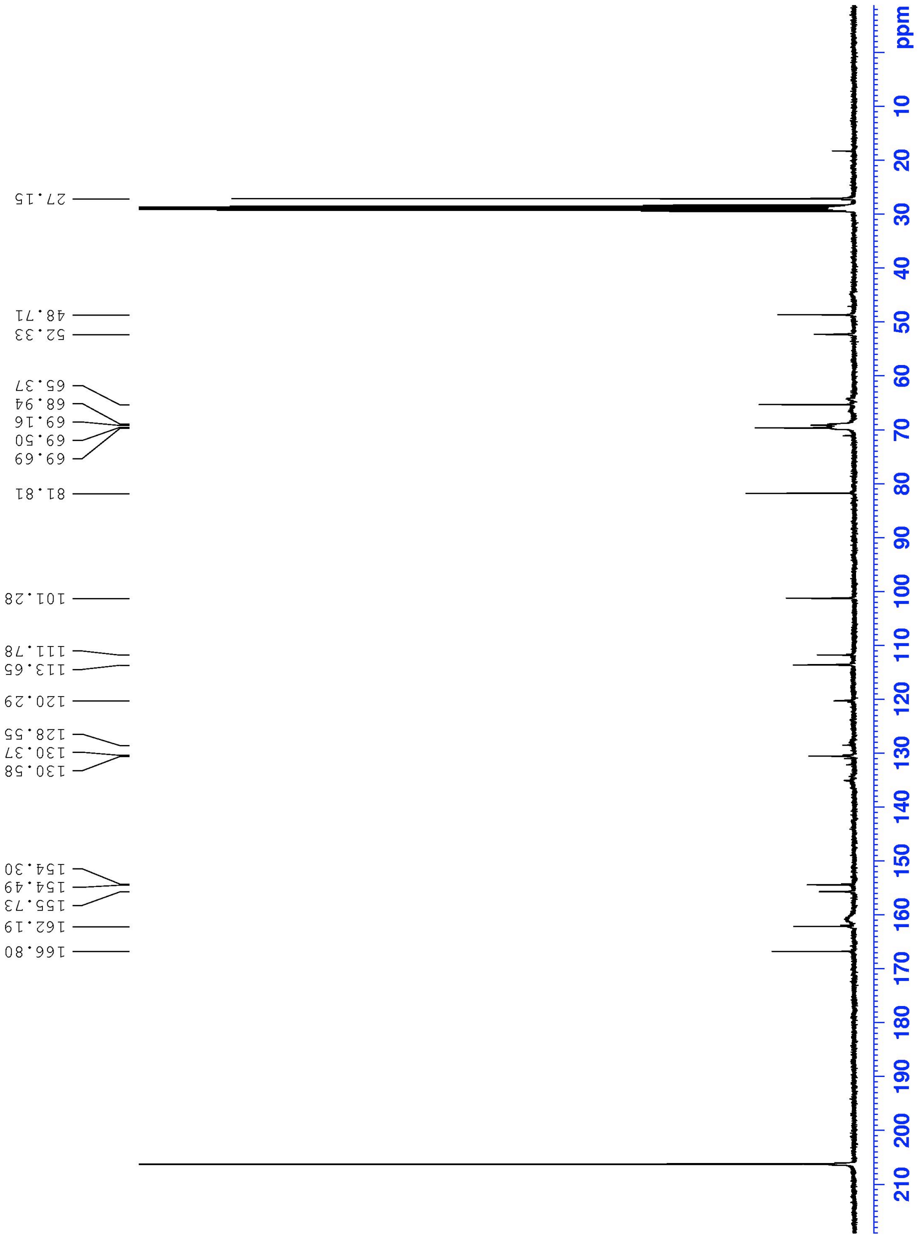

Figure A2-7. ^{13}C NMR spectrum of sensor **1**.

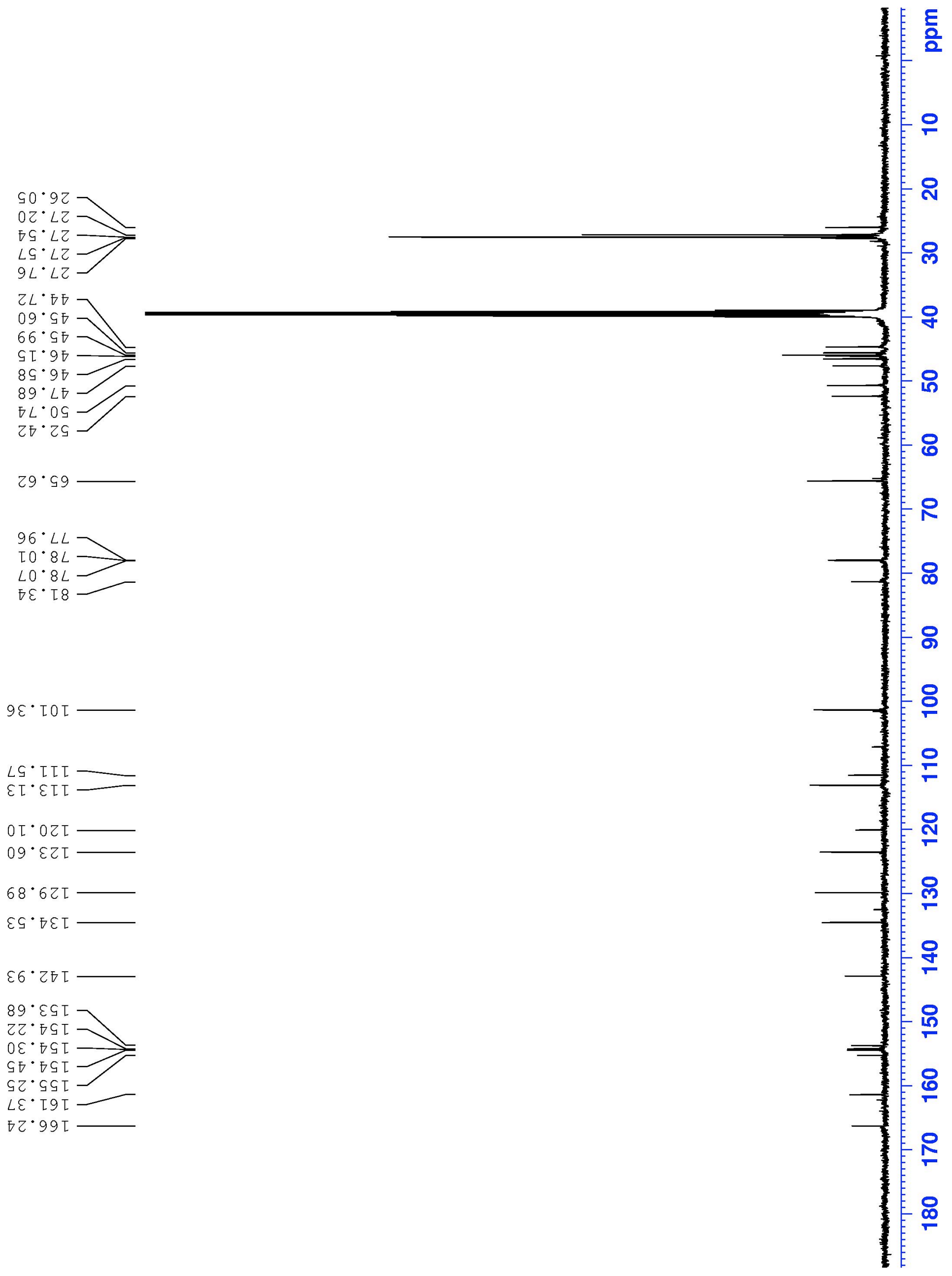

Figure A2-8. ^{13}C NMR spectrum of **N-boc-2**.

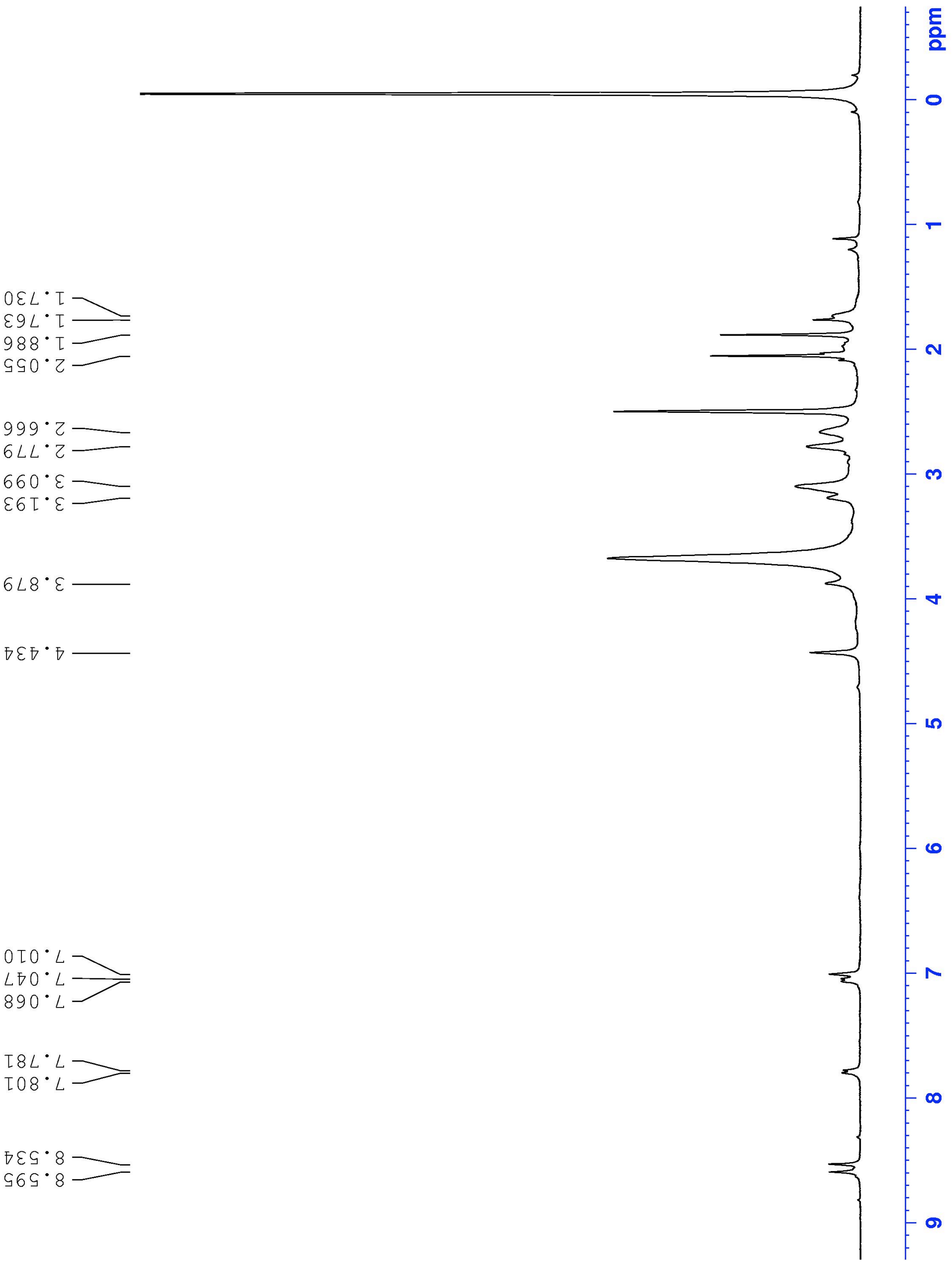

Figure A2-9. ^{1}N NMR spectrum of sensor **2.**

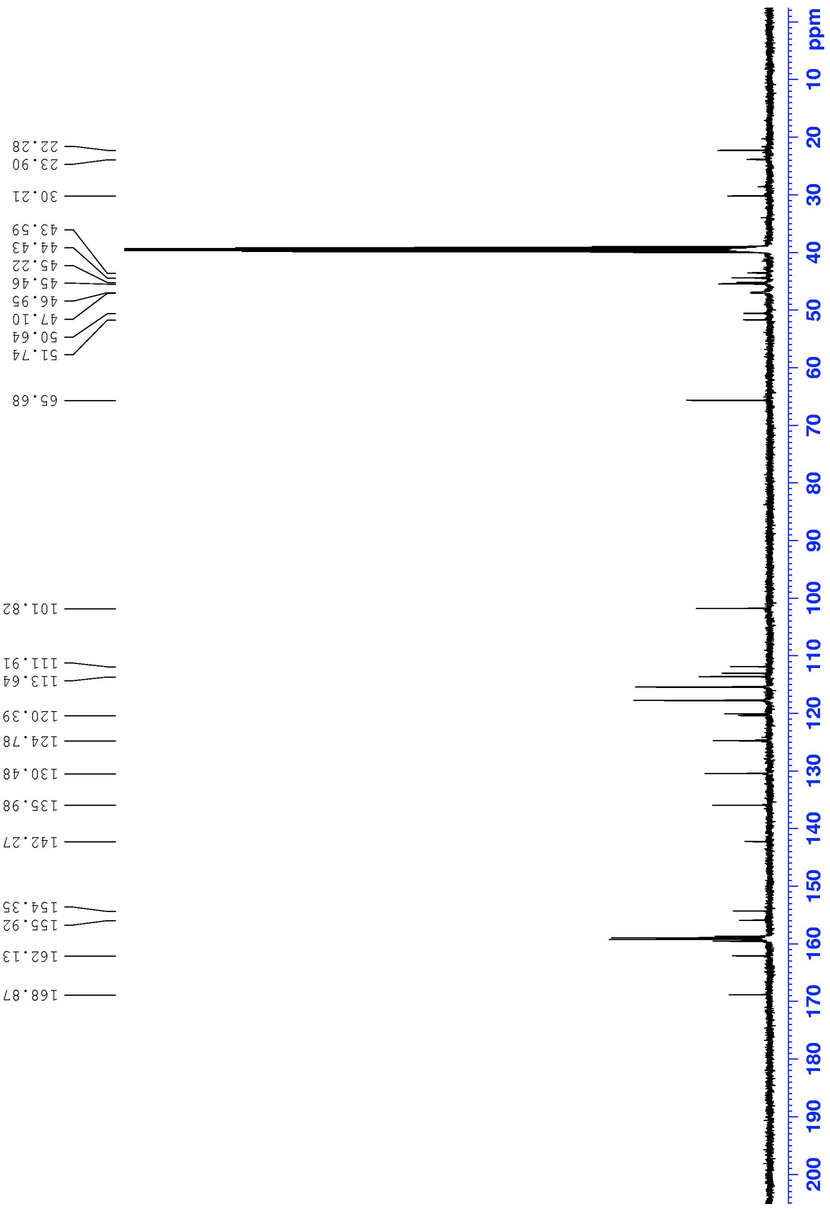

Figure A2-10. ^{13}C NMR spectrum of sensor **2**.

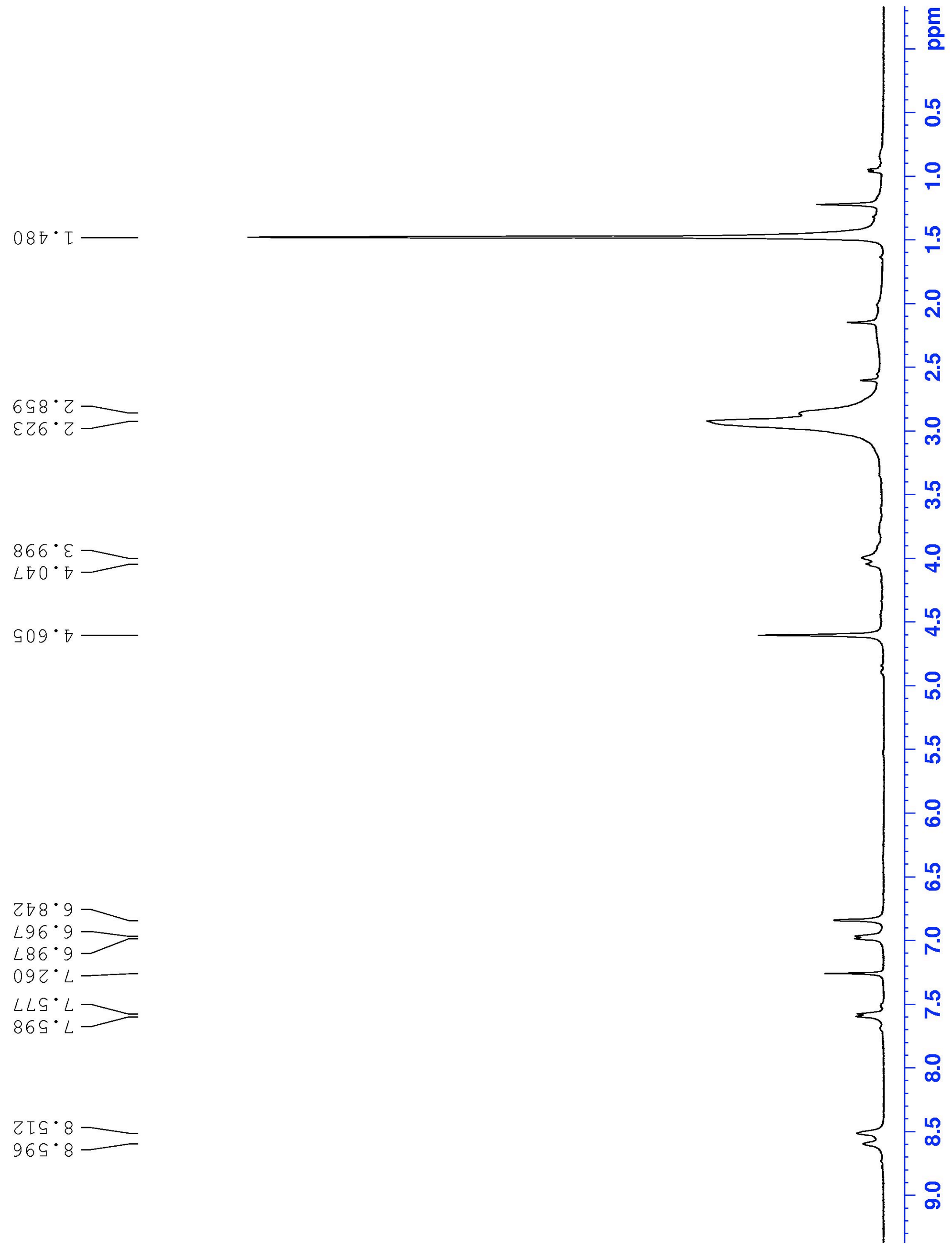

Figure A2-11. ^{1}H NMR spectrum of sensor **3**.

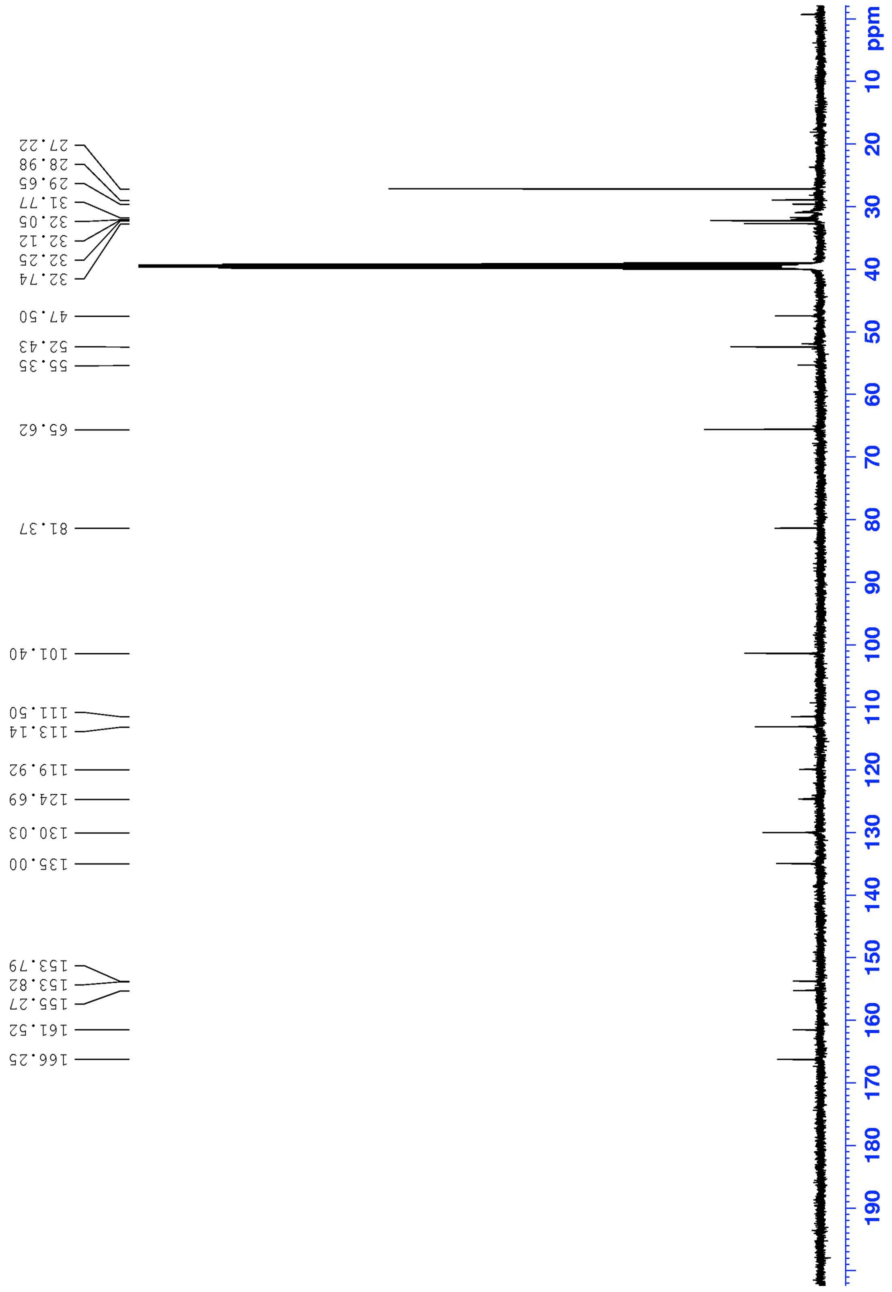

Figure A2-12. ^{13}C NMR spectrum of sensor **3.**

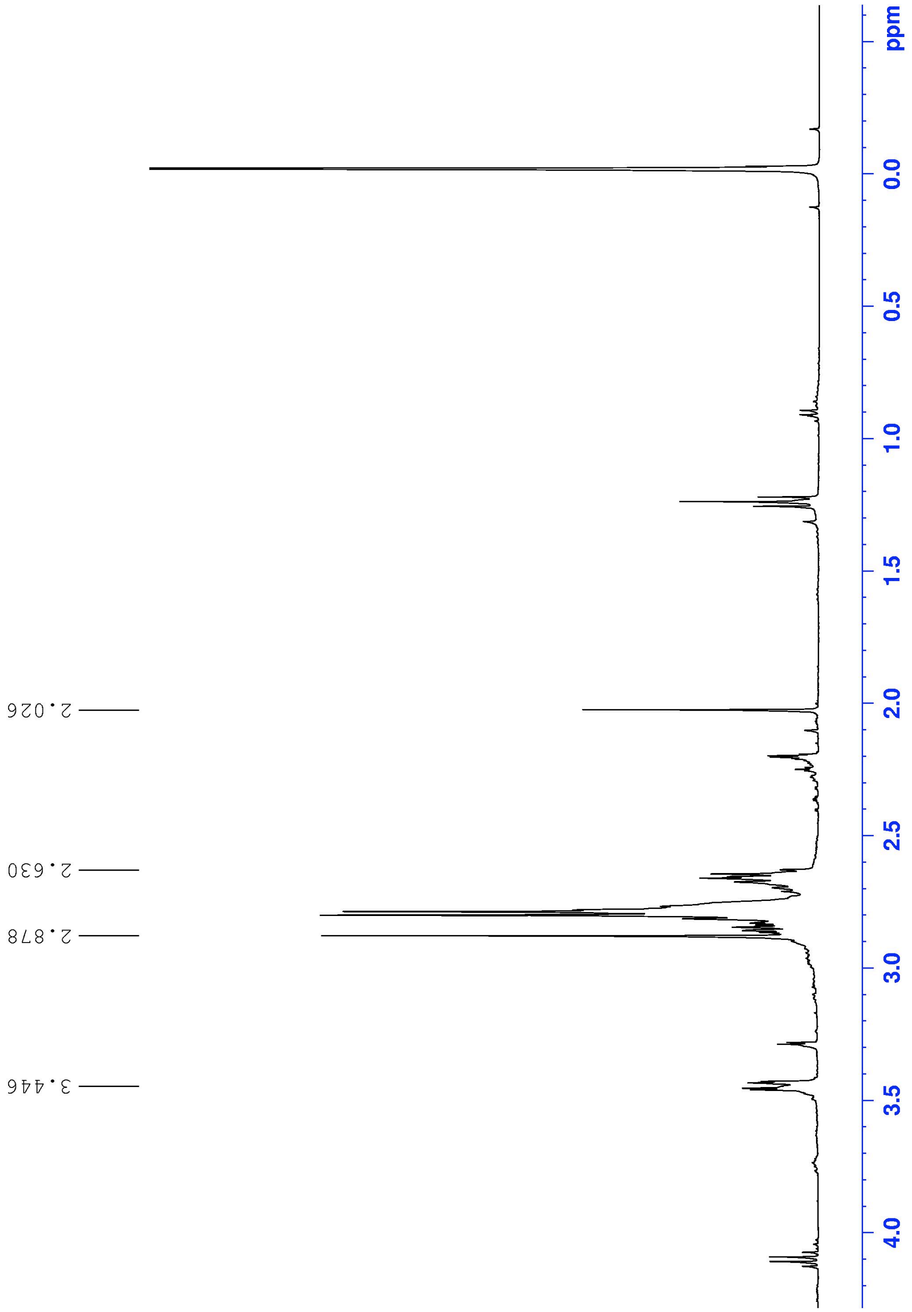

Figure A2-13. ^{1}H NMR spectrum of **9**.

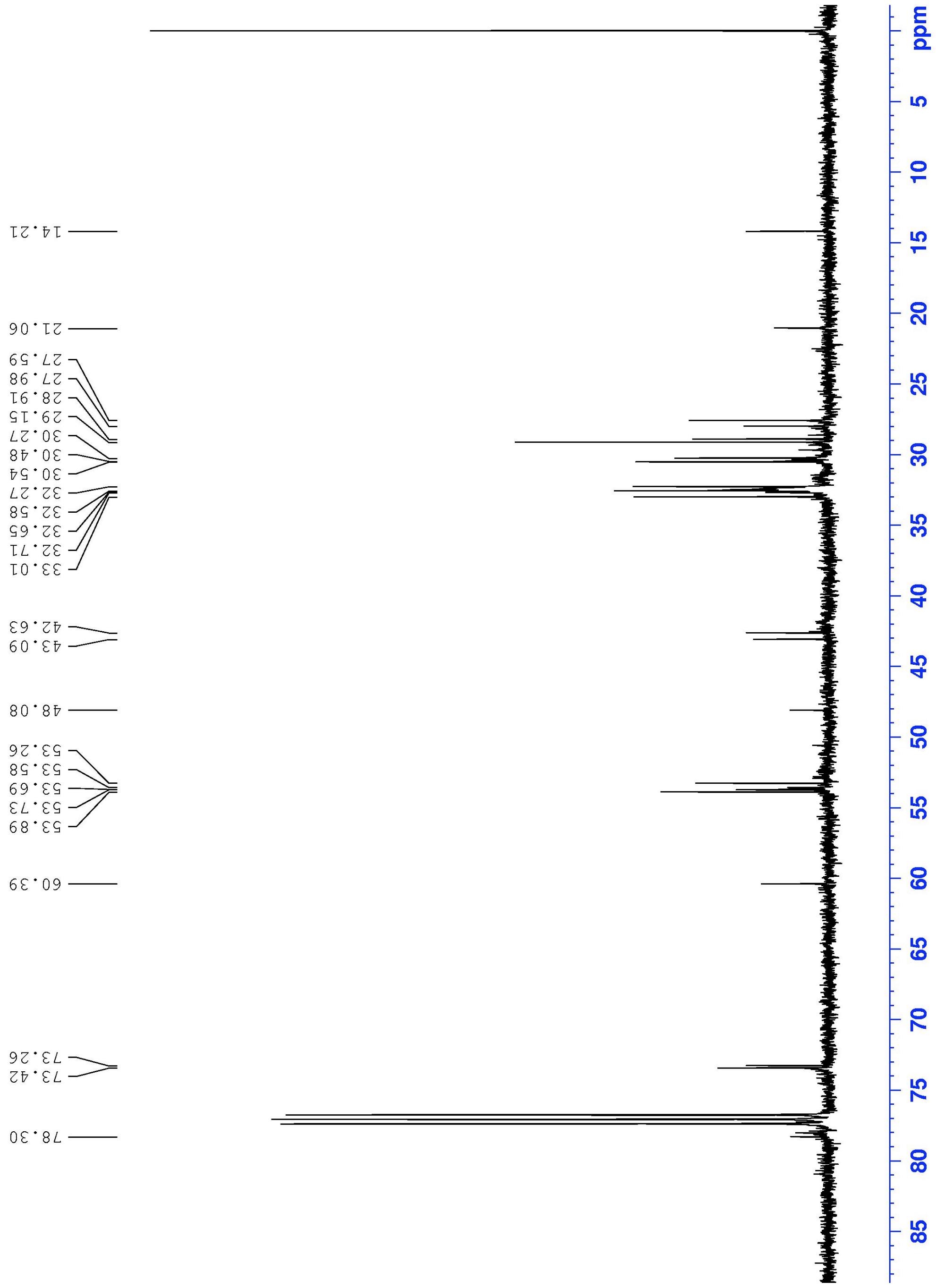

Figure A2-14. ^{13}C NMR spectrum of **9**.

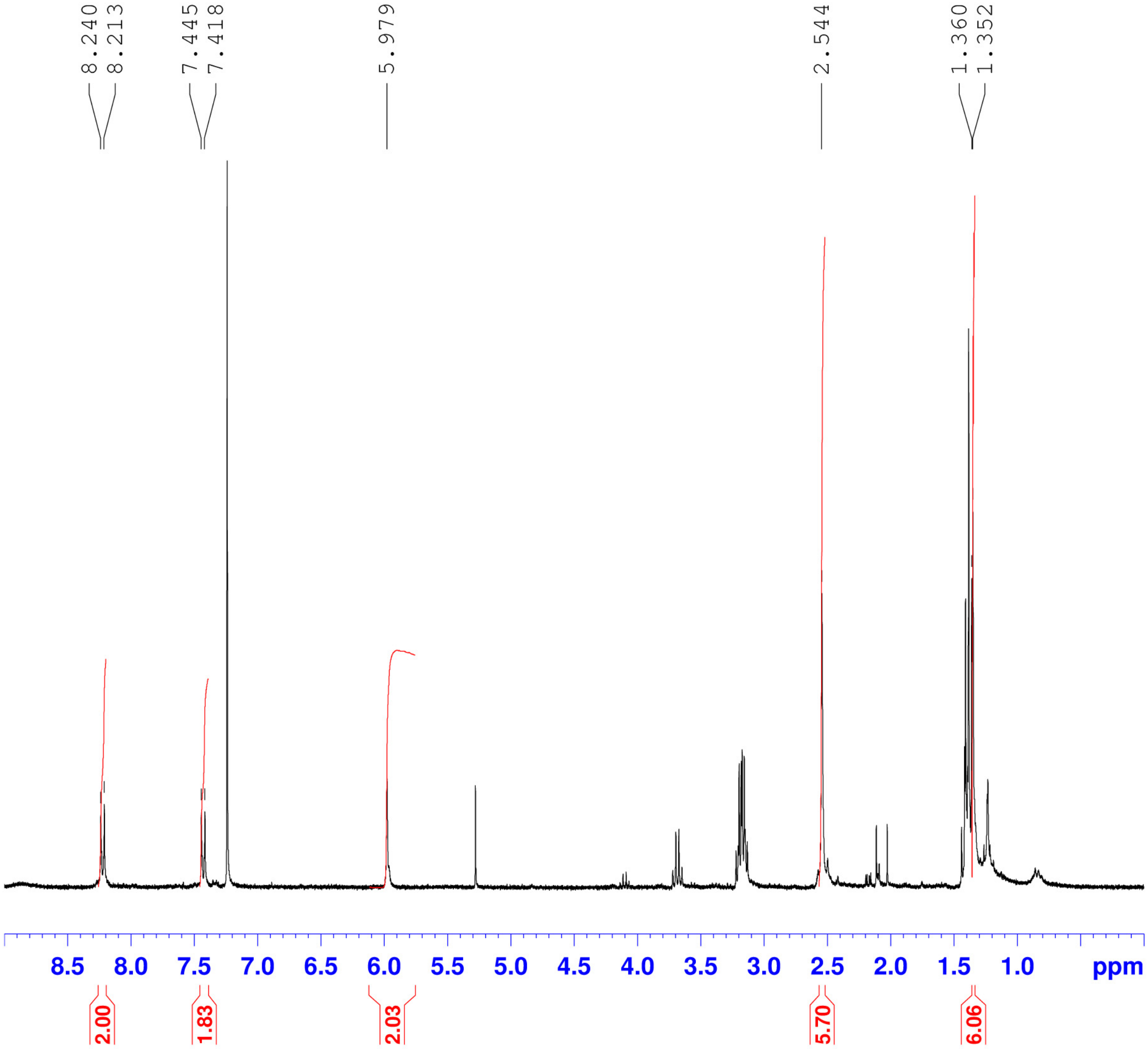

Figure A3-1. ^{1}H NMR spectrum of BODIPY-COOH

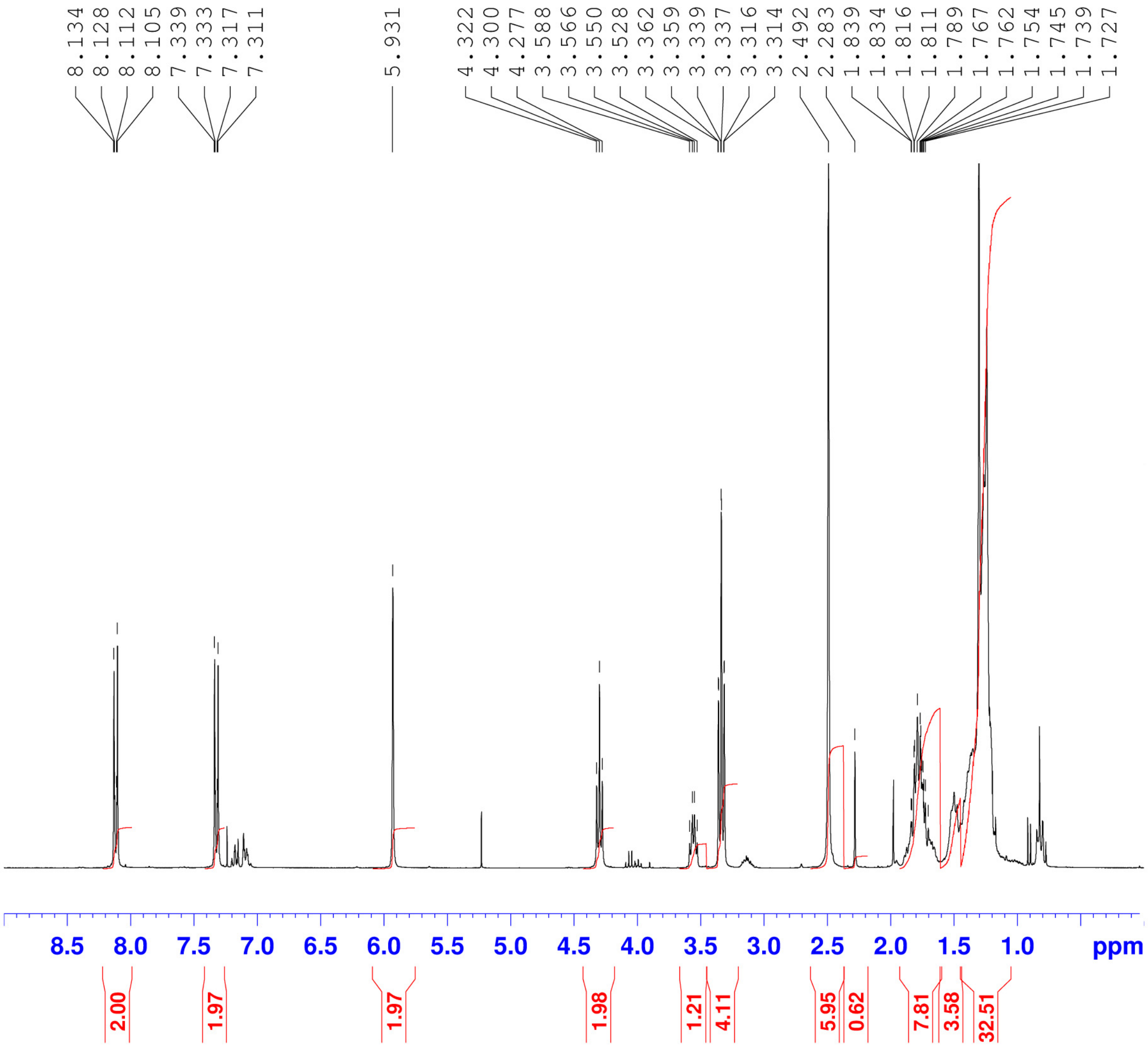

Figure A3-2. ^{1}H NMR spectrum of BODIPY-decylbromide.

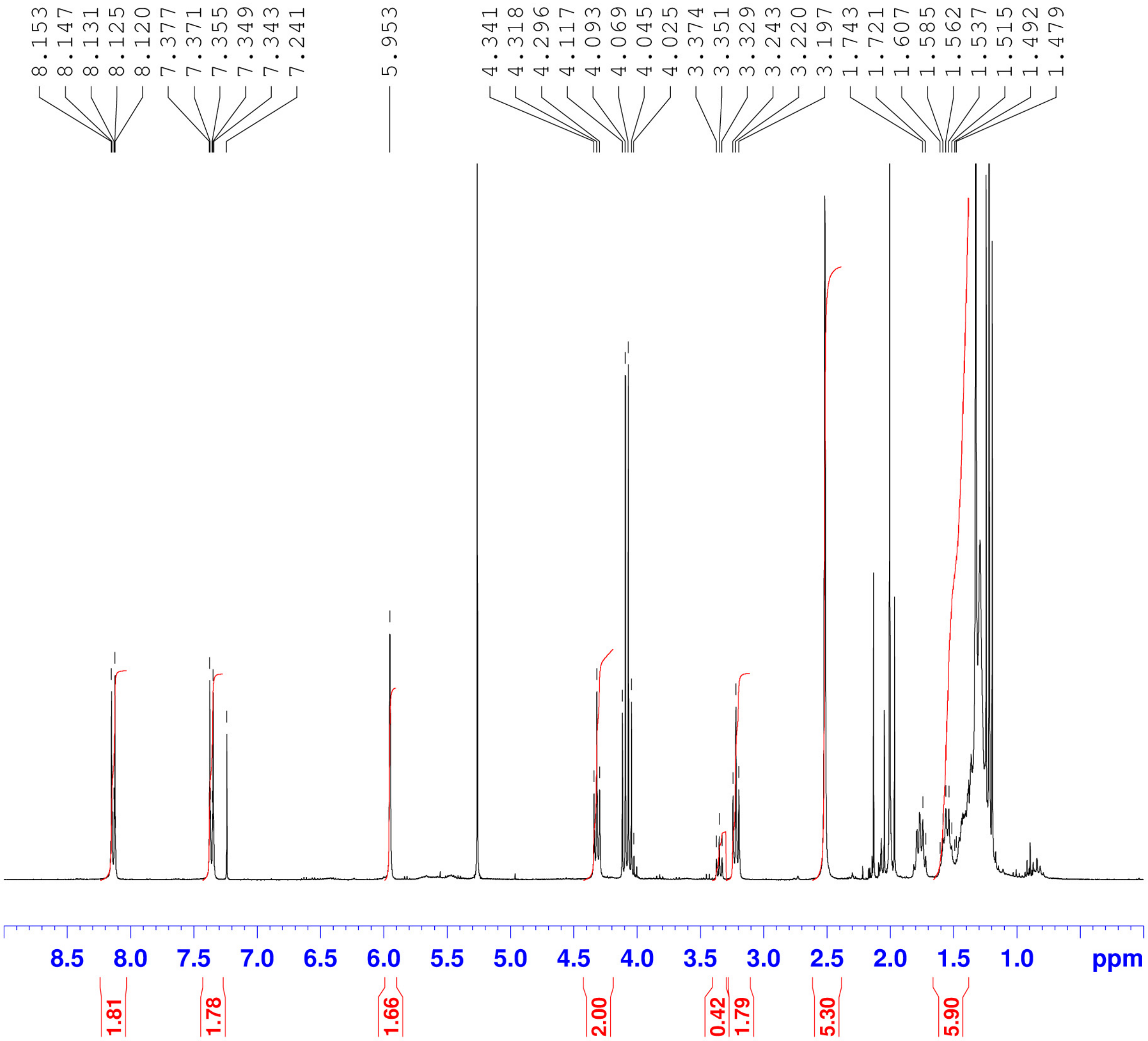

Figure A3-3. ^{1}H NMR spectrum of BODIPY-Azide, **11**.

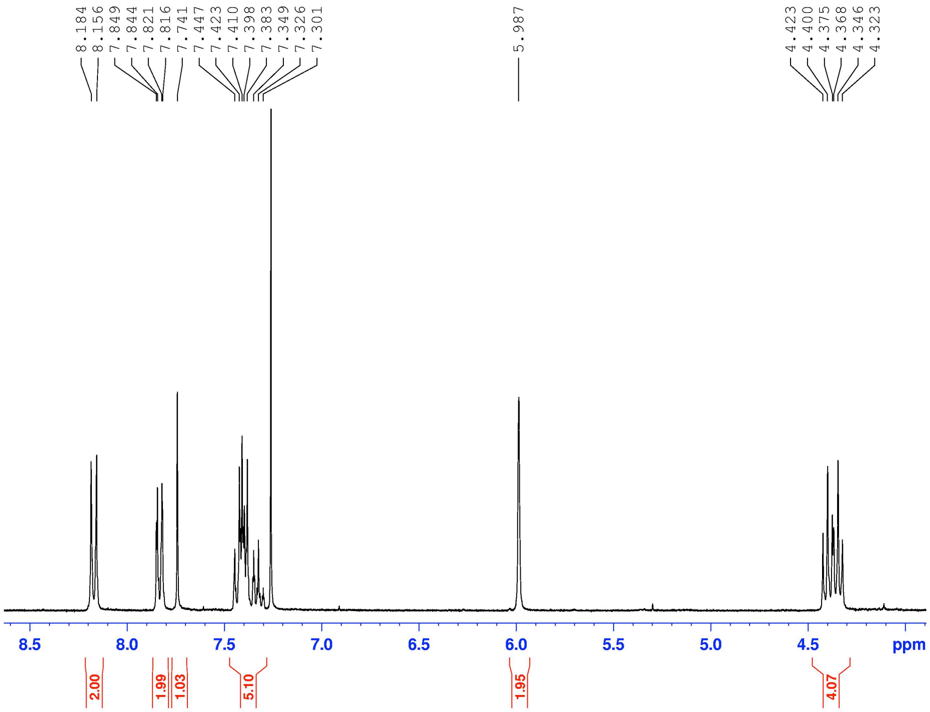

Figure A3-4. Expanded selected region of ^{1}H NMR spectrum of 1,2,3-triazole product **12**.

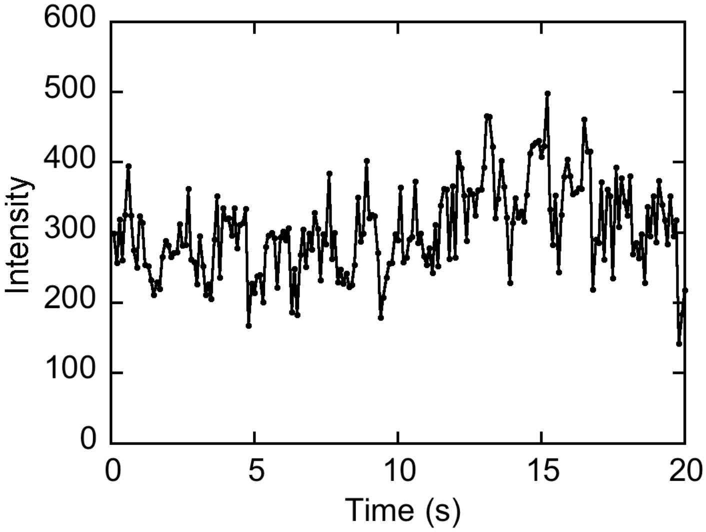

Figure A4-1. Fluorescence intensity vs. time trajectory of persistent bright spot in accumulated TIRF image (Figure 4-18-C1) showing no bursting events occurring.